Žičkus, Vytautas (2018) *Blood flow measurement in the zebrafish heart using light sheet microscopy.* PhD thesis.

https://theses.gla.ac.uk/30993/

Blood flow measurement in the zebrafish heart using light sheet microscopy

Vytautas Žičkus

School of Physics and Astronomy

University of Glasgow

This dissertation is submitted for the degree of

Doctor of Philosophy

College of Science and Engineering   October 2018

Abstract

The link between haemodynamics and cardiac tissue mechanics is an active area of research in developmental biology. Nevertheless, previous study of fluid-structure interaction in the developing heart was mostly confined to single projection blood flow measurements or computational fluid dynamics simulations using only the information of the heart wall structure. Hence, techniques capable of direct 3D + time resolved blood flow and heart wall motion are necessary to deepen the understanding of the cardiac function in the developing heart.

This work presents an imaging system which combines selective plane illumination microscopy (SPIM), with optical gating techniques, and micro particle image velocimetry (µPIV). This combination (referred here as SPIM-µPIV) allowed non-invasively measuring blood flow in the developing zebrafish heart in a depth and time-resolved manner. Our system surpasses conventional µPIV measurement systems based on wide-field illumination which suffer from measurement errors due to volume illumination of the sample.

The proposed SPIM-µPIV system was validated in a control microfluidics experiment where flow of fluorescent microspheres was measured in a 50 µm diameter tube. Both qualitative and quantitative analysis was performed to compare our SPIM-µPIV against conventional brightfield-µPIV measurements. Furthermore, this work implements a different metric for "cross-correlation" which was empirically found to perform better than the traditional algorithm used in PIV analysis, when motion of large particles is measured.

By implementing optical gating techniques to our analysis, 3D + time blood flow measurements in the beating hearts of 3, 4, and 5 day old zebrafish hearts were obtained. The recovered 3D + time velocity information enabled further investigation of the heart function such as the pumping efficiency which was obtained by calculating the flow rate through a section of a heart chamber.

In summary, it is proposed that SPIM-µPIV system can be a useful tool for direct blood flow measurements in transparent small-animal models. Such measurements would benefit the current knowledge of fluid-structure interaction phenomena in the developing heart, and could be used to validate previous work by other groups.

Declaration

I hereby declare that except where specific reference is made to the work of others, the contents of this dissertation are original and have not been submitted in whole or in part for consideration for any other degree or qualification in this, or any other university. This dissertation is my own work and contains nothing which is the outcome of work done in collaboration with others, except as specified in the text and Attributions.

Some of the work presented in this thesis has been published, and the relevant publications are listed below.

Publications

<div align="right">

Vytautas Žičkus
October 2018

</div>

Attributions

Some of the work carried out in this thesis heavily employed methods, tools, and techniques developed by other people and their contribution is summarized here

Selective Plane Illumination Microscopy (SPIM) microscope   The SPIM microscope used in this work (in particular, configuration A, shown in Figure 2.16) was built by Dr Jonathan M. Taylor, and later rebuilt by the author. Synchronization of camera and laser pulse timing in order to implement "PIV mode" described in section 2.3, was also carried out by Dr Jonathan M. Taylor. Configuration B of the SPIM system was proposed to Dr Jonathan M. Taylor by Dr Thai Truong, and implemented by the author. The "shadow reduction" mirror was implemented by the author and the source for this set-up is referenced in the caption of the diagram of our SPIM system.

Analysis and visualization   The computer code for SPIM acquisition, and most importantly, the heart phase recovery for both real-time and offline analysis (method described in Chapter 2 and used in Chapter 4) was developed by Dr Jonathan M. Taylor.

The Particle Image Velocimetry (PIV) analysis carried throughout this thesis was performed with a modified open-source OpenPIV Python code [1]. The code was modified to allow the use of different sized interrogation windows with the help of Dr Jonathan M. Taylor. The fast (C-based) implementation of the Sum of Absolute Differences (SAD) algorithm was written by Dr Jonathan M. Taylor. The synthetic data generation in the analysis in Chapter 2 was performed using PIVlab, a MATLAB package [2]. The qualitative analysis of depth-of-correlation in Chapter 3 was heavily based on the work by Hein et al. [3].

The type of visualization shown in Figure 3.11 was proposed by Richard Hoppe. 3D visualizations in Chapter 4 were rendered using an open-source Mayavi package [4]. Illustrations created with open-source vector drawing software Inkscape [5]. 2D plots and graphs were created with Matplotlib [6], and the information presented there was analysed using the functionality of Numpy [7] and Scipy [8] libraries, unless otherwise stated.

Raw data   The raw data used in the analysis of the results shown in Figure 4.4 (and other figures based on the same sample in Chapter 4) were obtained by Dr Jonathan M. Taylor. The raw data of the 3 day old zebrafish atrium heart was also obtained by Dr Jonathan M.

Taylor. All the analysis and visualization was carried-out by the author. All other raw data was obtained by the author.

Figures   Figures which were reproduced/adapted in this thesis clearly state "taken/adapted from" in their respective captions followed by the literature source. Some of these figures (Figure 1.1, Figure 1.2, Figure 1.4b, Figure 1.9) were under Creative Commons licence. Figure 1.8, Figure 4.3, and Figure 2.4 were reproduced/adapted with permission. Figures which were created by the author based on work by others is clearly indicated in the corresponding captions. Figure 1.7 was provided by Dr Jonathan M. Taylor. Figures created by the author which were published are clearly referenced in the corresponding captions.

Zebrafish samples   Zebrafish samples were maintained by Dr Carl Tucker, Dr Sebastien Rider, and Dr Charlotte Buckley at the University of Edinburgh zebrafish facility. Animals used in this work were maintained according to the Animals (Scientific Procedures) Act 1986, United Kingdom.

Acknowledgements

I would like to acknowledge the support and express my gratitude to the following:

My supervisor, Dr Jonathan M Taylor for his mentorship, patience, and ability to always remain optimistic, even when my research went awry.

Dr Hao Gao and Prof Xiaoyu Luo for their advice on computational fluid dynamics modelling.

The friendly people of the Imaging Concepts Group. In particular, PZ and PCK for their friendship and advice for the last 4 years.

PZ, PCK, CJN, IB, and JMT for their comments and proof-reading on my thesis and other work.

Dr Carl Tucker and Dr Sebastien Rider for teaching me how to perform microinjections in the zebrafish, and to Dr Charlotte Buckley for providing zebrafish samples.

The Engineering and Physical Sciences Research Council UK, which funded this PhD.

Finally, my mother for her support with which I was able to pursue higher education.

Table of contents

List of figures

List of tables

Abbreviations

Chapter 1

Introduction

1.1   Motivation

Blood flow plays a crucial role in the formation of the early embryonic heart, and compre-
hending fluid-structure interaction is necessary for accurate modelling of the heart function
[9]. Ability to accurately measure flow in the heart could allow studying drug and nutrient
transfer, or haemodynamic forces such as Wall Shear Stress (WSS), which is a particularly
interesting parameter. WSS plays a significant role in the cardiovascular system by trigger-
ing a response in endothelial cells (the inner lining of the heart and blood vessels) which in
turn controls the growth and shape of blood carrying organs [10, 11]. Direct measurement
of WSS in the heart is a particularly challenging task due to the highly dynamic nature of
the heart, and 3D+time information has been recently extrapolated from heart wall motion
information [9]. In an attempt to fill this lack of experimental methodology for direct blood
flow measurements in 3D + time, this thesis explores the use of Light Sheet Fluorescence
Microscopy (LSFM) for micro-scale flow measurements *in vivo*. This is realised in practice
by combining the following:

- Selective Plane Illumination Microscopy (SPIM), a type of light sheet microscope
  which utilises a cylindrical lens for light sheet formation [12].

- micro Particle Image Velocimetry (µPIV), a non invasive flow measurement technique
  derived from the macro-scale PIV techniques originally developed in the field of
  aerospace engineering[13].

- Optical heart gating techniques, which enable "computationally freezing" the heart,
  to facilitate 4D analysis [14, 15].

The thesis aims to investigate the feasibility of SPIM-µPIV system, and apply it to obtain 3D
+ time flow information in the developing zebrafish heart and to compare it to conventional
methods such as brightfield µPIV.

In particular, this work puts an emphasis on imaging blood flow in the developing zebrafish heart. This work utilises real time optical gating techniques developed by Taylor et al. [15, 16]. These techniques, discussed later, "computationally freeze" the beating heart, which allows examining the 3D structure of the heart at a particular time in the cardiac cycle.

1.2 Synopsis

The main objective of this work is to investigate the practicality of a Selective Plane Illumination Microscopy (SPIM)-micro Particle Image Velocimetry (µPIV) system for imaging living, beating zebrafish embryo[1] hearts. This chapter provides a brief overview of the relevant literature to set the scene for this thesis. A brief overview of small animal models for embryonic heart development will be presented, and 3D-capable microscopy techniques will be mentioned. Then, 3D+time zebrafish embryo heart structure reconstruction from Light Sheet Fluorescence Microscopy (LSFM) imaging will be described. Next, different flow measurement techniques will be discussed, with particular examples of applications for zebrafish heart imaging. Finally, wall shear-stress will be reintroduced in more detail as a potential parameter to be measured using the SPIM-µPIV system validated in this thesis.

In Chapter 2, the theory of Particle Image Velocimetry (PIV) will be described in more detail, and the standard terminology will be introduced. The chapter will begin by discussing the basic assumptions made in standard PIV measurements. The major factors affecting measurement accuracy will be described, and investigated using synthetic data. Then, additional considerations necessary for conventional micro-scale PIV will be discussed. Finally, a comparison between the standard PIV algorithm and the Sum of Absolute Differences (SAD) algorithm used in this thesis will be made.

Validation of SPIM-µPIV technique using semi-synthetic, as well as real experimental data will be described in Chapter 3. Here, the effects of volume illumination on µPIV measurement accuracy will be investigated. Most importantly, this chapter will illustrate the advantages of using LSFM for flow µPIV measurements.

Chapter 4 will begin by discussing aspects of the experimental methods for *in vivo* blood flow measurements in zebrafish embryos. Then, both single-plane and depth-resolved measurements in the main blood vessels of the zebrafish embryo will be presented. Next, the flow characteristics of fluorescent red blood cells, as well as microinjected fluorescent particles, will be examined. This chapter will culminate by introducing the most important results of this thesis - measurements in the zebrafish heart. The chapter will conclude by a series of post-acquisition validation of measurements, and proposed improvements for future work.

---

[1]Fish up to 5 days old are referred as embryos in this thesis.

Finally, Chapter 5 will summarise this thesis by revisiting the main achievements of this work and by discussing the remaining challenges with SPIM-µPIV for *in vivo* imaging, and suggest potential future directions to expand and build upon this work.

1.3 Literature review

The literature review carried out here aims to give an overview of the key relevant work carried out by researchers in the past. The main emphasis in this thesis is on applying and verifying three techniques: a well-established flow measurement method from the field of engineering, a relatively new fluorescence microscopy technique, and a novel computational method for *in vivo* cardiac imaging. Since the main motivation for this work is to develop a tool for measuring physiological flows in small animals past *in vivo* work, particularly in the zebrafish, will also be reviewed.

1.3.1 Animal models for cardiovascular research

Cardiovascular research is highly motivated by the fact that heart disease is the chief cause of death and debilitating conditions in economically advanced countries. A number of different small animals have been used in the past as models for human heart disease, such as the mouse and rat [17], chicken [18], and zebrafish [19]. While large animals (such as dogs, pigs and sheep) are used to deepen the understanding of cardiovascular disease [20], small animals provide financial, time, and ease-of-maintenance advantages. In particular, the fast breeding and development time permitted derivation of many genetically modified strains (e.g. expressing fluorescence in certain proteins, or gene-knockout animals which lack a specific gene).

The zebrafish is by far the most cost-effective animal with rapid and numerous breeding (fish can produce 30-50 eggs daily, or up to one thousand eggs once or twice weekly depending on the breeding protocol [22]). The fish grow from an embryo to a larva in just 5 days, see Figure 1.1 A-G. The optical transparency of the zebrafish at the early stages of its development, Figure 1.2, makes this an excellent animal for optical microscopy, and hence for Selective Plane Illumination Microscopy (SPIM). In the next paragraph, the zebrafish as an animal model will be briefly introduced, and the key reasons for the use of this animal in this project will be explained.

The zebrafish heart for studying human cardiovascular disorders   The zebrafish (*Danio rerio*) is a well established animal model for studying a variety of human conditions, which are simulated in the fish by creating mutant and transgenic fish [23, 24]. The zebrafish has been successfully used in studies for infection, inflammation, and cancer (reviewed in [23]), as well as kidney, muscle, central nervous system, ocular, and heart disorders (reviewed in [25, 26]). As the main results of this thesis is the application of the proposed SPIM-micro

Parameter	Typical value
Ventricle length	$200\,\mu\mathrm{m}$
Ventricle cross-section	$70\,\mu\mathrm{m} \times 100\,\mu\mathrm{m}$
Peak velocity	$5\,\mathrm{mm\,s^{-1}}$
Total blood volume	$100\,\mathrm{nL}$
Hearbeat rate	$2\,\mathrm{Hz}$
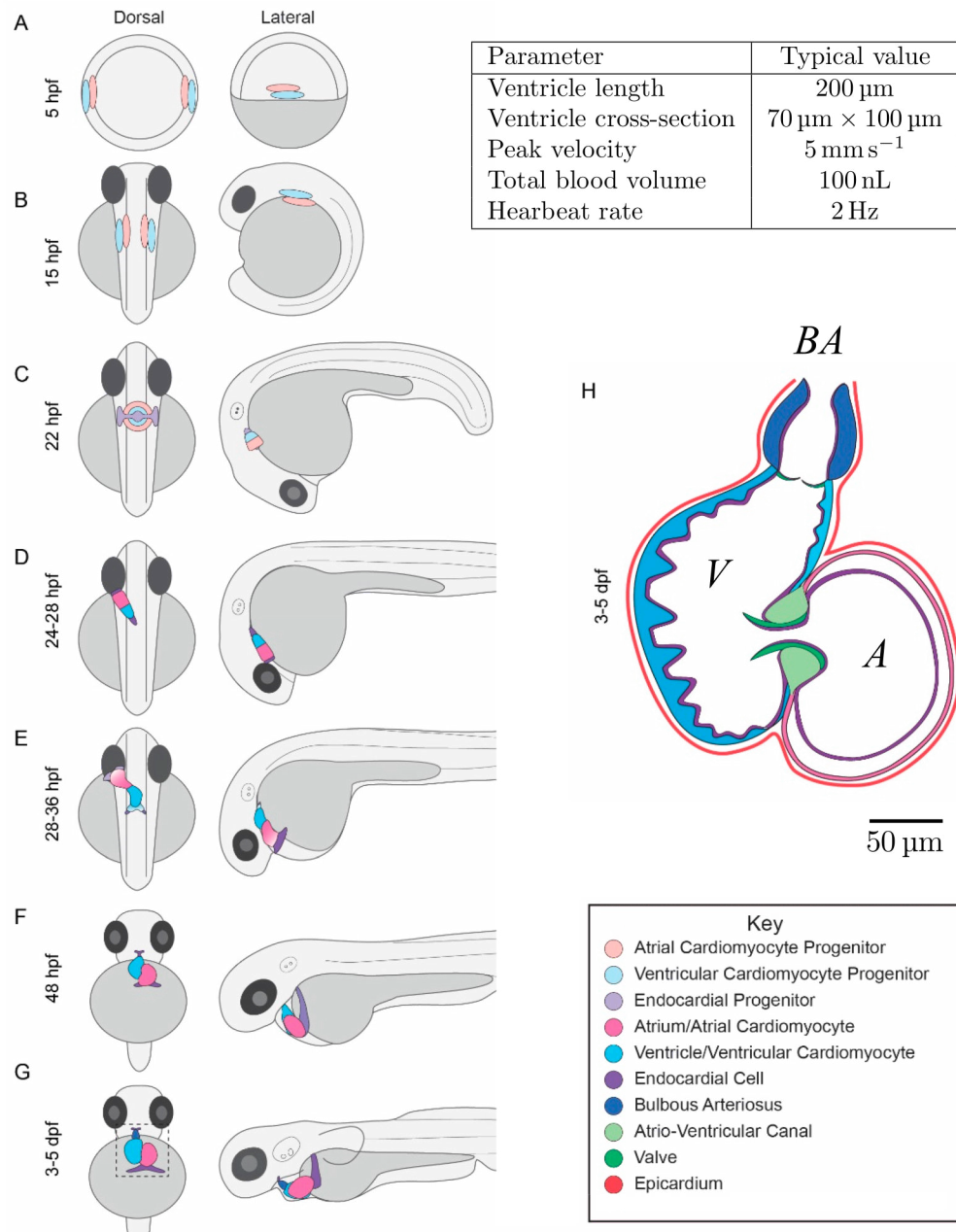
Fig. 1.1 The development of the zebrafish and its heart from 5 hours to 5 days is illustrated in **A**-**G**. The early heart is a tube, which starts undergoing looping at around 28-36hpf, **E**. The atrium and ventricle chambers are formed by day 2, **F**. Bulbus arteriosus forms at the outflow of the ventricle by day 3, **G**. Note the change of orientation of the heart between **F** and **G**. Figure **H** shows a cross section of the zebrafish heart, *A* - atrium, *V* - ventricle, *BA* - bulbus arteriosus. Note that the wall of the ventricle facing the atrium is corrugated. This corresponds to the trabecular region. The valve leaflets form fully by day 5. Some approximate typical values of relevant parameters for this thesis are summarised in the table. Figure adapted from [21].

wt   *alb^{nk1}*

(a)   (b)
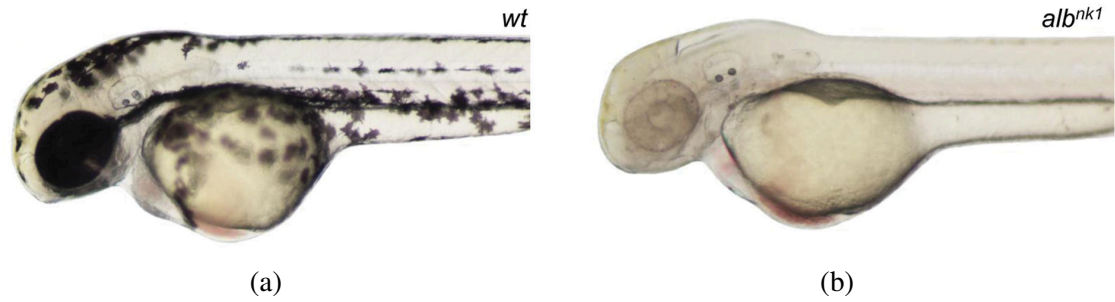
Fig. 1.2 Transparency of zebrafish at the embryonic stage enables the use of optical microscopy for imaging. Wild type (*wt*) zebrafish exhibit good optical transparency at the embryonic and larval stage of their development, an example of a *wt* embryo at 48 hpf is shown in (a). If the pigmentation is problematic for a particular imaging target, the pigment can be removed with chemical treatment [27]. Alternatively, mutant strains such as the albino (*alb*) mutant shown in (b), can be used instead. The embryos at 3-5 days are about 4 mm long. Images from [28].

Particle Image Velocimetry (μPIV) system for imaging blood flow in the zebrafish heart, the remaining discussion will focus on the use of zebrafish for cardiovascular research.

While the zebrafish heart only has two chambers, see Figure 1.1 H, and therefore is a prototype for the vertebrate heart, it is a good model for the early mammalian heart, in particular for studying congenital heart disease [25, 29, 21]. The zebrafish allows researchers to investigate early heart disorders *in vivo* - this is because the zebrafish can obtain oxygen and nutrients through diffusion, therefore fish with defective hearts can survive up to 3 days post fertilization (dpf) [25]. In fact the zebrafish heart is of particular interest due to its regenerative heart abilities (reviewed in [30, 31]). In humans, myocardial infarction causes scar tissue formation which in turn weakens the heart muscle and increases the risk of heart failure, however, the zebrafish does not form scar tissue while repairing its heart [30]. Notably, the zebrafish has been shown in the past to be able to fully regenerate its heart, after 20% of its ventricle has been resected [32] or after the same amount of cell apoptosis via cryoinjury [33]. Potentially such research can lead to discoveries for treating human heart disease. Furthermore, the zebrafish has been a valuable tool for drug discovery (reviewed in [34]). One notable example of direct correlation between drug effects in the zebrafish and humans, was the reproduction of pharmacological effects on the zebrafish with 22 out of 23 chemical compounds which had an effect in humans [35]. On the other hand, the obvious potential limitation of the zebrafish heart as a model for the human heart is the two chamber structure.

The regenerative properties of the zebrafish heart, as well as pharmacological effect conservation for drugs affecting human hearts, provide solid reasons to pursue further knowledge about its heart. Since mechanical forces have significant influence on the formation of the heart, it is crucial to understand the Fluid-Structure Interaction (FSI) in the zebrafish heart. The next section will review past work on heart structure imaging in small animal models, which typically preceded the somewhat more challenging aspects of blood

flow imaging in the heart. Nonetheless, they are crucial for this work as it will be shown later that techniques for structural imaging can be adapted for flow imaging. Furthermore, the two imaging modalities which are well-suited to exploit the optical transparency of the zebrafish heart will also be described.

1.3.2   Imaging the zebrafish heart structure

In vivo heart geometry imaging is not unique to zebrafish and have been performed in other small animal models using a variety of different imaging modalities, which are briefly mentioned here. For example, mouse embryos have been imaged using ultrasound [36], magnetic resonance Magnetic Resonance Imaging (MRI) [37] and Photo-acoustic Imaging (PAI) [38], and Optical Coherence Tomography (OCT) [39]. Computed tomography Computed Tomography (CT) [37] and 3D Ultrasound (US) have been used to image the hearts of rats [40]. MRI and OCT have also been used for imaging chicken embryo hearts [41, 42].

For zebrafish embryo heart imaging, the above techniques generally have insufficient spatial and/or temporal resolution to accurately capture the heart structure. For example, the cutting edge 7 Tesla MRI systems can only achieve spatial resolution of $0.25 \times 0.25 \times 0.4$ mm [43], which is larger than the embryonic zebrafish heart ($\approx 200\,\mu$m across at 5 dpf). The similar is true for CT systems, where the voxel resolution around $200\,\mu$m can only be achieved at the cost of increased radiation dose [37].

US provides an improvement in the spatial resolution over CT and MRI. Using US imaging lateral and transverse resolution of $25 \times 56\,\mu$m has been obtained [44]. However, while US based imaging techniques have been successfully applied, they still lack the necessary resolution to image the embryonic heart structure at single-cell resolution. Moreover, US in general requires direct contact with the sample, and would be highly challenging at the scales of the zebrafish embryo (the zebrafish embryo can be approximated as 4 mm long cylinder with 1 mm diameter).

PAI is a recent imaging technique which combines US imaging and thermoacoustic properties of matter (as opposed to mechanical like in standard US) [45]. While work on imaging the beating zebrafish heart with PAI is yet to be published, Chen et al. [46] imaged blood vessels in the zebrafish with lateral and axial resolution of 1.5 and $18\,\mu$m respectively. While the axial resolution is still relatively poor compared to optical microscopy, the lateral resolution of PAI is a significant improvement over the aforementioned techniques. The key advantage of PAI is its non-invasive and label-free imaging. However, the axial resolution of PAI is too low for zebrafish heart imaging in 3D.

Compared to the aforementioned techniques OCT can provide the highest lateral *and* axial resolution for embryonic imaging [47]. For example Lopez et al. [48] were able to image the mouse embryo heart at approximately $4\,\mu$m axial and $5\,\mu$m lateral resolution. However, imaging of the zebrafish heart is yet to be shown, and previous work utilising
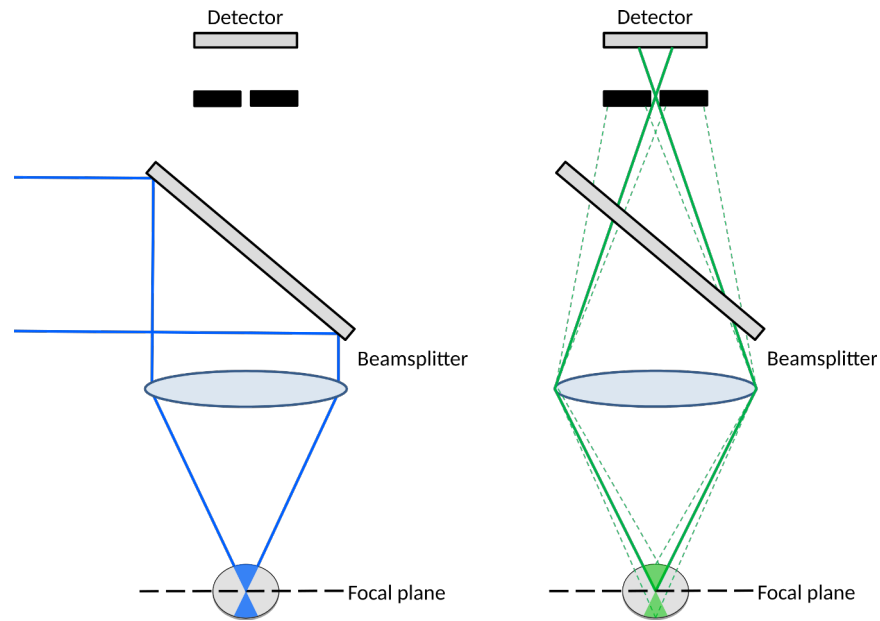
Fig. 1.3 Schematic of a confocal microscope system. The illumination path of a confocal system is essentially the same as in an epi-fluorescence microscope (Left). This illuminates the whole thickness of the sample of interest. Insertion of an aperture blocks the out-of-focus light (indicated by the dashed lines on the Right) which comes from above and below the focal plane of the objective (indicated by a finely dashed black line). This blocking of the out-of-focus light significantly improves the contrast and axial resolution, and enables depth-sectioning. Figure based on [50].

OCT in zebrafish imaging was limited to muscle structure or retinal studies [49]. Similarly to PAI, OCT does not depend on specimen labelling.

The optical transparency of the zebrafish embryos, and their fluorescently labelled hearts have been exploited using confocal [14], and light-sheet fluorescence microscopy [16]. In the rest of this section, these two imaging modalities will be introduced, and their *in vivo* imaging capabilities will be compared.

Confocal microscopy The invention of confocal microscopy principle is dating back to 1950s is attributed to Minsky [51]. Despite being commercially available since the 1980s they are still widely used for imaging thick fluorescent biological samples (a review of different confocal systems can be found in [50]). This popularity could be partially attributed to the fact that the system is embedded in a "normal" microscope, which means that majority of users can quickly adapt to using it. Moreover, since confocal-microscopes became available, they faced no competition in optical microscopy for 3D imaging (the first commercial light-sheet systems only became available in the second half of the year 2000).

A basic confocal system, shown in Figure 1.3, will illuminate the whole sample just like a standard epi-fluorescence microscope. However, unlike in epi-fluorescence microscopy, where both in and out-of focus light will reach the detector, confocal microscopy uses a small aperture to prevent the out-of-focus light reaching the detector, as illustrated in Figure 1.3. By stopping the light originating outside of the focal plane in the sample from
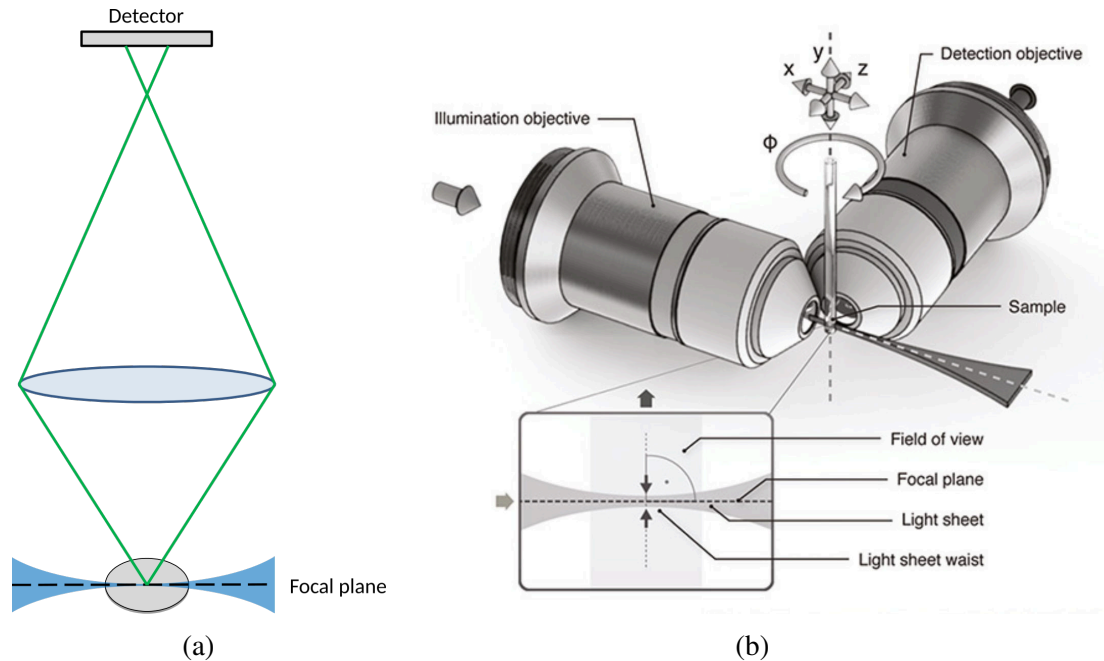
Fig. 1.4 Illustration of a common light sheet microscopy configuration, which has not changed since it was first proposed in 1903. (a) Unlike confocal microscopy which illuminates the sample above and below the focal plane, the light sheet only excites fluorophores at the focal plane, minimising photodamage. Because the whole FOV is illuminated at once, there is no need for scanning of the sample in the focal plane like in confocal microscopy - this allows capturing dynamic events in the whole FOV. (b) Two microscope objectives are placed at a right angle to each other for illumination and detection. The two most common approaches of creating a light sheet is by using a cylindrical lens (instantaneous full FOV illumination), or by scanning a focused circular beam. The sample is usually suspended in a tube of a refractive material matching the immersion media (typically water). A cylindrical tube enables easy translation and rotation of the sample. Note that in (b) the *y* direction would be perpendicular to the optical bench (i.e. the microscope is flipped by 90 degrees compared to a conventional epi-fluorescence/confocal microscope). Figure (b) taken from [53].

reaching the detector, confocal microscopy enables depth-sectioning of thick transparent samples, revealing their inner structures. The main disadvantage of confocal microscopy are image acquisition times (although recent advances improved this substantially) and excess illumination of the samples (the light is still illuminating the whole sample), causing photodamage in the whole sample volume [52], limiting the applicability of this technique for long-term imaging. A much more "gentle" imaging alternative to confocal is selective plane illumination microscopy, introduced next.

Selective plane illumination microscopy   Confocal-microscopy effectively illuminates the whole sample volume in order to obtain a single, optically-sectioned image of the sample. In contrast, SPIM illuminates *only* the plane of interest, which is generally in the Depth of Field (DOF) of the microscope (see Figure 1.4a). This can be achieved in a SPIM by using a cylindrical lens to expand a laser beam to a sheet, and a microscope objective, which then

focuses the light-sheet further [12]. An alternative way to achieve light sheet illumination is by rapidly scanning a circular beam [54], such systems are referred to as digital scanned laser light-sheet fluorescence microscopy (DSLM).

In SPIM, each sample plane is illuminated only once in order to obtain the full 3D information. This is the crucial difference and advantage of SPIM compared to confocal-microscopy and is illustrated in Figure 1.5. Another important benefit that SPIM provides is that the whole sample plane (i.e. whole FOV) is illuminated at once. Since the basic confocal microscopy uses point-scanning to acquire an image its data throughput and temporal resolution is low[2]. Contrary to confocal, the instantaneous full FOV illumination in SPIM provides superior data-throughput and temporal resolution. In fact, Light Sheet Fluorescence Microscopy (LSFM) systems in general had achieved such high rates of data acquisition, that data management and analysis requires significant hardware and software consideration [55]. While SPIM clearly provides significant advantages over a confocal system for in-vivo 3D imaging, it was not widely adopted until 2004, despite the first light-sheet microscope set-up being proposed in 1903 by Siedentopf and Zsigmondy [56], where they had added a second microscope objective on a conventional inspection microscope in order to achieve a 90 degree configuration of the objectives, similar to the one shown in Figure 1.4b. It was not until 1993 when this optical arrangement resurfaced [58] once again. While this work was seminal in the field, it did not have a wide reaching impact; Keller and Dodt [59] argue that this is due to lack of visually appealing 3D reconstruction of the images, and application of the technique on a single inner ear organ (which had limited biological relevancy). SPIM did not seem to be widely recognised until the publication by Huisken et al. in 2004 [60], where they demonstrated the ability to perform optical sectioning *in vivo* in an embryo of a Medaka fish. This had a significant impact, since whole transparent organisms could be imaged without the need for physically slicing them [59]. Since then, LSFM was used in an array of applications *in vivo*, and was also adopted by the open source community developing an open source project *OpenSPIM* [61]. LSFM systems are rapidly incorporating advances in optical and computational microscopy, such as 2-photon light sheet and wave-front coding techniques (reviews can be found in [62–64]).

While LSFM provides an excellent alternative to confocal microscopy for imaging live samples with minimal photodamage, imaging dynamics in the heart in 3D requires sophisticated computational methods, in order to recover 3D + time information. The next section will explain the reasons imaging the heart is challenging, and discuss the methods necessary for 4D heart imaging using optical sectioning microscopy techniques.

---

[2]Spinning disk confocal microscopy can improve the temporal resolution somewhat.
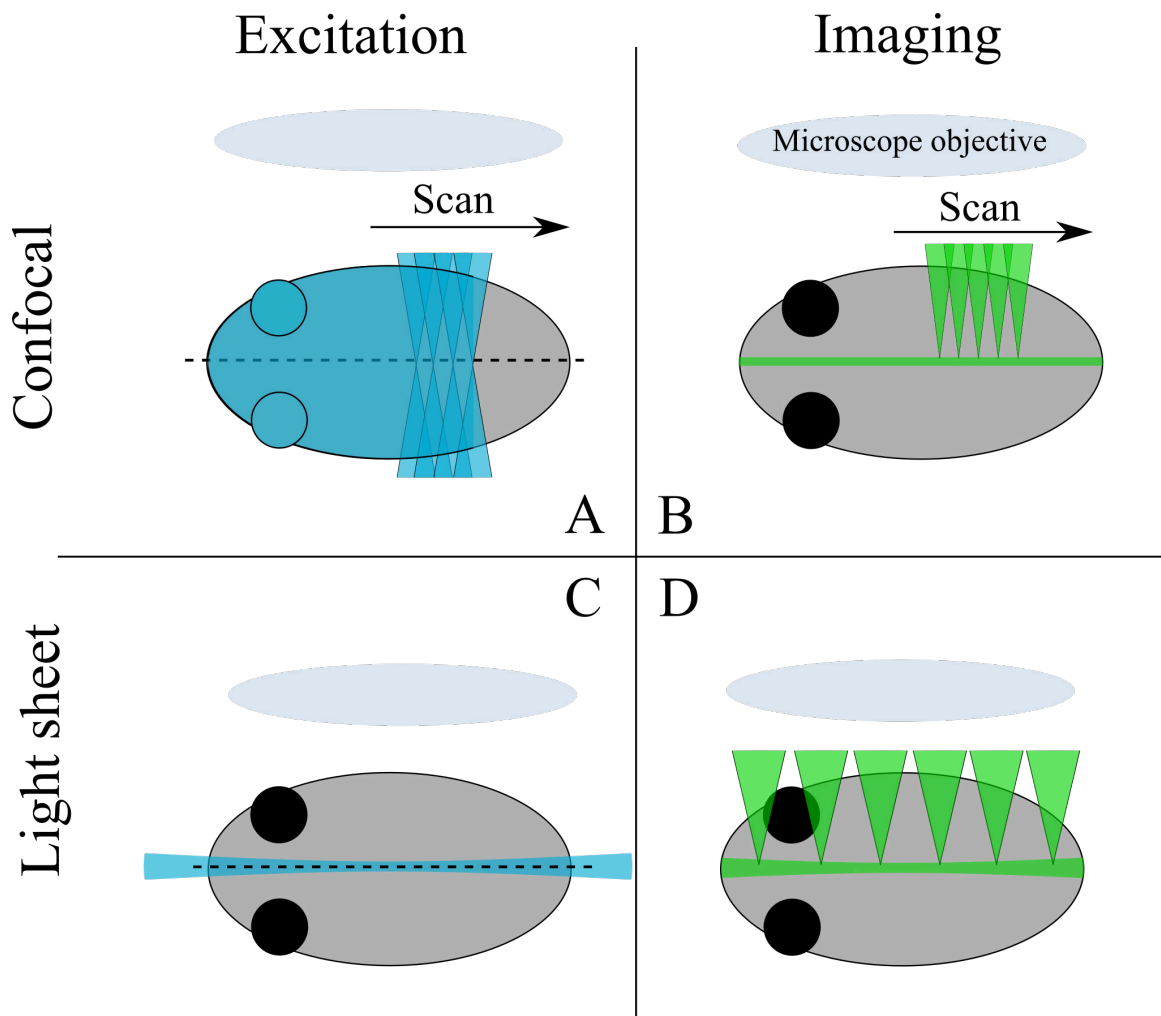
Fig. 1.5 Comparison of sample illumination with confocal and light sheet microscopy. Typical confocal microscope illuminates the whole sample while focusing on the plane of interest, which excites fluorophores everywhere in the sample to a certain degree (A). This out-of-focus light gets rejected with the help of an aperture in-front of the detector (B). Prolonged exposure during to excitation light can eventually photobleach the sample, as well as lead to photodamage. Instead, SPIM illuminates only the plane of interest and does not affect the fluorophores elsewhere in the sample, minimising negative photoeffects (C). Since the whole plane of interest is illuminated at once, imaging dynamics is essentially only limited by the camera and laser pulse timing electronics (D). Figure based on [57].
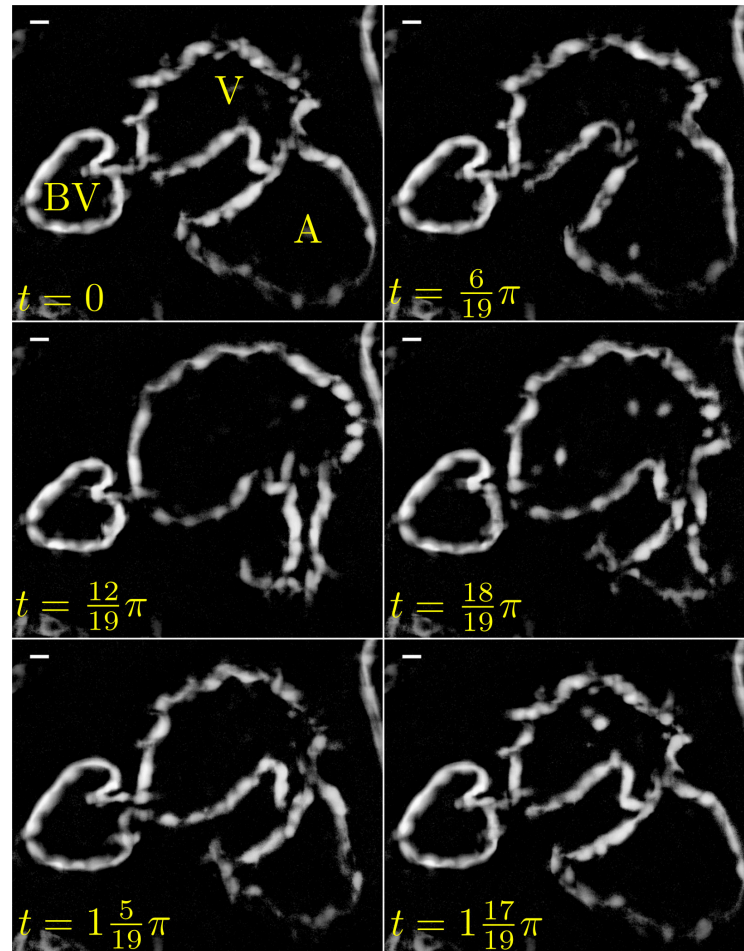
Fig. 1.6 Heart wall motion of a 4 day old zebrafish heart expressing green fluorescence. BV - bulbus venosus, V - ventricle, A - Atrium. Not shown here, but the sinus venosus joins at the atrium. $t = 0$ corresponds to the end of atrial diastole. Full cardiac cycle is 2π long. Note that some blood cells are occasionally visible in the GFP channel due to their broad excitation and emission spectra. Scale bars $= 10 \mu m$.

1.3.3 4D heart image reconstruction

The embryonic heart is a highly dynamic system, constantly changing its shape and size through growth and cardiac looping. In less than half a second a 5 day old zebrafish heart undergoes a contraction of Sinus Venosus (SV) which pushes blood into the atrium. The atrium then contracts and pushes blood into the ventricle via the atrioventricular (AV) valve. After a brief pause during which the AV valve closes, the blood rushes to the bulbus arteriosus (BA) through the ventriculobulbar (VB) valve, before the cycle repeats again (see Figure 1.6 for 6 equally spaced in time images of the heart wall in a 4 day old zebrafish heart). Capturing all of this process instantaneously with high *xyz*-resolution is not feasible with the current state of available imaging modalities as discussed earlier. In fact, in the past drugs have been used to completely stop the motion of the zebrafish embryo heart even when imaging with a conventional epi-fluorescence microscope [65], as well as in confocal [66–68]. However, as we have seen Wall Shear Stress (WSS) caused by bloodflow plays a crucial role in heart development. In fact, it has been empirically shown that affecting

(a)												(b)
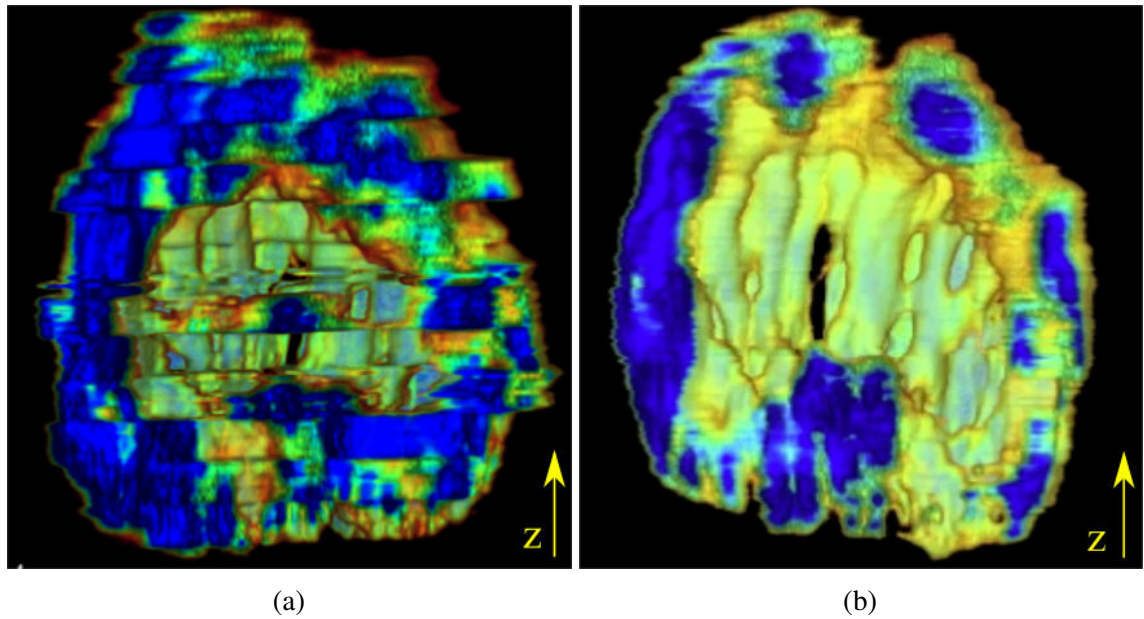
Fig. 1.7 Comparison of heart structure reconstruction without (a) and with (b) computational methods. The images show a cut-plane rendering of a zebrafish heart ventricle obtained with SPIM. A reconstruction of a beating heart using optical sectioning microscopy would contain snapshots at random phase in the cardiac cycle, failing to recover the true structure of the heart (a). Computationally "freezing" the heart allows recovery of the true structure of the heart at a fixed point in time, without the need to physiologically stop the heart using drugs or otherwise. Figures provided by Dr Jonathan M. Taylor.

the blood flow has a notable impact on the heart function and shape [69, 70]. Therefore, imaging fish which have physiologically stopped hearts cannot reveal the true representation of *in vivo* structure, and an alternative way is needed. In the next paragraphs, computational methods exploiting the periodic motion of the heart will be presented as this alternative.

Retrospective optical gating   If one were to obtain a z-stack (e.g. with confocal or SPIM) of a beating heart and attempt to reconstruct a 3D image, the outcome would very likely not be resembling a heart structure, see Figure 1.7a. This is because at each z position, the heart will be at a different point in time of the cardiac cycle. In other words, images of the heart section are captured at random phases in the heartbeat. If image data of different depths in the heart were acquired at the same phase, then the reconstructed image would be a true representation of the heart structure at that phase, see Figure 1.7b. One approach to achieve this, is to obtain a large sequence of images at each z-position in the heart. The image sequences from each plane then can be used to align phases from different heart planes after the acquisition, see Figure 1.8. This is referred to as retrospective optical gating of the heartbeat, and was first proposed by Liebling et al. [14] in 2005. Liebling et al. used this method to recover 3D information in the living zebrafish heart using confocal microscopy. It was later significantly improved to account for slight variations (e.g. arrhythmia) in the heartbeat length [71].
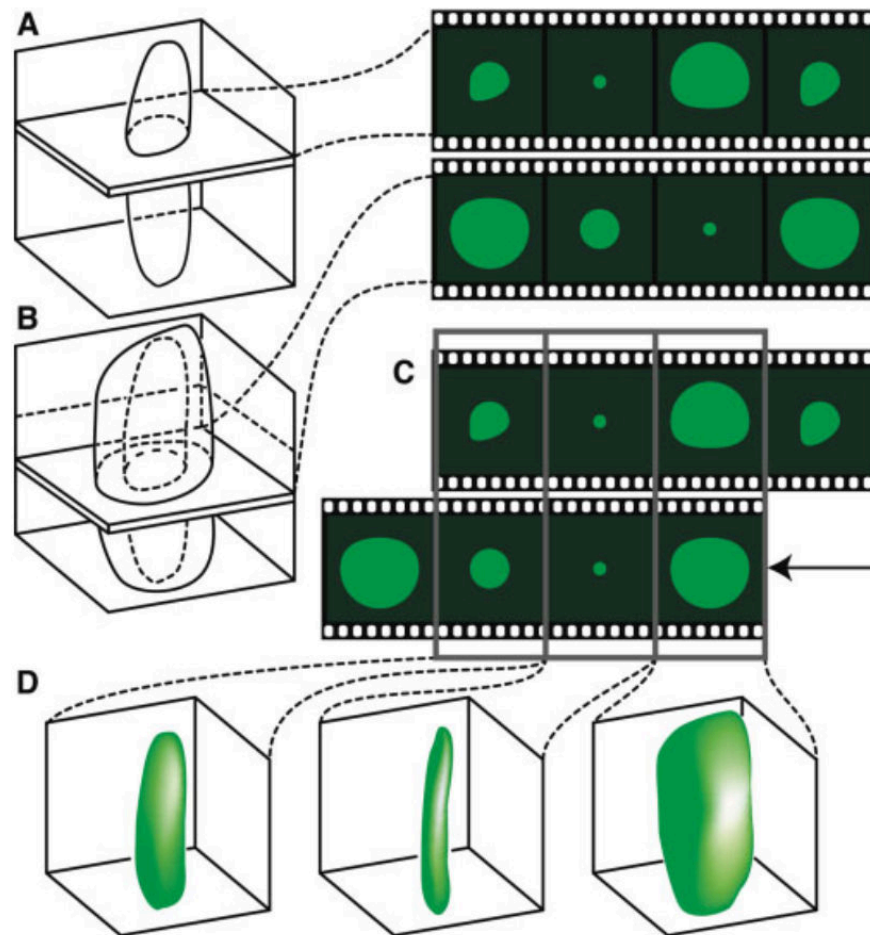
Fig. 1.8 Illustration of 3D geometry reconstruction of *in vivo* zebrafish heart using retrospective optical gating. **A, B** Different planes in the heart are imaged continuously while the heart is beating. Notice that imaging at any plane can start at a random position in the cardiac cycle. **C, D** Heart images from different are synchronised in post-acquisition to the same phase (according to image similarity metric). The 3D geometry can be then recovered from the synchronised stacks. Figure reproduced with permission from [72].
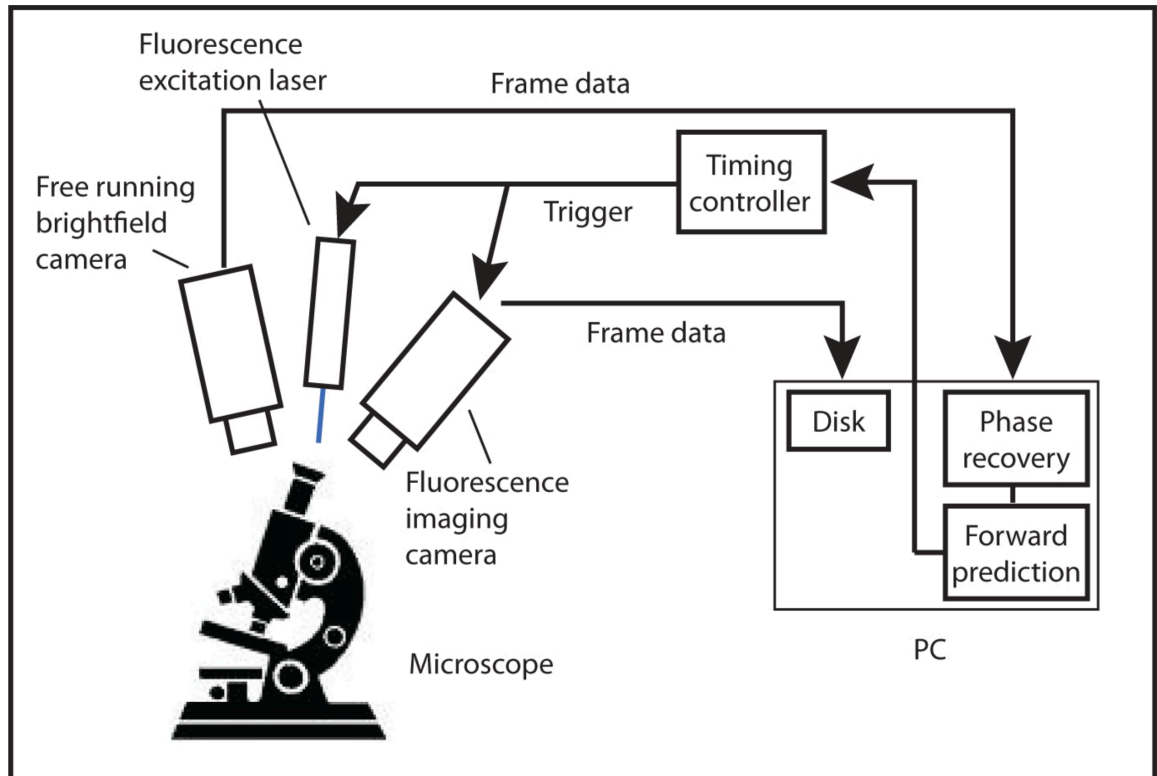
(a)
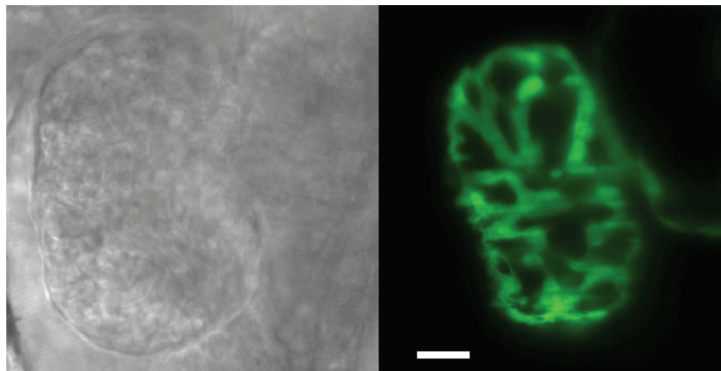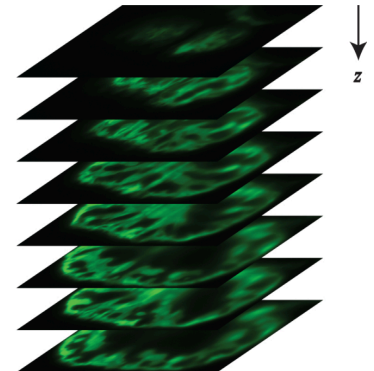
(b) (c)

Fig. 1.9 Real-time heart synchronization using a brightfield channel in addition to SPIM. (a) A free-running brighfield channel incorporated in a SPIM system provides a reference signal for prospective optical gating. (b) Throughout a z-scan, BF images are analysed in real time to estimate when the heart will be at a particular phase, and only triggers the illumination laser at that point (scale bar = 20 μm). (c) Each plane in a z-stack is only illuminated once at the same phase, limiting the sample exposure. Figures taken from [16].

Prospective optical gating The downside of the retrospective gating technique is the necessity to obtain large amounts of data at each sample plane. Prolonged exposure to excitation light can have detrimental effects on the sample (review of photodamage can be found in [73]). While obtaining 3D information of the heart *at each phase* has its merits, if the object of study only happens at a particular phase in the heart cycle (for example the AV valve opening/closing) whole cycle information is not needed. In such case, it would be beneficial to *lock* on to a particular phase in the heart cycle. Imaging only at a particular time using some other signal from the object of interest is referred to as prospective gating.

For example, prospective gating, using Electrocardiogram (ECG) as the reference signal, has been used for human cardiac CT to image the heart at the diastole phase [74]. However, while ECG for zebrafish embryos is possible [75], it requires expertise in micro-manipulation as the zebrafish embryo is 4 mm long and no more than 1 mm thick at the yolk sac. Using electrodes can also be impractical to use while imaging (e.g. electrodes could obscure the illumination/imaging path). Hence an alternative signal is necessary to perform perspective gating for zebrafish heart imaging. Taylor et al. [15] proposed using a BF channel which continuously acquires data during SPIM acquisition of the zebrafish heart structure in order to perform prospective gating. Their prospective gating method is illustrated in Figure 1.9, and can be dissected in the following way:

1. A *reference* heartbeat period was obtained using the BF channel, Figure 1.9a.

2. Using custom built, high-frequency response timing hardware, the BF channel images were compared against the reference frames in real time. A Sum of Absolute Differences (SAD) metric was used to measure similarity between the frames, Figure 1.9b.

3. A forward prediction algorithm was then used to fire the excitation laser at a desired phase, at each z-position throughout the z-stack, Figure 1.9c.

Prospective gating has a clear "gentle imaging" advantage over retrospective gating, as each plane is only exposed to laser light once. Furthermore, the data necessary to reconstruct the full 3D structure of the heart is significantly reduced. However, both methods have their pros and cons depending on the application, and are reviewed in [76]. Both methods enabled studying the 3D heart wall structure of the *in vivo* zebrafish heart. However, while heart geometry received much interest from the research community, there have only been a few published attempts to directly measure the blood flow dynamics in the zebrafish heart in 3D. Instead, researchers have opted to extrapolate flow information using wall motion information only [9, 77]. In the next section flow measurement techniques, which have been used for quantifying blood flow in the zebrafish heart, will be introduced.
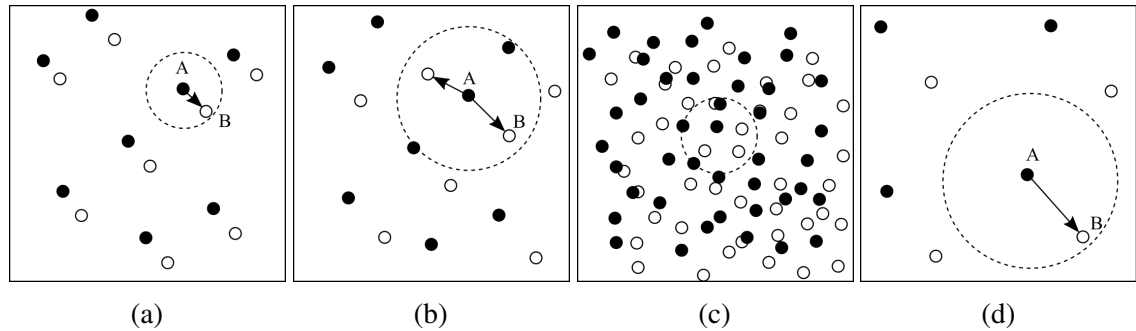
Fig. 1.10 Particle tracking velocimetry for different particle concentrations and velocities. Particles at time A are shown as black circles and particles at time B are shown in white circles. (a) When the particles are sparsely seeded and their motion is small, correct particle pairs (indicated by an arrow) can be easily identified in the search region (dashed circle). (b) The search region has to be enlarged for increasing particle motion, this can lead to wrong particle pairing if the particle seeding density is not reduced. (c) PTV is not suitable for large particle seeding density, as matching particles becomes significantly ambiguous even at small displacements. (d) On the other hand, large displacements can be recovered if the number of particles is very low. Figure based on [78, p. 19].

1.3.4   Flow measurement techniques

The flow measurement techniques that have been used in measuring blood flow in the zebrafish heart can be categorised in three types, are based on:

- single particle tracking, where the motion is obtained via localization of *individual* particles in the fluid;

- estimation of the statistically most likely motion of *groups* of particles;

- measurement of apparent motion using computer vision algorithms.

A brief overview of the techniques is given below.

Particle Tracking Velocimetry   Early implementations of Particle Tracking Velocimetry (PTV), to quantify fluid flows in the field of engineering date back as far as 1930s [13]. The rudimentary PTV measurement would consist of image segmentation where particles are identified, localisation of the said particles (e.g. via centroid calculation), and comparison of the distance between the locations of two neighbouring particles. The velocity is then obtained by simply dividing the distance by the time difference between two exposures. This technique works well when the number of particles in the fluid is low, when the average distance between particle images is much larger than their average displacement [78, Sec. 1.2.7]. Otherwise, identifying the correct particles to compare the distances between becomes ambiguous, as illustrated in Figure 1.10. The next technique does not suffer from this limitation.

Particle Image Velocimetry   The first use of particle image velocimetry dates back to the 1980s [13], evolving from laser speckle velocimetry. Since then it has become the standard fluid measurement technique for macro-scale experimental fluid dynamics [79], as well as for microfluidics, where an extension of Particle Image Velocimetry (PIV) (referred to as µPIV) has been successfully used [80, 81]. Unlike PTV, PIV measures the motion of *groups* of particles. This is achieved by cross-correlating (in space) images of fluid seeded with a large number of particles, which are acquired in short time interval. The correlation will be best at the offset location where most particles from first image in the frame pair overlap in the second image. This location is then used as the statistically most likely shift between the two images.

The choice of PIV as the flow quantification technique for this thesis, was motivated by the similarities between a typical PIV system used in the field of engineering, shown in Figure 1.11, and the SPIM system.

Optical Flow   Optical Flow (OF) has its origins in computer vision, and has been in development for more than 3 decades [83]. It is distinct from the aforementioned PTV and PIV techniques as it does not rely on discrete particle images for estimation motion. The definition of OF as given by [84] is the following: "*The optical flow is defined as the velocity field in the image plane that transforms one image into the next image in a time sequence*", hence it can be interpreted as a mathematical operator. While OF has been suggested as a complementary technique for PIV soon after the latter gained popularity in the 1990s, the interest in OF for fluid dynamics measurements only appears to have resurfaced recently [84, 85]. The potential advantage of OF over standard velocimetry techniques for flow measurements, is that the mathematical framework of OF allows incorporation of continuity or Navier-Stokes equations into the constraints of the transformation [85, 86]. Unfortunately, there appears to be a lack of microfluidic measurements with OF, and hence the knowledge base is not as vast as it is in the PIV community.

Blood flow measurements in the zebrafish cardiovascular system   The aforementioned flow measurement techniques have been successfully utilised with different imaging modalities for measuring blood cell motion in the cardiovascular system of small animals such as rodents, chicken embryos, and zebrafish which are reviewed in [87]. A summary of blood flow quantification in the heart of the zebrafish will be presented here.

Hove et al. [69] were the first to apply µPIV for blood flow measurements in the zebrafish heart. They used BF images acquired with high-speed camera (400-1000 Frames Per Second (FPS)) to estimate the flow in a 4.5 dpf zebrafish heart, and measured a peak velocity of 5mm/s through the AV valve, and used the µPIV velocity measurements to estimate WSS in the zebrafish heart. They recognised potential velocity underestimation due to the use of unfiltered BF images in µPIV analysis. That is, both the heart walls and non-moving tissue in the optical path were contributing to the Cross-Correlation (CC)
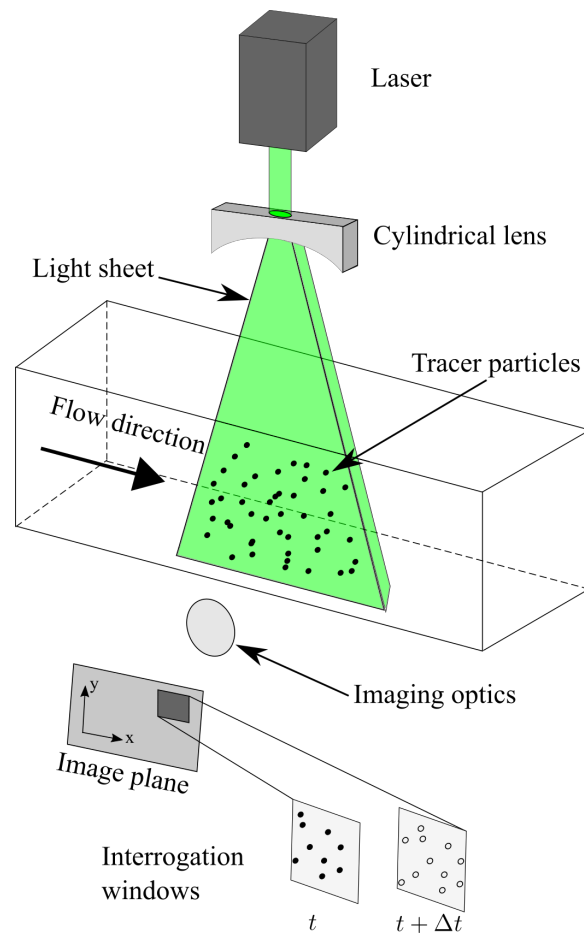
Fig. 1.11 Typical set-up of a particle image velocimetry system in aerospace engineering applications. In a typical macro-scale PIV system, a cylindrical lens is used to create a light-sheet, which illuminates a fluid of interest. The fluid is seeded with scattering or fluorescent particles, which act as tracers for the fluid flow. The flow is typically imaged in image pairs with a high speed camera (not shown here). These image pairs are then divided into smaller areas, called interrogation windows which are then cross-correlated. The peak of cross-correlation result indicates the statistically most likely motion between the two frames in an image pair. Note that this set-up resembles a SPIM microscope, where a cylindrical lens is also used for light sheet formation, enabling optical sectioning. The black circles indicate the location of the particles in the IW at time t and white circles indicate the particles at time $t + \Delta t$. Figure based on [82, p. 4].

results. Interestingly, they did not consider this in terms of the theory of out-of-focus particle motion effects for µPIV measurements developed previously by Olsen & Adrian [88], who showed that volume illumination can cause velocity underestimation in µPIV analysis. Finally, Hove et al. proposed that the embryonic heart functions as a peristaltic pump, which was later shown to act a suction pump by Forouhar et al. [89], where they used particle tracking to measure the dynamics of blood cells.

Jamison et al. [90] proposed a cardiac-phase filtering technique to improve µPIV measurement accuracy when using BF image data. Essentially, they used a type of retrospective gating, where the velocity measurements themselves were used to extract phase of the heartbeat. This was achieved by performing PIV analysis on a small segment of a time-series of BF heart images. The recovered time-velocity profile (see [90, Fig. 1]) of the blood flow was then used to identify the onset of each heartbeat. After a division of the cardiac cycle into smaller bins, average images of the heart for each bin were computed. In theory, subtracting this average image from the corresponding bin for each cycle, should remove the heart walls and static structures. While this cardiac-phase filtering approach did not completely remove the contribution of structures other than blood cells, the velocity measurement values after filtering have increased almost 4-fold. This work illustrated how severe the contribution of the heart wall and static structures can affect BF-µPIV measurements. They also found that between zebrafish aged 3 to 6 dpf the average velocity through the VB region in the heart decreases from ≈ 2 to $\approx 1\,\mathrm{mm/s}$. Later, the same filtering approach was used to investigate WSS measurements in the ventricle of the zebrafish heart [91]. It was found that WSS, as well as the time the ventricle is exposed to maximum shear, decreases as the heart develops.

The methodology used by Jamison et al. was a significant improvement over the work carried out by Hove et al. [69], as the periodic nature of the heartbeat was exploited to perform what is essentially high-pass filtering of the images, in order to greatly reduce the influence of non-moving structures to the velocity measurements. Nevertheless, the theoretical analysis on the effects of image processing on out-of-focus structures in µPIV measurements suggests that high-pass filter can at most halve the depth over which these structures significantly contribute to the measurements [92]. This means, that the velocities measured by Jamison et al. can still be affected by non-blood structures or cell motion outside of their DOF.

While the work carried out by Hove et al. and later by Jamison et al. presented important quantitative information of the blood flow in the zebrafish heart, these measurements lacked depth resolution. Therefore, the information was limited to a single 2D projection of the blood cell motion. Lu et al. [93], and Chan & Liebling [94] attempted to overcome this limitation and extend the measurements to 3D.

Lu et al. [93] performed 3D-PTV inspired by "Defocusing PIV" technique [95] to image blood flow in a 32hpf zebrafish embryo. They used a standard epi-fluorescence microscope with a 3 pinhole aperture mask attached on at the back of a $20\times 0.75\mathrm{NA}$ objective in order to extract the z-coordinate via triangulation. The system had a z detection range of up to

40 µm and a depth resolution in the order of 100 nm, however, the authors note that the *sensitivity of depth position* was 1 µm for displacement in *z*. 1 µm diameter fluorescent beads were microinjected into the zebrafish to act as tracers. Epi-fluorescence imaging of the beads means that unlike in BF-µPIV measurements described above, only the tracer particles (and not other cells/tissue) should contribute to velocity measurements. However, microinjected beads eventually deposit into the heart and vessel walls and can affect the flow measurements in the previously described way. The authors measured, for the first time, the instantaneous Three Dimension-Three Component (3D3C) velocities of 6 individual particles in the zebrafish atrium during diastole. While this technique is able to obtain *single-snapshot* 3D information without the need for optical sectioning, the 3 pinhole mask reduces the available Numerical Aperture (NA) and the optical throughput of the system. Moreover, the imaging requires very low seeding density, as the triangulation and/or tracking (recall Figure 1.10) might become ambiguous. That, combined with rapid bead deposition in the vessel walls, was the likely reason for only 6 *xyz* velocity measurements in the *whole* atrium. Unfortunately, the flow was sampled too sparsely to provide useful information about the haemodynamics, such as the WSS for example. https://link.springer.com/protocol/10.1007

Chan and Liebling [94] proposed that it is possible to recover 3D3C flow information by using BF images of the heart of a 60 dpf zebrafish, if imaging is performed from multiple orientations (this was achieved by rotating the sample in their case). That is, the 3D velocity field can be recovered by precisely combining the measured 2D velocity projections from each imaging orientation (essentially this is a tomographic reconstruction, similar to the one used in [96]). Further, they ensured that the recovered 3D flow field preserved fluid incompressibility. This was achieved by performing a divergence-free fitting when the 2D flow data, obtained using OF was combined to recover the 3D flow field. The major advantage of this technique is that it only requires a simple BF capable microscope and a high-speed camera. Furthermore, the mathematical framework should automatically ensure that the measurements conserve mass, and can be viewed as a robust, self-validating approach.

However, while the reconstructed 3D flow field qualitatively appeared convincing (see the smooth flow fields in [94, Fig.4]), there are several issues with this work that would need further investigation. Firstly, the flow measurements displayed for each BF orientation appear significantly noisy (see [94, Fig. 3]) and any "smoothing" with divergence-free fitting is not discussed. That is, it appears that the enforced incompressibility condition ensures that *some* flow field will be recovered. Secondly, it is unclear whether OF suffers from similar "velocity averaging over depth" effects that volume illumination causes for conventional µPIV analysis.
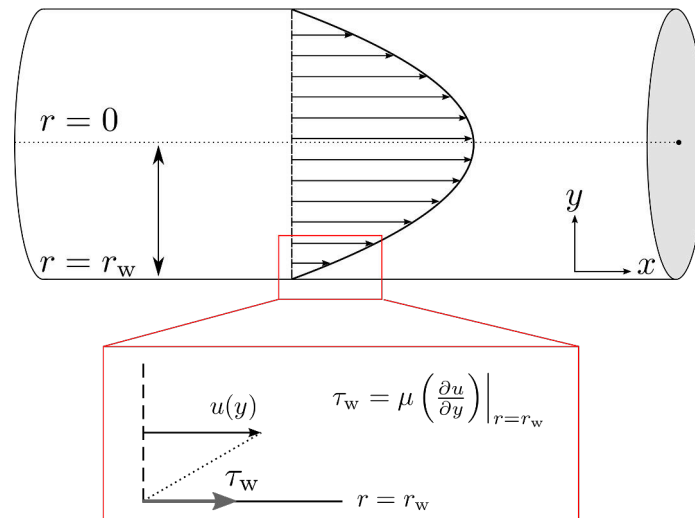
Fig. 1.12 An illustration of the wall shear–stress in a circular tube with radius $r = r_\mathrm{w}$. The wall shear-stress, τ_w is maximum at the vessel wall and is parallel to the direction of the fluid motion. Its magnitude depends on the viscosity of the fluid, μ, and the velocity gradient close to the vessel wall, $\partial u/\partial y$, indicated by the dotted line in the inset plot. Figure based on [99] and [100].

1.3.5 Wall shear-stress

As mentioned in the Motivation, WSS is of interest to cardiovascular research due to its part in influencing the changes in morphology of heart and blood vessels. For example, it has been shown that laminar shear-stresses trigger endothelial cells to orient in the direction of the flow [97]. More recently, a substantial amount of work, reviewed in [98], has shown that WSS is crucial for gene expression, activates cyto-skeletal deformation, and has been linked to vascular remodelling. In this thesis a flow measurement tool will be proposed, that could be used for accurate WSS measurement.

In essence, wall shear-stress "expresses the force per unit area exerted by a solid boundary on a fluid in motion (and vice-versa) in a direction on the local tangent plane" [101]. An illustration of WSS acting on the wall of a circular tube (a model blood vessel) is shown in Figure 1.12. The presented WSS formalism depends on the *no-slip* condition, which states that the velocity of the fluid at a solid boundary (e.g. wall of the tube) is zero. It must be noted that it has been recently shown that the no-slip condition can be violated in certain circumstances [102], and several groups interested in WSS effects on blood vessels have in fact considered this (summarised in [103]). However, the no-slip condition appears to be a standard assumption in cardiovascular modelling [9, 104, 105], and is generally accepted as a reasonable one. In fact, WSS measurments in the zebrafish heart performed by Jamison et al. [91] relied on this condition. However, their measurements were limited to a single focal plane of the heart, limiting the available information.

1.4   Summary

In this chapter, a substantial amount of publications indicating the importance of the role of fluid flow in heart morphogenesis was presented. The suitability of the zebrafish as an animal model for this study was discussed and the main advantages such as its optical transparency and fast breeding, as well its use in wider heart research was explained. Two optical depth-sectioning capable systems used in *in vivo* imaging were introduced. It was also shown that imaging the heart is particularly challenging due to its vigorous nature and fast development. Computational methods enabling 4D heart structure acquisition were introduced. Finally flow measurement techniques, which have been utilised in the past to study blood flow in the zebrafish heart were summarised, and similarity between Particle Image Velocimetry (PIV) and Selective Plane Illumination Microscopy (SPIM) system was noted. In the final review of blood flow measurements in the zebrafish heart using the aforementioned techniques, the current shortcomings were outlined, specifically, the use of volume illumination. This reiterates the motivation of this work: to investigate SPIM-micro Particle Image Velocimetry (µPIV) as an *in vivo* flow measurement technique, capable of depth-resolution without the artefacts common to conventional µPIV systems.

This investigation will begin by summarising the theoretical background necessary for this thesis in the next chapter. Chapter 2 will begin by expanding on the principles of PIV briefly introduced here. Perhaps most importantly, analysis of synthetic motion will explain the motivation for the use of Sum of Absolute Differences (SAD) metric for motion estimation when dealing with large particles such as red blood cells, which are used as tracers in Chapter 4.

Chapter 2

Technical background

This chapter will provide an overview of the technical details of the techniques used in this thesis. Firstly, fundamentals of PIV will be summarised and important concepts will be illustrated using synthetic image data. Note that the discussion will begin by considering the macro-scale PIV applications, which historically were the initial applications of the techniques. This will lead to a discussion about µPIV, where specific micro-scale aspects will be explained. Then, the equations describing Gaussian beam parameters will be introduced along with the description of the SPIM system used for experimental measurements in this work. The estimated beam parameters will be compared to experimental results. Finally, a brief discussion on the application of optical gating techniques for flow measurements in the zebrafish heart will be provided.

2.1 Fundamentals of PIV

As introduced in Chapter 1, Particle Image Velocimetry (PIV) is a well-established flow measurement technique. It is based on estimating the *statistically* most likely motion of *groups* of particles in a fluid of interest. This section aims to provide an understanding of the core practical aspects of PIV. The experimental set up shown in Figure 1.11 will be revisited and discussed in more detail in terms of light sheet formation optics and fluid tracer particles used. Then, the algorithms for measuring motion will be explained, and techniques for obtaining subpixel accuracy will be introduced. Next, the experimental aspects affecting the accuracy of PIV will be illustrated. Furthermore, bias and random measurement errors will be quantified for different flow scenarios using synthetic data. Finally, the considerations necessary for transitioning from macro to micro-scale PIV will be discussed. In particular, the effect of Depth of Correlation (DOC) will give a clear motivation for the use of Light Sheet Fluorescence Microscopy (LSFM) for micro Particle Image Velocimetry (µPIV).
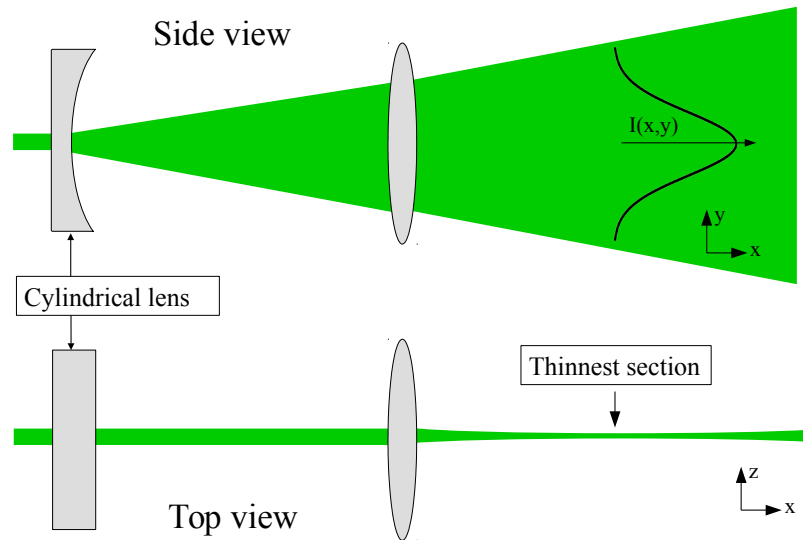
Fig. 2.1 Schematic of light sheet formation optics used in PIV. In PIV systems using lasers with small beam diameters and divergence, a single cylindrical lens can be used to create a thin sheet of light. The figure shows two views of the imaging system. A cylindrical lens expands the collimated laser beam, which is then focused by a spherical lens. The spherical lens can be used to adjust the position of the thinnest section of the light sheet. Different optical arrangements using multiple cylindrical lenses can be found in [82, Sec. 2.4]. Note that due to high energy lasers typically used in PIV measurements, the orientation of lenses are an important consideration. In this example, the cylindrical lens is oriented to minimise reflection hazard. Figure based on [78, Fig. 5.7].

2.1.1 Illumination

As shown in Figure 1.11, macro-scale PIV systems illuminate the fluid of interest with a sheet of laser light, which is perpendicular to the imaging path. The formation of a light sheet in macro scale PIV applications can be achieved in several ways, all of which utilise a cylindrical lens, and are discussed in [82, p. 44]. The simplest light forming optical arrangement using one cylindrical lens is illustrated in Figure 2.1. The sheet dimensions used in PIV can extend for many meters, while keeping the sheet thickness small. For example, Adrian and Westerweel [78, p.173], state that a common light sheet thickness of 1 mm can be maintained for over 3 m with an illumination laser at a 532 nm wavelength. The equations describing light sheet parameters will be introduced in section 2.3, as they also describe the light sheet formation in a Selective Plane Illumination Microscopy (SPIM). While it is not an issue for the SPIM-µPIV used in this thesis, it is interesting to note that long illumination distances and potentially large Field of View (FOV) requirements necessitate high power lasers. In fact, careful health and safety risk assessment is generally necessary due to use of class 4 lasers (highest laser radiation class, with possibility of combustible material ignition) [78, p. 172] in macro scale applications.

2.1.2   Tracer particles

The theory for PIV was derived assuming the use of discrete, point-like particles[1] in the fluid to act as tracers for the flow, it is important to consider the relevant properties and equations describing the behaviour of spherical particles in a fluid. In particular, these equations aim to describe how well a *particle* approximates the motion of the *fluid* it is embedded in. Note that since mathematical derivation of the equations governing particle motion are beyond the scope of this thesis, relevant equations will be stated without proof.

Difference between fluid and particle motion   It is important to realise that particles in the fluid are affected by a number of different forces, and therefore in practice do not follow the flow perfectly. However, careful choice of particle density and diameter can ensure that the *true* motion of the fluid is approximated very closely. While the mathematical formulation of spherical particle motion in fluids is incomplete and of high complexity [78, p. 40], certain measures can give a good estimate of the particle behaviour. For example, the *velocity lag* describes the difference between fluid and particle motion in a continuously accelerating fluid at low Reynolds number. The velocity lag, $\mathbf{U_{lag}}$ is defined as:

$$\mathbf{U_{lag}} = \mathbf{U}_p - \mathbf{U}_f = d_p^2 \frac{\rho_p - \rho_f}{18\mu_f} \mathbf{a_f} \tag{2.1}$$

where $\mathbf{U}_f$ and $\mathbf{U}_p$ are the instantaneous velocities of the fluid and the particle respectively, d_p is the particle diameter, and μ_f is the dynamic viscosity of the fluid, ρ_p and ρ_f are the particle and fluid densities respectively, and $\mathbf{a_f}$ is the fluid acceleration, as presented in [82, p. 16]. This shows that the particle size has a large contribution to the net effect of density mismatch. For example, the effects of mismatch in densities (in the case where $\rho_p > \rho_f$) can be alleviated by using smaller particles. However, smaller particles generally scatter less light than larger particles, and at very small scales Brownian motion effects become important (discussed in section 2.2). In general, a balance must be struck between particle size, density, and the signal intensity they provide. A detailed investigation on particle choice for PIV measurements can be found in [107]. It is worth mentioning that for water (or highly water based liquid) flow measurements, polystyrene particles are a good choice of tracers due to a variety of sizes, and their density being close to water (namely, $\rho = 1.05\,\mathrm{g/cm^3}$).

In experiments carried out in this work 0.39 and 0.39 μm diameter fluorescent beads, and fluorescent Red Blood Cell (fRBC)s that can be approximated to be as $2.5 \times 6.5\,\mu\mathrm{m}$ disks were used. The expected $\mathbf{U_{lag}}$ given a unit of fluid acceleration for the 0.39 μm and 1.04 μm diameter beads are $\approx 5 \times 10^{-4}\,\mu\mathrm{m/s}$ and $\approx 3.3 \times 10^{-3}\,\mu\mathrm{m/s}$, which is negligible. The lag for the fRBC ($\rho = 1.1\,\mathrm{g/cm^3}$ [108]), assuming the worst-case scenario of the largest area of the disk facing the flow, was found to be $\approx 0.264\,\mu\mathrm{m/s}$. This is significantly more than

---

[1]Note that PIV analysis can be successfully applied in motion of different structures (such as cells [106]), so long as there are enough *features* in the image

for the small polystyrene beads, and the implications of this for μPIV measurements will be considered again in chapter 4.

Particle signal   Conventionally, PIV measures light scattered by the particles. This light scattering is described by Lorenz-Mie theory (typical particles used are $> 1\,\mu m$ diameter), and is mentioned here for completeness, but is beyond the scope of this thesis and not applicable for fluorescence case. In essence, the particle scattering properties are described by its size (larger particles scatter more) and difference in refractive index of the particle and the surrounding fluid (same particle would scatter more in air than in water). This is discussed in detail from the perspective of PIV experiments in [78, Sec. 2.3]. The disadvantage of collecting scattered light, is that any other surfaces in the imaging volume can also scatter light, which decreases the contrast of particle images [109]. This can be overcome by the use of fluorescent tracer particles. The use of fluorescence imaging allows separation of excitation (laser) and emission (fluorescence) light. Therefore, any unwanted reflections are filtered out.

2.1.3   Measuring motion with cross-correlation

The statistical nature of motion estimation in PIV can be illustrated with the following example (illustrated in Figure 2.2). Consider a pair of particle images captured at time $t = t_0$ (black circles) and $t = t_1$ (white circles) shown in Figure 2.2a. If an attempt was made to track the individual particles, issues due to incorrect matches would be encountered as discussed in subsection 1.3.4. Instead, one could consider *all* the possible matches for each particle image. That is, if a single particle from time $t = t_0$ was paired with all the particles from time $t = t_1$, each overlap location could be represented on a 2D histogram, as shown in Figure 2.2b. In this example, each particle overlap contributes equally to the histogram. If this pairing is then performed for all particles between $t = t_0$ and $t = t_1$, the contributions of each could be summed to give the *statistically most likely* shift of a group of particle images between two frames.

Note, that the above example technically could be considered as probabilistic *tracking* as each particle position needs to be localised first. However, the statistical principle is the same in PIV, where *spatial cross-correlation* is used to determine the most likely shift of an image pattern, without the need for knowledge of individual particle locations. Cross-Correlation (CC) in 2D is defined as:

$$R(\mathbf{s}) = \int \tau_1(\mathbf{X})\tau_2(\mathbf{X} + \mathbf{s})d\mathbf{X} \tag{2.2}$$

where $\mathbf{s}$ is a 2D displacement vector, τ_1 and τ_2 are particle image patterns in the image plane $\mathbf{X}$, as shown in [78, Sec. 319]. Rigorous statistical derivations for PIV motion estimation using cross-correlation can be found elsewhere [110, 111, 82, 78]. Note that due to image

quantization (or pixelization) the discrete cross-correlation is used instead of the continuous one, and this will be described next.

Discrete cross-correlation   The Discrete Cross-Correlation (DCC) value for a pair of images with intensities I_1 and I_2, is described as:

$$R(\Delta i, \Delta j) = \frac{1}{M}\frac{1}{N}\sum_i^M\sum_j^N (I_1(i,j) - \bar{I}_1)(I_2(i+\Delta i, j+\Delta j) - \bar{I}_2) \qquad (2.3)$$

where $R(\Delta i, \Delta j)$ is the CC value at the shift of $\Delta i, \Delta j$ pixels in the x, y direction, I_1 and I_2 are the image intensity values at pixel (i,j), $\bar{I}_1, \bar{I}_2$ are the mean intensity values of the corresponding images, and N and M correspond to the pixel width and height of I_2. The purpose of subtracting the mean intensity value is to reduce the correlation between mean and fluctuating intensities and is referred to as image normalization [111]. Typically, the images are split into smaller areas, called IWs (i.e I_1 and I_2 terms are defined by the IW size in Equation 2.12). Commonly, different size IWs are used, with the smaller IW being treated as the I_2 term. In this case, I_2 can be treated as an image template, which is used to search for the closest image match in the larger I_1. This pixel-by-pixel template matching is illustrated in Figure 2.3. The product calculation at each pixel combination can become computationally costly. Willert and Gharib [112] proposed exploiting the correlation theorem in order to speed up the computation with the use of Fast Fourier Transform (FFT). The flow chart of obtaining CC matrix in this way is shown in Figure 2.4. The use of FFT reduces the number of computational operations from $O[N^4]$ in the case of DCC to $O[N^2\log_2 N]$ for correlating two $N \times N$ IWs [82, p. 136]. In the remainder of this thesis, this method will be abbreviated as Fast Fourier Transform Cross Correlation (FFTCC). Whichever CC method is used, the obtained CC matrix must be carefully evaluated for the next step of flow estimation, as explained next.

Peak detection   Once the CC result is recovered, it can immediately reveal the quality of the result. For instance, if the highest correlation peak is significantly larger than the surrounding peaks, this implies that there is a single unambiguous shift for which particles match well between two frames. This ratio is referred to as peak-to-peak (p2p) ratio, adopting the term from [1], but the same concept is also called differently in the literature (for example, *peak detectability* in [78, p. 343]). However, this p2p ratio is not a definitive parameter of PIV measurement reliability: for example an extremely bright particle appearing in the second frame of an image pair, can cause a sharp and tall CC peak to appear at the location of the bright bead, which might not match with the motion of the whole *group* of particles. Moreover, p2p measure is not effective for low seeding density images [78, p. 418], or when the particle image size is large compared to the IW, since the correlation peak can span the whole IW. Therefore additional validation of the

(a)

(b)
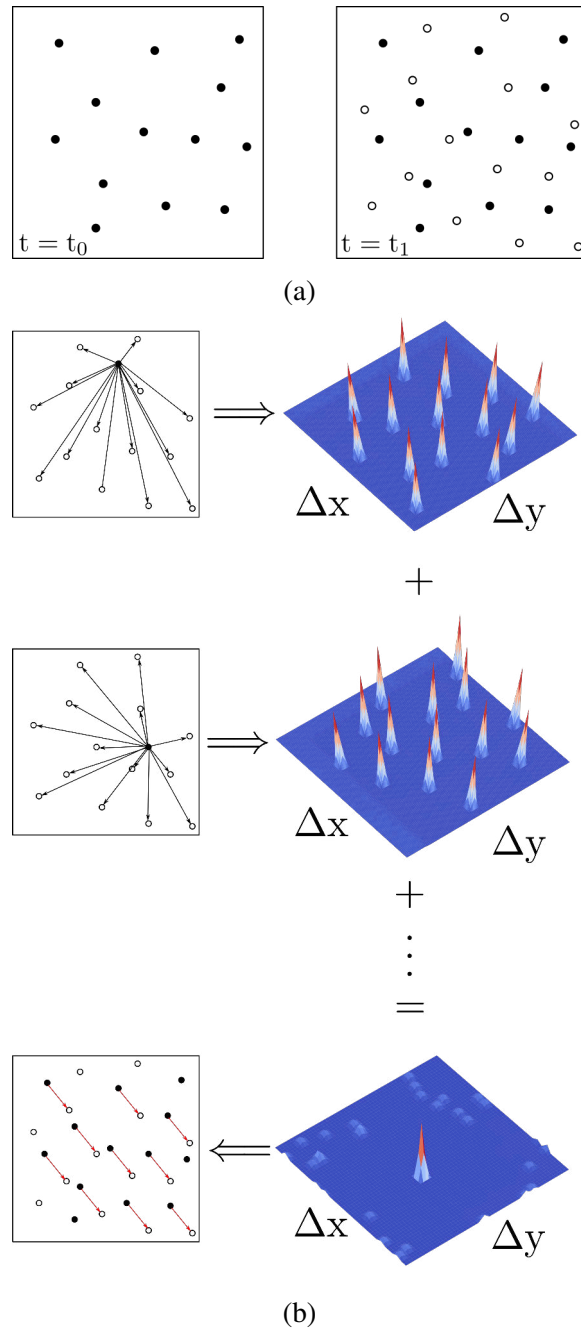
Fig. 2.2 Illustration of statistical motion estimation for PIV. (a) Shows the motion of a group of particles between two frames. The particles from time t_0 are shown as black, and particles from time t_1 as white circles. Notice that some black particles left, and some white particles entered the area of interest. If standard PTV methods were applied (see chapter 1) to measure the motion of these particles, these methods would struggle to match the correct particles, due to the high particle density, and proximity between particles. Instead, the most statistically likely motion of all particles could be estimated as shown in (b). Each (black) particle from frame at t_0 could be matched with all the particles in frame at t_1, as shown on the left of (b). The algorithm would essentially output a binary answer: 1 for an overlap or 0 for no overlap. The location of these results could be presented as a histogram, as shown on the right column of (b). If the above routine was carried out for each particle from frame at t_0, the histograms could be added. The sum of these histograms, would indicate the statistically most likely motion of all the particles. This would yield the correct pairing for the majority of particles, as shown in bottom left of (b). Figure based on [78, p.318].
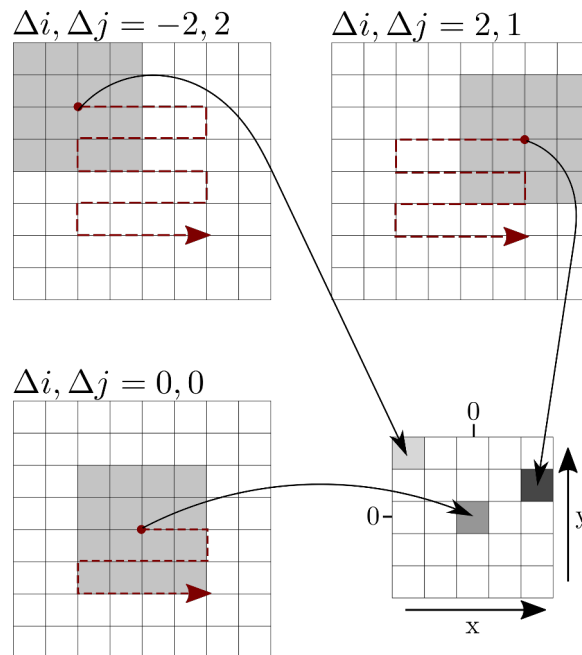
Fig. 2.3 Illustration of discrete spatial cross-correlation. The smaller IW, shown as a gray 4×4 grid, is compared against the larger IW, shown as a 8×8 white grid. The DCC value is calculated at each location in the larger IW, where the small IW can be contained within the bounds of the large one. The red dashed line indicates the "route" the smaller IW takes, which can be arbitrary as long as all possible pixel-overlap combinations between the two grids are covered. The DCC value calculated at each step, contributes to the CC results (or CC matrix), indicated by the 5×5 grid. In this example, the DCC value was found to be highest at $\Delta i, \Delta j = 2, 1$, indicated by the dark pixel in the CC matrix. In this case, the most likely shift would be estimated as $(2, 1)$ pixel in the (x, y) directions respectively. The size of the CC depends on the two IWs Figure based on [82, Fig. 5.12].
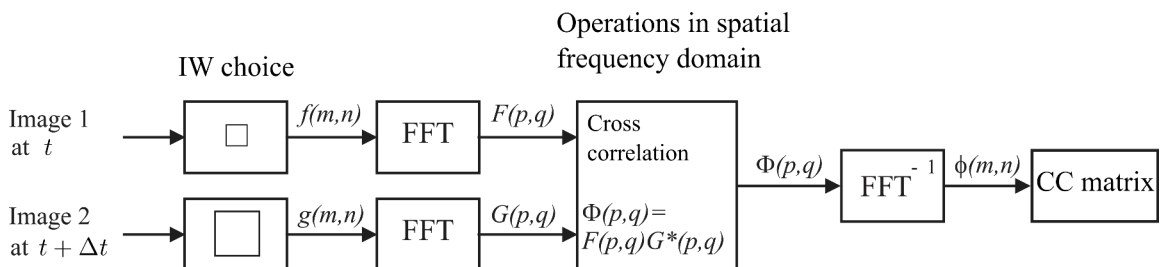
Fig. 2.4 Instead of multiplying intensity values pixel by pixel, CC is calculated by operating in the spatial frequency domain. Each IW is transformed using FFT before complex conjugate multiplication. Taking the inverse FFT produces the CC matrix. Figure adapted from [112].

measurement reliability is necessary. One such method is the examination of the velocity component distribution, discussed in subsection 2.1.5.

Subpixel fitting   The CC matrix obtained with the methods described above, only estimates the motion to an integer pixel value (which implies an uncertainty of $\pm\frac{1}{2}$ pixel). In order to recover more detail about the *mean* motion of the particle pattern, subpixel estimators can be applied, and the commonly used [82, 78] *three-point* estimators will be summarised here [2]. As the name suggests, the subpixel fits are achieved using three points: the peak value in the CC matrix, and the two closest pixel-neighbours in *x* and *y* axes. The subpixel position can be estimated with the following methods (using notation from Equation 2.12 and following [82, p. 160]):

- **Centroid**. The centroid localization (or centroiding) is a popular method for estimating the centre of some intensity distribution [114–116]. The subpixel location, x_0, can be estimated in the following way:

$$x_0 = \frac{(i-1)R_{(i-1,j)} + iR_{(i,j)} + (i+1)R_{(i+1,j)}}{R_{(i-1,j)} + R_{(i,j)} + R_{(i+1,j)}} \tag{2.4}$$

  and similarly for y_0.

- **Parabolic fit**. The maximum of a parabolic function $f(x) = Ax^2 + Bx + C$ fitted to the three points, is used as the supixel estimator. Unlike the centroid, the parabolic fit is dealing with a peak, such that $R_{(i,j)} > \frac{1}{2}(R_{(i-1,j)} + R_{(i+1,j)})$ [78, p. 375] and is described in the following way:

$$x_0 = i + \frac{R_{(i-1,j)} - R_{(i+1,j)}}{2\left[R_{(i-1,j)} - 2R_{(i,j)} + R_{(i+1,j)}\right]} \tag{2.5}$$

  and similarly for y_0.

- **Gaussian fit**. Similar in the mathematical expression to the parabolic fit, the Gaussian fit is a standard choice in PIV literature, this is because the shape of the correlation matrix approximates a Gaussian [112] [3].

$$x_0 = i + \frac{\ln R_{(i-1,j)} - \ln R_{(i+1,j)}}{2\left[\ln R_{(i-1,j)} - \ln 2R_{(i,j)} + \ln R_{(i+1,j)}\right]} \tag{2.6}$$

  and similarly for y_0.

While advanced subpixel estimators exist (compared in [117]) the 3 methods mentioned, in particular the Gaussian fit, can perform well in most cases for standard PIV analysis. Throughout this thesis, unless otherwise stated, the Gaussian fit subpixel estimation is used

---

[2]The statistical aspects of different subpixel fitting functions are discussed in detail in [113, Sec. 3.9].
[3]The cross-correlation of a Gaussian function yields another Gaussian function.
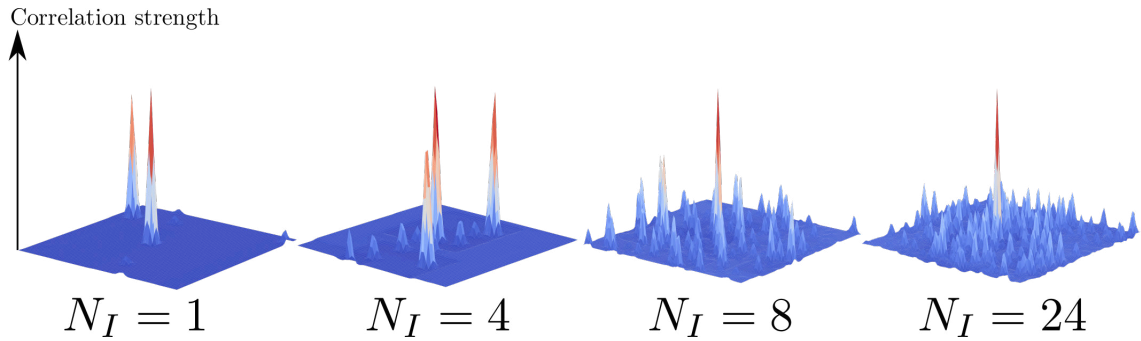
Fig. 2.5 Cross-correlation results for varying number of particles per interrogation window, N_I. As the particle image density grows, the p2p ratio increases. This suggests that there is less chance that the CC resulted in an erroneous measurement. While not shown here, significantly increasing the number of particles produces speckle patterns (for scattering particles), which are not suitable for PIV analysis. Figure based on [78, Sec. 8.3].

for CC results obtained with FFTCC. In principle, these fits should give arbitrary accuracy, but the next section will discuss the effects of experimental parameters on measurement reliability.

2.1.4 Measurement reliability: main considerations

The success of a PIV measurement largely depends on the number of particles that appear in both images used for CC. In the ideal case, the image patterns used for CC in Equation 2.12, would remain identical between image pairs (i.e. the relative distances between particles in the second image would remain the same despite some translation of the whole group of particles). However, in practice the number of particles and their patterns change between image frames due to properties of the flow. Following [110] and [78, Sec. 8.3], the parameters describing these effects are introduced below.

Tracer particle density   Perhaps the most important variable for robust statistical estimation of motion using CC, is sufficient number of particle images. This is usually described as the average number of particles per interrogation window (also known as particle image density), N_I. If N_I is very low, then there is not enough pattern to determine the particle motion unambiguously, on the other hand, if N_I is very high, the particle images start overlapping, and speckle pattern will form scattering tracers, and individual particles will not be distinguished any longer in fluorescent tracer case. In the very high N_I case, laser-speckle velocimetry is used [13]. For the low density case PTV is normally used. However, a statistical method to artificially increase the N_I will be introduced in subsection 2.2.1.

Keane & Adrian [110] used Monte Carlo simulations to estimate the minimum particle density for reliable PIV measurements, where they used a p2p ratio of 1.2 as the reliability measure. They found that in the absence of any *in-plane* or *out-of-plane* particle loss, $N_I > 6$ is needed for a 95% probability of valid peak detection. Of course this number could be

lower if the p2p threshold was lowered, as Raffel et al. argue [82, p. 171], and add that theoretical minimum (derived from Poisson statistics) should be $N_I = 3$. The effect of varying particle image density is shown in Figure 2.5. In practice, adequate seeding is ensured at the onset of a PIV experiment. However, microscopic flows generally cannot be adequately seeded due to practical limitations, and computational methods are necessary to overcome this issue. These methods necessary for analysis of experiments presented in this thesis, will be discussed later in this chapter.

Effect of in-plane motion The next parameter might appear almost trivial at first sight, however, it is essential to consider it for successful PIV analysis. This parameters, F_I, describes the fractional loss of particles between images of the flow due to *in-plane* motion, and is expressed as:

$$F_I = 1 - \Delta X / D_{\text{IW}} \qquad (2.7)$$

Where ΔX is the image displacement, and D_{IW} is the dimension of the IW. Degree of in-plane motion is particularly important if both IWs used are of the same size (the calculation of CC is made possible by *zero-padding* the second IW to accommodate the pixel-by-pixel search of the first one [111]). Clearly, if F_I is too small (in other words, the in-plane shift is too large), there will be a loss of CC strength between two images of the fluid motion. The effect of different in-plane motion amounts on the CC results are illustrated in Figure 2.6. Note that in the case when same sized IWs are used for analysis with FFTCC algorithm, there is very high probability that the peak will "wrap" around the correlation matrix when the in-plane motion exceeds half the IW size. This is effect can be seen in Figure 2.6a for $F_I = 0.125$. This is due to the assumption that the information in the image is periodically repeating when FFTCC is used (details are discussed in [82, p. 136], see also [118, Fig. 5] for an illustration of this effect in the image domain).

One way to circumvent the effect of in-plane motion on CC results, is to decrease the time between frame capture, Δt. However, this can lower the dynamic range of recovered velocities. A better alternative is using IW offset (where the second same sized IW is shifted by the amount of expected flow) [119], or using pairs of different-sized IWs [111]. The purpose of the latter two techniques is to preserve all the particle pattern information between the two IWs. The effect of different IW size for correct CC peak recovery is shown in Figure 2.6b, where the size of different IWs is expressed as a ratio. The size of IW(A) used in the analysis of the synthetic results shown here was 32×32 pixels. In the past, the main downside of using significantly larger IW was the increased computational time, however, it is not an issue with modern computational power [78]. For the experiments carried out in the next two chapters, in general the dimensions of the IW(B) are at least twice the size of IW(A) to accommodate the in-plane motion.

$F_I = 0.75$ $\qquad$ $F_I = 0.50$ $\qquad$ $F_I = 0.25$ $\qquad$ $F_I = 0.125$

(a)

$F_I = 0.00$

$\text{IW}(B/A) = 1$

$F_I = 0.00$

$\text{IW}(B/A) = 2$

$F_I = -0.25$

$\text{IW}(B/A) = 4$

(b)
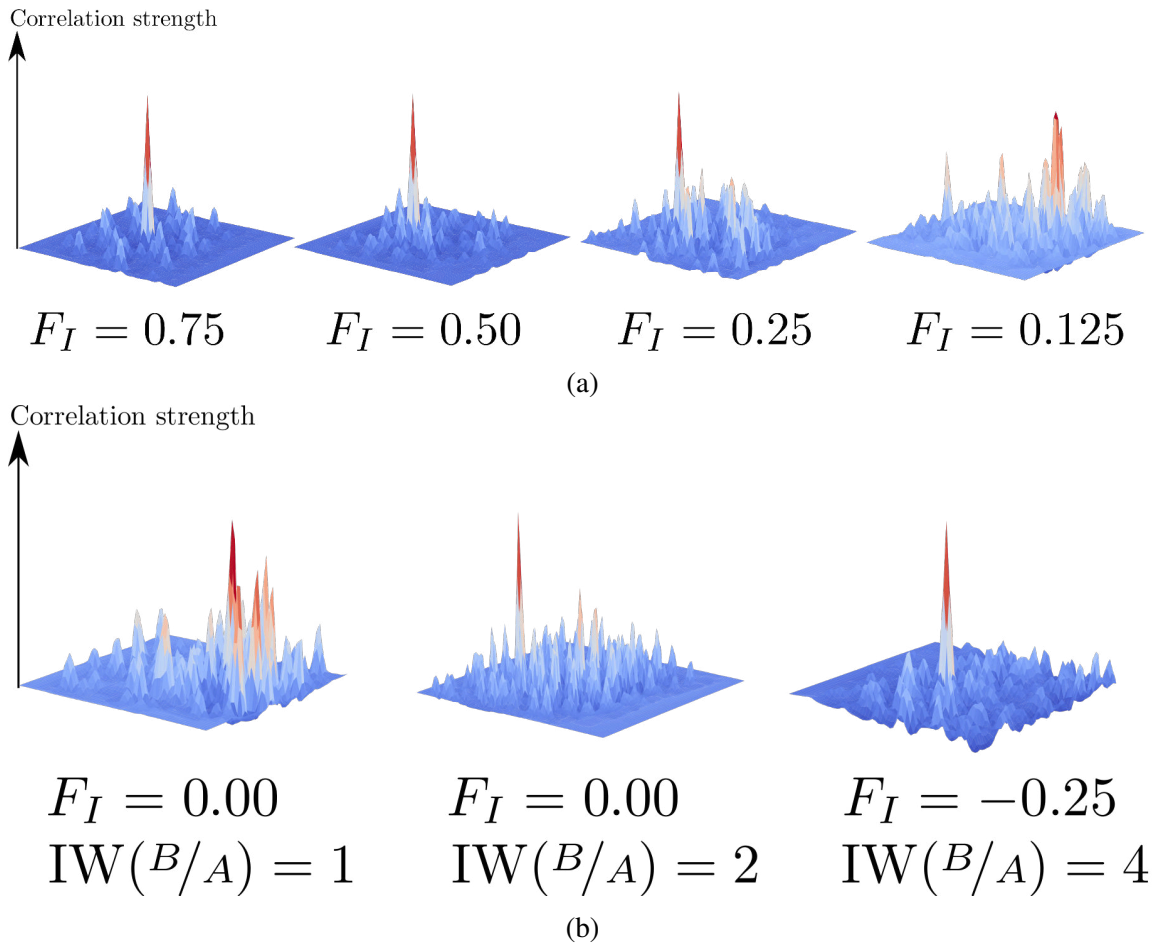
Fig. 2.6 Effect of in-plane particle loss on cross-correlation result. (a) Particle loss due to in-plane motion becomes significant above $F_I = 0.25$. After this value, the correlation peak is likely to "fold" around the CC (for detailed explanation of the effect see [118]), as shown for the $F_I = 0.125$ case in (a). A possible solution to prevent particle loss due to in-plane motion, is to use different sized IWs. Consider two frames A, B captured at a small time difference Δt. If the IW size in the second frame, $IW(B)$, is sufficiently large to contain all the particles from the IW in frame A, $IW(A)$, this means that there is effectively no particle loss between the IWs in the two frames. The effect of varying $IW(B)$ and $IW(A)$ size ratio is shown in (b). Note that since the CC matrix size increases with increasing IW size (see Figure 2.3), only a small region around the highest peak are shown in (b). Figure (a) is based on [78, Sec. 8.3].

(a)

$F_0 = 0.75$ $F_0 = 0.50$ $F_0 = 0.25$ $F_0 = 0.125$

(b)
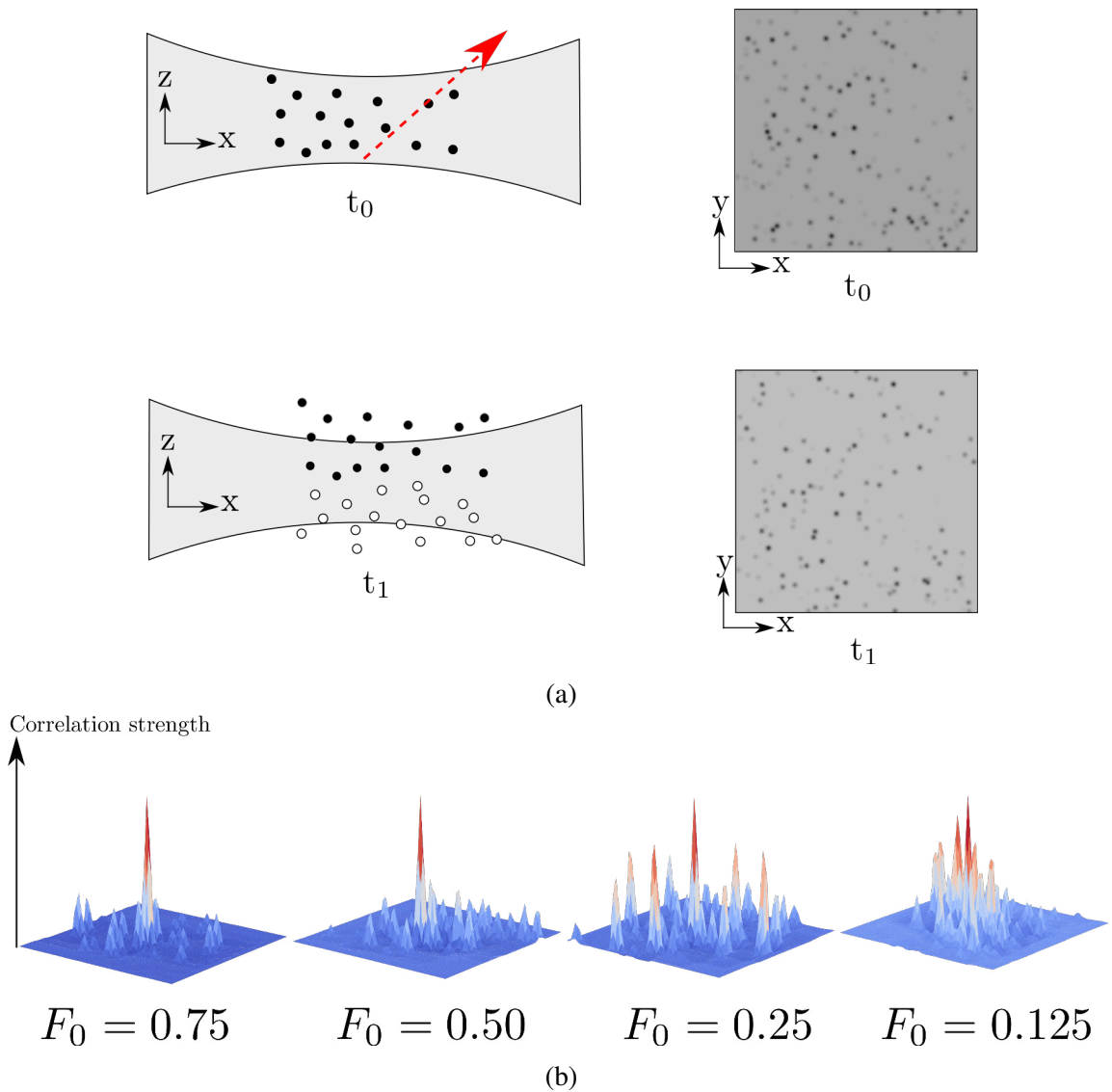
Fig. 2.7 Out-of-plane motion and its effects on the cross-correlation results. In a flow with significant out-of-plane motion the change of particle pattern due to tracers entering and leaving the light sheet (in the depth direction) can cause similar effects on peak detectability as *in-plane* loss of particles does, as shown previously. (a) Illustrates the particles leaving and entering the light sheet in a flow with a large OOPM component. Original particles captured in the light sheet at t_0 are shown in black, and new particles entering the light sheet at t_1 are shown in white. The images on the right of (a) show the image plane (as seen by the camera) at time t_0 and t_1. Even for a human observer, inferring the correct motion would be significantly challenging. (b) Shows the effect on the CC matrix with increasing OOPM component. However, since the *probability* of valid detection decreases, it remains possible to recover the true motion of the flow, even in large F_O condition. For example the highest correlation peak shown for the $F_O = 0.25$ case in (b) is in the correct location, albeit surrounded by large erroneous peaks. Figure (b) based on [78, Sec. 8.3]

Effect of out-of-plane motion   If the fluid of interest has a velocity component perpendicular to the light sheet, such motion is referred to as *out-of-plane* motion. The loss of particles between frames due to OOPM, has a similar effect on the CC matrix as in-plane motion. That is, the particle pattern will change due to particles appearing/disappearing in the light sheet, as illustrated in Figure 2.7a and a loss of CC strength will occur. The parameter describing the fractional loss of particles due to OOPM, F_O, is defined as:

$$F_O = 1 - \Delta z / \Delta z_0 \tag{2.8}$$

where Δz is the OOPM and Δz_0 is the light sheet thickness for a uniform (or top-hat function) intensity light sheet profile [4]. F_O describes the ratio of out-of-plane motion component, to the thickness of the light sheet. Increasing F_O has a similar effect on the peak detectability, as increasing F_I does, this is illustrated in Figure 2.7b. Notice that even at significant amounts of OOPM, there is still a chance that the highest peak is representing the true motion in the image. In other words, despite the fact that conventional PIV only measures velocity components in a 2D plane (i.e. Two Dimension-Two Component (2D2C) PIV), it can be successfully used to measure flows with significant amount of OOPM. In fact, this property is of crucial importance for measurements in the zebrafish heart which will be discussed in chapter 4.

Rafell et al. [82, Sec. 5.5.8] propose that in the same way as mitigating the effect of in-plane loss, reduction of Δt can reduce F_O. Another strategy to cope with OOPM is to align the light sheet with the flow in such a way that the F_O is minimized. Alternatively, the light sheet can be shifted in z between exposures in order to capture the same particle images (in other words, the light sheet is moved in z by the same amount as the anticipated out-of-plane velocity component in the flow to ensure the same particle pattern is captured in the two frames). This technique is proposed by Adrian & Westerweel [78, Sec. 8.8.3]. Finally, the thickness of the light sheet can also be increased (at the expense of decreasing illumination intensity and z resolution) in order to accommodate F_O.

Effect of spatially varying flow   Large scale spatial gradients have significant influence on the quality of CC matrices. Since there are many variations of spatial gradient types that can appear in a fluid flow, formulating a universal parameter describing the loss of correlation effects is not trivial [120]. However, Adrian & Westerweel [78, Sec. 8.4.2] provide an approximate generalization of shear effects by considering the local displacement variation, a, described as:

$$a = M_0 |\Delta \mathbf{u}| \Delta t \tag{2.9}$$

where M_0 is the magnification of the system, Δt is the time difference between two image frames, and $|\Delta \mathbf{u}| = \partial \mathbf{u} / \partial \mathbf{x} \cdot L$ is the variation of the velocity field in the interrogation *volume*

---

[4]Strictly speaking, for a Gaussian intensity profile $F_O = \exp\left(-4\Delta z^2/\Delta z_0^2\right)$ [78, Eq. 3.82]. However this does not change the discussion presented here.

$L^3 = \Delta z_0 D_{\text{IW}}^2 / M_0^2$. Westerweel [120] investigated the effect of simple and uniaxial shear on correlation matrix quality. Detrimental effects were observed for simple shear when its magnitude was greater than twice the size of particle image diameter. In simple shear cases, such as observed in laminar flow in a pipe, it is sufficient to make the IWs sufficiently narrow in the direction of velocity gradient, in order to minimize effects on CC matrix quality. On the other hand, rigorously adjusting PIV analysis parameters to account for shear is not trivial, as it requires an advanced technique, referred to as *interrogation window deformation* [121]. In essence, a standard PIV analysis is done first in order to estimate the motion of the particles. Then, using the information of the flow from the "first pass" PIV analysis, the shape of the IWs is adjusted to accommodate the spatial gradients in the fluid. Normally, high spatial gradients are encountered in turbulent flows, or flows with high vorticity. In this thesis, the regions of potentially high shear were limited to small region of the heart at the valves. Because this area was only a small fraction of the whole heart volume, it was decided that window deformation techniques are beyond the scope of this thesis, and are presented for the purpose of a broad overview of potential issues and techniques to resolve them.

General guidance   Adrian & Westerweel [78, Sec. 8.3.6] propose four "design rules" for PIV measurements. These rules were the result of extensive Monte Carlo simulations, exploring various combinations of N_I, F_I, and F_O. The suggested rules are the following:

Number of particles per IW	$N_I > 10$
In-plane motion	$F_I > 0.75$
Out-of-plane motion	$F_O > 0.75$
Displacement variation in an IW	$a < d_p$

It is important to note that these rules are only meant as a guide in order to limit trial and error in establishing initial experimental parameters for a PIV experiment. In addition to this, in the particular case of $F_I > 0.75$ rule, this was suggested when computational power was limited, and using different-sized IWs to allow larger motion was not practical (these rules are based on seminal work carried out in early 90s [78, Sec. 8.3.6]). The similar argument is true for the spatial gradient rule, where window deformation can be used to measure velocity in flows with $a > d_\tau$. As will be shown later, for this thesis the parameters of main concern were the N_I and F_O. The reasons for this, as well as suggested approaches in order to ensure reliable PIV results, will be discussed in section 2.2. Note, that the above discussion on various flow parameter effects, did not discuss the effect of particle size. It has an effect on the velocity measurement error [122], and will be investigated in the next section.

2.1.5   Measurement uncertainty: bias and random error

The discussion in the previous section aimed to provide an understanding of the role of different flow dynamics on CC matrix quality. All the effects shared a common feature of the CC peak becoming more noisy (i.e. the p2p ratio decreasing). Nevertheless, it was already pointed out that even a CC result with a somewhat poor p2p can still contain the highest peak at the location of the true motion of the flow (see Figure 2.7b). It is therefore more useful to judge the quality of velocity measurements by quantifying the average measurement uncertainty. This quality can be estimated by measuring the *bias* and *random* errors. For a large number of measurements of a flow with constant motion, the bias is defined as the difference between the true velocity value and the average value of all the measurements, and can be expressed as:

$$\varepsilon_{\text{bias}} = \frac{1}{N} \sum_{i=1}^{N} u_{\text{meas}} - u_{\text{true}} \tag{2.10}$$

where N is the number of measurements, u_{meas} and u_{true} is the measured and the true fluid motion respectively. The random error in the aforementioned case would be the spread of velocity values around the mean, namely:

$$\varepsilon_{\text{rms}} = \sqrt{\frac{1}{N} \sum_{i=1}^{N} \left[\overline{u_{\text{meas}}} - u_{\text{true}}\right]^2} \tag{2.11}$$

where $\overline{u_{\text{meas}}}$ is the mean of u_{meas} and other symbols are as described above.

Unfortunately, these measurements rely on knowing the true velocity with no uncertainty, something that is not feasible with real experiments. Nevertheless, this can be achieved by simulating a chosen number of flow images with known properties (flow dynamics, particle size, laser sheet thickness etc.) using the Monte-Carlo technique. The key aspect of the simulations is that each frame pair used for PIV analysis contains a *random* distribution of particle images as would be seen in a real experiment but without the impracticality of obtaining a sufficiently long dataset to draw statistically meaningful conclusions. While there appears to be no rule for the minimum number of samples (in terms of image pairs), other researchers have generated between one and ten thousand image pairs to deduce the performance of PIV analysis with different parameters [123, 124]. A random PIV image generator provided as part of the *PIVlab* MATLAB package [2] was used for synthesizing images in the following analysis. The implementation is based on the description provided in [82], which simulates particle images as Gaussian spots. Note that studies on bias and random error are very common in PIV literature, and have been investigated for a variety of different flow conditions in the past [111, 82, 78, 123].

However, as will be shown in chapter 4, it was found that the standard CC approach performs poorly in a specific circumstance. In particular, if a high intensity feature (which

could be stationary with respect to the flow) appeared in an IW, this bright feature would often "pull" the correlation peak (and hence the recovered velocity) towards its location. It was proposed that this was due to the pixel intensity product used in the CC algorithm. This prompted a search for an alternative algorithm to perform tracer particle pattern matching. Due to its computational simplicity, and successful application in real-time optical gating of the beating heart [15, 16], the Sum of Absolute Differences (SAD) algorithm was implemented. Unlike the standard CC approach, Sum of Absolute Differences (SAD) aims to find the location of the *minimum difference*, rather than *maximum product*, of pixel values between two images. Similarly to the Equation 2.12, the SAD matrix can be described in the following way:

$$SAD(\Delta i, \Delta j) = \sum_{i}^{M} \sum_{j}^{N} |I_1(i,j) - I_2(i + \Delta i, j + \Delta j)| \qquad (2.12)$$

The reason this is introduced at this point, is because the accuracy analysis results shown in the next paragraph revealed interesting properties of SAD, which complement the standard FFTCC algorithm in certain conditions. In fact, the analysis below provides strong evidence that for measurements performed in chapter 4, SAD is more suitable. Note, in what follows the term CC matrix will be used as a general term to refer to the result of the pixel-by-pixel calculation for either the SAD or FFTCC algorithms, even though strictly speaking SAD is not cross-correlation (i.e. it is not point-wise multiplication of two function values).

2.1.6   Measurement uncertainty: SAD vs FFTCC

The results shown in this section consider uniform motions in the *x* direction (sampled at 0.1 pixel steps) of particles with 4 different diameters. Namely, these diameters are 2, 4, 9, and 18 pixels (the diameters here are the physical size, before convolution with the Gaussian beam). The first reason for this choice of diameters is to test the performance of SAD on tracers in the particle image range of 2 to 4 pixel diameter which is referred to as optimal in the PIV literature [122], [78, p. 294]. Secondly, the 9-18 pixel range was used to simulate the approximate size of $6.5\,\mu\text{m}$ red blood cells (for 10 and $20\times$ magnification respectively), which were used as tracer particles for *in vivo* measurements, as will be shown in chapter 4. For each particle size, the random error and bias, as well as scatter plots at the pixel shift of minimum/maximum of SAD random error, are shown below. For each plot, the results from SAD algorithm are shown in red crosses, and black dots for FFTCC data. In the bias and random error plots, the data points are joined with straight lines. The FFTCC results are fitted with a Gaussian curve Equation 2.6, and SAD results - with a parabolic curve Equation 2.5, which in practice perform best for each CC method.

2 pixel diameter   For the smallest particle image size used in this analysis, FFTCC showed significantly smaller bias than SAD, see Figure 2.8b. Note, that the bias appears to be lowest for FFTCC, when it is highest for SAD. In terms of the experiments performed in this thesis, the smallest particles used were 0.39 μm diameter, which spanned just over 2 pixels in the image plane, and the FFTCC algorithm instead of SAD should be used if smaller bias is required. On the other hand, the random error (Figure 2.8a), is somewhat more similar between the two algorithms. However, SAD appears to have lower random error values at integer displacements, but FFTCC performs better at half integer shifts. The *uv* scatter plots, showing all the velocity components measured at a particular pixel shift, are displayed in Figure 2.8c, and Figure 2.8d for 0.5 pixel and 1.0 pixel shifts respectively. As indicated in Figure 2.8a, there is more spread at 0.5 pixel shifts than at 1.0 pixel shifts. This effect (larger/smaller error at specific integer values) is known as *peak-locking* [125], and is particularly apparent for smaller than 2 pixel diameter particles [126]. The fundamental reason for this effect, is that a smooth curve is being fitted on a discrete data with a very sharp peak (in the case of small particle images).
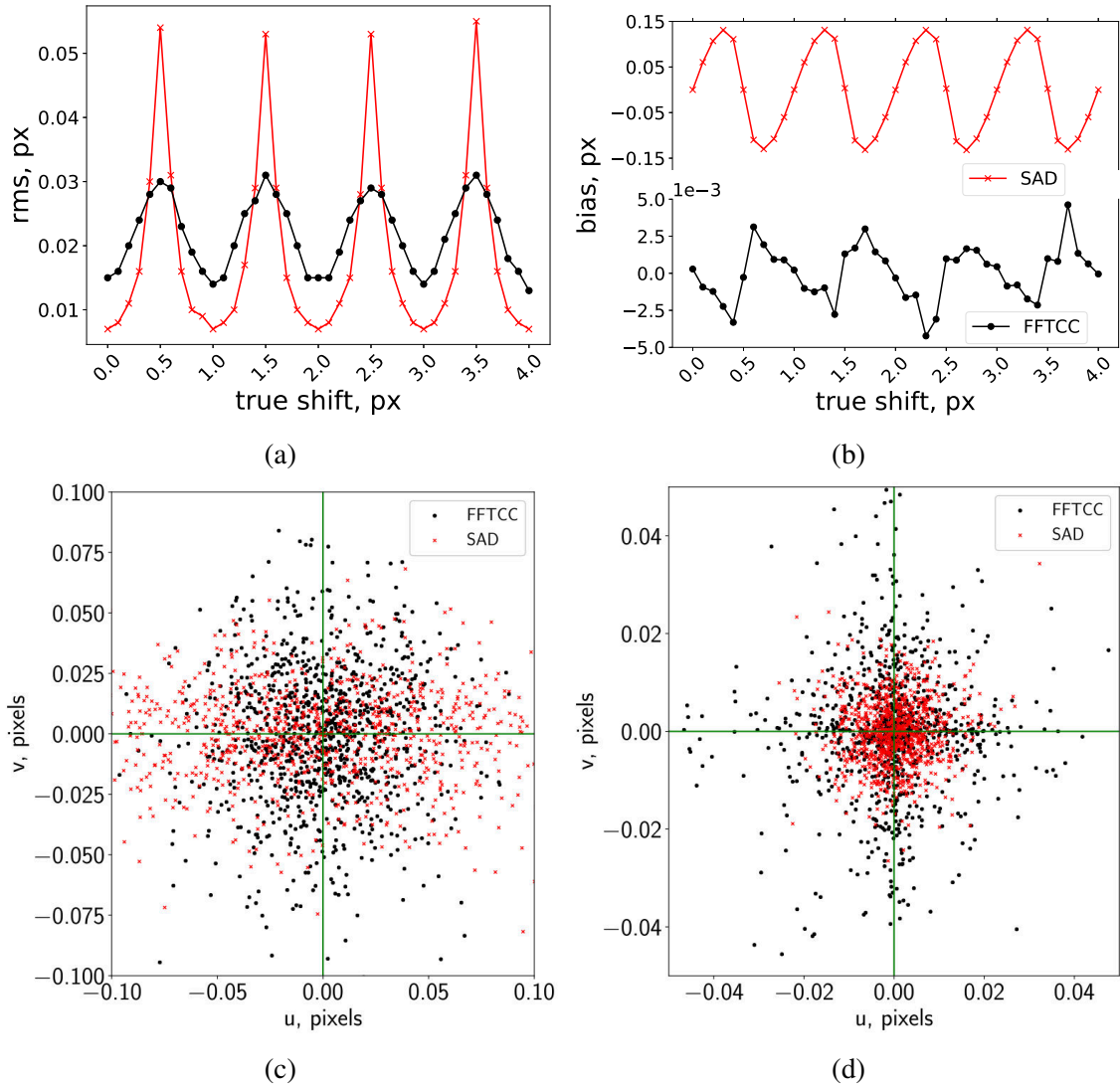
Fig. 2.8 Bias and random error for 2 pixel diameter tracers using 32/64 IW size. (a) Shows the random error for motion estimation with SAD (red crosses and lines) and FFTCC (black dots and lines). (b) Shows the bias of the measurements (the lower plot has the *y* scale in 10^{-3}). Notice the periodically varying behaviour, for both of these results. This variation appears "in phase" for random error, but is "out of phase" for the bias (i.e. the minimum/maximum bias for SAD/FFTCC share the same pixel displacement). The scatter plots illustrate the raw *uv* velocity component measurements for the selected image shifts of 0.5 and 1.0 pixel in (c) and (d) respectively.

4 pixel diameter   At 4 pixel diameter, the peak-locking is negligible for the FFTCC results (Figure 2.9a, Figure 2.9b), as the diameters of the images increase, and the intensity profile of the particle becomes smoother (and hence more suitable for fitting a smooth function). On the other hand, the effect resembling peak locking in standard CC algorithms, remains for the SAD data. This can be explained by the sharp peak, that SAD CC seems to maintain for the 4 pixel case. However, it will be shown later that the peak does become smoother when the particle size increases. It is interesting to note that there is an asymmetric spread along the *y*-axis in the 0.5 pixel shift *uv* scatter plot shown in Figure 2.9c. The cause for this is unclear, but this behaviour remains unchanged throughout the rest of this analysis. This asymmetric spread does not appear in the 1.0 pixel shift *uv*-plot Figure 2.9d.
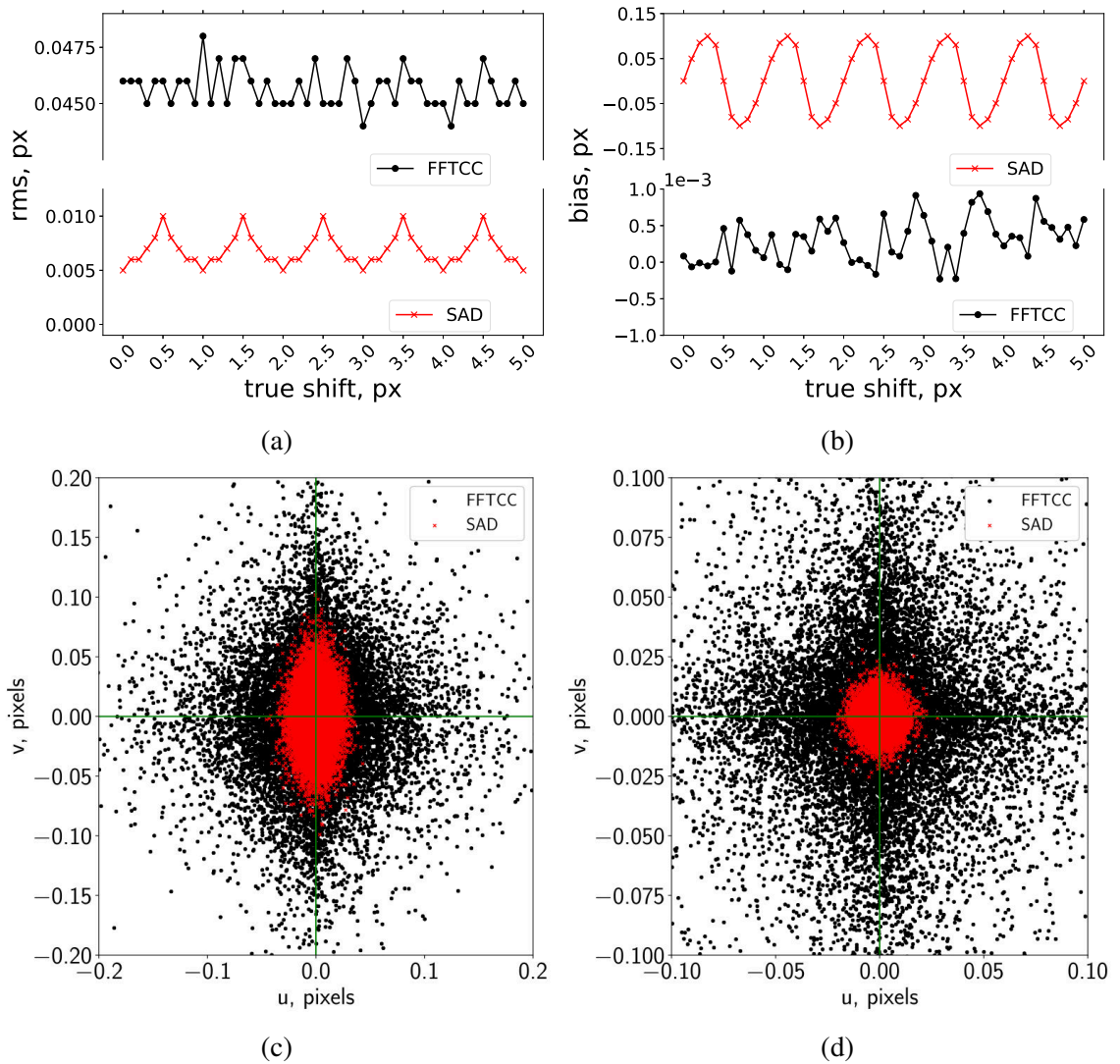
Fig. 2.9 Bias and random error for 4 pixel diameter tracers using 32/64 pixel IW size. (a) Shows the random error for motion estimation with SAD (red crosses and lines) and FFTCC (black dots and lines). (b) Shows the bias of the measurements (the lower plot has the *y* scale in 10^{-3}). (a) Compared to Figure 2.8a, the random error for FFTCC varies less with pixel shift. While the random error on SAD data is still periodically varying with pixel shift, the amplitude is an order of magnitude lower than in the 2 pixel particle diameter case. (b) The amplitudes of the bias variation remain essentially the same as in the 2 pixel diameter data, however, there does not seem to be any significant periodic variation in bias for the FFTCC data. The scatter plots illustrate the raw *uv* velocity component measurements for the selected image shifts of 0.5 and 1.0 pixel in (c) and (d) respectively. (c,d) The *uv* show substantially less spread in the SAD data compared to FFTCC, however, the cause for an asymmetric spread for SAD datapoint in the 0.5 pixel shift case (c) needs further investigation.

9 pixel diameter   As the particle image diameter increases, the differences between SAD and FFTCC become more apparent, particularly for smaller IWs. For motion measurements of 9 pixel diameter particle images, using a small/large IW combination of 32/64 pixels, leads to a large random error for FFTCC measurements, which starts at around 0.9 pixels and increases to around 1.6 pixels when the image shift equals the diameter of the particle, as shown in Figure 2.10a. In contrast to this, the SAD measurements retain a strict periodic variation, with the amplitude barely exceeding 0.01 pixel. On the other hand, bias does not differ significantly between the two methods Figure 2.10b. Nevertheless, it is clear that like in the random error case, the bias varies periodically in the SAD case, whereas it increases almost linearly in the FFTCC case. The *uv*-scatter plots in Figure 2.10c, Figure 2.10d illustrates that the difference between the two methods is now clear, compared to the smaller particle diameter cases.
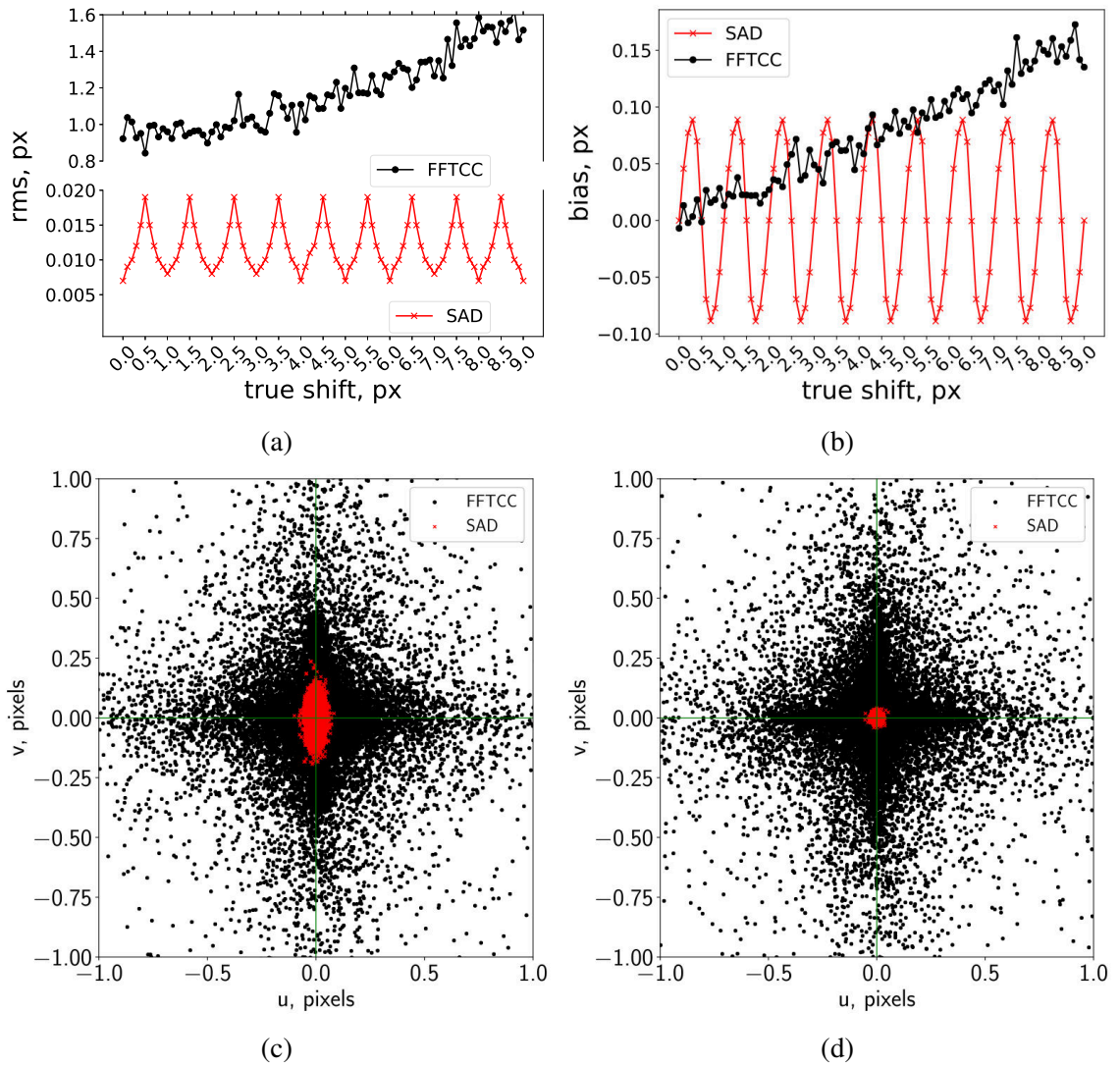
Fig. 2.10 Bias and random error for 9 pixel diameter tracers using 32/64 pixel IW size. (a) Compared to SAD, FFTCC results suffer from significant amounts of random error when relatively large particles are used as tracers. Notice that the random error increases with increasing motion. (b) Bias errors remain similar, but an increasing trend can be seed for the FFTCC data. The scatter plots illustrate the raw *uv* velocity component measurements for the selected image shifts of 0.5 and 1.0 pixel in (c) and (d) respectively.

However, if the IW size is increased twice (to 64/128 pixels) the bias and random error decreases substantially for the measurements obtained with FFTCC as shown in Figure 2.11a. This is because for a uniform particle motion, the random error is proportional to N_I and the relative width of the CC displacement peak (d_D/d_r, where d_D is the peak width and d_r is the pixel pitch of the camera sensor) [78, Sec. 8.5.6]. In other words as the IW size decreases, the random error increases (as fewer particles are enclosed in the IW). The bias also behaves in a similar way: it increases for smaller IW size For SAD the improvement is less, nevertheless, it is a twofold reduction of the random error. Interestingly, the bias on FFTCC data decreases to almost negligible, while SAD bias remains similar to the 32/64 pixel IW case, see Figure 2.11b. The scatter plots illustrate the raw *uv* velocity component measurements for the selected image shifts of 0.5 and 1.0 pixel in (c) and (d) respectively. Note that the spread of *v* has decreased for the SAD datapoints, as shown in Figure 2.11c.
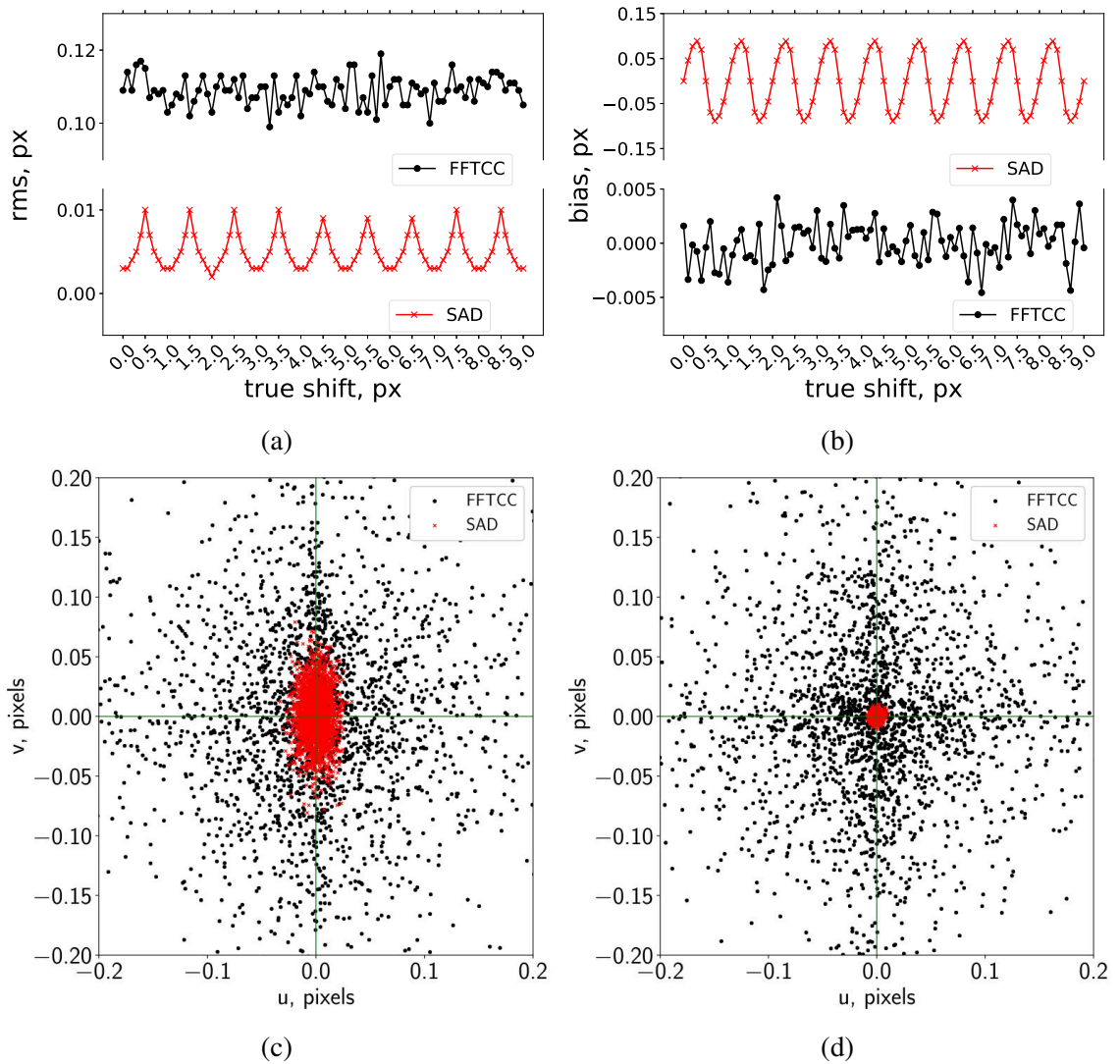
Fig. 2.11 Bias and random error for 9 pixel diameter tracers using 64/128 pixel IW size. (a) Shows the random error for motion estimation with SAD (red crosses and lines) and FFTCC (black dots and lines). (b) Shows the bias of the measurements. Use of larger IWs significantly reduce the errors on the FFTCC measurements (a,b) compared the smaller IW case (see Figure 2.10). The scatter plots illustrate the raw *uv* velocity component measurements for the selected image shifts of 0.5 and 1.0 pixel in (c) and (d) respectively. While the general effect on SAD results is minimal, there is a noticeable reduction in the variation of *v*-values for the 0.5pixel motion case as shown in (c). Note that there are fewer data points in the *uv*-scatter due to use of larger IWs.
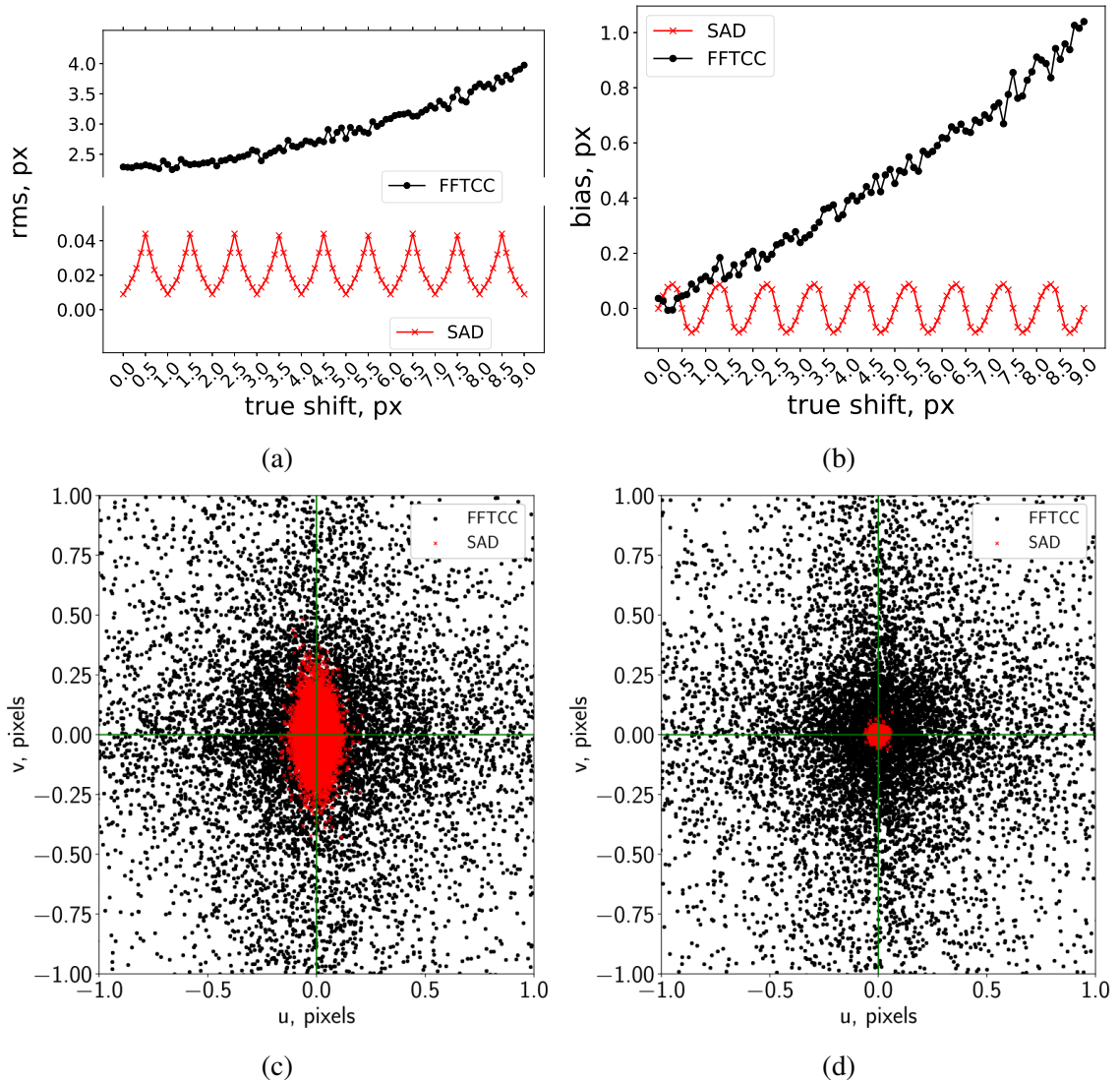
Fig. 2.12 Bias and random error for 18 pixel diameter tracers using 32/64 IW size. (a) Shows the random error for motion estimation with SAD (red crosses and lines) and FFTCC (black dots and lines). (b) Shows the bias of the measurements. (a) At very large tracer particle sizes (comparable to red blood cells discussed in chapter 4), the FFTCC suffers from significant random errors, which increase with particle motion. (b) The bias for FFTCC is increasing at a rapid rate, with a gradient of about 1 in 9 pixels, compared to the ≈ 1 in 60 gradient in the 9 pixel diameter case Figure 2.10b. The scatter plots illustrate the raw *uv* velocity component measurements for the selected image shifts of 0.5 and 1.0 pixel in (c) and (d) respectively. The substantial spread of *u* and *v* measurements estimated using FFTCC can be seen (c,d). The SAD algorithm clearly performs more reliably when the particle size increases.

18 pixel diameter beads The previous result hinted that increasing IW size might allow for a reduction of errors when using FFTCC to estimate motion of large particles. However, the results shown here indicate that while the errors can be reduced, they are still large for IW sizes used in real experiments in this thesis. When a smaller size IW pair is used, the random error for the FFTCC ranges from under 2.4 pixels to about 4.0 pixels at 9 pixel

shift, see Figure 2.12a. The error has more than doubled compared to the results shown in the 9 pixel diameter case (shown in Figure 2.10a).

It is not surprising that the FFTCC performance plummets as it has been shown to perform best only when the particle image size is small compared to the IW dimensions, namely $d_p \ll D_{IW}$ [78, Sec. 8.4.1]. Remarkably, SAD results preserve low values, and the periodically varying nature of bias and random errors despite very large particles.

The bias for FFTCC, shown in Figure 2.12b, shows an approximately linearly increasing trend, which has a larger gradient than the results shown in Figure 2.10b. The significantly poorer performance of FFTCC compared to SAD is best illustrated in the *uv*-scatter plots for 0.5 and 1.0 pixel shifts, shown in Figure 2.12c and Figure 2.12d.

Doubling the IW sizes, did not have as large an effect as it did for the 9 pixel diameter case. While the random error for FFTCC decreased Figure 2.13a, it was still two orders of magnitude higher than for SAD. The bias, on the other hand, did improve significantly, where on average the FFTCC results had smaller bias than SAD did, see Figure 2.12b. Much like in the 9 pixel diameter case, increasing the IW size, decreased the v spread in the 0.5 pixel shift case shown in Figure 2.12c, and did not have any noticeable effect on the uv-scatter at 1.0 pixel shift.
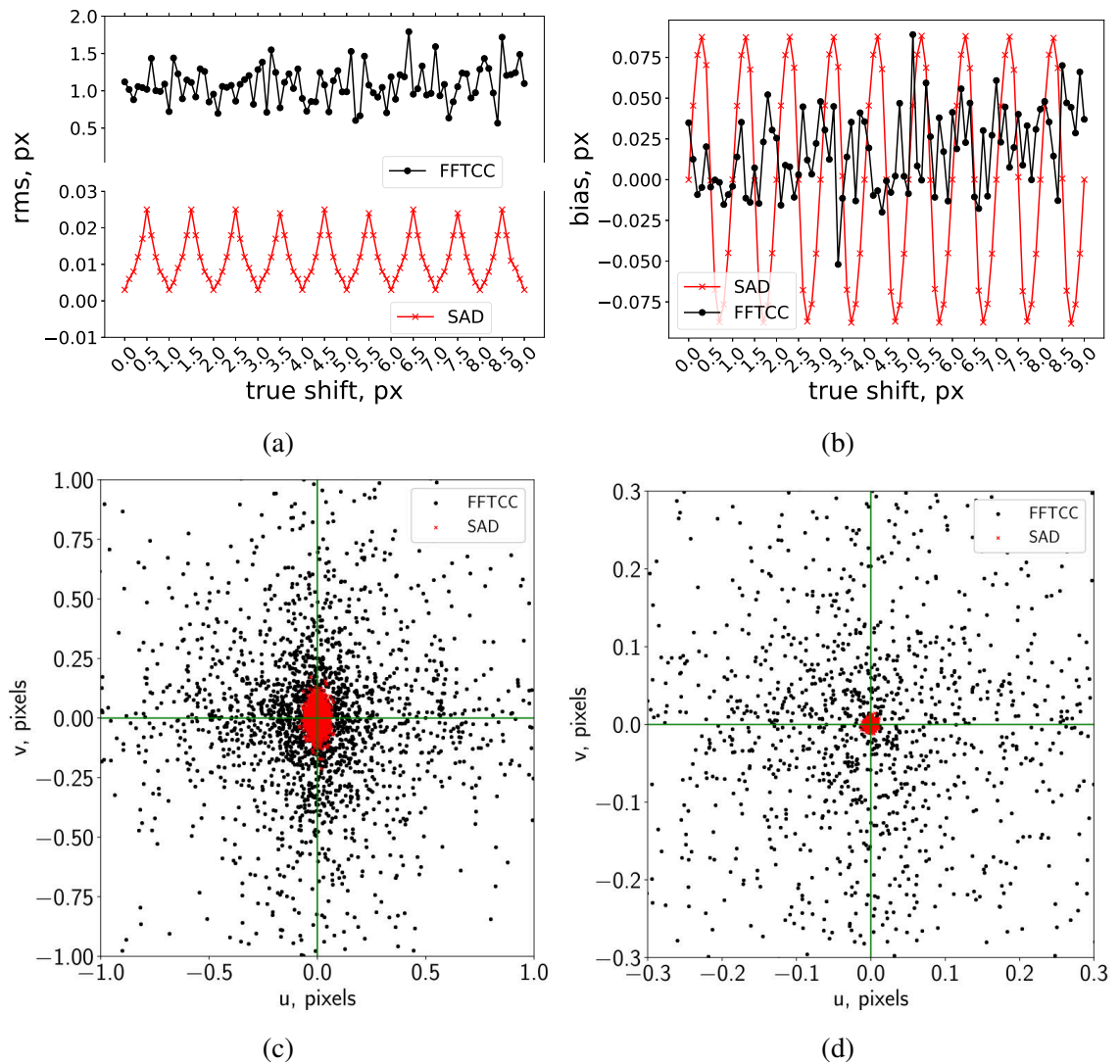
Fig. 2.13 Bias and random error for 18 pixel diameter tracers using 64/128 pixel IW size. (a) Shows the random error for motion estimation with SAD (red crosses and lines) and FFTCC (black dots and lines). (b) Shows the bias of the measurements. (a) Increasing the IW size only partially decreases the random error for results obtained with FFTCC. (b) The bias error for FFTCC does improve with larger IW size, and is at the same order of magnitude as for SAD measurements. The scatter plots illustrate the raw *uv* velocity component measurements for the selected image shifts of 0.5 and 1.0 pixel in (c) and (d) respectively. (c,d) The *uv* scatter plots retain similar features as shown in scatter plots for previous cases.

Summary: SAD vs FFTCC for large particles   The above analysis strongly suggests that SAD can provide PIV measurements with significantly less random error than the FFTCC when using large particles with relatively small IW size (see Figure 2.14 for the mean rms and bias values for each parameter combinatino examined). While increasing the size of the IWs did improve the FFTCC results (substantially in the 9 pixel diameter data), the improvement was not as significant for the 18 pixel particle image diameter case). The FFTCC results could be improved by further increasing the IW size, on the other hand, increasing IW size comes at the price of reduced spatial resolution (since it is partially defined by the IW size).

This analysis also revealed that the SAD random error and bias vary in a strictly periodic nature, which does not change with the particle size (the amplitude does however). In principle, this could allow estimating the errors on real measurements. Alternatively, a better fit could be explored for SAD CC peak. In fact, Taylor et al. [15] used a "V" fit, to perform subpixel fitting for SAD measurement of image similarity.

Clearly, the current analysis is limited to the simple case of flow with no out-of-plane motion, shearing, or optical aberrations, therefore a more thorough investigation is necessary to compare SAD and FFTCC fully.

(a)   (b)
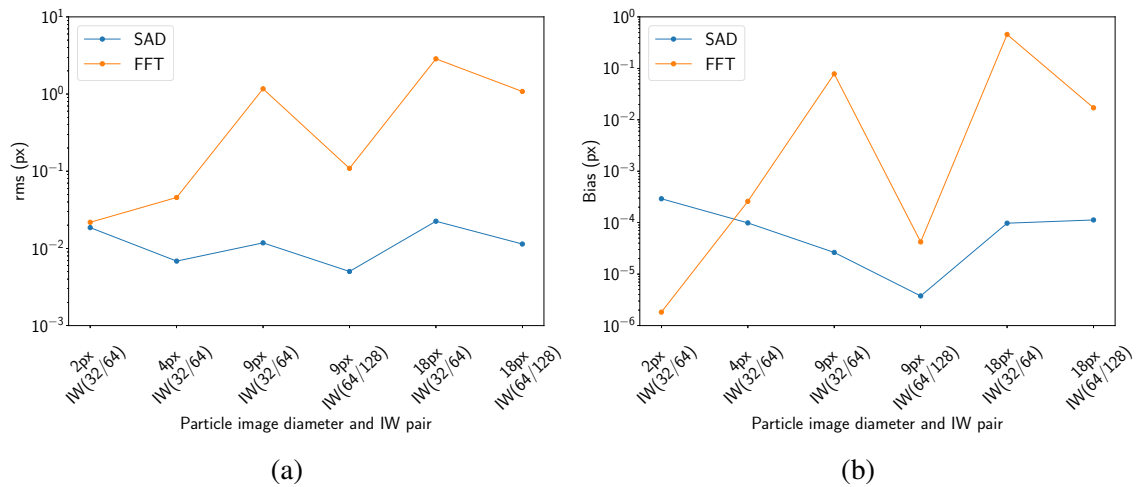
Fig. 2.14 Summary of bias and random error for different particle, interrogation window size, and correlation method. In general the mean values obtained using SAD outperform FFTCC. The decrease in both bias and rms at 9 pixel diameter particle image and 64/128 IW pair hints at the best combination for the parameters examined.

2.1.7   Conclusions

This section introduced some of the key aspects of PIV for flow measurements, both from the practical (illumination and tracer particle choice) and computational (discrete cross-correlation and subpixel fitting) point of view. Various flow dynamics, affecting the reliability of CC results (by inspecting the p2p ratio) were reviewed. In particular, it was pointed out that a low p2p does not necessarily mean an invalid measurement, which

explains why the "design rules" for PIV are only meant as a guide. Finally, using synthetic images, novel results on analysis of the performance of SAD for varying particle sizes were presented. The results provided evidence that SAD is a good alternative to FFTCC for measuring motion of large particles.

The principles discussed and illustrated here, will be useful in the next section, where application of PIV techniques at microscopic scales will be explained. In particular, additional considerations, not applicable for macro scale PIV will be made clear.

2.2 Microscopic PIV: general considerations

There are no fundamental limitations that prevent applying Particle Image Velocimetry (PIV) techniques to measure flow at microscopic scales. However, creating PIV systems which use very thin light sheets was not considered practical in the past [78]. Instead, conventional full-volume illumination microscopes were used, and Santiago et al. were the first to propose a micro Particle Image Velocimetry (μPIV) system using an epi-fluorescence microscope. The approach was adopted as standard in microfluidic visualization measurements, and reviews of the recent developments in μPIV can be found in [80, 81]. However, the use of volume illumination introduces additional sources of measurement error, which do not occur in macro-scale PIV measurements. Furthermore, since tracer particle sizes can be in the order of nanometres for quantum dots [127], random molecular collisions can affect the path of the tracer particles. Finally, the number of tracer particles used in μPIV are generally very low [80, 81], and require statistical methods to computationally increase the effective particle number. In this section, these μPIV specific challenges will be introduced.

Brownian motion Santiago et al. [128] showed that *Brownian motion* defines the minimum time difference between two frames, Δt, and tracer particle diameter, d_p. They concluded this by expressing the relative error due to *Brownian motion* in the following way:

$$\varepsilon_B = \frac{\langle s^2 \rangle^{0.5}}{\Delta x} = \frac{1}{u}\sqrt{\frac{2D}{\Delta t}} = \sqrt{\frac{2}{\Delta t}\frac{k_B T}{3\pi\mu d_p}} \tag{2.13}$$

where $\langle s^2 \rangle^{0.5}$ is the random error on the displacement, Δx is the particle displacement in a steady state flow, over time Δt with velocity u. D is the diffusion coefficient ($\approx 1.0 \times 10^{-12}$ m/s^2 for 1 μm diameter particle [80]), k_B is the Boltzmann's constant, T is temperature, μ is the dynamic viscosity of the fluid, and d_p is the particle diameter. Brownian motion becomes important in practice when particles smaller than 500 nm are used in flows slower than 1 mm/s [81]. In this work 0.39 μm particles were used to trace flow in the blood vessels of the zebrafish, where velocities can be drop below 1 mm/s magnitude, and increase the measurement uncertainty. However, the error due to Brownian motion can

be reduced by averaging over time (in a steady state or periodically varying flow). This temporal averaging in order to improve the quality of μPIV data is introduced next.

2.2.1 Correlation averaging

In order to deal with low seeding density, poor quality images, and effects of Brownian motion, Meinhart et al. [129] investigated time averaging techniques for μPIV measurements. For a steady state flow, they compared three averaging methods: velocity averaging, image averaging, and correlation averaging.

In velocity averaging, vectors from the same Interrogation Window (IW) are averaged over time. This method can be significantly affected by a few large erroneous velocity vectors. In image averaging, the spatial information of IWs is averaged before the cross correlation is obtained. While this approach does increase the measurement validity up to a certain point, eventually the particle images start overlapping. At this point no improvements to measurement accuracy occur, and eventually the accuracy drops off when the image density becomes too high and individual particles are no longer visible.

In correlation averaging, the Cross-Correlation (CC) result from the same IW is averaged before the final subpixel fitting is done. The effect of correlation averaging on the appearance of CC is the same as increasing tracer particle number, as shown in Figure 2.5. However, unlike the image averaging approach (or increasing the N_I), correlation averaging can in principle be performed indefinitely (since there is not image overlapping). Correlation averaging depends on the fact, that each image pair is sampling the *same* flow pattern (in a steady-state or a periodically varying flow at the same phase in the cycle). This means that the CC is likely to contain the true displacement peak, which might be much smaller than the random noise. However, if CC is time-averaged sufficiently long, the peak of the true signal will increase, while the random noise will be suppressed. This technique will become particularly important in chapter 4, where the periodic nature of the heartbeat will be exploited in order to achieve better quality μPIV measurements of blood flow. While correlation averaging is a robust technique and is recommended for μPIV measurements [80], the μPIV specific effect discussed next cannot be alleviated with this technique.

2.2.2 Depth of Correlation

In macroscopic PIV, the thickness of the light sheet is generally smaller than the DOF of the imaging objective [78, p. 366] and all illuminated particles appear in focus. Since μPIV measurements are typically performed with conventional epi-fluorescence microscopes, the whole fluid of interest is illuminated, and particles outside of DOF can contribute to flow estimation [88]. The depth over which defocused particles significantly contribute to μPIV analysis, is referred to as DOC, and was first mathematically formulated for low Numerical Aperture (NA) air objectives by Olsen & Adrian [88]. The formulation was later expanded
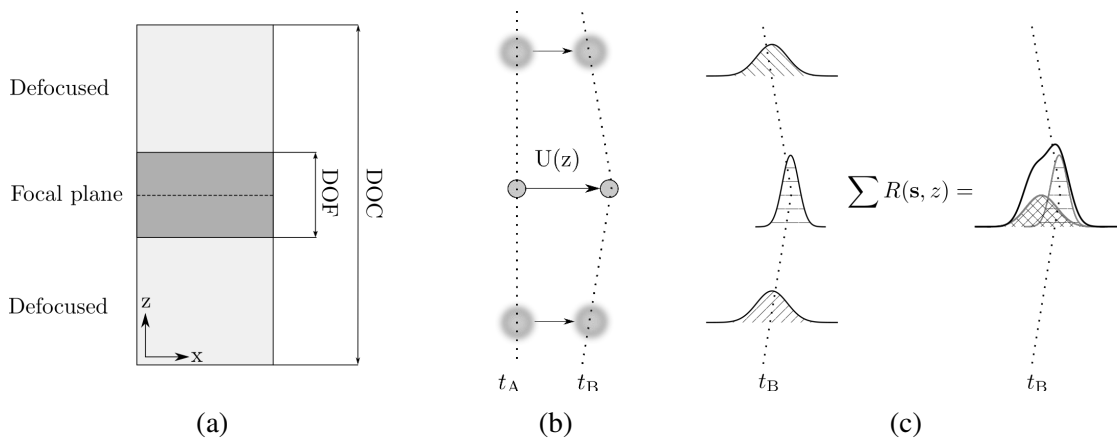
Fig. 2.15 Schematic of DOC effects in μPIV measurements. (a) Illustrates the difference in the extent of DOF (shown in dark grey) and DOC (light grey). Images contained close to the focal plane of the system appear focused in the DOF and contribute to flow measurements equally. However, due to volume illumination, defocused particles in DOC can still have a strong effect on estimating the true velocity. (b) Shows an example of a semi parabolic-flow, $U(z)$. There, the defocused particles (which are at different z-positions in the fluid) move at a different velocity to the particle in focus. If CC of each individual particle were plotted, they would be similar to the ones shown on the left of (c). That is, defocused particles have a broader shape with lower maximum value than the in focus particle. Since all of the particles contribute to the image, the net effect can be considered as a summation of all matrices, as shown on the right of (c). Depending on the flow profile in the DOC, this can have different effects on the measurements (discussed further in the main text, and in chapter 3). Figure based on [78, Fig.8.42] and [80, Fig.3].

for high NA immersion objectives by Bourdon et al. [130], and is presented here:

$$z_{corr} = 2\left(\frac{1-\sqrt{\epsilon}}{\sqrt{\epsilon}}\left[\frac{n_i^2 d_p^2}{4\text{NA}^2} + \frac{5.95(M+1)^2\lambda^2 n_i^4}{16M^2\text{NA}^4}\right]\right)^{0.5} \quad (2.14)$$

where z_{corr} is the correlation depth (i.e. DOC), ϵ is the relative threshold value defining where the out-of-focus particles cease contributing to the velocity measurement (typically $\epsilon = 0.01$ [130]), n_i is the refractive index of the immersion medium, d_p is the particle diameter, NA is the numerical aperture of the immersion objective, M is the objective magnification , and λ is the wavelength of the signal light. This predicts that z_{corr} imaging $d_p = 1\,\mu\text{m}$ tracer particles with M $= 20\times$, 0.8NA water immersion objective ($n_i = 1.33$), will be $\approx 7.2\,\mu\text{m}$.

However, the model shown in Equation 2.14 does not take spatial velocity gradients of the flow into account. Olsen [131] has later proved that the DOC depends on the fluid shear. It was shown there that the DOC varies in the direction of the shear, and higher NA objectives suffered from larger DOC compared to smaller NA objectives. Shortly after Olsen [132] investigated the effect of out-of-plane shear on DOC and proposed that out-of-plane shear reduces the DOC (this can be understood by considering a case of linearly increasing shear in z, where the contributions of correlation peaks from different z to the focal plane are well separated). There it was also concluded that such effects are negligible, unless the out-of-plane shear is significantly larger than in-plane shear. Mustin and Stoeber [133] have verified the previous findings of Olsen, and described dimensionless parameters to estimate the effects of velocity gradients on DOC.

While the analytical treatment of DOC is beneficial for conceptual understanding, such treatment is not always sufficient in practice where experimental errors might not be trivial to predict in advance. Hein et al. [3] proposed an experimental approach to measure DOC for a particular flow. They used a sample of fluorescent beads fixed on a slide to obtain images at desired z-positions in an epi-fluorescence microscope. The images from different depths were then summed in order to simulate out-of-focus particle contribution. By iteratively removing each image, they were able to judge the influence of particles at each plane, on the measurement accuracy. This allowed the researchers to quantify DOC for a number of different objectives (a variation of this approach was adopted in this thesis, and will be discussed in chapter 3).

2.2.3 Summary

This section described the challenges associated with applying PIV techniques on microscale flows. At microscopic scales, random molecule interactions become important, as the tracer particle size can be in the order of nanometers. The small scales of typical systems imaged in µPIV applications generally require low tracer particle density, which is generally not

sufficient to provide reliable CC results. However, both Brownian motion and low tracer particle number can be solved by implementing the correlation averaging technique, which allows averaging single frame pair results in steady-state or periodically varying flows.

Nevertheless, the biggest challenge in µPIV appears to be DOC, which is an artefact due to volume illumination used in standard microscopy. Several works have proposed analytical treatment of DOC and provided insight in the effect of different flow behaviour on DOC. However, such analyses often assume ideal flows, and neglect optical aberrations in the experimental set-up [3]. A more reliable way to estimate DOC is to use precisely controlled measurements, which can be used to synthesize flow for µPIV analysis, from which DOC can then be estimated. Still, such experimental measurement of DOC is only feasible for simple flows with well known geometries. A much better approach would be to eliminate DOC completely. The "simplest" solution would be to ensure that only the focal plane is illuminated, which can be achieved with Selective Plane Illumination Microscopy (SPIM), described in the next section.

2.3   Light sheet formation in SPIM

Current limitations in the field of micro Particle Image Velocimetry (µPIV) due to conventional microscopy techniques provide the motivation to explore Light Sheet Fluorescence Microscopy (LSFM) as a system to improve microfluidic flow measurement accuracy. Here, the Selective Plane Illumination Microscopy (SPIM) system which was briefly introduced in subsection 1.3.2 will be discussed in more detail. In particular, the schematic for the SPIM system used throughout this thesis will be introduced. The basic equations predicting the light sheet parameters will be summarized, and experimental "sheet-profiling" results will be compared against the predicted sheet thickness.

2.3.1   Experimental arrangement

In Figure 2.1, the basic units of light sheet formation consisted of a plano-concave cylindrical lens expanding the collimated laser beam, which was focused to a thin sheet by a spherical lens. For a rudimentary "SPIM" system, a single plano-convex cylindrical lens is sufficient to focus[5] a collimated beam into a thin sheet of light. In fact, in the first use of LSFM for optical sectioning experiments in biological organs carried out by Voie et al. [58] the illumination system consisted of a laser, a beam expander, a collimating lens, and a plano-convex cylindrical lens (see [58, Fig. 2]).

The optical components in a basic modern SPIM still incorporate the same basic parts that were used in the very first light-sheet system, but the biggest difference is the addition of a microscope objective. Greger et al. [12] claim that addition of a microscope objective is

---

[5]There is no beam expansion in a plano-convex lens.
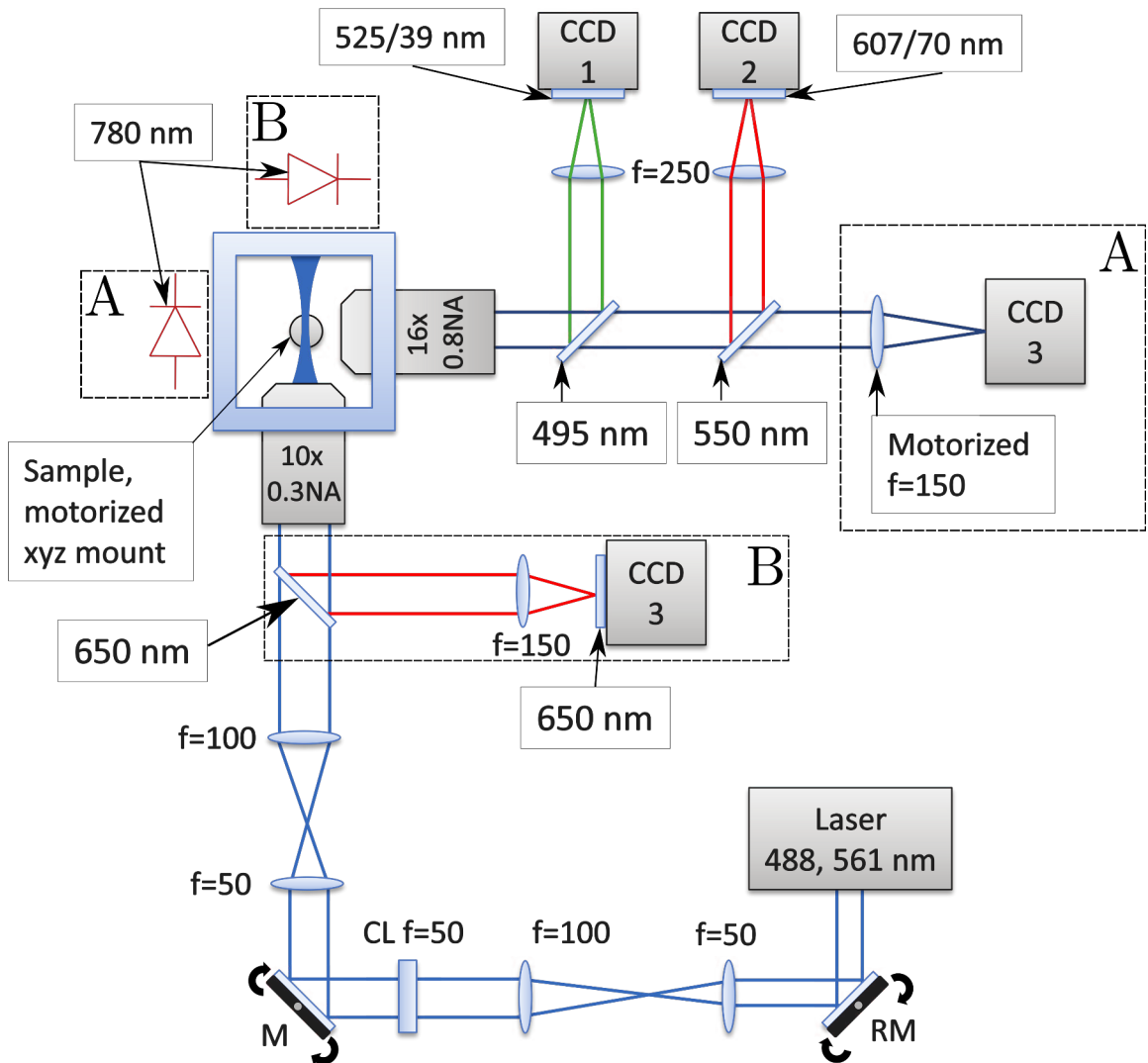
Fig. 2.16 Schematic of the SPIM system used throughout this thesis. The light generated for the sample illumination was provided by either a *Coherent Obis* 488 nm laser (up to 30 mW power) which was used for the tube flow experiments, or an *Omicron Versalase* multiwavelength laser system which could supply 488 and 561 nm beams (up to 50 mW power) which was used for zebrafish imaging experiments. The laser beam would then deflect from the galvonometric mirror (RM) which resonates at 4 kHz in order to reduce shadow artefacts [134] (discussed further in main text). The beam then passes a 4f relay/beam expander, before it is focused to a sheet by a $f = 50$ mm cylindrical lens (CL). The sheet is deflected from a gimbal mirror (M) which can be used to adjust the axial and lateral position of the sheet in the imaging chamber. The beam passes through another 4f relay, before reaching a *Nikon* 10× 0.3NA air objective, which focuses the light sheet to around 2.5 μm FWHM thickness (see subsection 2.3.2 for more details). The sample is then imaged with a *Nikon* 16× 0.8NA water dipping objective. Long-pass dichroic beam splitters (488 nm,550 nm) deflect the fluorescence signal onto the 12-bit CCD cameras (*QImaging QIClick*). Fluorescence emission filters are placed in front of these cameras in order to filter out stray light. The A and B configurations indicated by the dashed rectangles, are discussed in the main text. Figure based on [135].

necessary because using only a cylindrical lens can cause large aberrations in the light sheet. Hence the similarities between the optical configuration of Particle Image Velocimetry (PIV) and SPIM become even more apparent (i.e. the use of an additional lens after the cylindrical one). Moreover, in contrast to the system used in [58], modern SPIM microscopes also allow for lateral and axial light sheet adjustment (through the use of gimbal mirrors). This allows more control and freedom on alignment of the light sheet.

The schematic of the SPIM system used throughout this thesis is presented in Figure 2.16. Note that two variations of the same system were used, and components which belong to the separate variants are shown in dashed boxes and labelled A or B. The data is obtained by translating the sample (which is suspended vertically with respect to the optical bench) through the light sheet using a motorized stage. The sample mount allows sample rotation around the vertical axis. Other components are listed in the caption of Figure 2.16, but additional discussion on the Brightfield (BF) imaging with the two variants will be discussed below. Moreover, a separate discussion on the use of a resonating mirror in order to reduce image shadows will be provided.

Brightfield channels   As explained in subsection 1.3.3, BF images of the heart allow real-time optical gating. In this work, two separate optical configurations were implemented. In configuration A, the BF information for heart phase recovery, is obtained by illuminating the sample with a near infra-red Light Emitting Diode (LED) (780 nm) and is imaged with an 8-bit camera (*Allied Vision GS650*). Notice that in variant A, the BF collection stage is motorised, which allows refocusing the sample (in BF) during the z-scan. This configuration was proposed by Taylor et al. [16] in order to enable performing real-time optical gating throughout the whole z-scan. In subsection 1.3.3 it was explained that prospective optical gating relies on comparing continuously acquired BF images of the heart, against a reference heartbeat. If the images of the heart become significantly different (due to the sample moving from/to the imaging objective), the synchronisation fails, as the heart images no longer appear similar. Hence the need for motorised BF collection lens in order to refocus throughout the z-scan.

In configuration B, a short pass dichroic mirror (650 nm) allows imaging through the $10\times$ 0.3NA *launch* objective (the BF illumination is provided by a 780 nm LED). This eliminates the need for refocusing of the BF images. However, image translation (in x in the reference frame of the BF camera) must be corrected for. This is done in real time with the custom built software developed by Dr Jonathan M. Taylor. This configuration was originally suggested to Dr Jonathan M. Taylor by Dr Thai V. Truong during a conference. Notice that in variant B, a fluorescence emission filter (650 nm) is used at the camera to eliminate stray fluorescence/laser light. However, this is not strictly necessary as camera "cascading" routines can employed to prevent fluorescence/laser light contamination. This is explained in the context of zebrafish heart imaging in the next paragraph, which introduces a specific laser timing mode for PIV measurements.
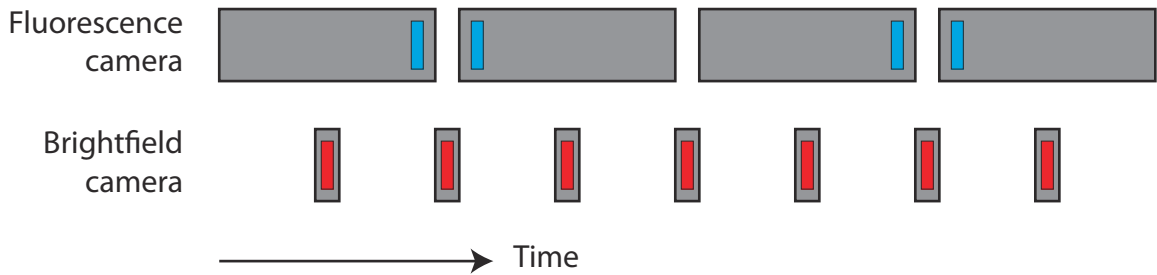
Fig. 2.17 Multi-channel timing diagram for blood flow imaging in the zebrafish heart. The brightfield channel is necessary for assigning the phase to the fluorescence images. The laser pulse is indicated by the blue stripes, and the BF illumination - by the red. Notice that the BF camera is set to expose at times when the laser is off, in order to prevent any laser light contributing to the BF channel. Figure as submitted to [135].

Illumination timing The highly dynamic nature of cardiac function requires high temporal resolution to properly measure blood flow properties. We found that even cameras capable of imaging at 800 Frames Per Second (FPS) are not sufficiently fast to capture blood cell motion at the peak velocities. However, exploiting the high response rate of the timing hardware necessary for heart synchronization, allows improving the temporal resolution beyond the limits of the camera. In fact, this can even be used with "slow" cameras (such as *QImaging QiClick*, which can only achieve about 30 FPS while allowing large enough field of view for imaging at least one chamber in the zebrafish heart). Consider a PIV frame pair, frame A and frame B. If the laser is pulsed at the end of the camera's exposure for frame A, and then again at the beginning of the camera's exposure for frame B, the temporal resolution can be significantly enhanced (see the "Fluorescence camera" part of Figure 2.17 for a schematic). In fact, this concept is often referred to as "PIV mode" and variations of it are discussed in [78, Sec. 5.2]. Furthermore, custom built timing hardware can be used to prevent cross-talk between different channels. Generally, only the BF channel is affected when stray laser illumination light gets registered by the BF camera. This poses issues for accurate phase recovery, as the heart rate synchronization algorithms cannot tolerate large amounts of image saturation (since features are hidden under the same signal saturation level). This is solved by using camera *cascading*. Essentially, the BF camera starts exposing immediately after, the Fluorescence (FLR) exposure ends. By selecting an appropriate FPS for both cameras, it is possible to ensure that a sufficient large gap between any two fluorescence camera exposures, in which a BF exposure "fits" without capturing any laser light (see Figure 2.17).

Shadow reduction If the light sheet encounters highly absorbing cells (for example skin cells with pigmentation on the zebrafish embryo), streaks (or stripes) of shadows contribute to the images (see Figure 2.18a for an illustration). These highly absorbing cells prevent the light sheet from exciting fluorescent molecules, decreasing the information content in an image. An approach compatible with the SPIM system is rapid translation of the light sheet
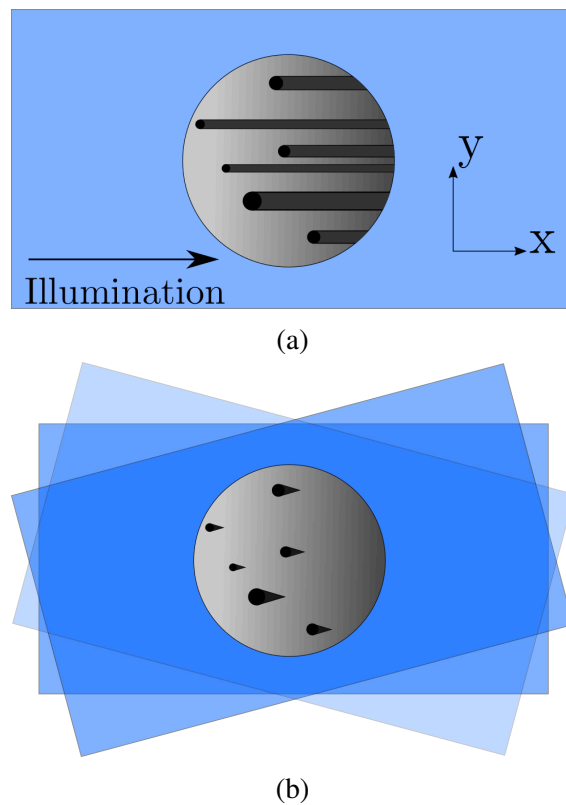
Fig. 2.18 Shadow artefacts and their reduction in SPIM system. (a) Pigment or opaque cells can absorb/block the light sheet penetrating through the whole sample. This results in shadows or stripes. Fluorescent molecules are not illuminated in those regions and information is lost. (b) If the light sheet is pivoted (e.g. with a resonating mirror, see RM in Figure 2.16), the light can reach fluorescent molecules which would not be reached with as static sheet. Figure based on [134, Fig. 1].

up and down before it enters the launch objective [134]. This requires a fast galvanometric mirror (RM in Figure 2.16), which sweeps the light sheet back and forth in the vertical direction (with respect to the optical bench). This means that the light sheet will illuminate the sample from different angle in the *xy*-plane. The effect of minimising the stripe pattern is illustrated in Figure 2.18b. Note that it is important to match the full sweep of the mirror with the camera exposure, otherwise the cumulative image will not be symmetric in *y*.

Alternative beam shapes   It is worth mentioning alternative beams used in light sheet microscopy, such as Bessel [136] or Airy [137] (see [64] for an overview of such methods). The main advantage of these beams is the improvement of penetration depth into scattering tissue (due to their "self-reconstruction" or "self-healing" ability), and unifrom illumination accross an extended Field of View (FOV) compared to Gaussian beams. However, loss of contrast is generally an issue as the penetration depth increases. Furthermore, deconvolution is necessary to recover artefact-free depth information. For the experiments carried out in this thesis, the penetration depth was generally not a considerable obstacle, therefore such systems were considered not necessary. Moreover, it is important to consider that both Bessel and Airy systems referenced are based on scanned beam, therefore the flow fields would not be captured instantaneously across the FOV and depending on the flow features, might not be adequate.

2.3.2   Gaussian beam parameters

The properties of the light sheet formed in basic SPIM systems can be well approximated using *Gaussian beam* formulation. In terms of this work, the most important parameters are the Gaussian *beam waist*, which defines the maximum obtainable *z*-resolution, and the *Rayleigh length*, which in practice describes the FOV of the system. To understand these parameters, consider a cylindrical Gaussian laser beam, with a radius *r*. The light intensity decrease is described by a Gaussian curve (reducing towards the edges of the beam). The light intensity, *I*, of a Gaussian beam can be expressed as:

$$I(r,z) = I_0 e^{-2r^2/w(z)} \tag{2.15}$$

where *z* is the position in the beam along the direction of its propagation, I_0 is the peak intensity amplitude, and $w(z)$ is the *beam width* [138, p. 594]. The location where the intensity drops off to $\approx 14\%$ of I_0 (i.e. $r = w(z)$) is referred to as the *beam half-width* [138, p. 595]. See Figure 2.19a for illustration of the intensity distribution. Note that when a light sheet is formed, the radial symmetry is not applicable any more, that is the beam is no longer a cylinder (recall that the beam is focused in one dimension with a plano-convex cylindrical lens). Despite this, the conventional notation (i.e. *r*) will be conserved, but it is
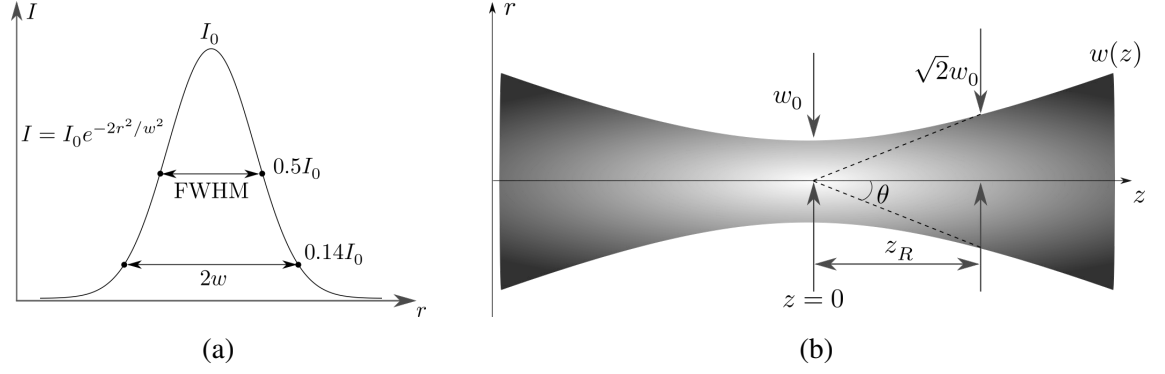
Fig. 2.19 Illustration of the main Gaussian beam parameters. (a) The Gaussian intensity profile ($I(r,z) = I_0 e^{-2r^2/w(z)}$) implies that highest fraction of total intensity lies in the $2w$ region of the beam, which is defined as the location of $\approx 14\%$ of the beams maximum intensity. r is the radial direction, increasing from the centre of a cylindrical Gaussian beam. (b) For a light-sheet (i.e. no longer a cylindrical beam), the beam waist, w_0 defines the thinnest part of the beam. The Rayleigh length z_R describes the distance at which the beam width increases to $\sqrt{2}w_0$. Twice the Rayleigh length is normally used as the FOV in a SPIM system. The Gaussian beam divergence angle θ, is related to the NA of the objective lens focusing the light sheet (discussed further in the main text), and describes how fast the sheet diverges. Note that in (b) r is in the direction of the sample depth, and z is in the direction of the horizontal FOV. Figures based on [138, p. 595].

worth noting that from the point of view of the imaging optics/camera, parameter r is along the depth and z is along the horizontal FOV. Next, the sheet thickness is discussed.

The beam width is an important parameter which defines the thickness of the light sheet, and is used to describe the axial resolution of SPIM system [64]. Following Hecht [138, p. 595], the beam width can be expressed as:

$$w(z) = w_0 \left[1 + \left(\frac{z}{z_R} \right)^2 \right]^{1/2} \qquad (2.16)$$

where w_0 is the beam waist at $z = 0$, which defines the minimum width of the Gaussian light sheet, and $z_R = \frac{\pi w_0^2}{\lambda}$ is the *Rayleigh length*, which is defined as the *distance over which the cross-sectional area of the Gaussian beam doubles* [138, p. 595]. In other words, a distance such that $w(z_R) = \sqrt{2}w_0$. Rayleigh length typically defines the FOV in a SPIM system [134], where a compromise between z_R and w_0 must be made, as thinner sheets diverge faster (i.e. $z_R \downarrow$ as $w_0 \uparrow$). This can be understood by considering the half-angular width of the beam (or beam divergence), θ, which can be approximated as $w(z)/z$ when $z \gg z_R$ [138, p. 595]. The $z \gg z_R$ condition simplifies Equation 2.16 to:

$$w(z) \approx \frac{\lambda z}{\pi w_0} \qquad (2.17)$$

and hence,

$$\theta \approx \frac{\lambda}{\pi w_0} \approx 0.32 \frac{\lambda}{w_0} \tag{2.18}$$

In fact, this beam divergence can be linked back to the NA of the objective focusing the light sheet [64, Eq. 6]. The numerical aperture for an objective focusing a Gaussian beam can be written as:

$$NA = n \sin \theta \tag{2.19}$$

where n is the refractive index of the medium. Combining Equation 2.18 with Equation 2.19 gives:

$$w_0 \approx 0.32 \frac{n\lambda}{NA} \tag{2.20}$$

In theory, the thinnest achievable light sheet in the SPIM system used in this work Figure 2.16 is $2w_0 \approx 1.39\,\mu m$[6], for $n = 1.33$ and $\lambda = 488\,nm$. In practice, the whole diameter of the rear aperture of the objective is not used (around half of it was used in our SPIM system), and this decreases the illumination NA, as NA is also related to the physical properties of the objective in the following way:

$$NA = \frac{d_{obj}}{2f} \tag{2.21}$$

where d_{obj} is the diameter of the objective lens, and f is its focal length. In the system used here, about a third of the aperture of the 0.3NA objective is illuminated, and the expected beam waist is therefore $2w_0 \approx 4.15\,\mu m$. Note that in practice, it is often more common to express the sheet thickness as FWHM, which is $\approx 2.4\,\mu m$ for the above case. The relation between beam waist and FWHM is $w_0 = 0.849 \times FWHM$, given in [139]. The next part of this section experimental results estimating the light sheet thickness will be compared against the theoretical values.

2.3.3   Predicted vs measured beam profile

In order to measure the light sheet thickness and hence compare against the predicted values, a sparse sample of $1.04\,\mu m$ diameter fluorescent beads was imaged. The details of the sample preparation are provided in chapter 3. In summary, a single bead was slowly scanned through the light sheet and the images were captured by a CCD camera at a known frame rate. This was repeated at several locations along the direction of propagation of the light sheet. A small region around the image of the bead was then selected. The z-stack was then analysed using *FIJI*'s [140] "Plot Z-axis Profile" function, which plots the average image intensity value against the frame number. Since the FPS of the camera, and the motion of the stage is known, the FWHM of such profile can be easily estimated. This is done by measuring the distance between the points which have half the maximum mean intensity

---

[6]Note, often in the field of LSFM the $2w_0$ value is referred to as *the* beam waist, although strictly speaking it is half that value, i.e. w_0.
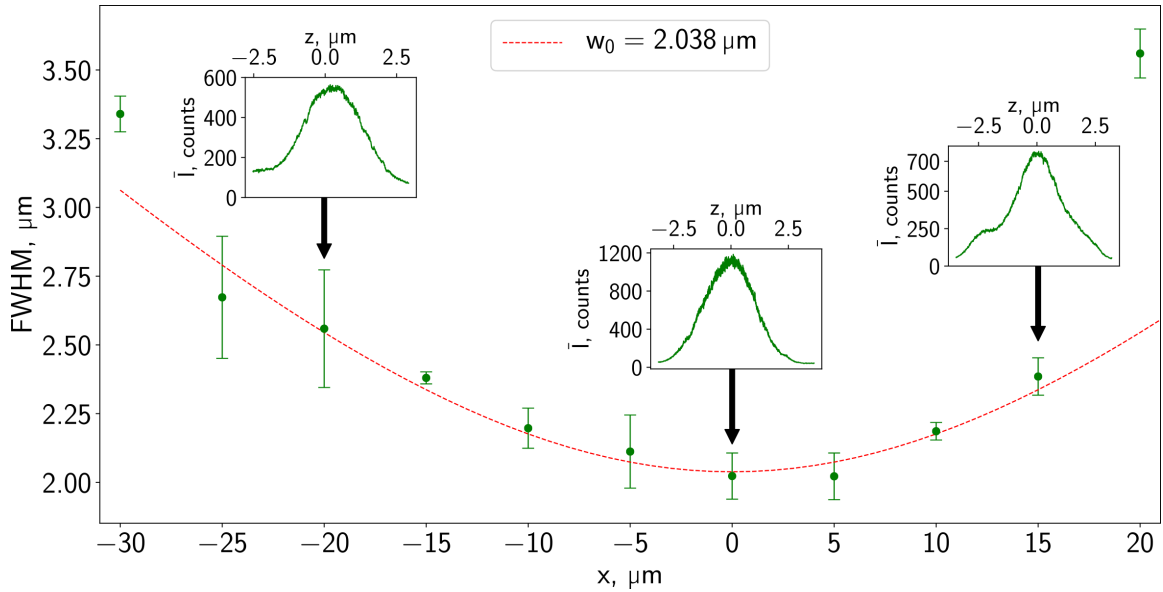
Fig. 2.20 Measurements of light sheet thickness of the SPIM system. Each data point (green dots) represents a 3 measurement average of the FWHM at a particular point in the light sheet, along the FOV of the camera (i.e. along the z direction in [138]). The error bars represent the standard deviation of the 3 measurements for each point. The three inset plots show the z-axis profile of mean image intensity of the z-stack of $1.04\,\mu m$ (obtained with *FIJI*, and explained in more detail in the main text). The theoretical sheet width is plotted for a beam with $w_0 = 2.038\,\mu m$ and fits majority of the data well. The potential cause for the two outliers is discussed in the main text.

value (the three inset plots in Figure 2.20 demonstrate the mean intensity profiles in z). Each measurement was repeated 3 times. The measurements with their standard deviations are shown in the main part of Figure 2.20, where the theoretical beam with FWHM $= 2.4\,\mu m$ is also plotted. Note that the fit appears asymmetric (range from -30 to $20\,\mu m$) as the predicted centre was found to be $5\,\mu m$ off from the actual location (for measurements in a $50\,\mu m$ lateral range). Apart from the two (suspected) outliers at each end of the lateral range, the data points seem to agree with the predicted values well. The cause for the two outlier points is unclear, however, it appears that the line profiles are broadened by an additional peak in the z-axis profile (the onset of this effect is seen at the inset plot at $x = 15\,\mu m$). This suggests that the intensity distribution in the light sheet is "splitting", but further analysis would be required to understand this effect.

2.3.4 Summary

In this section, the experimental arrangement of a basic SPIM system was reviewed. It was shown that the main light sheet formation components used in SPIM had counterparts in macro scale PIV systems. The two possible implementations of heart imaging-specific BF channels were summarised and it was implicitly shown that the custom-built system used here can be easily modified to fit specific needs. The reduction of shadows with the use of a rapidly pivoting mirror was explained this minimizes data loss due to absorption of light by

the cells in the sample. The fundamental theory of Gaussian light sheet parameters was also introduced and a link between the NA of the objective, and minimum light sheet thickness expressed as beam waist, w_0, was established. Finally, the predicted sheet size was verified with a simple sheet profiling experiment, where a good agreement was found between the measured and predicted values.

The technical background necessary for this thesis will be complete after a brief expansion on the optical gating technique used throughout this work, in the next section.

2.4   Optical gating for PIV measurements

The correlation averaging technique introduced earlier, assumes that the flow is either steady or periodically varying. In the latter case, it is also assumed that the phase information associated with such a flow can be accurately acquired. In principle, this can be known precisely if a flow experiment with a fixed frequency piston is used to create a periodic motion of the flow. Then, Particle Image Velocimetry (PIV) analysis would sum Cross-Correlation (CC) results at each period for every Interrogation Window (IW) in order to carry out correlation averaging. However, if the exact periodicity is not known, and can in fact vary, obtaining phase information might not be trivial. This problem becomes even more challenging, if the fluid of interest is in a living system such as the zebrafish heart. In subsection 1.3.3, the optical gating techniques which allow computationally freezing the heart, have already been introduced. Here, the use of those techniques for micro Particle Image Velocimetry (μPIV) analysis with correlation averaging is discussed.

Since correlation averaging requires a number of image pairs to improve the accuracy of μPIV measurements, it is reasonable to assume that retrospective gating is the preferred method (as images are acquired throughout the whole heartbeat, rather than at a specific phase). However, as was already explained, the computational analysis for retrospective gating approach is rather time consuming, and the phase information is limited by the frame rate of the fluorescence camera. More importantly for this thesis, imaging only the motion of blood cells (i.e. no heart wall information) does not provide easy access to phase information. This is because the blood cells are randomly and relatively sparsely distributed in the heart chamber at each phase of the heartbeat. This means that contrary to the heart wall data case, there is no continuous structure between nearby z planes for the same phase that can be used for phase-alignment of blood flow in 3D.

An alternative approach, is to use the real time synchronisation algorithms developed for prospective gating, but for *phase-stamping* offline. Recall that prospective gating (introduced in chapter 1) is normally used to predict when the heart will be at a specific (single) phase in the cardiac cycle, at which point the laser is triggered. This prediction is performed by first capturing a reference heartbeat in the Brightfield (BF) channel, which is used to establish the phase of any other BF image of the heartbeat. However, the phase-stamping algorithm

can be done in a post-acquisition way. That is, rather than providing laser trigger input during acquisition at a particular phase, the phase is assigned for *each* BF frame (and hence to corresponding Fluorescence (FLR) frame) during post-acquisition analysis. The phase annotation of the BF images typically only takes a few minutes for datasets with images in the order of 10^5. Assigning phase to the fluorescence data usually takes several minutes, this is simply due to a lack of efficiency in the code written in Python [141]. This method of using algorithms developed for real-time imaging in an offline manner, was key to the μPIV analysis performed in this thesis.

The main advantage of this technique is the fact that throughout the *z*-scan of the heart, the BF images remain essentially the same (i.e. the heart remains in focus either through the use of motorised lens, or by imaging through the launch objective as shown in Figure 2.16). This means that there is no need to align different fluorescent slices like in retrospective gating, which adds complexity to the method. Moreover, it was already highlighted that images of blood cell flow only (i.e. without simultaneously imaging fluorescent heart walls, as was the case in this thesis) cannot provide sufficient periodically repeating information to align different *z*-slices of the heart. Therefore, the "off-line" prospective optical gating described by [15], was used for blood flow measurements in the heart, described in chapter 4.

2.5 Conclusions

In this chapter, the main aspects of the Particle Image Velocimetry (PIV) method relevant to this work have been introduced. The typical experimental set up was presented, and the statistical approach forming the core of PIV was introduced through an intuitive example. Then, the standard analysis used for PIV flow measurements was explained, followed by a specific focus on cross correlation peak detection. It was shown how peak detection is affected by different flow conditions. This led to the key emphasis that the statistical nature of PIV means that the true motion of the fluid flow can be recovered, even when conditions are far away from the ideal ones, which are proposed as PIV design rules in the literature.

Next, the key result of this chapter, the bias and random errors of PIV measurements were quantified by using synthetic image data. Sum of Absolute Differences (SAD) and Fast Fourier Transform Cross Correlation (FFTCC) algorithms were compared for estimating motion for different sized particle images. It was found that SAD behaves in a very predictable manner and is, in fact, significantly less affected by bias and random errors when flow with large particles are imaged. This analysis serves as the justification for the use of SAD for micro Particle Image Velocimetry (μPIV) measurements described in chapter 4.

Furthermore, the specific difficulties of applying PIV techniques to microscopic flows, were discussed. It was shown, that the small particle size used in μPIV can be affected by Brownian motion. Moreover, it was discussed that microscopic fluid systems constrain the usable number of particles, which leads to lower probability of valid peak detection. In

order to overcome this, correlation averaging was introduced as a method to artificially increase the particle image density. Next, the concept of Depth of Correlation (DOC) was introduced, which is the main technical challenge in conventional μPIV systems. This gave a clear incentive to investigate Selective Plane Illumination Microscopy (SPIM) as a μPIV system, which in theory should virtually eliminate DOC effects.

The chapter then discussed the experimental and theoretical aspects of the SPIM system. A connection between the experimental set ups in SPIM and PIV systems was drawn, implicitly further motivating the investigation of SPIM-μPIV combination. This section finished by experimentally verifying the theoretical predictions for the light sheet thickness.

Finally, the theoretical background was concluded with an expanded discussion of optical gating techniques introduced in chapter 1, and discussion on their role in correlation averaging of μPIV data used in chapter 4. It was explained that real-time optical gating techniques developed by the supervisor of this project, can be successfully applied in post-acquisition analysis. It was explained, that this technique provides advantages in speed of analysis, and most importantly, the more elegant solution for computationally freezing the heart.

To sum up, the theoretical aspects discussed here indicate, that SPIM-μPIV should in principle be a superior technique for microscale flow measurements compared to conventional volume illumination microscopy methods (such as Brightfield (BF) or epi-fluorescence). This is because of the predicted suppression of DOC effects on flow measurements. In fact, the advantages of optical sectioning in SPIM will be the main theme in the next chapter. Finally combining: a) the low photo-damage of SPIM discussed in chapter 1 with b) optical gating techniques (which allow correlation averaging), and c) the use of SAD to cope with large size of the fluorescent red blood cells, has a large potential to recover high quality flow measurements even in challenging *in vivo* conditions in the zebrafish heart.

The next chapter will continue with the narrative of validation of the techniques. As opposed to Chapter 2 where sythetic data was used, Chapter 3 will make use of real experimental data in highly controlled environments. Particular focus will be given to investigating Depth-of-Correlation in SPIM-μPIV measurements, as well as effects of out-of-plane motion on measurement accuracy. These considerations will establish the validity of the technique, which will be then used in the living zebrafish heart in Chapter 4.

Chapter 3

SPIM-µPIV validation

Generally, parameters relevant for PIV experiments in aerospace engineering are validated using Monte Carlo simulations, however, the field also benefits from a vast number of "practical" experiments carried out in the past. Since SPIM-µPIV has not been explored in the past experimentally, an investigation of the feasibility of the proposed technique was imperative. To accomplish this investigation, the following experiments were carried out:

1. Comparison of flow measurements in a 50 µm diameter pipe with SPIM-µPIV and Brightfield (BF)-µPIV. The purpose of this experiment was to investigate if significant improvement in estimating the true 3D flow profile came be achieved when using SPIM as the imaging modality.

2. Quantitative description of Depth of Correlation (DOC) for µPIV measurements with the aforementioned imaging modalities, in a flow with a depth-varying velocity gradient. The aim here was to test the hypothesis that the DOC in SPIM is confined to the thickness of the light sheet.

3. Estimation of measurement error due to varying amounts of Out-of-Plane Motion (OOPM) for different correlation algorithms and particle sizes. The goal of this was to investigate the robustness of SPIM-µPIV system against a velocity component in the z-direction. This becomes particularly relevant when discussing blood flow measurements in chapter 4, where the complex motion of the heart might produce considerable Out-of-Plane Motion (OOPM) of the blood cells.

These three validation experiments form the bulk of the following chapter. The shared purpose of these investigations is to measure the reliability of SPIM-µPIV in relatively controlled experiments. These tests emulate certain features that are expected in measuring blood flow *in vivo* in the zebrafish heart as described in chapter 4.
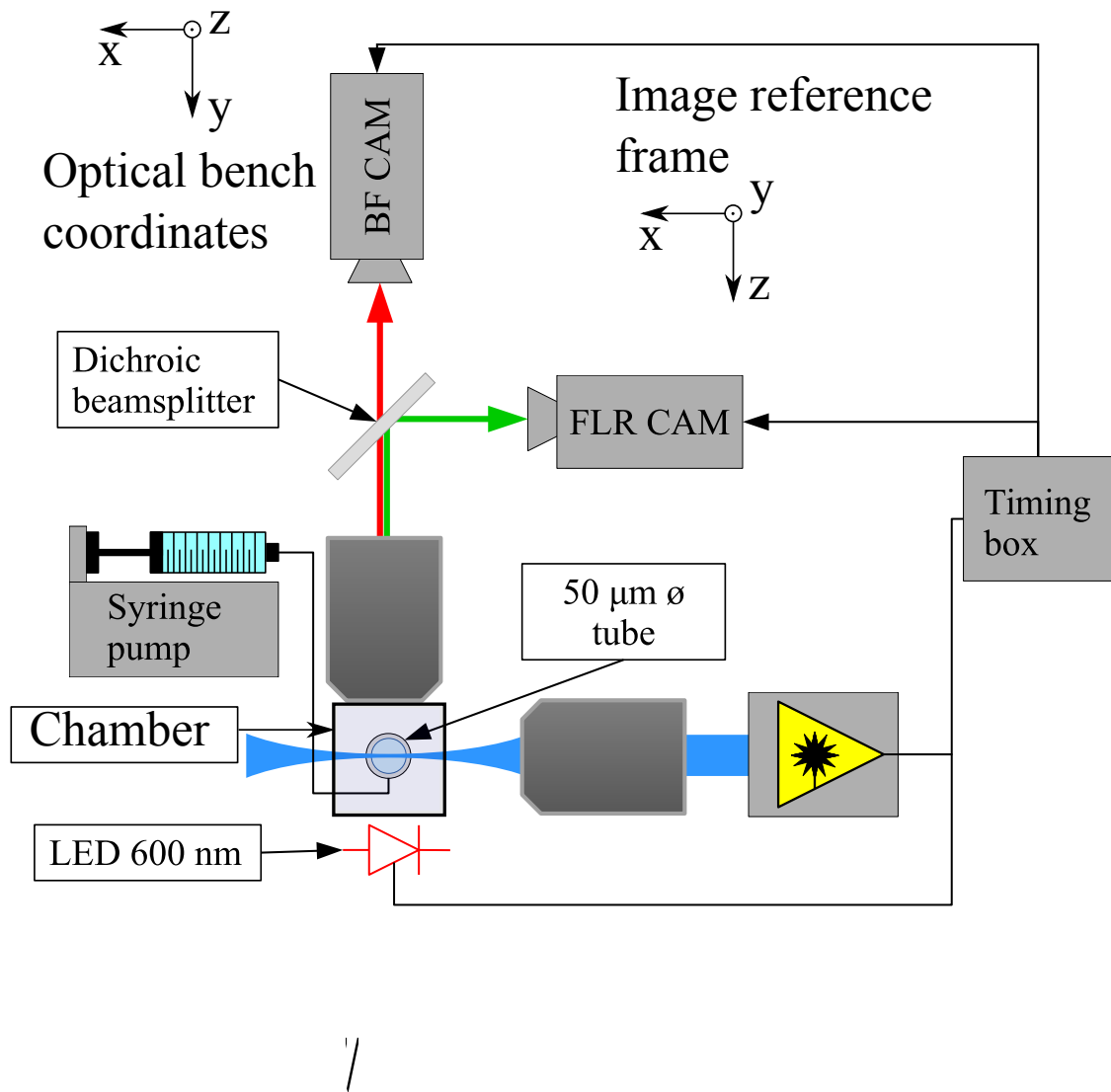
Fig. 3.1 Simplified sketch of the validation experiment set up with majority of optical components omitted (the complete components are shown in Figure 2.16). An LED is used as the light source for the brightfield (BF) channel. The timing box synchronizes the illumination of the LED and the laser diode according to the exposure of the cameras. A syringe pump is used to provide a constant flow of fluid at a set flow rate. Using fluorescence and brightfield imaging channels simultaneously, a direct comparison between SPIM and BF PIV can be achieved.

3.1 Materials and methods

To investigate applicability of Selective Plane Illumination Microscopy (SPIM)-micro Particle Image Velocimetry (µPIV) system for measuring real flows, a rudimentary microfluidics system was integrated into the SPIM microscope, see figure Figure 3.1. The aim of this experiment was to measure flow of 1.04 µm diameter fluorescent beads in a 50 µm diameter Fluorinated Ethylene Propylene (FEP) tube with SPIM and Brightfield (BF) simultaneously, and to compare the velocimetry analysis results. The following experimental procedure was carried out:

1. The tolerances provided by the manufacturer implied a significant variation in the diameter of the FEP tube (50 ± 25 µm), therefore the tube section to be used was visually inspected using a conventional transmission microscope, and any sections with defects were discarded.

2. The small diameter FEP tube used in this experiment meant that any debris (e.g. particles remaining from the manufacturing process) can affect the flow (if inside the tube) or imaging quality (if outside the tube). Therefore, it is good practice to wash the tube from particles and oils. This is achieved by immersing the tube in a centrifuge tube and sonicating it in a ultrasonic bath for 10 minutes. The tube is then rinsed and purged with Purified Water (purH$_2$O). The sonicating process is repeated with ethanol, and then purH$_2$O, where it is stored before use. Any handling of FEP tubes is carried out using gloves to prevent contamination with oils. An essentially identical approach is used to clean 100 µl *gas-tight* syringes used in this experiment together with a syringe pump to drive the fluid flow.

3. The fluorescent beads in this experiment were obtained as a liquid suspension. This suspension includes preservatives and detergents such as Sodium Azide and Tween 20. In order to avoid any influence of these components on the fluid vessels or the flow characteristics (particularly important when using *in vivo*), the beads were first washed. The washing is carried out by diluting the required volume of bead solution in 1 ml of purH$_2$O, and centrifuged for 4 minutes at 9800 Relative Centrifugal Force (RCF). The washing is considered successful if the beads clump into a ball, which is then removed with minimal withdrawal of the purH$_2$O. This is performed twice. After the beads are washed, they are diluted to a desired concentration with purH$_2$O.

4. During storage and handling of beads (such as centrifugation), some beads tend to form aggregates (clumps of small groups of beads). These aggregates can potentially clog microfluidic systems (as large clumps of beads tend to easily merge with other large groups), and yield a very large fluorescence intensity signal, saturating the exposed pixels. Furthermore, bead aggregates violate the uniform seeding density assumption that Particle Image Velocimetry (PIV) makes, as discussed in chapter 1.

To alleviate aggregation, the beads we sonicated for 10 minutes in an ultrasonicator bath and were then used in measurements immediately.

5. Once the FEP tube, syringe and the beads are washed the FEP tube is then "threaded" through a custom built tube holder Figure 3.2, which was made to fit into the imaging chamber and hold the tube vertical. Next, the tube is connected to the syringe using standard microfluidics ferrule connectors (see Figure 3.3). Using the BF imaging channel, the tube is adjusted to be taut and vertical by tweaking the moveable holder parts, shown in Figure 3.2b. While this vertical alignment is not crucial, it ensures that the angle the light enters is as perpendicular to the surface of the FEP tube as possible. While the refractive index of FEP is close to water it is not exact, therefore any refractive mismatch effects will be amplified by angled interfaces. Furthermore, vertical alignment minimizes aggregation of beads on the walls as gravity is parallel to the surface of the tube walls.

6. The FEP tube is then flushed with the solution of beads at the desired concentration. This has a twofold effect. Firstly, it allows the bead concentration to reach the desired number by pushing out the purH$_2$O water and any air bubbles remaining in the tubes after the last washing step. Secondly, any leaks in the system are likely to become apparent at this point, as the flow rate used is at least double than the value used during data acquisition. Leaks can be caused by high pressures (due to clogging or very high flow rate), but are often due to improper set-up of fittings (see left of Figure 3.3).

7. Once the system is purged and any leaks are fixed, flow rate calibration is performed. This is executed by measuring the volume ejected from the 100 µl syringe, and comparing it to the volume set in the syringe pump.

8. Next, during the volume calibration step, the imaging parameters for PIV (laser/Light Emitting Diode (LED) and camera exposure and laser inter pulse time) are adjusted. The main emphasis is on achieving maximum signal strength without motion blur, and avoiding too much motion between frame pairs (recall discussion on correlation loss in chapter 2). This is accomplished by imaging the plane in the centre of the tube in order to observe the peak motion.

9. Finally, a step-wise z-stack of the data is obtained. This means that the flow in the tube is imaged in a series of discrete z-planes for an extended period of time, rather than performing a continuous scan in depth. This was carried out in order to capture enough data to utilize correlation averaging techniques, introduced in chapter 2.
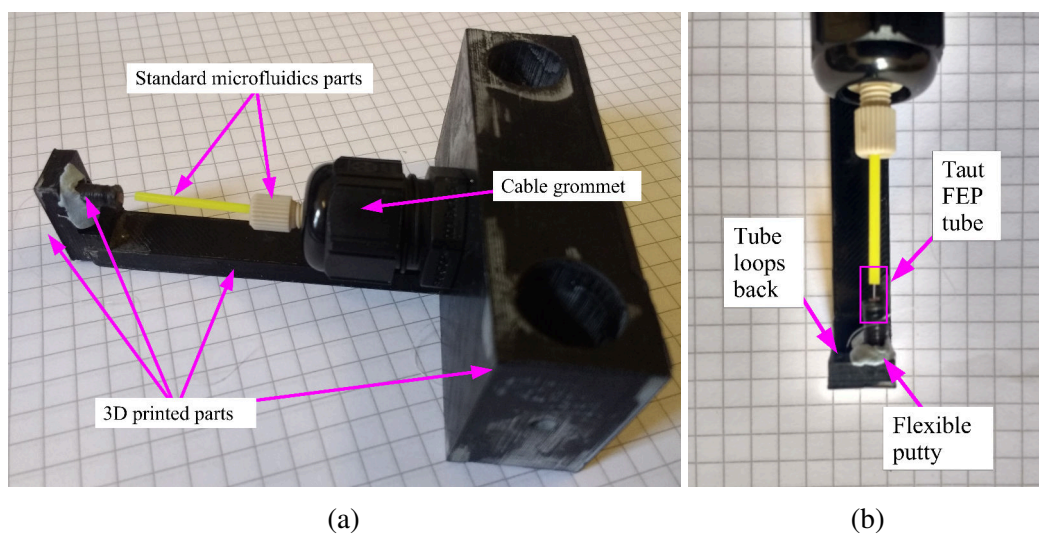
Fig. 3.2 Custom built 50 μm tube holder. (a) The custom build holder utilizes standard microfluidics parts such as the tube sleeve (shown in yellow) and a flangless holder (shown in grey), 3D printed parts, and an inexpensive cable grommet. (b) The FEP tube is held taut under slight tension to keep it straight. Flexible putty (*Blu Tack*) allows minor adjustments to ensure the tube is not significantly curved. The tube loops back out of the system to prevent contamination of imaging chamber with the imaged fluid. Note that image is slightly blurred to help reveal the location of the scale. Background grid is spaced 5 mm apart.
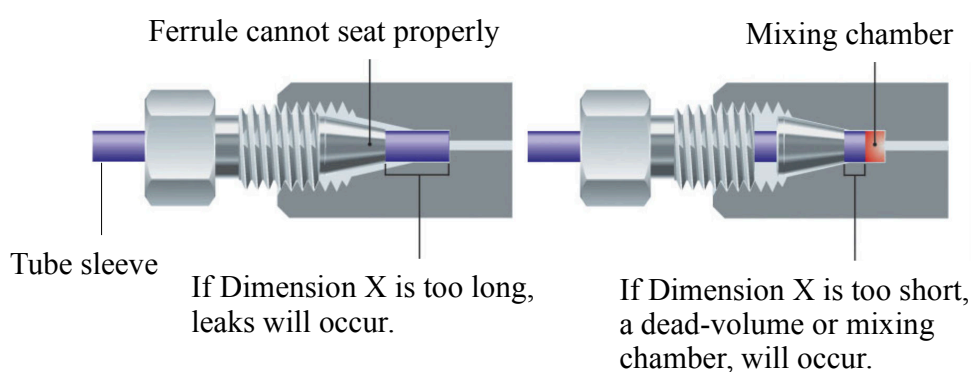
Fig. 3.3 Common problems in microfluidic joints. (Left) Excess length of the tube sleeve ("Dimension X") prevents a tight fit of the ferule in the union part, which causes leaks. (Right) Insufficient tube sleeve length causes a so-called dead-volume, which can have influence on flow rate calibration without causing leaks. Image from [142].

3.1.1 Acquisition and PIV parameters

In this section, the experimental and PIV analysis parameters used will be stated, and the reasons for their choices will be explained. This part will firstly describe an additional purpose of the previously described sample alignment, and the importance of having the image appearing horizontal on the sensor. A real example of different sized Interrogation Window (IW) use will be given, illustrating the technique introduced in chapter 2. Finally, the link between the size of the IW and tracer particle seeding density will be given. These parameters, in particular the seeding density, will become a useful tool when correlation averaging (described in chapter 2) will be illustrated using experimental data obtained here. Finally, potential reasons why in some cases even correlation averaged results do not pass the peak-to-peak (p2p) threshold will be given.

Sample orientation In order to minimize out-of-plane motion and reduce the complexity of the experiment, the tube mounting was manipulated so that the plane of the flow was closely aligned to the plane of the laser sheet (and hence the focal plane of the objective) with a 3D printed mount as explained in item 5 in section 3.1. Furthermore, the cameras were rotated in such a way that the image of the tube would appear as close to horizontal orientation as possible. Such alignment allows achieving the maximum camera Frames Per Second (FPS), by reducing the vertical dimension of the region of interest (the FPS for the cameras used depends on how much of the sensor is used vertically).

Parameter	Flow rate	
	0.5 µl/min	1.0 µl/min
Laser pulse length, ms	0.02	0.01
Inter-pulse time, ms	0.3	0.5
z-step, µm	2	2
Camera pixel binning	1×1	1×1
Small IW (LxH), pixel	32×12	32×12
Big IW (LxH), pixel	128×16	128×16
Frame pairs per z-step	∼250	∼ 150
Peak-to-peak threshold	1.10	1.10
Mask around peak, pixel	7×7	7×7

Table 3.1 Main experimental and PIV analysis parameters summarised for the validation experiment. Effective single pixel size was 0.3225 µm (at 20× magnification). The number of frame pairs is approximate, as it varied slightly from one plane to another due to somewhat changing frame rate of the "master" camera (fractions of a frame variation), but was the same for brightfield and SPIM data ("slave" camera acquires images at the same time as the master). Table as published in [135].
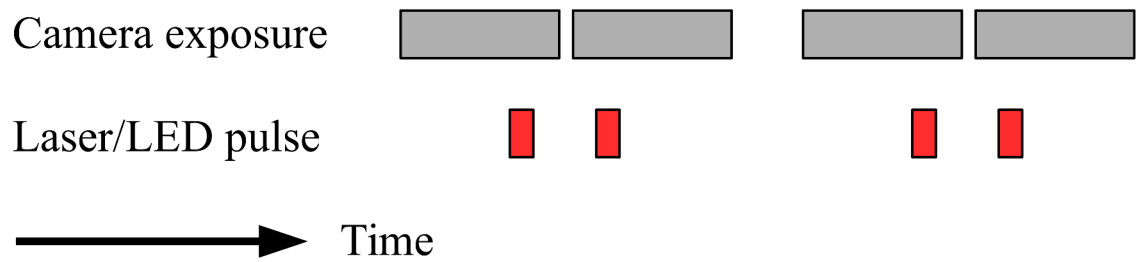
Fig. 3.4 Timing diagram of the tube validation experiment, which is similar to Figure 2.17 but is used as an aid to define the timing parameters. Since the laser/LED illuminates only the fraction of the whole camera exposure, the flow features are not averaged over the whole exposure time. Furthermore, by illuminating the sample with the laser and LED light (red rectangle) pairs at the end/beginning of the exposure (gray rectangle), the temporal resolution can be improved beyond the minimum camera exposure (as opposed to illuminating at the same point along the exposure in both frames in the image pair). The choice of illumination IPT (defined as the time difference between the midpoints of the paired light pulses) and LPL depends on the dynamics of the fluid, where a balance between signal strength and motion blur must be struck. Note, that fluid features over longer time scales could be resolved by using data acquired with illumination pulses at the end/beginning of exposure (as opposed to the reverse case).

Key imaging and PIV parameters   The key imaging and PIV analysis parameters are presented in Table 3.1. The 488 nm laser and the 600 nm LED were pulsed simultaneously via the timing electronics, as schematically shown in Figure 3.4. The flow rates used for beads in water were 0.5 μl/min and 1.0 μl/min. These flow rates were sufficient to prevent bead deposition/settling in the system but not too high to cause leaks.

The choice of illumination Laser Pulse Length (LPL) depends on the bead signal strength and the motion blur Figure 3.4. As suggested in [78, p. 59] the visibility of scattering particles should have intensity of at least 30-50% of the saturation level of the sensor. Note that it can be argued that this requirement could be relaxed for fluorescent particles imaged with SPIM (due to excitation light being filtered out, and hence yielding a better signal to background ratio). The choice of Inter-Pulse Time (IPT) essentially defines the temporal resolution of the PIV system. The keen-eyed reader might be suspicious of the fact that in this experiment higher flow rate used a longer IPT. The purpose of this was to test a larger peak pixel shift between two frame pairs ($\approx$7 pixels against $\approx$25 for flow rates of 0.5 μl/min and 1.0 μl/min respectively).

Interrogation window size and shape   As explained in the previous chapter, interrogation windows play a significant role in the spatial resolution of PIV measurements, and their shape can be adapted to the flow features, to better recover them. The aforementioned horizontal alignment of the tube facilitated the use of highly elongated IWs. Due to the laminar condition of the flow in a cylindrical tube, no variation in velocity values is expected along the length of the tube. Therefore, in principle, it should be possible to use IWs as

long as the Field of View (FOV). Nonetheless, as will be shown later, it was not practical to achieve a perfect alignment of the tube throughout the whole horizontal FOV, and therefore somewhat shorter length IWs were used.

Different sized IWs were used in the analysis of these results, that is a smaller IW from one frame was cross-correlated with a larger IW of the second frame, for an image pair. The width of the larger IW was sufficiently long to ensure that the particles from the smaller IW can still be found in the larger IW from the next frame. As mentioned above, the velocity profile is not expected to change significantly along the length of the tube and relatively long IWs can be used. However, because of the small diameter of the tube, the radial flow profile is expected to change relatively rapidly across the diameter of the tube. Therefore, this requires higher spatial resolution along the radius of the tube compared to along its length, for the flow to be sampled at a meaningful resolution. To this end, the height of small/big IWs was limited to 12/16 pixels, giving a y resolution of $3.87\,\mu m$ compared to the $10.32\,\mu m$ x-resolution for the magnification and pixel size used. Furthermore, a 50% overlap of IWs was used to observe small scale variations in the flow. While this is a standard practice in PIV, it might be considered as oversampling as the resolution is still confined to the size of small IW. To understand this better, consider three nearby square IWs which overlap by 50%. The IW in the middle is not technically sampling unique information (particles in each half of the middle IW contribute to the two IWs on either side). However, the use of overlap does help to visualise small scale variations better (i.e. better spatial sampling of the flow), and hence its implementation in standard PIV analysis.

Seeding density and correlation averaging   The nominal seeding density per small IW was 0.2 particles. One reason for the choice of such a low seeding density (much smaller than the recommendation in the PIV literature of > 10 particles per IW as discussed in chapter 2) was to simulate conditions for future zebrafish microinjection experiments discussed in the next chapter, where low seeding density is used to minimally perturb blood flow dynamics. Such particle concentration is prone to yield erroneous PIV measurements, as illustrated in top of Figure 3.5. However, the steady state flow (provided by a constant flow rate by the syringe pump) allowed for a straightforward application of correlation averaging techniques (introduced in chapter 2), allowing to artificially increase the number of tracer particles (without issues of particle overlapping encountered in image averaging approaches, or sensitivity to large outliers in velocity averaging from individual frame pair results, as discussed in the previous chapter). The effect of correlation averaging is illustrated in Figure 3.5.
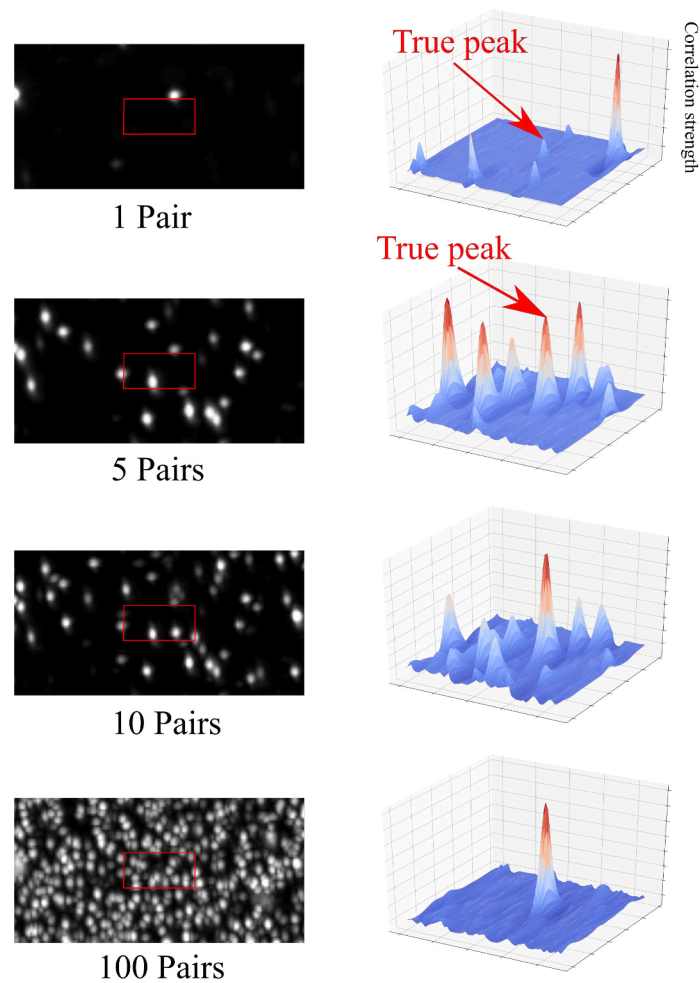
Fig. 3.5 Illustration of correlation averaging and seeding density. As described in chapter 2, a seeding density of 10 particles per IW is recommended for reliable PIV results. Here, the increase in seeding density by correlation averaging is illustrated. The column on the left shows a sum of images (1 to 100), which correspond to the "first" frame in a PIV image pair (the second frame is not shown). The red rectangle represents the smaller IW, and the big IW is the size of the image in this example. The column on the right shows the corresponding correlation matrix after *N* pairs were correlation averaged.

When the seeding density is low (or the correlation averaging is not performed sufficiently long) incorrect peaks can be significantly taller than the signal peak (see 1 and 5 pair examples). Summing correlation results for a steady state, or phase aligned periodically varying flows, can improve the results by bringing the signal peak up and dampening the random noise, see 10 pair example (the highest peak is the true peak). Performing correlation averaging over a sufficient number of pairs dramatically increases correlation p2p ratio. Note that if the *images* and not the correlation results were summed, image overlap would prevent from increasing measurement quality, but were useful here to illustrate the increase of "artificial tracer number". In principle, increasing the number of pairs for correlation averaging, can allow single particle resolution [143]. That is, the smallest achievable IW size could reach the size of the particle image.

Rejected vectors   Despite averaging over hundreds of frame pairs, measurements which do not pass the p2p threshold (explained in chapter 2, still occur). Normally this is due to mismatch between the flow features and the PIV parameters. For example, if the IW size is too small to capture enough particles during the correlation averaging. This can also occur due to the placement of the IW in the FOV, for instance, if the small IW is at the very edge of the tube, there might be very few beads passing through that area due to the no-slip boundary layer, where the velocity is zero. In this particular experiment, another possible reason for vector rejection could be several very bright and large bead aggregates spanning several IWs in height, passing through the tube. The extreme brightness will give rise to a strong correlation which will remain in correlation matrix throughout the correlation averaging. In turn, the size would yield a very flat correlation result, which is likely to significantly affect other peak despite correlation averaging, and the *p2p* threshold would discard this measurement.

3.1.2   Results and discussion

In this section, measurements of a fully-developed laminar flow in a 50 μm FEP tube with BF-PIV will be presented. The section begins by examining the geometry of the flow vessel in more detail, as this can have an effect on the data analysis. This is because the measured velocity data is fitted with a model based on Hagen-Poisseile law for laminar flow in a pipe (see [144] for a historical review). Finally, the results are summarised and potential limitations of the analysis are discussed.

(a)   (b)
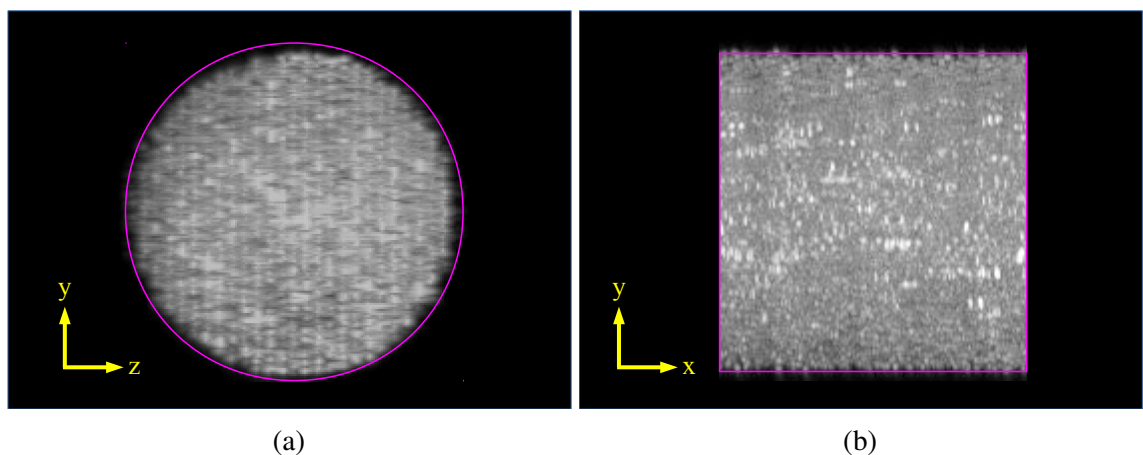
Fig. 3.6 A maximum intensity projection was used to investigate the quality of the geometry of the raw data of motion of the beads acquired using SPIM. a) Shows the *yz*-plane of the MIP projection, which reveals that the tube is indeed circular. No crimping or bulging was observed along the length of the tube, as illustrated by a small section of the *xy*-plane (a rectangle is drawn in magenta). Reminder: *xy* is the imaging plane in the conventional sense, and *z* is the depth in the sample.

Geometry of the FEP tube   As mentioned in section 3.1, due to the poor tolerances on the FEP tube diameter used here, the tube section used in this experiment was first inspected using a standard low-magnification (5×) microscope for any obvious defects. To inspect the tube geometry in more detail, the flow data itself was used. The fluorescence z-stack of a small section of the tube in the FOV was used to create a MIP, see Figure 3.6. Essentially, an MIP projects only the highest intensity pixel (that appears in each slice over time) on a 2D plane [145]. These projections revealed that the beads are indeed confined to a tube with a cross-section that is close to a perfect circle. Furthermore, the MIP along a section of the tube length did not reveal any significant deformation. This allowed fitting the velocity data using standard laminar flow equations, described in the next paragraph.

3D velocity fitting   The depth-resolved PIV results obtained with BF and SPIM imaging are presented in Figure 3.7, Figure 3.8 respectively. Figure 3.7 shows velocity profiles along the xy and xz planes (see Figure 1.12 for a Poisseulle flow along the xy plane). That is, for a fixed x and z in along the xy plane case (or a fixed x and y in the xz case), u-components of the raw velocity data obtained in BF in a 50 μm diameter tube containing flowing water seeded with 1.04 μm beads are plotted. For a steady, laminar flow in a tube, the expected flow profile in 3D is a paraboloid, that falls off to zero values at the edges of the tube. The expectation is that depth-sectioning provided by the SPIM will allow resolving such profile accurately in 3D. On the other hand, flow measurements acquired with BF data, are expected to show a flattened profile in the depth direction. In other words, the expected 3D flow profile recovered from BF imagery is expected to be asymmetric in shape. To test this hypothesis (i.e. BF $\implies$ asymmetric and SPIM $\implies$ symmetric 3D flow profile), a parametric fit was carried out to the full depth-resolved dataset. The fit was based on a model of Poisseulle flow without the assumption of circular symmetry (i.e. the model can also fit a tube of an elliptical shape, where the semi-major/minor axes are not equal). This asymmetric flattening of the profile is attributed to the effect of Depth of Correlation (DOC), which was introduced in chapter 2. In fact, this flattening has been observed in the past in *in vivo* measurements by Poelma et al. [146], who attributed this to the size of fluorescent Red Blood Cell (fRBC)s not being adequate for resolving the flow features in z accurately. Indeed this is true and will be discussed in the next chapter. On the other hand, the authors used BF illumination for their measurements. This, combined with the relatively large size of fRBCs, implies a significant role of DOC in their depth-resolved velocity measurements. Note that DOC will be discussed in more detail in the next section, but an illustration of the effect relevant to this experiment is given in Figure 3.9). Briefly, fast moving particles in the centre of the tube, can broaden the correlation peak, offsetting it toward larger shift than would be expected there. In turn, this causes the depth-resolved flow profile to broaden away from the centre of the tube (i.e. velocity values are overestimated). That is why it is necessary to add an extra degree of freedom to the Poisseuile flow model. The equation for
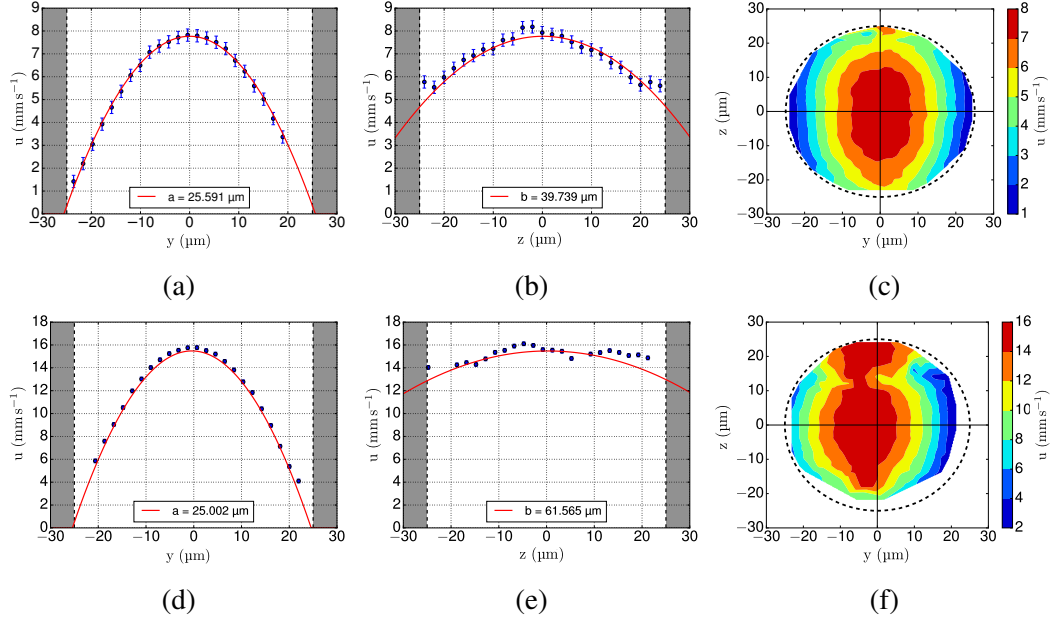
Fig. 3.7 µPIV analysis results of the FEP tube experiment data acquired using BF channel. Top row: flow of 1.04 µm beads at a nominal flow rate of 0.5 µl/min ; bottom row: same beads at 1 µl/min flow rate. The velocity measurements along the *xy*-plane (a line through z = 0 in figures (c) and (f)) fitted with the model (red curve) are shown in (a) and (b) for the 0.5 µl/min and 1.0 µl/min flow rate data respectively. Similarly, the velocity values along *yz*-plane (a line through y = 0 in figures (c) and (f)) are shown in (b) and (e) respectively. The tube walls for a 50 µm nominal diameter are depicted in gray. Error bars included are ±0.1 pixel large (which is ≈ 0.03 µm/s) to account for maximum subpixel fitting error as discussed in chapter 2. BF-PIV performs seemingly well at recovering the *u*-components of velocity along *xy* plane (a,d), and the profiles have similar shapes for both flow rates (semi-minor axis is in the range of ≈25.0 - 25.6 µm). However, the effects of volume illumination effects can be clearly seen along the *xz* plane (b, e) causing a flattening of the flow profile in depth, with increased "stretching" at higher flow rate (semi-major axis growing from ≈39.8 to 61.6 µm). The unphysical recovered profile is further illustrated by the use of contour plots (c,f) of the *u*-velocity magnitudes in the *yz* plane. The dashed line indicates the nominal FEP diameter of 50 µm. Figure as published in [135].

the model, describing the velocity profile in 3D is:

$$V(x, y, z) = V_{\max}\left(1 - \left(\frac{(y - y_c)^2}{a^2} + \frac{(z - z_c)^2}{b^2}\right)\right), \tag{3.1}$$

where $V_{\max}$ is the peak velocity of the flow, y_c and z_c are the locations of the centre of the flow axis in the y and z planes (x centre is assumed to be the centre of the image along its length), a and b are the semi-minor and major axes of the flow profile.

As mentioned in subsection 3.1.1, an effort was made to align the system well, however, to account for a small tilt of the tube, the model included parameter fitting for the tilt of the tube in yz and xz planes. In practice, the tilt in yz was at most 2°, while in the xy-plane it was negligible as the camera's sensor was aligned with the tilt of the tube (by using the edge of the Region of Interest (ROI) of the camera as a guide). For a circular tube, the 3D flow

profile (that is the true, physical flow profile) should be a paraboloid with semi-major/minor axes being equal (i.e. $a = b$). Since no significant deformation of the tube was observed as shown in Figure 3.6, any notable deviations from circular symmetry (in other words, $a \neq b$) can be attributed to expected DOC effects. Hence, a and b are used as independent parameters, as indicators for how well the flow estimation was performed. The radius was measured using BF images in the centre of the tube, by a *rectangle selection tool* in an open source biological image analysis tool Fiji [140], and found to be $26.5 \pm 0.6\,\mu\text{m}$. BF imagery instead of MIP was chosen because of simplicity, and the fact that the actual wall is visible, and any "no-slip boundary layers" are excluded (possible lack of observed particles there could give smaller estimate of the wall diameter).
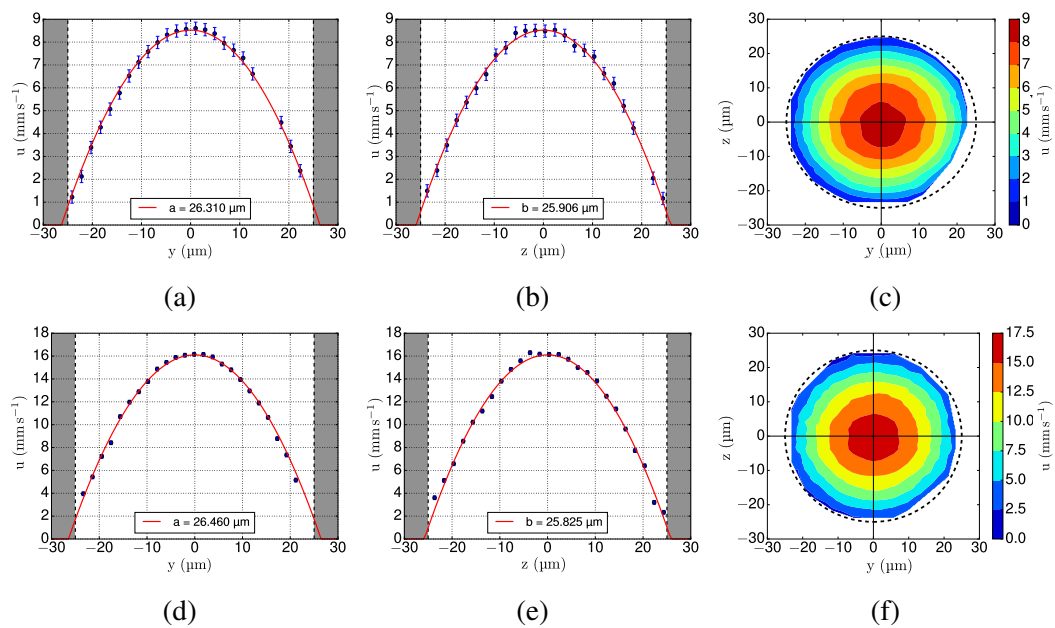
Fig. 3.8 SPIM-μPIV analysis results of flow of beads in an FEP tube. Top row: $0.5\,\mu\text{l/min}$ nominal flow rate, bottom row: $1\,\mu\text{l/min}$ beads. The tube walls for a $50\,\mu\text{m}$ nominal diameter are depicted in gray. Error bars included are ±0.1 pixellarge (which is $\approx 0.03\,\mu\text{m/s}$) to account for maximum subpixel fitting error as discussed in chapter 2. The profiles of the u-components of velocity along the xy-plane (a line through z = 0 in figures (c) and (f)), shown in (a,d) have much the same profiles for both flow rates (semi-minor axis ranges $\approx 26.3 - 26.5\,\mu\text{m}$). The same is true for the profiles along the xz planes (a line through y = 0 in figures (c) and (f)) are shown in (b,e) (semi-major axis ranges $\approx 25.9 - 25.8\,\mu\text{m}$). Since both the flow profile shape and the b parameter values are with good agreement with the expected ones along the xz plane, this illustrates the lack of volume illumination effects on μPIV measurements using SPIM-μPIV for 3D flow mapping. The colourmaps (c,f) showing the u-component of the flow in the yz plane, illustrates the recovered circular symmetry, as expected for laminar flow in a tube. The dashed line indicates the nominal FEP diameter of $50\,\mu\text{m}$. Figure as published in [135].

There was some deviation from the measured radius and the fitted semi-minor axes, a, for both flow rates. The difference was 3.25% and 5.47% for the $0.5\,\mu\text{l/min}$ and $1\,\mu\text{l/min}$ BF datasets respectively, see Figure 3.7a and Figure 3.7d. While the recovery of the flow

(a)   (b)   (c)
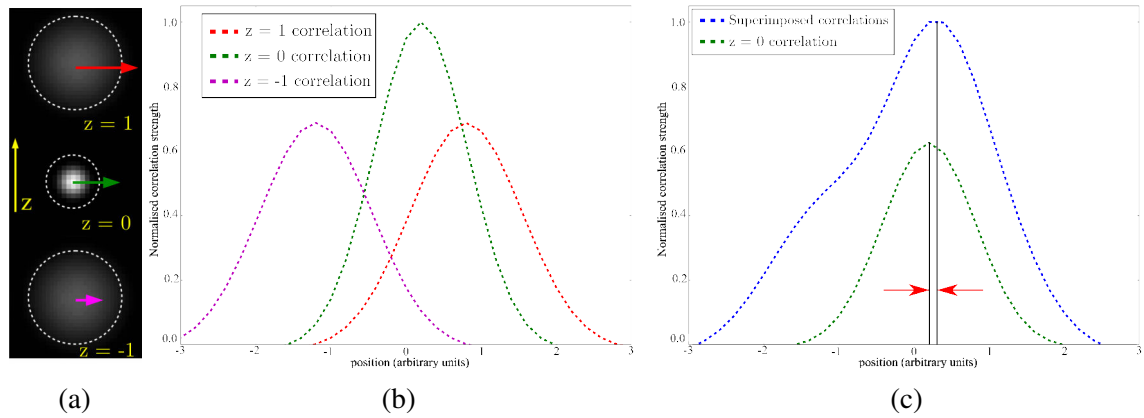
Fig. 3.9 Effect of varying flow gradient in a volume illumination μPIV system. Consider imaging fluorescent beads in a depth-varying flow gradient in a system where the DOC is large, like illustrated in (a). If the individual contributions of each particle to the cross correlation were plotted, they would appear like shown in (b) - the in-focus particle would have the tallest and sharpest correlation peak. However, since all three particles are projected onto a 2D plane, the correlation results will be a superposition of the three correlations, as shown in (c). This can yield velocity under/overestimation, depending on the flow gradients surrounding the focal plane. The red arrows indicate the difference between the location where the peak of the true motion should be, and where the peak of the superimposed correlations is. In an extreme case, "peak splitting" would be observed. That is, correlation results would have well defined peaks corresponding to motion from different depths. This is discussed in more detail later in this section.

profile shape along the *xy*-plane appeared successful, the profiles along the *yz*-plane suffered from significant flattening of the parabolas (increasing *b*), as shown in Figure 3.7b, and Figure 3.7e. This can be explained by the fact that BF data at any imaging depth, includes practically all particles flowing through the FEP tube, due to volume illumination used in BF. DOC effects lead to the correlation peak broadening towards higher velocities in this particular flow scenario, as explained in Figure 3.9.

The analysis results of the counterpart dataset obtained with SPIM (simultaneously with BF) are shown in Figure 3.8. At first glance, the profiles along the *xy*-plane (a,d) do not seem to differ qualitatively from the BF dataset shown in Figure 3.7, however, a closer inspection reveals that SPIM measures higher peak velocities (and indeed DOC effects cause peak measured velocity to be underestimated). The percent difference between peak velocities measured with the SPIM and BF imaging modalities, were $\sim 9.68\%$ and $\sim 4.03\%$ for $0.5\,\mu l/min$ and $1.0\,\mu l/min$ flow rate datasets respectively. Furthermore, the percent ratio of the fitted semi-minor, *a*, and the measured radius was much smaller than for the BF dataset, at 0.72% and 0.15% for the $0.5\,\mu l/min$ and $1.0\,\mu l/min$ flow rate datasets respectively. While these findings could be considered as subtle differences, there is a pronounced improvement in recovery of the flow profile along the *yz*-plane, as can be seen in Figure 3.8 (b, e). The ratio of the semi-major/minor (b/a) axes were found to be ~ 0.98 for both flow rates. This shows that SPIM data does not noticeably suffer from DOC effects. While this finding

Data	Fitted $V_{\max}$, mm/s	Fit a, μm	Fit b, μm
BF, $Q^* = 0.5$	7.769 ± 0.003	25.591 ± 0.008	39.739 ± 0.033
SPIM, $Q = 0.5$	8.521 ± 0.002	26.310 ± 0.005	25.906 ± 0.004
BF, $Q = 1.0$	15.479 ± 0.011	25.002 ± 0.014	61.565 ± 0.090
SPIM, $Q = 1.0$	16.102 ± 0.004	26.460 ± 0.006	25.825 ± 0.005

Table 3.2 Fitting parameters from Figure 3.7 and Figure 3.8. The tube radius was measured from the images to be 26.5 ± 0.6 μm. Parameters a and b are the semi-minor and major axes of a parabolic flow profile. A Poisseuille flow in a tube will exhibit a parabolic flow profile, which falls of to null at the rigid boundary of the tube. In this ideal case, the semi-minor and major axes a and b will equal the radius of the pipe. Notice the largely erroneous estimation of the b parameter when brightfield data is used for μPIV analysis is used (see Figure 3.7). (*) Q is flow rate in μl/min. The standard deviation in the fit parameters is returned by Python's "scipy.optimize.curve_fit" function. As published in [135].

Dataset,μl/min	BF(b/a)	SPIM(b/a)	$\dfrac{V_{max\_BF}}{V_{max\_SPIM}}$	$\dfrac{V_{max\_BF}}{V_{max\_th}}$	$\dfrac{V_{max\_SPIM}}{V_{max\_th}}$
0.5	1.55	0.98	0.91	0.92	1.01
1.0	2.46	0.98	0.96	0.92	0.95

Table 3.3 Comparison of parameters and theoretical from Figure 3.7 and Figure 3.8. The theoretical peak velocity for a pipe with a nominal diameter of 50 μm, V_{max_th} is calculated using $V_{max\_th} = 2Q/(\pi R^2)$, where Q is the flow rate, and R is the radius of the tube. $V_{max\_th}(Q = 0.5, R = 25) \approx 8.454$ mm/s. Parameters a and b are the semi-minor and major axes of a parabolic flow profile. While the tube radius at the site of imaging was measured from the images to be 26.5 ± 0.6 μm, 25 μm was used to estimate the average flow rate. This was done by assuming that the average tube diameter over the whole length was 25 μm.

is only to be expected for, it demonstrates the importance of using optical sectioning to eliminate DOC effects and recover the true flow.

Finally, a comparison between the theoretical and the measured flow profiles in a 50 μm diameter tube is made. The measured profiles with both imaging modalities are represented in Figure 3.10. The purpose of these plots is to emphasise the qualitative difference in the recovered flow profiles. The quantitative values and their analysis are recapitulated in Table 3.2 and Table 3.3. The next paragraph aims to provide more intuition on the reasons for the observed broadening of the velocity profile measured with BF-μPIV.

Qualitative description of correlation peak broadening A brief explanation for the velocity profile broadening, when using volume illumination microscopy, was proposed in the beginning of this section (see also Figure 3.9). Here, a closer look will be taken at the information preserved in the correlation matrices, from the FEP tube flow measurements described earlier in this section.

To do this, a position in the centre of the tube in the xy-plane was selected, which corresponded to a centre of an IW. The correlation results from IWs with the same xy-
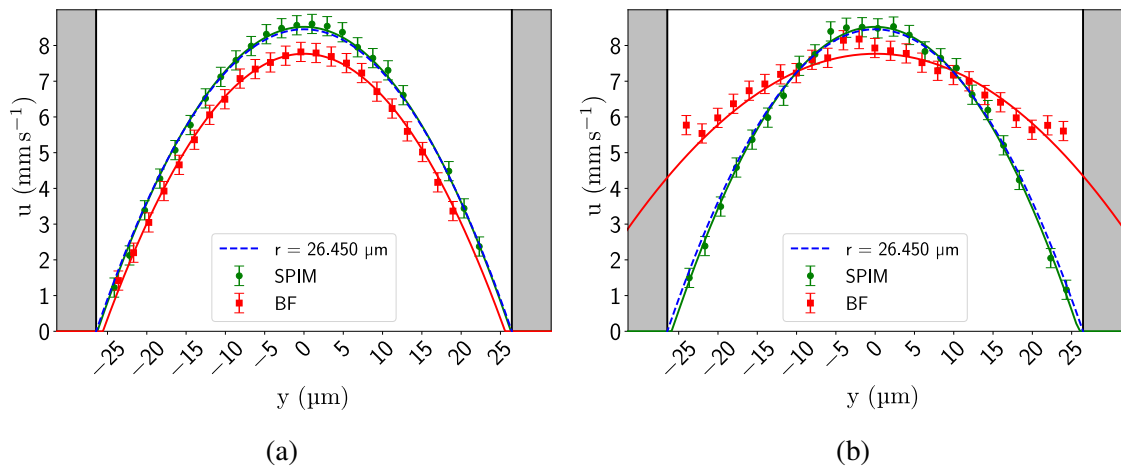
Fig. 3.10 Comparison of the theoretical and measured velocity flow profiles in an FEP tube, for the nominal flow rate of $0.5\,\mu l/\min$. The theoretical velocity profile is plotted in dashed blue line. Data fitting is shown in solid lines. (a) Shows the *xy*-plane profile, where both modalities recover a plausible flow profile in a tube (i.e. a parabola). Notice the flow underestimation by the BF data shown in red squares, this is a predicted phenomena due to DOC [88]. On the contrary to the *xy* profile, the BF modality does not recover a physically meaningful flow profile, while the SPIM data resembles the theoretical value (b). The interpretation for this profile broadening in BF-PIV data is given in Figure 3.9.

coordinate through depth were recovered. Then, for each correlation matrix from each depth plane, the row with the peak correlation value (which indicates the most likely shift) was selected. This single pixel-wide column was then plotted against its *z*-position. Repeating this for each *z*-plane allowed recovering a cross-correlation depth heatmap, as shown in Figure 3.11. These peak positions for each column were annotated to indicate the flow profile measurements observed in Figure 3.7 and Figure 3.8. This essentially follows the same approach that was taken to create *uz*-plots (b,e) in Figure 3.7 and Figure 3.8, except here the focus is on the correlation matrices from which the *u*-velocity component was extracted.

Again, it can be clearly seen that the BF results (a, c) suggest a much broader flow profile than SPIM results (b,d). Notice, that the correlation value spread in each column around the peak value (red squares) increases for the BF dataset when moving from the centre to the edges. In contrast, SPIM results have a much tighter spread around the peaks. This spread can be explained by the aforementioned peak-splitting effect:

Consider measuring flow at an *xy*-plane located at the centre of the tube, (see the red dashed line in the centre of Figure 3.12). The large DOC means that the particles flowing outside of the focal plane will contribute to the image data, and hence the flow measurements will be influenced by these out-of-focus particles. Since the flow is parabolic, there are a number of particles on both sides of the focal plane flowing at the same velocities (which are lower than at the focal plane). These out-of-focus particles broaden the correlation matrix and affect the estimation of the true flow value. Note, that due to the flow profile changing
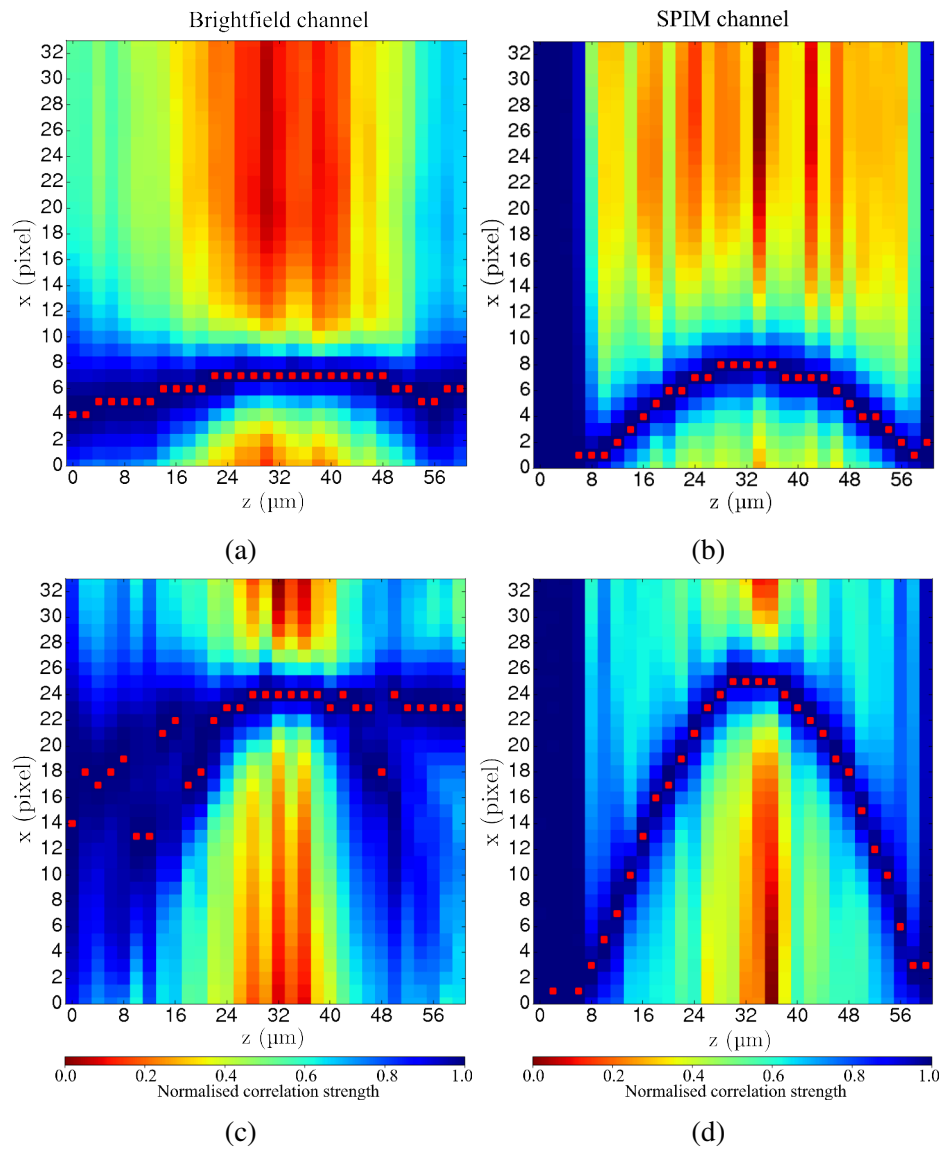
Fig. 3.11 Heatmaps of the cross-correlation results through the depth (*z*) of a 50 μm FEP tube for a particular interrogation window, for the results shown in Figure 3.7 and Figure 3.8. Each column in the heatmaps represent a single-pixel wide section of the correlation result, along the *x* axis, in a single IW at a particular depth in the tube. This section runs through the peak of the cross-correlation matrix. The peak values along the columns are annotated with red points (after sub-pixel fitting, these positions are used to estimate the flow at that IW). (a,b) Show the results for the 0.5 μl/min flow rate dataset acquired with BF and SPIM respectively. (c,d) Show the equivalent for the 1.0 μl/min dataset. Notice that an "impression" of a parabola exists in the (a,c) dataset. These results are discussed in more detail in the main text. This particular way of representing the correlation data was suggested by a undergraduate project student Richard Hoppe. Figure as published in [135].
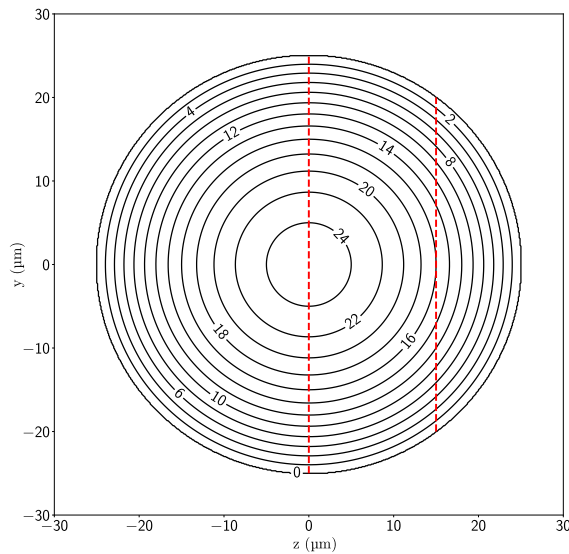
Fig. 3.12 Contourplot of laminar flow in a circular tube of 50 µm diameter and peak velocity of 25 mm/s. The *x*-direction is into the page. Notice that the rate of change of peak velocity increases towards the edges of the tube. The main text considers the implication of measuring an ideal laminar flow through two *xy*-planes (shown in red dashed lines) in a system with a large DOC.

relatively slowly around the centre of the tube, the underestimation is not significant here, as can be seen in the centre of the heatmap plots (Figure 3.11).

On the other hand, if flow is imaged at a depth away from the centre of the tube (see the red dashed line at $z = 15$ in Figure 3.12), two things happen. Firstly, the rate of change of maximum flow along depth is greater around $z = 15$, than the one surrounding the plane in the centre of the tube ($z = 0$). This means that correlation peak splitting is more likely, because the correlation peaks due to out-of-plane particles are more likely to be distinguished (recall Figure 2.15). Secondly, the symmetry of the flow profile around the focal plane no longer holds. This is because the flow gradient there is less varying in depth. This means there is a larger number of particles flowing at similar velocities than on the other side of the focal plane, where the velocities change more rapidly towards the tube walls. In this particular example, the particles on the side of the focal plane towards the centre of the tube ($z > 15$) will be statistically more likely to influence the correlation results towards higher values than the particles closer to the centre of the tube ($z < 15$). These two aspects provide the explanation for the velocity estimation bias towards higher velocities. In an extreme case of very large velocity gradients, a clearly defined peak splitting would be observed. In our case the gradients are not sufficiently large, and peak broadening is not observed (as illustrated in Figure 3.9). This also explains why a "phantom" of a parabolic flow profile can be seen in the BF correlation heatmaps (i.e. it is the beginning of the peak splitting effect).

In contrast, the correlation results in SPIM-µPIV have a much more narrow spread of around the correlation peaks (red squares in Figure 3.11), which allows to estimate the true

flow features with significantly less uncertainty, compared to using volume illumination microscopy modalities. As will be discussed in the next section a hypothesis is proposed that the DOC in SPIM-μPIV system will be defined by the thickness of the light-sheet used. In other words, any depth-averaging of velocity values would only be significant within the illumination of the light sheet. In the next paragraph, improvements to the experiments explained above will be proposed.

Possible pitfalls and limitations   Before concluding this section, it is worth discussing potential issues with this study and/or future iterations of the experiment. While the experimental set-up in itself is rather rudimentary, certain microfluidics-specific issues required attention for successful implementation of the validation experiment.

For example, compliance of the microfluidic system is a major cause for concern when using syringe pumps. Since syringe pumps inject at a steady rate, a flow rate of a constant value is expected to be observed in the system over a long time. However, if the FEP tubes would expand (a concern when using such small diameters with a wall thickness of only 75 μm), this would increase the cross sectional area, and hence decrease the expected peak velocity. At the flow rates used in this experiment, this did not appear to create a noticeable problem.

Compliance due to air bubbles was a significant problem, and purging of the system was necessary. Any air bubbles in the microfluidic system will act as springs, absorbing the pressure of the fluid, which has detrimental effects on response time of the fluid to changes in flow rate (for instance when simulating pulsatile flow). When syringe pumps are used, air bubbles can cause the pressure in the system to increase significantly, which can cause the FEP tube to be ejected from the tube sleeve holding it. While there are several ways to minimize the number of air bubbles in the system, the approaches used in this validation experiment, relied on backfilling the syringes (standard filling of syringe by withdrawing would introduce air due to the air gap between the plunger and the hub) with the bead-water solution, and purging the system with fluid of interest for several volumes of the tube length before the actual experiment was carried out.

Furthermore, it must be taken into account that the syringe pump operates by using stepper motors, hence there exists a possibility that approximation of continuous flow rate might not be entirely accurate. However, since the aim of this experiment was a direct comparison between two imaging modalities for PIV analysis, this was not a major concern (in addition to the fact that "step-periodic" flow was not observed at the temporal resolution of imaging). Therefore this aspect was ignored and assumed to be negligible.

Note that, the current imaging system was limited to imaging particles of one size of 1.04 μm. While this image is actually in the "optimal" diameter range (spanning ≈ 4 pixels across [78, p. 294]), fRBCs, which act as natural tracers in chapter 4 are several times larger. The reason larger beads were not used, was due to their fast settling velocity (i.e. the time it takes for a particle to reach the bottom of a vessel if it is not acted upon by an external

force). The use of larger beads (7.32 μm diameter) was attempted, however, in a few minutes the beads would deposit on the bottom of a syringe, as the flow rates used did not provide enough pressure. A possible solution to this is continuously rotating the syringe along its axis. However, it is not practical, and manual handling can cause inconsistencies in the flow rate. A further issue with larger beads at the size of the FEP used here is clogging. Nevertheless, for the purposes of testing the hypothesis of seeing a difference in depth profiles with BF and SPIM imaging modalities, the small bead size was not a limitation.

Finally, the syringe pump calibration procedure could be improved by the use of highly accurate scales. That is, the volume of liquid ejected from the FEP tube could be compared to the volume set in the syringe tube. This in principle should help getting a better estimate of the expected peak value or the average FEP tube diameter. However, similarly to the above point, this should not change affect the testing of our hypothesis.

3.1.3   Conclusions

The experiment carried out here measured the flow of beads in water in a 50 μm diameter FEP tube using BF and SPIM as the imaging modalities for μPIV. It was found that while the BF data may have a parabolic flow profile in *xy*-plane, it underestimates the peak velocities, due to volume illumination. More importantly, a significant difference in the quality of the recovered velocity information was seen when comparing the *yz*-plane measurements, where SPIM data provided significantly more accurate results. The BF-μPIV analysis results overestimated the velocity values at the wall of the tube. On the contrary, SPIM-μPIV performed remarkably well, as indicated by the overlap with the ideal profile shown in Figure 3.10. Finally, a qualitative description of the effect of large DOC on flow measurements in a fluid a depth-varying flow profile was also presented. The findings here shown that SPIM-μPIV measurements can provide accurate measurements at the wall in 3 dimensions, enabling Wall Shear Stress (WSS) measurements (introduced in Chapter 1). In the next section, a method for quantifying DOC for both BF and SPIM-μPIV systems, using a method developed by Hein et al. [3], will be presented.

3.2 Investigation of Depth of Correlation in a circular tube

Based on the evidence shown in the previous section we proposed that the flattening parabolic profile observed in the Brightfield (BF)-micro Particle Image Velocimetry (µPIV) results was due to Depth of Correlation (DOC), an experimental parameter which depends on the optics, particle image size, and on the characteristics of the fluid flow itself. An example of a typical flow underestimation due to DOC in a flow with a depth-varying flow gradient was presented in the previous section. This section will investigate the hypothesis, that DOC for Selective Plane Illumination Microscopy (SPIM)-µPIV is confined by the thickness of the light sheet.

3.2.1 Materials and methods: Synthesizing flow using real image data

In order to better understand the cause for flow profile measurement broadening, shown in subsection 3.1.2, real experimental images of static beads were obtained in both BF and SPIM. Beads were imaged stepwise at different planes in depth without adjusting the focus or the position of the light sheet. These images were then used to simulate PIV measurements of a parabolic flow in the centre of a tube. The experimental procedure is summarised here:

1. For both imaging experiments, the 1.04 µm beads were prepared in a similar fashion as described in section 3.1.

2. For the BF it was crucial to obtain a sample with a single layer of beads. This is because the contribution of out-of-focus beads needs to be controlled in this investigation, as will become evident later. The beads were mounted on a microscope glass coverslip. A small drop of sparse bead and ethanol solution was placed on the coverslip. They were then placed on a hotplate set at 50 °C, and allowed to dry while being gently stirred with a soft brush. The stirring prevents aggregation of the beads as the liquid dries. The sample was then put aside, covered from light and left to cool.

3. After the coverslip had cooled, it was washed using a stream of Purified Water (purH$_2$O) using a wash bottle. This clears the coverslip of weakly adhered beads, which could detach during imaging in the SPIM chamber and contaminate it.

4. The coverslip was then mounted in the SPIM chamber and aligned to be perpendicular to the imaging objective. This was carried out by observing the focus of the beads across the Field of View (FOV) while translating in *xyz* and rotating around the *y*-axis.

5. Once alignment was satisfactory, the sample was imaged over a depth range of 60 µm at 0.1 µm *z*-steps. At each step, a number of images were taken, which will later allow inclusion of real imaging noise in the analysis, as will be explained in the next paragraph.

6. For the SPIM dataset, the coverslip sample was not used, as the edge of the glass slide would be in the path of the light sheet. This could cause additional aberrations, therefore a sparse sample of beads was mounted in 2% agarose gel (which has essentially same refractive index as water), and held in an Fluorinated Ethylene Propylene (FEP) tube.

7. This bead sample was then inspected until a well isolated single bead was located. After adjusting exposure to prevent saturation of the camera, the bead was scanned at 0.1 μm step for 60 μm range in *z*.

Simulating flow data   The following description of simulation of a flow in a tube, and the analysis of the effect of out-of-focus particles on μPIV measurements, follows the approach taken by Hein et al. [3], which was introduced in chapter 2. However, instead of summing the *images* of particles at different planes, the *cross-correlations* of bead images from different planes were used. That is, images from each *z*-plane were cross-correlated with one another (per plane). The reason for this approach is twofold:

To understand the first reason, it worth briefly revisiting the different approaches for improving velocimetry results through averaging. In chapter 2 it was explained why correlation averaging is a superior technique to individual velocity vector averaging, or the use of image averaging. Recall that large errors in individual velocity values can have significant weight on the average velocity. The main issue with image averaging was the possibility of particle image overlap. Correlation averaging, on the other hand, does not suffer from this issue, and correlation results could in principle be summed indefinitely. Therefore Cross-Correlation (CC) results were summed to simulate the volumetric flow.

The second reason arises from the experimental set-up for BF imaging. Since the quality of BF illumination is not crucial for the main purpose of the SPIM system, which is zebrafish heart imaging, it is not as well aligned as a commercial inspection microscope would be. While steps were taken to achieve a uniform illumination (by the use of a diffuser), the illumination for the BF channel was not precisely aligned (i.e. the light would illuminate the sample at a slight angle, as opposed to perpendicular to the sample). Therefore the images of the beads would appear to shift between different depth-planes. If images of these beads were summed, then an unknown translation would be introduced to the synthetic images. However, if cross-correlation is used at each imaging plane (when the beads are static), the correlation result will indicate no motion. In other words, summing correlations of static beads preserves the image information (in this case, the change in focus), without introducing a shift. Note that the image correlations were performed using both Sum of Absolute Differences (SAD) and Fast Fourier Transform Cross Correlation (FFTCC), so the two algorithms could be quantitatively compared.

The plane which had the image of the beads in focus (judging from the intensity profile in *z* for the SPIM data, or the sharpness of the images for the BF data), is referred here
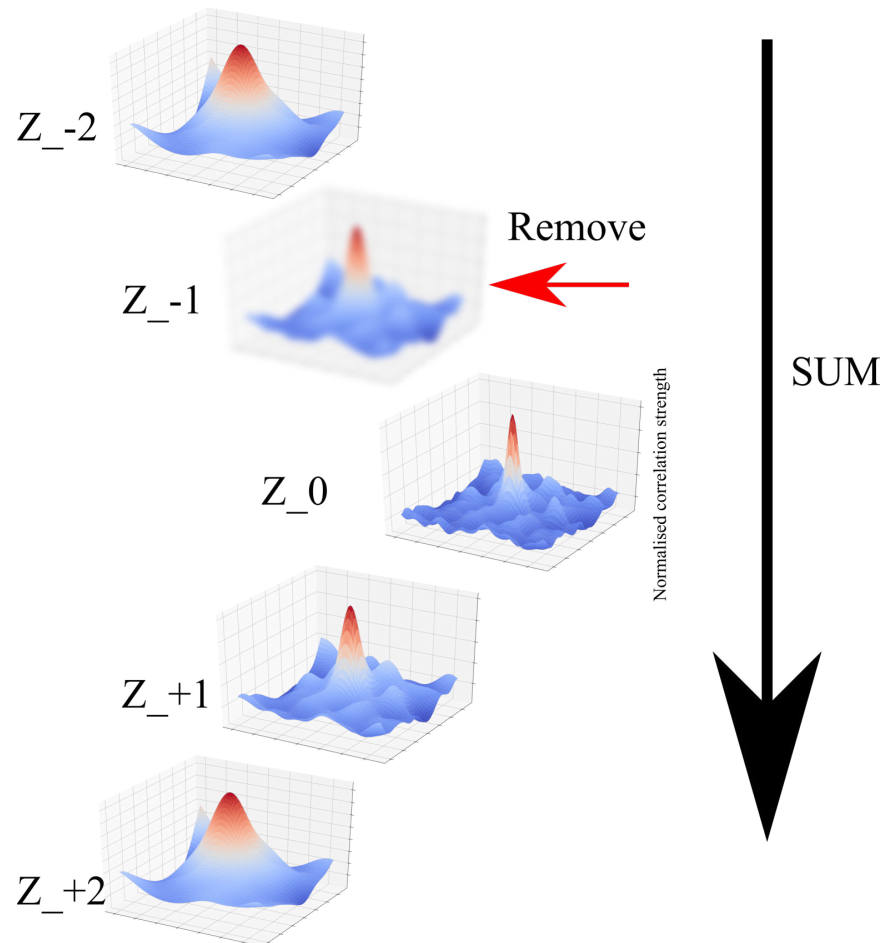
Fig. 3.13 Schematic illustration of the method for determining the influence of out-of-focus particles on μPIV measurement accuracy. In μPIV, particles illuminated outside of the DOF can still contribute to flow measurements. This out-of-focus particle contribution can be interpreted as a superposition of the cross-correlation of particle images from different planes, throughout some distance in depth. To investigate the impact of each plane on velocity measurement, the CC results from each plane were iteratively subtracted (illustrated by blurry CC). Then the position of the resultant correlation peak was compared to that of the *reference correlation*, which is the sum of all CC matrices in different planes. The results of influence of each plane for SAD and FFTCC for BF and SPIM data are shown in Figure 3.14 and Figure 3.15 respectively.

as the focal plane. For our model, this plane is treated to be in the centre of a $50\,\mu$m tube, as the focus was adjusted on the central plane of the tube in the real experiments. Each correlation matrix corresponding to beads at different planes was then shifted according to an ideal parabolic flow profile, so that the motion of each plane was known precisely. These correlation results were then summed into one matrix, which simulated imaging of a depth-varying flow. This correlation matrix including all the planes is referred to as the *reference correlation*. The image synthesis is illustrated in Figure 3.13. This synthetic data allowed quantifying the following information:

- **Peak velocity underestimation.** While DOC theory predicts peak velocity underestimation due to out-of-focus motion, *a priori* quantification can be challenging if the geometry, and expected peak velocity is not exactly known. Here, by comparing the locations of the peaks of the correlation matrix containing only the focal plane data (i.e. the ideal case where no out-of-focus particles contribute to the image) to the reference correlation (which simulates flow in a tube, with the focal plane shifted by the same maximum amount), it is possible to directly measure the underestimation. The results are presented in the next section.

- **DOC in the centre of a circular tube**. The next section will also describe the analysis of how out-of-focus particles contribute to the flow estimation using different imaging modalities. In particular, by examining how each individual plane affects the velocity measurements, we will quantify the DOC for both imaging modalities. This is achieved by comparing measured flow using reference correlation against the reference correlation *without* a contribution of a correlation matrix corresponding to a specific depth plane (illustrated in Figure 3.13). In other words, the measured shifts are compared in the absence of beads in a particular plane. Plotting the shift difference against z-position, quantifies the effect of out-of-focus particle motion on velocity measurements.

3.2.2   Results and Discussion

This section discusses the results of measuring flow in a tube using synthetic data. The section will begin by comparing the flow velocities in a tube with and without contribution of out-of-focus particles. That is, an ideal case, where only particles in focus are contributing to the measurements, will be compared against the case with out-of-focus particles contributing. Next, the main results of this chapter - the quantification of Depth of Correlation, will be discussed.

Peak velocity underestimation   Comparison of the focal plane only correlation to the reference correlation was performed using both BF and SPIM data. The peak flow used in the analysis were 8 and 24 pixels, which mimics the experimentally recovered values

	Shift difference, px			
pixelshift	BF FFTCC	BF SAD	SPIM FFTCC	SPIM SAD
8	1.78	0.66	0.00	0.01
24	5.98	1.05	0.01	0.02

Table 3.4 Comparison of PIV analysis on in-focus only plane vs overlaid planes. The shift difference is calculated by subtracting the measured flow value of the reference correlation from the correlation of in focus beads only. As expected from the DOC theory, for the particular case of a parabolic flow profile, and the FP image being at the centre of the tube, the peak velocity value is underestimated, due to out-of-focus particles. The FFTCC performs significantly worse than SAD in BF case due to the beads in images not behaving as Gaussian points - an assumption in PIV theory. The superior depth-sectioning of SPIM allows a very accurate estimate of the true flow (note, that standard sub-pixel fitting algorithms in general have an uncertainty of ± 0.1px).

observed in the previous section (see Figure 3.11). The differences are summarised in Table 3.4.

The results obtained here agree with the observations in the previous section, where volume illumination caused peak velocity underestimation. It is interesting to note that FFTCC understates the maximum velocity by $\approx 2.7 - 5.7$ times more than the SAD does for the same maximum pixel shift of 8 and 24 pixels respectively. One explanation for this is the lack of contrast (compared to fluorescence) in the bead images, so the CC tends to be significantly broader than in standard Particle Image Velocimetry (PIV) images. In other words, the peak broadening is likely to be more significant for FFTCC. On the other hand, since SAD depends on measuring the match between *features* (i.e. the pattern or shape will weigh more in an SAD correlation than intensity product), the underestimation of the peak velocity is lower. This is not unexpected, since out-of-focus images have less features associated with them, and hence contribute less to the SAD correlation.

In comparison to BF, the optical depth-sectioning ability of the SPIM system, allows recovery to very high accuracy for the case of a flow in a 50 μm tube. The difference in the measured peak velocities between 8 and 24 pixel shifts, can only be seen at the order of 10^{-3} pixel. However, since the subpixel fitting in general can have an uncertainty of up to ± 0.1 pixel, only 2 decimal point precision was used to display the results.
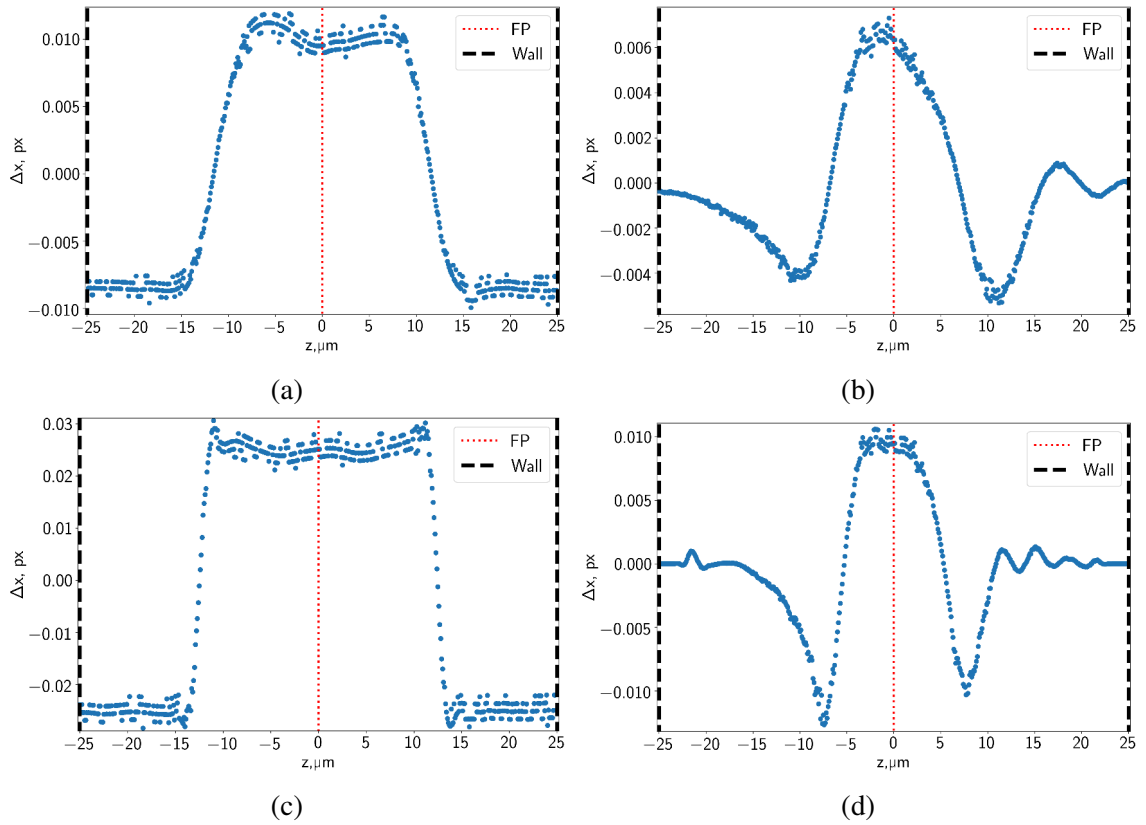
Fig. 3.14 Out-of-plane influence function for different correlation methods and peak velocities for BF dataset. The pixel difference, Δx between the shift estimated using the reference correlation matrix and the same correlation matrix with a particular plane subtracted is plotted against the depth in the 50 μm tube. Top and bottom rows show the results for the 8 and 24 maximum pixelshift of particle in the tube, respectively. The PIV analysis results using FFTCC are show in (a,c) and using SAD in (b,d). In (a,c), the particles out-of-plane overestimate the velocity values up to about 10 microns inward from the tube wall before sharply overestimating it. In the case of SAD, (b,d), the overestimation of the velocity gradually increases to about 15-17 μm inwards of the tube, before sharply increasing at the centre. The influence function of SAD results changes more gradually, and is narrower than the influence function for the FFTCC results. The position of the plane in focus is abbreviated as FP and is indicated by the red dashed line in order to help notice any symmetries.

DOC in the centre of a circular tube   According to the theory of DOC, in volume illumination μPIV, out-of-focus planes will contribute to the flow estimation depending on the parameters of the imaging modality, as well as the flow tracers and fluid motion. By considering the flow estimation in the absence of a particular plane, it is possible to quantify the influence of the out-of-focus particle there [3].

In the results presented here, the subject of attention was the depth through the centre of the plane (i.e. the plane with images in focus was positioned in the centre of an artificial tube, and contained particles with the highest peak velocity). The measured shift difference (between the shift obtained from reference correlation only and reference correlation with a particular image plane omitted) was plotted against the depth for both imaging modalities and correlation methods, shown in Figure 3.14, Figure 3.15. These results shed more light on the flow measurements in a real tube, described in the previous section. The shift difference, Δpx can be expressed in an equation form as:

$$\Delta \text{px} = R_{\text{ref}} - R_{\text{ref}-z_n} \tag{3.2}$$

where R_{ref} is the reference correlation, and $R_{\text{ref}-z_n}$ is the reference correlation which excludes the contribution from plane z_n (see Figure 3.13). Therefore, a negative Δpx value means that the particle motion from the excluded plane was pulling the CC peak towards a smaller displacement, than the one at the focal plane. In other words, the Δpx curve, can be interpreted as an *influence function* of a particular plane in the volume, on the velocity measurements at the focal plane. In the ideal case, where particles to the velocity measurements only contribute at the focal plane, the expected shape of the influence function would be a Dirac delta function, at $z = 0$.

As can be seen by comparing columns in Figure 3.14, there is a noticeable difference in the shape of the influence functions for BF dataset, depending on which correlation method is used. Both FFTCC results, Figure 3.14a and Figure 3.14c, can be interpreted as a rectangular function (but with a *y* range of (-1,1)), with a full width of 50 μm. It is interesting to note that even particles at the very wall of the tube still contribute to the measurements and the velocity profile does not drop off to zero. The general shape of the graphs do not appear to differ significantly between the 8 and 24 pixel maximum motion. However, a greater maximum pixel shift difference was observed, which seems to scale linearly with velocity (≈ 0.01 to ≈ 0.03).

Findings with the SAD metric, on the other hand, reveal a shape that is similar to a Sinc function. Compared to the FFTCC results, the influence function has a less dramatic change between positive and negative difference and a somewhat smaller "Full Width at Half Maximum (FWHM)", of ≈ 12 and 10 μm for the 8 and 24 pixelmaximum shift cases. However, the influence of out-of-plane particles are noticeable for a range of about 30 μm. Unlike the FFTCC results, the influence of images far from the focal plane approaches null values.
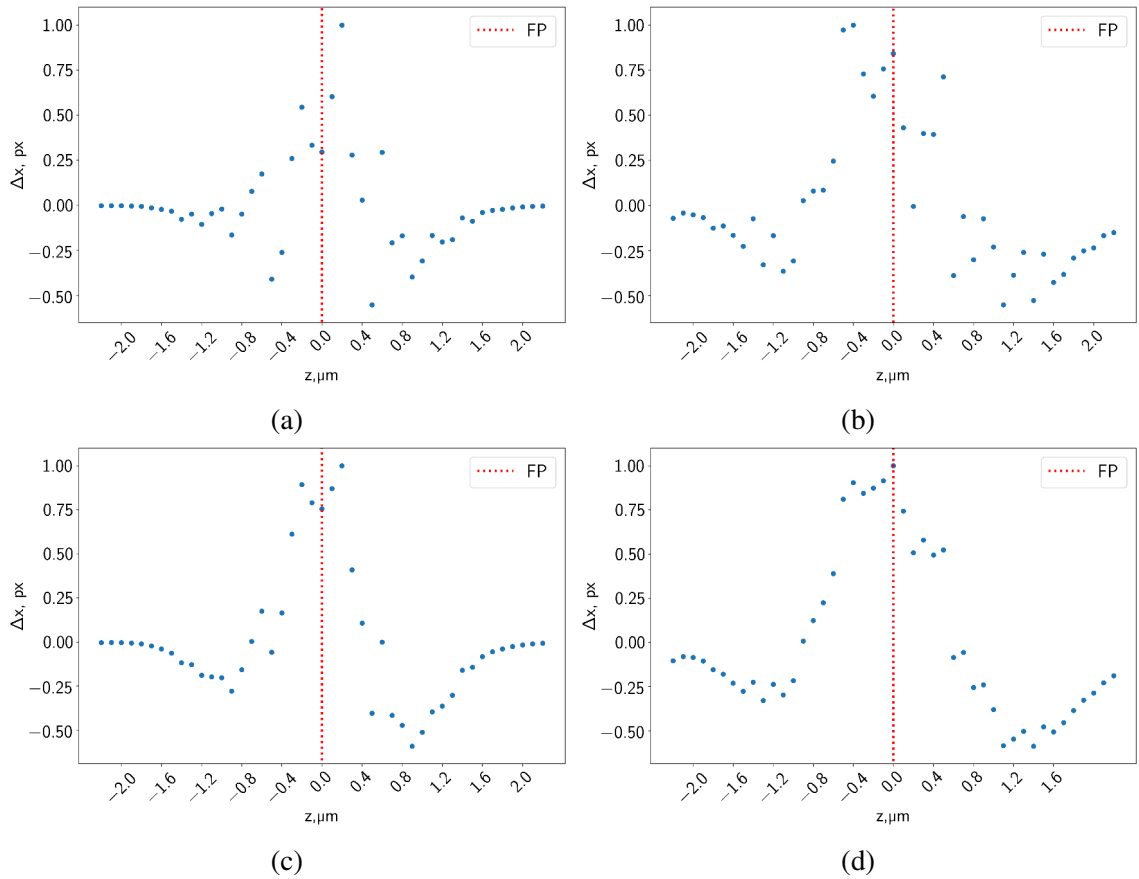
Fig. 3.15 Normalised out-of-plane influence function of SAD and FFTCC for the SPIM dataset. The pixel difference, Δx between the shift estimated using the reference correlation matrix and the same correlation matrix with a particular plane subtracted is plotted against the depth in the 50 μm tube. Top and bottom rows show the results for the 8 and 24 maximum pixelshift of particle in the tube, respectively. The PIV analysis results using FFTCC are show in (a,c) and using SAD in (b,d). Due to the thin sheet of light used in SPIM the influence function is limited to a range of about from -2 to 2 microns, at which point the removal of any plane has a negligible contribution. The red dashed line indicates where the plane of images with estimated focus was in the simulated tube. Unlike the results shown for BF data in Figure 3.14, the shape of the influence functions does not differ significantly between SAD and FFTCC data.

Both algorithms have negative values at the outer part of the tube, and positive at the inner part, which indicates that velocities are over and under-estimated in the respective regions. The general trend of both functions agrees with the findings in the tube experiment described in the previous section, and indeed with findings by Hein et al. in a *rectangular* channel [3]. It is worth drawing attention to the fact that SAD performs better than FFTCC in volume imaging conditions, which provides an additional advantage to using this correlation function. The suggested explanation remains the same as in the case of comparing the focal plane only against the reference correlation. SAD relies more on image *features* rather than intensity. Significantly defocused particles do not possess noticeable features, and hence have a lesser influence on the SAD algorithm. However, even with the use of SAD, BF-μPIV still performs substantially worse than the SPIM-μPIV, discussed next.

In contrast to BF or conventional epi-fluorescence microscopy, SPIM is capable of "true" optical sectioning (as opposed to discarding light using a pinhole as in confocal microscopy), therefore depth-averaging effects due to out-of-plane measurements in μPIV with SPIM should be limited to the beam waist (defined in chapter 2) of the Gaussian light sheet. Indeed, Figure 3.15, shows exactly that. Note that here the influence functions are normalised to draw the attention to the actual shape, rather than the measured difference values. There is a clear difference in the range of significant effects by out-of-plane particles, namely about 2.4 and 3.2 μm around $z = 0$ for the 8 and 24 pixel maximum shift cases respectively. As expected, both of these values lie within the beam waist (for a Gaussian beam of 2.4 μm FWHM, the beam waist is just over 4 μm). In contrast to the performance by the two correlation functions, SAD appears to be ever so slightly more sensitive to out-of-plane particles. Once again this could be explained via the "intensity product vs. feature" argument, explained previously. Regardless of the minuscule differences in the sensitivity, the important aspect here is that the strongest impact on the measurement comes from the planes around the estimated focal plane (recall that depth was sampled at 0.1 μm steps), and drops off rapidly, compared to BF results.

Future iterations   The analysis shown here can be carried out with the focal plane placed in an arbitrary position, as long as there are sufficient out-of-focus planes to simulate the rest of the tube. It could be potentially interesting investigating how focusing on a non-central plane in a flow in a tube would affect measurement accuracy using volume illumination technique. In general, the approach of this analysis could be used to simulate flow with a variety of flow profiles if needed.

Note, that BF dataset could benefit from obtaining a larger z-stack to investigate when does the contribution of out-of-focus planes becomes irrelevant to the measurement accuracy.

It appears the SAD has advantages over FFTCC for BF-μPIV analysis. It would be interesting to investigate the behaviour of SAD in the case of processed BF imagery.

Finally, it could be argued that technically more than one fluorescent bead should be used to synthesize images. Using more beads would slightly increase the correlation noise

(due to all small peaks appearing due to all possible bead overlap combinations). However, if the seeding density was sufficiently large, the "true" correlation peak would be significantly higher than the rest, and it seems that a significant advantage would not be gained.

3.2.3 Conclusions

The goal of this section was to quantify the peak velocity underestimation and individual plane influence on velocity measurements, due to out-of-plane particle motion. Both results agreed with the real experimental data shown in the previous section. It was found that SAD performed better than FFTCC when determining the velocities from BF images. This effect was attributed to its "bias" to match image features rather than intensities. Finally, the most important result of this chapter - the trial of the hypothesis that DOC in a SPIM system is described the light sheet thickness - was verified. These findings suggest that any flow measurements performed with volume illumination microsopy on flows with a depth-varying flow gradient, can be greatly improved using SPIM-PIV system.

3.3   Out-of-plane motion tolerance

In the previous section it was shown that Depth of Correlation (DOC) effects on micro Particle Image Velocimetry (µPIV) analysis can significantly impact the accuracy of velocity measurements when volume illumination is used. As long as the depth-varying flow gradients are varying over a significantly larger distance than the thickness of a light sheet used in Selective Plane Illumination Microscopy (SPIM), any depth-averaging effects are negligible. This is a clear advantage over conventional microscopy-µPIV systems, in particular for imaging highly complex geometries, such as the zebrafish heart.

However, an important source of measurement error, the introduction and/or loss of particles due to Out-of-Plane Motion (OOPM) (introduced in chapter 2), can still hinder the reliability of flow measurements. This happens even when using imaging systems capable of optical sectioning. This segment will describe the use of real images of different sized beads along with correlation averaging, to probe the robustness of the SPIM-µPIV system against out-of-plane motion. In this section, empirical measurements were carried out to investigate maximum acceptable OOPM levels.

3.3.1   Materials and methods

The intent of this experiment is to obtain real experimental data, which can be used to simulate out-of-plane motion. This data is acquired by scanning fluorescent bead samples, fixed in agarose gel, through the light sheet. The sample preparation was essentially the same as described in the previous section. Sparsely seeded 1.04 and 7.32 µm diameter fluorescent polystyrene beads were used as the tracers in this experiment. The choice of 1.04 µm diameter microspheres was mainly due the their use in *in vivo* zebrafish microinjection experiments, described in the next chapter. The 7.32 µm were selected due to their comparable size to fluorescent Red Blood Cell (fRBC)s, which are used as tracers when imaging the blood flow in the living zebrafish heart, described in the next chapter.

Synthetic flow   To mimic out-of-plane motion, a *z*-stack of images with a known depth difference, Δz, were firstly paired. Then, a synthetic *in-plane* shift of 24 pixels was applied to the second image, to simulate a known in-plane shift. This amount of shift was similar to the diameter of the particle image of the 7.32 µm bead. Δz acted as the known OOPM component between the two images in a frame pair. These image pairs were then analysed in the usual way for Particle Image Velocimetry (PIV) analysis (i.e. divided into Interrogation Window (IW)s, and cross-correlated, followed by peak-to-peak (p2p) ratio validation and subpixel fitting).

<div align="center">

Z = 0 µm   Z = 4 µm $\sum_{n=1}^{16} \mathrm{CC}(\mathrm{IW}_n)$

(a)

</div>

<div align="center">

Z = 0 µm   Z = 24 µm $\sum_{n=1}^{16} \mathrm{CC}(\mathrm{IW}_n)$

(b)

</div>
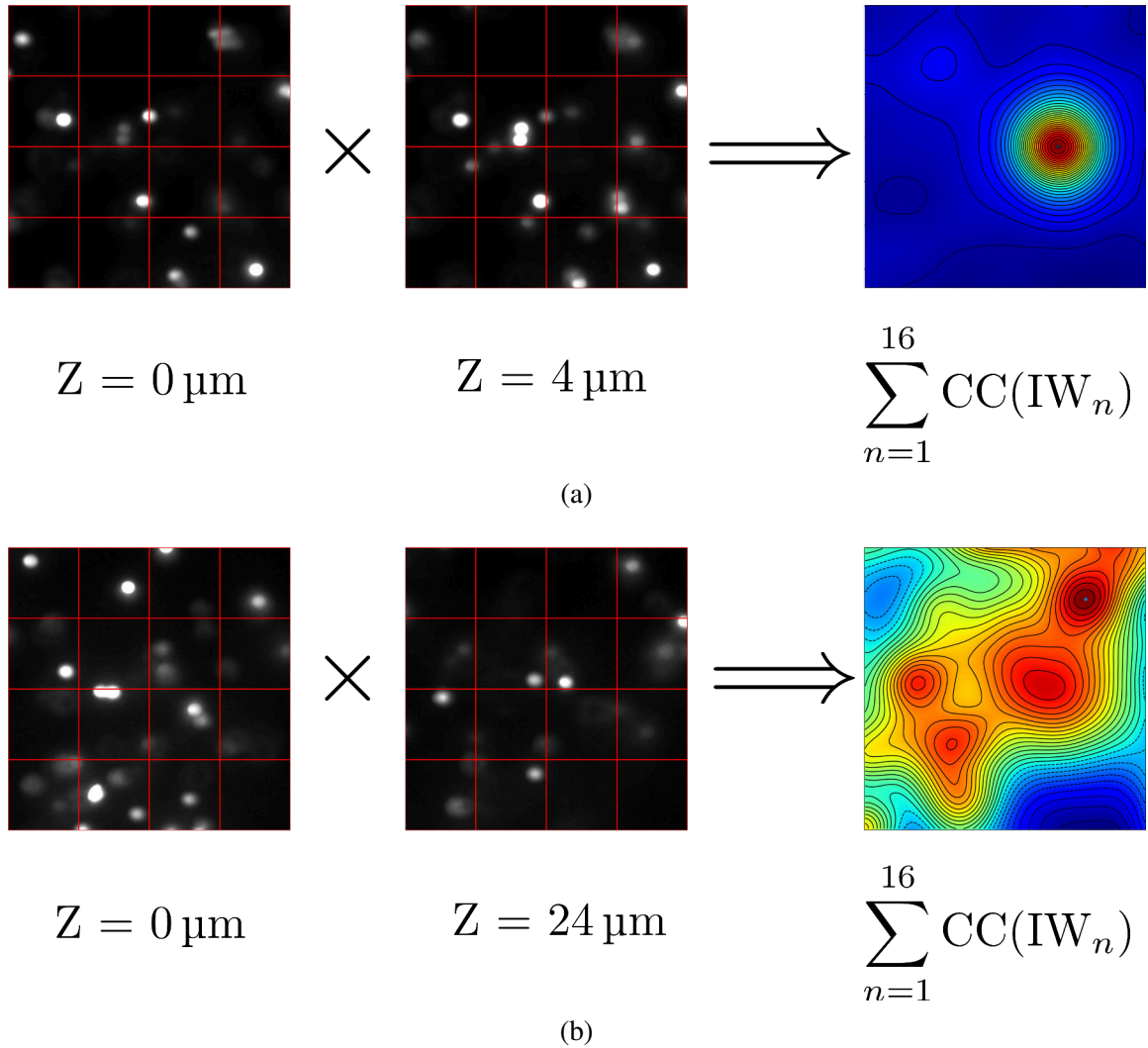
Fig. 3.16 Illustration of the correlation averaging approach to probe OOPM effects on measurement accuracy. Images with a known *z*-position difference are paired. The second image in the frame pair, is then synthetically shifted by a known amount of pixel motion. The images are then cross-correlated in the usual way. The correlation matrices from each IW (shown in red squares) are then summed. This is repeated for over ≈ 10 image pairs (which are not sampling the same bead images) for each *z*-step difference. (a) Shows an example of the raw images, as well as a heatmap of the correlation matrix, for a *z*-motions of 4 µm. The heatmaps shows a well defined peak, with little surrounding noise. On the contrary, results shown in (b) illustrate, that a significant amount of *z*-motion leads to an erroneous measurement. It is clear from the heatmap in (b) that the correlation results is significantly noisy. By comparing the correlation peaks against the known flow values, the maximum tolerable OOPM can be defined.

In order to perform the correlation averaging, the particle images were unique to each image pair. In other words, the information content between image pairs was uncorrelated. Otherwise, if there was some information overlap, it would be possible that the highest peak in the averaged Cross-Correlation (CC) result is simply due to correlating essentially the same information content (even if defocused). In other words, the correlation averaging might appear to perform better, than if the particle distribution was random for each image pair. To ensure this, sections in the *z*-stack of 15 µm in the case of 1.04 µm diameter beads or 30 µm depth for the 7.32 µm spheres, were omitted between image pairs. These CC results from 8 to 10 frame pairs with the same Δz were then summed to simulate contribution of particles outside of the Depth of Field (DOF), see Figure 3.16 for illustration of this approach.

The measured horizontal displacement was then compared against the ideal shift of 24 pixels for both the Sum of Absolute Differences (SAD) and Fast Fourier Transform Cross Correlation (FFTCC) results. 4 and 5 independent sample volumes for 1.04 and 7.32 µm beads were used respectively, and are summarised in Figure 3.17, and discussed in the next section.
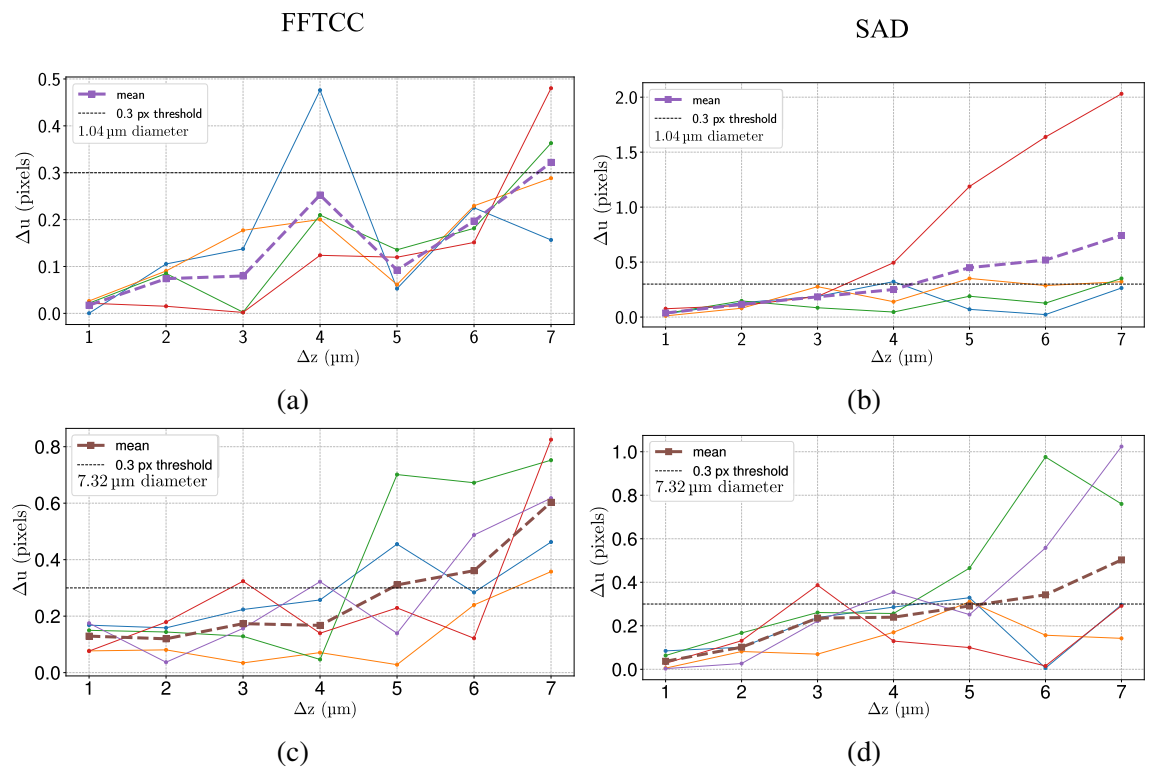
Fig. 3.17 OOPM effect on µPIV measurement accuracy for 1.04 µm and 7.32 µm diameter beads. Solid lines represent measurements at different samples (i.e. different different volumes in the FEP tube). The 0.3 pixel threshold based on [3] is indicated by the fine dashed line. The mean of the shift measurements is indicated by the bold dashed line. Results for 1.04 µm diameter beads, using FFTCC are shown in (a) and appear to perform moderately better than the SAD results in (b). For 7.32 µm diameter beads, both measurements using FFTCC, shown in (c), and SAD, in (d), have similar trend and values. Figure (d) based on [135].

3.3.2   Results and Discussion

This section interprets the results obtained in order to quantify the acceptable out-of-plane-motion levels for SPIM-μPIV measurements. These results are particularly important when measuring blood flow in the zebrafish heart, described in the next chapter. Improvements to the current approach are also briefly discussed.

Maximum acceptable OOPM   The plots presented in Figure 3.17, show the absolute difference between the true and measured horizontal shift, Δu, against the OOPM, Δz for both bead sizes and CC algorithms. Both datasets show that up to ≈ 4 μm *z*-motion, SPIM-μPIV can on average recover velocity values with better than ±0.3 pixelaccuracy. This ±0.3 pixelaccuracy is deemed acceptable in PIV literature [143]. Note that the ≈ 4 μm OOPM value lies below this threshold regardless of the correlation algorithm used. Recalling that the Full Width at Half Maximum (FWHM) of the light sheet used in these experiments was ≈ 2.5 μm (which implies the beam waist of just over 4 μm), the observed limiting OOPM value is not surprising.

On the other hand, it is interesting to note that the average velocity errors (dashed lines in the aforementioned plots, Figure 3.17) do not increase significantly until the OOPM reaches ≈ 7 μm. One potential explanation for this is that the effective thickness of the light sheet can broaden as it enters the sample (due to a round surface of the FEP tube, and slight mismatch between the refractive indices of water-FEP-agarose-sample). An alternative cause for the apparently reasonable velocity estimates beyond the expected beam width might be statistical. It is possible that there remains some correlation between significantly out-of-focus beads just entering/leaving the light sheet in the image pair. More importantly, since the *uv* components of the flow are always the same, it is likely that each image pair will give small CC signal indicating the true in-plane motion (while other peaks will be random for each frame pair). In this case, if correlation averaging is performed sufficiently long, the signal of the true in-plane motion will rise above the random noise.

In fact, the above point is crucial in this work, where intrinsically Two Dimension-Two Component (2D2C) PIV techniques are applied with optical sectioning to recover Three Dimension-Two Component (3D2C) flow information. While the recovery of 3D flow information using conventional standard PIV is not novel [147, 148], the literature reviewed in this work did not indicate application of correlation averaging for extending the tolerable OOPM (recall that Adrian and Westerweel [78] suggest that OOPM should not exceed one-quarter of the light sheet thickness). Therefore, in complex flow geometries where there is a risk of relatively high OOPM (such as the beating zebrafish heart), correlation averaging can provide a way to robustly measure in-plane motion, and hence 3D2C + time measurements, when combined with SPIM.

Potential improvements   Certain aspects that can be improved in this investigation, as well as the limitations of these experiments, are summarised in the following way:

- **Data exclusion**. The large step sizes in depth between image pairs ($15 - 30\,\mu m$) could in principle be halved to allow for more correlation averaging.

- **Large dataset**. The datasets used here totalled in just under 100 GB of space to provide a large amount of images for correlation averaging. However, it could be argued whether 4-5 (for each particle size) independent datasets are truly sufficient to make conclusions about tolerable OOPM levels. Since obtaining larger datasets is not practical, Monte-Carlo simulations would be beneficial for this type of study.

- **Particle shape**. The purpose of this investigation is to simulate conditions expected when imaging blood flow in the zebrafish heart. However, tracers used for *in vivo* measurements in the heart are fRBCs, which have a pancake like shape. Hence, using spherical beads might not provide the complete insight on expected OOPM effects.

- **Comparison to epi-fluorescence**. It would be interesting to include experimental results using epi-illumination. It is possible, that OOPM effects could be more severe there, due to full volume illumination.

In principle, the points summarised above are not critical issues which invalidate the findings described in this section, and are mostly presented as suggestions for future improvements. However, the most important step would be the increase of datasets used to draw the conclusions.

3.3.3   Conclusions

In this section, by acquiring particle image data at different z-planes, and applying synthetic image shifting, effects of OOPM on correlation-averaged μPIV analysis was investigated. Satisfactory measurement uncertainty under 0.3 pixelwas observed for up to $4\,\mu m$ OOPM. In essence, the use of correlation averaging techniques enables accurate measurements which are reliable even with a significant amount of out-of-plane motion.

3.4   Summary

This chapter aimed to empirically validate Selective Plane Illumination Microscopy (SPIM)-micro Particle Image Velocimetry (μPIV) as a flow measurement capable system. In the first part of this chapter, SPIM and Brightfield (BF)-μPIV measurements of flow in a micron-diameter tube were compared. Then, the Depth of Correlation (DOC) for both imaging modalities were quantified, by synthesizing a parabolic flow profile using real experimental data, which was the key result of this chapter. Finally, reliability of SPIM-μPIV for imaging

flow with varying Out-of-Plane Motion (OOPM) was investigated. Here the main findings are revisited.

It was shown that SPIM-µPIV outperforms BF-µPIV for both determining the peak velocity, and resolving the depth information of a flow in circular tube.

These differences were attributed to the different size of DOC in the two imaging modalities. While the DOC is a dynamic parameter (meaning it can change depending on the flow features), any "depth-averaging" of velocity measurements in a SPIM-µPIV system are heavily confined by the thickness of the light sheet. This presents a unique advantage in microscopic velocimetry over conventional imaging technique, allowing to investigate flows with complex depth-varying patterns. Furthemore, this also means that 3D Wall Shear Stress (WSS) measurements could be performed accurately using a SPIM-µPIV system.

However, even optical sectioning techniques are not immune to OOPM. Nevertheless, it was shown that the genuine concern of correlation signal dampening due to new/old particles appearing/disappearing, can be solved for flow with OOPM components of up to 4 µm. This is achieved by making use of correlation averaging technique, allowing to capture the signal of the true motion reliably.

Note, that as a by-product of the analysis presented here, further evidence was shown to illustrate the advantage of using Sum of Absolute Differences (SAD) correlation for brightfield images. Recall that qualitative benefits of SAD Cross-Correlation (CC) algorithm were previously stated in chapter 2. In fact, SAD will be used extensively in the next chapter for blood flow imaging in the zebrafish heart.

In conclusion, both experimental and synthetic data illustrate that SPIM-µPIV is capable of obtaining high accuracy flow information, in conditions with large gradients throughout the depth of the sample, as well as in flows with OOPM up to the size of the light sheet. In the next chapter, the robustness of the system will be put to the test, where results of *in vivo* imaging will be presented. Chapter 4 will begin by discussing measurements of flow in the blood vessels of the zebrafish, for which the flow in the Fluorinated Ethylene Propylene (FEP) tube presented here was the model. The optical gating technique introduced in Chapter 1 and expanded in Chapter 2 will be crucial for blood flow measurements in the heart introduced next. The chapter will end by returning to the dominant theme of this thesis - validation of the results

Chapter 4

Blood flow measurements in the zebrafish

In the previous chapter it was demonstrated that the proposed SPIM-µPIV system can successfully recover Three Dimension-Two Component (3D2C) velocity data of a flow of beads in 50 µm tube [1]. Most importantly, it was shown that the DOC in SPIM-µPIV measurements of a parabolic flow is limited to the thickness of the light sheet used. This ability to accurately predict the DOC *a priori* is a significant advantage of SPIM over conventional microscopy techniques used for µPIV measurements. This improvement motivated the aim of this chapter - the application of SPIM-µPIV in an *in vivo* setting. This ultimately resulted in the main experimental finding of the whole of this thesis - Three Dimension-Two Component (3D2C) + time resolved velocity measurements in the developing zebrafish heart.

This chapter will describe the approach taken to reach this goal, and will begin with a description of the sample handling aspects, which play an important role in the quality of acquired data. Then, the motion properties of fluorescent red blood cells (which were used as tracer particles here), and their implication on µPIV measurement will be discussed. Next, 3D2C + time velocity measurements in the major vessels of the zebrafish will be presented. This will be followed by description of flow measurements using microinjected fluorescent beads, and a direct comparison of fluorescent Red Blood Cell (fRBC) and bead motion will be made. Then, the depth resolved velocity measurements in the zebrafish heart will be presented, which allowed quantifying the pumping efficiency of the heart. Next, examination of any apparent OOPM in the heart will be presented. Finally, this chapter will conclude by discussing the reliability of phase information recovery, which was performed by examining the velocity measurements themselves.

---

[1] In the field of PIV, depth-resolved measurements recovering 2 component velocity information are referred to as 3D2C measurements.
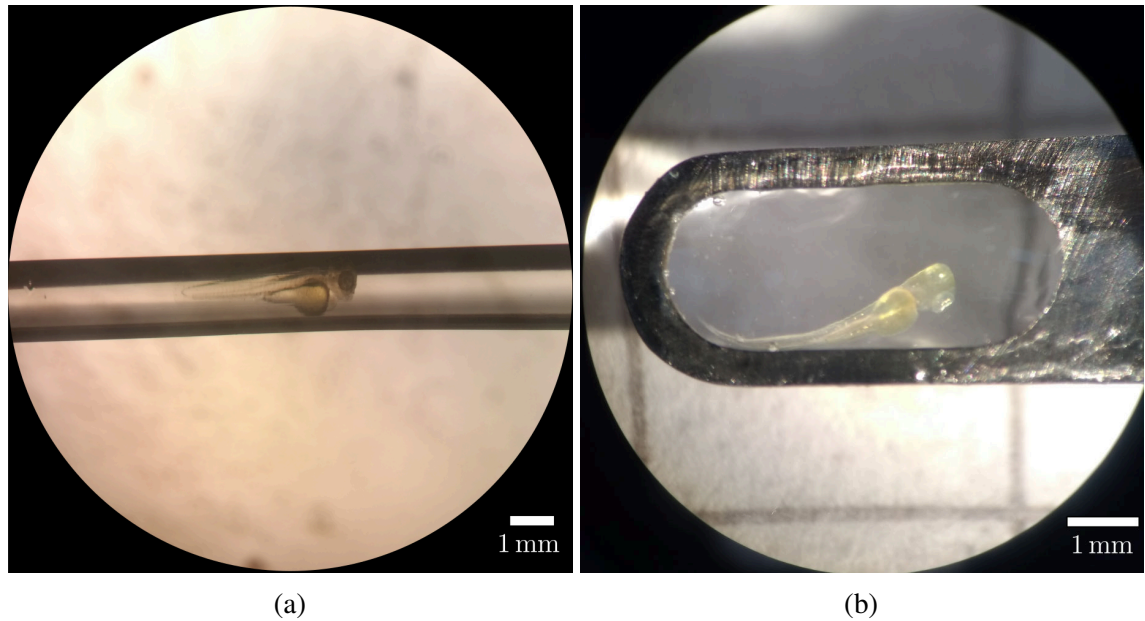
Fig. 4.1 Zebrafish embryo holders for the SPIM. a) A syringe with a blunt needle (not shown) is used to hold the FEP tube, which is visible here because the tube is shown in air. The zebrafish embryo suspended in liquid agarose solution is then carefully withdrawn inside the FEP tube. Not shown here, but it is possible to eject a small amount of solid agarose with the fish in it, to minimise the number of interfaces the excitation, and emission light has to pass. b) An alternative approach, that has previously been tested by Strobl et al. [149] for use in Drosophila embryos, uses a thin flat loop of steel in which the sample is held by the tension of agarose film. This improves the image quality by removing the need for full enclosure of the fish by a holder (such as an FEP). However, this somewhat limits the viewing angles to 4 orientations in steps of 90°, and requires the whole sample chamber to be filled with water suitable for the zebrafish (specific mineral salts content).

4.1 Methods

Handling and imaging a living sample spanning a few millimetres in size such as a few days old zebrafish embryo requires significant preparation. Here the general aspects of imaging the zebrafish for Particle Image Velocimetry (PIV) measurements will be discussed. The section will describe sample handling and preparation, as well as the chemical treatment of the zebrafish embryos in order to prevent development of pigment. A short discussion on microinjections will be presented, before discussing the necessary adaptations of the Selective Plane Illumination Microscopy (SPIM) system for blood vessel measurements. Finally, the range of angles of sample orientation available for the least amount light scattering in SPIM will also be examined.

4.1.1 Sample mounting

Due to the vertical sample mounting used in a SPIM microscope, a common approach to mount samples such as zebrafish, fruit fly, or C. elegans embryos, is by using an FEP tube which is typically filled with ≈0.5-2% agarose. Normally, low-melting point agarose is used,

which has a gelling temperature in the range of $26 - 30$°C, which matches the temperatures that the zebrafish embryos can tolerate well [150]. Syringes are routinely used as part of the mount, which allows easy withdrawing and ejection of samples in agarose, like shown in Figure 4.1a. The size of the FEP tube used seems to vary among research groups, as some prefer more space in the sample than others, but generally the inner diameter is around 1mm.

As discussed previously, the refractive index of FEP tubing is well matched to the surrounding medium of water, aberrations are considered to be negligible in practice if the sample is mounted appropriately. That is, the curvature of the tube can cause image distortion if the sample is touching the FEP wall. Hence, it is crucial to keep the sample away from the walls, and ideally - in the centre of the tube, so both the excitation and fluorescence light is not significantly affected by the round surfaces. Withdrawing an embryo into the FEP tube often leads to adherence to the wall. In order to minimise this effect, the tube was first coated with methylcellulose (by purging it through the FEP) before withdrawing the zebrafish, as described in [151]. The thin layer of methylcellulose prevented any sticking of the embryo to the walls. It is worth noting, that when using agarose only, it requires significant pressure to eject the fish from the FEP tube, and the lubrication provided by the methylcellulose, enables smooth motion of the fish in agarose. In fact, this can be beneficial for experiments involving a change of concentration in some drug (since agarose gel is at least 98% water, diffusion through it is rather fast), or in order to minimise optical distortions.

It is possible to bypass the use of an FEP tube by using a mount which relies on holding the sample in place by an agarose film spread on a thin loop of metal, as shown in Figure 4.1b. This approach, first proposed by Strobl et al. [149], was developed specifically for Drosophila embryos, but was tested in this work for mounting zebrafish. It required more skill to mount samples in this way, as an initial approach of using an artist's brush to spread a layer of agarose on the metal loop proved to be challenging, and there was practically no control on the initial orientation of the embryo, once mounted on the film. Eventually, it was found that simply dipping the metal loop in agarose gel would successfully form a film, without the need to use a brush at this stage, however, the zebrafish would still be mounted using an artist's brush limiting the control on the sample orientation. This mounting method was not pursued further due to time constraints, however, it can be potentially beneficial for low signal experiments, as agarose is known to be weakly autofluorescent.

4.1.2 Anaesthesia

While agarose gel can prevent the sample from drifting, an alert zebrafish embryo is able to move rather vigorously in the gel. In order to prevent this, and to minimise the discomfort to the animal, anaesthetic is used throughout the experiment. Tricaine Methanesulfonate is the standard anaesthetic in zebrafish imaging. While the concentration of the anaesthetic

can vary depending on the experiment, around 150mg/L is common [22]. It must be taken into account that tricaine affects the heart rate and contraction [152], however, the heart rate of the animals used in this work, was not observed to significantly differ from the baseline. On the other hand, a lack of change in heart rate does not imply that the contraction strength is not affected.

4.1.3 Pigmentation and dechorionation

As discussed in chapter 1, there exists a large number of zebrafish strains. The available strains for this project were limited to *wild-type* (strain line abbreviation: WIK) and a mutant line called *casper*. Both strains were further derived to express red fluorescence in erythrocytes, through the transgenic construct Tg(gata1:dsRed) and/or green fluorescence in the heart muscle and blood vessels, through transgenic construct Tg(flk1:GFP). In contrast to WIK, the casper strain does not develop skin pigmentation which can block the optical access to the heart or the blood vessels (fish with and without pigment were shown in Figure 1.2). However, we have observed that the casper strain tends to have noticeably fewer fluorescent Red Blood Cell (fRBC)s in the blood. This means that longer imaging is required to build up the signal peak with correlation averaging, as discussed in the previous chapter. This, in addition to the fact that the casper line became depleted during the early stages of this work, left the wild-type fish as the only practical option. In order to prevent the zebrafish from developing pigment, ≈ 24h embryos were treated with 0.003% 1-Phenyl-2-thiourea (PTU). As a side-effect, this treatment hardens the egg chorion of the zebrafish and postpones hatching, which would normally occur around $48 - 72$h, hence the fish have to be dechorionated before imaging. Dechorionation involves using fine tipped tweezers to carefully tear the chorion open, hence freeing the fish from its egg chorion.

4.1.4 Fluorescent particle microinjection

It will be shown later in this chapter, that the size of the fRBCs somewhat limits how well the flow can be resolved in the blood vessels. If higher spatial resolution is desired, it is possible to introduce artificial tracers in the zebrafish through microinjection. It is crucial to deliver precisely controlled volumes of tracers, so as to minimise the effect on the natural blood flow.

It is known that the total volume of blood in the zebrafish is estimated to be around 90 nL at 2 days old [153, 154]. Since the injections in this work are typically done around 3 day mark, a total blood volume of about 100 nL is assumed to be a reasonable ballpark. In order to minimally disturb the haemodynamics by injecting beads, the total injection volume should not be more than 5 nanolitres for this volume (according to [154]). Highly reproducible volumes at picolitre scale can be achieved using a pneumatic microinjector, such as the *World Precision Instruments PV820 Pneumatic Picopump*. The volume cali-
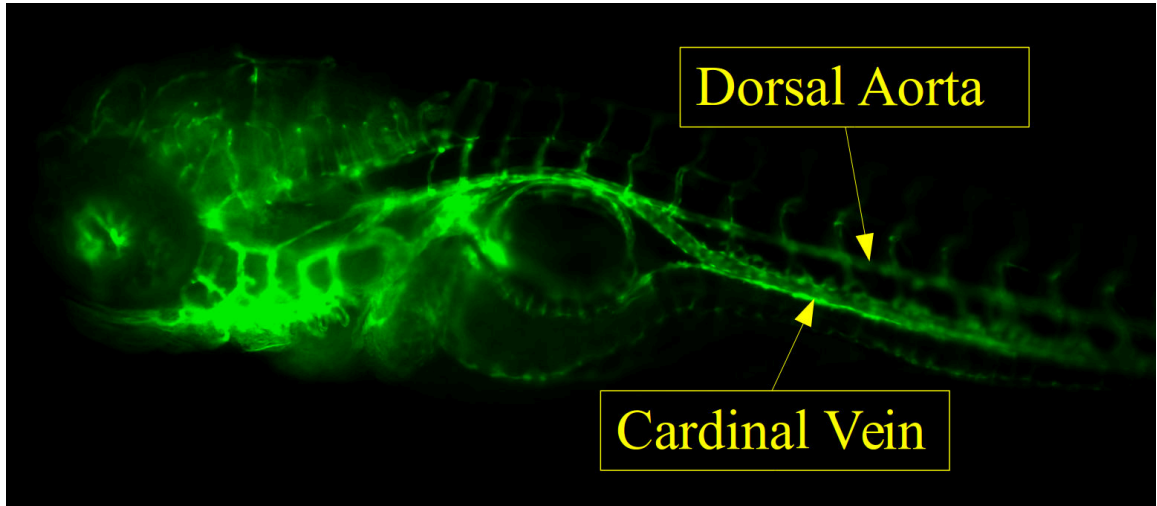
Fig. 4.2 Main blood vessels in the zebrafish embryo (*flk1:GFP* transgenic line). Dorsal Aorta DA and Cardinal Vein CV are the two main blood vessels in the zebrafish. DA has a smoother structure compared to CV which has structures called *blood islands*. Because of these structure, when fluorescent beads are microinjected, they tend to deposit and aggregate in the CV to a higher degree than in DA.

bration step is done by injecting a bolus of bead solution into a drop of mineral oil, placed on a stage micrometer with 0.01 mm graduation. Since the injected bead solution can be well approximated as a sphere, the volume can be inferred from the observed radius using $V = \frac{4}{3}\pi r^3$, where V is the volume of the sphere with radius r. For example, a bolus of diameter 0.1mm gives a volume of ~ 0.5nL. After the calibration is done in the mineral oil, it is important to adjust the pressure to adjust for the capillary suction, as blood from the fish can be accidentally withdrawn. The adjustment is done in water, when the Picopump is set to have a slight continuous outflow from the glass needle. The needle tip can then be washed by dipping it in ethanol followed and then in purified water, before the actual injection in the zebrafish.

At around 72h the Common Cardinal Vein (CCV) (a vessel which leads to Sinus Venosus (SV), which in turn leads to the atrium) is transforming from a flat and wide vessel to a cylindrical one. The flatness of the vessel presents a suitable area for microinjections. During the insertion of the needle, care must be taken not to puncture the vessels on both sides to minimise the damage to the animal. Injecting at a shallow angle to the vessel tends to work best. However, the body of the fish is rather elastic, and often the needle punctures through both walls of the vessel, as the body snaps back to its normal shape. This requires a slight retraction of the needle to reposition it in the centre of the vessel. An injection is considered successful if there are no beads outside of vessels, and the heartbeat is not affected.

4.1.5 Time-resolved blood flow measurements in blood vessels

Blood vessels in the zebrafish (see Figure 4.2) provide an intermediate ground between the controlled experiments of flow in a 50 μm tube and the beating zebrafish heart, for applying SPIM-micro Particle Image Velocimetry (μPIV). This is because both the structure of blood vessels, and the features of blood flow inside them, make it a less challenging system than the heart, for μPIV measurements. The main reasons are summarised in the following list:

- Roughly half of the body length of the fish is in its tail. Here, the cross-sectional area is much smaller than the torso of the fish, where the heart is. This means, that there is less scattering tissue for both illumination and imaging light to pass.

- The rate of change of velocity in the blood vessels is less severe than in the heart. This is because the vasculature dampens the pressure forces provided by the heart [155]. This reduction in peak velocities allows the use of longer laser illumination to increase the signal levels.

- In experiments involving microinjection of fluorescent beads, the relatively smooth inner walls of the DA is less susceptible to bead deposition in the walls, compared to heart walls. While the beads eventually do deposit in all vessels, the DA allows more acquisition time with freely flowing particles.

- Finally, the negligible contraction of the vessel walls (likely due to a residual pressure wave generated by the heart [155]), and the relatively simple tube-like shape of the vessels suggest that the flow should be mostly two-dimensional. In other words, it is expected that the velocity is dominated by the two in-plane components. This means that if the sample is aligned parallel to the light sheet, the recovered Three Dimension-Two Component (3D2C) flow information should be the true representation of the complete 3D flow.

It is important to note that the blood flow in the DA and the intersegmental vessels branching from DA is still pulsatile. Therefore phase information is necessary in order to perform correlation averaging (see chapter 2 for a reminder on correlation averaging concept). However, despite the above list of advantages, obtaining Brightfield (BF) images of the heart for phase recover is more difficult than when imaging the heart in both channels.

In order to understand this, it is necessary to recall the experimental set up shown in Figure 2.16. The standard configuration has the camera sensors centred on the same point in the object plane (for configuration B in Figure 2.16, the same is true despite the BF camera now imaging through the laser launch objective). Because the blood vessels with least surrounding tissue (and hence yielding best image quality) are in the second half of the tail - this leaves the heart beyond the Field of View (FOV) of the BF camera when the sample is moved. Hence, it is impossible to obtain simultaneous heart images in BF an Fluorescence (FLR) images of blood flow in the blood vessels.
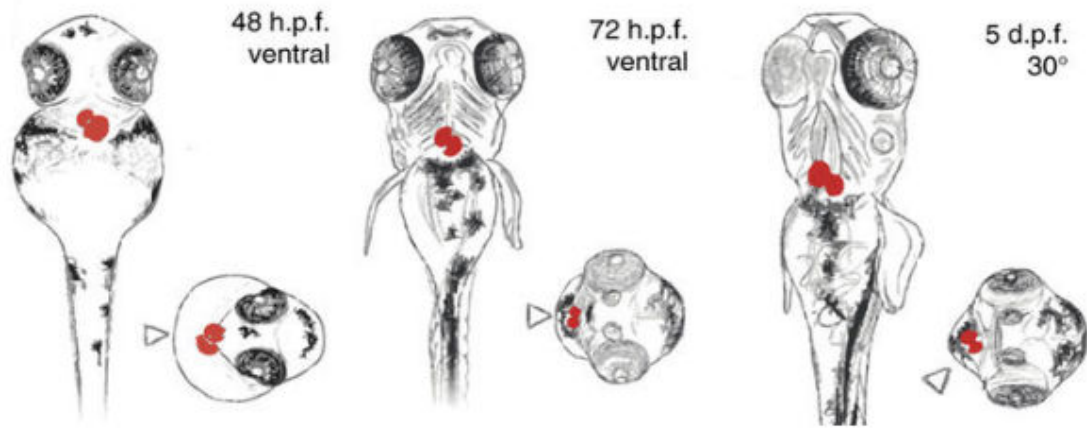
Fig. 4.3 Orientation of the heart in the zebrafish at different ages. As the fish and its heart grows, imaging difficulty and image quality changes. Since the illumination and imaging are at right angles, some orientations of the embryo yield better data than others. Mickoleit et al. [156] suggest that the three orientations shown here for 2,3 and 5 dpf fish should yield best results when imaging with SPIM. However, if multi-view reconstruction were required, we observed that the best image quality would be obtained $\approx \pm 30\,$deg around the locations indicated by the arrows. The atrium is located at the right hand side in both the ventral (belly facing the reader) and anterior view (head is facing the reader). Image adapted from [156, Fig. 3]

One solution to this, is to change the *xy*-position of the BF camera sensor (while keeping the it normal to the object plane). However, there is a limit to how much the BF camera can be shifted, as eventually the image will be *cropped* due to the finite aperture size of the objective/lenses. Alternatively, it is in principle possible to recover phase information by imaging "residual" motion of the heartbeat. This can be described as a shock wave travelling through the body/vessels of the fish during the heartbeat. By using the same image analysis techniques used in optical gating [15], the periodically moving tissues can sometimes be used successfully to extract phase information without even seeing the heart itself. This idea was implemented by Dr Jonathan Taylor. However, this seems to work best when imaging blood vessels relatively close to the heart, where the improvements in image quality are not as good, as they are further in the tail of the fish.

4.1.6 Sample orientation for heart imaging

Both the zebrafish body and its heart undergo significant changes in the first few days of its development. In less than five days, the heart evolves from a simple contracting tube, to a two chamber heart, with valves, and complex trabeculae structures in the ventricle. The fish transforms from a curled up shape (with the tube-heart relatively deep in the body) to an elongated shape, with a two-chamber heart which shifts closer to the ventral side of the fish (refer to Figure 1.1 for a reminder). This has implications on the optimal orientation of the embryo for cardiac imaging. While the heart does move to the periphery of the

fish, it is still enclosed by relatively thick tissue on the lateral sides, see Figure 4.3. This means that if the embryo is oriented with the ventral side facing the incoming light sheet, the fluorescence emission light will pass through all the scattering tissue, before it reaches the imaging objective. A better approach is to orient the fish around $30-45°$ to the light sheet. Nonetheless, a compromise will always be necessary between image quality and light scattering. For example, depending on the orientation, it is possible to obtain good quality information from one chamber, but not the other (this is due to beam divergence discussed in subsection 2.3.2). Note that the orientation of the fish for BF data acquisition (for heart phase recovery) is not as important as it is for FLR images, as long as the BF illumination provides sufficient illumination through the zebrafish tissue to illuminate the heart.

4.1.7 A note on long term imaging considerations

A final comment: it is worth mentioning that the agarose concentration and the temperature of the sample chamber becomes important in long-term imaging. The aspects are particularly important in the first 72 hours, where the rate of growth of the embryo is particularly rapid (as shown previously in Figure 1.1. It was previously found by Weber et al. [151] that the use of agarose concentrations above 0.5% has an effect on the morphological changes in the zebrafish. The ideal temperature for embryo development is at 28.5 °C, but the fish can successfully develop between 25 and 33 °C, with a slower and faster development rate respectively. These considerations where assumed to not be a major concern in this work, as the fish were imaged from 3 days old onwards, and for no longer than 30 minutes per z-scan.

4.1.8 Summary

This section outlined the main experimental considerations for this work. These key aspects can be summarised as follows:

- Image quality is affected by the zebrafish mounting mechanism, which introduce aberrations. For example, this can arise due to spherical surfaces in an FEP tube, despite its refractive index being close to that of water.

- Aberrations can also arise in the zebrafish itself. It was explained that tissue surrounding the heart and blood vessels scatters the light, and pigmentation can block the light completely.

- Microinjection requires specialist equipment capable of delivering precise volumes at the nanolitre scales. Furthermore, the nature of injections requires significant practice time.

- Phase information recovery requires imaging indirect information of the heartbeat or necessitates a different arrangement of BF are, on the SPIM system.

	Tracer particles	
Parameter	fRBCs	0.39μm beads
Laser pulse length, ms	1.5	1.0
Inter-pulse time, ms	2.0	1.5
z-step, μm	4	N.A.
Camera pixel binning	1×1	1×1
Small IW (LxH), pixel	32×24	32×16
Big IW (LxH), pixel	96×48	128×32
Frame pairs per phase	~ 30	~ 30
Peak-to-peak threshold	1.025	1.025
Mask around peak, pixel	7×7	7×7

Table 4.1 μPIV analysis parameters for flow measurements in the zebrafish embryo blood vessels. The much smaller size of beads compared to fRBCs allows using smaller IW with more tracers. In principle, the size of IW could reach the size of single particle image, provided correlation averaging is done over an extended period. Note, that while illumination power was not included, fluorescent beads are significantly brighter than fRBCs.

Solutions for each items in the above list were presented, which were used throughout this thesis. These methods were first applied for *in vivo* measurements in the zebrafish blood vessels, described in the next section.

4.2 Blood flow measurements in zebrafish blood vessels

The previous section introduced the general practical aspects of imaging blood flow in the zebrafish. In this section, several results of micro Particle Image Velocimetry (μPIV) analysis in the blood vessels of the zebrafish will be presented. Imaging and quantifying flow in blood vessels, particularly in the tail of the zebrafish, is less challenging compared to flow in the heart, due to reasons explained in the previous section. Therefore measuring flow in the blood vessels is a suitable first experiment for testing how Selective Plane Illumination Microscopy (SPIM)-μPIV can cope with *in vivo* imaging conditions. This section will present μPIV measurements using both fluorescent Red Blood Cell (fRBC)s and fluorescent beads as tracer particles. The reasons for differences between the velocity field recovered using both methods will be considered towards the end of this section, where the behaviour of individual tracers will be examined.

4.2.1 Flow of erythrocytes in the main vein and artery

As explained previously, PIV requires tracers in the fluid in order to measure the statistically most likely motion between successive images. Recall that these tracers are typically microspheres chapter 2, nevertheless, in biological systems cells can act as tracers [157,
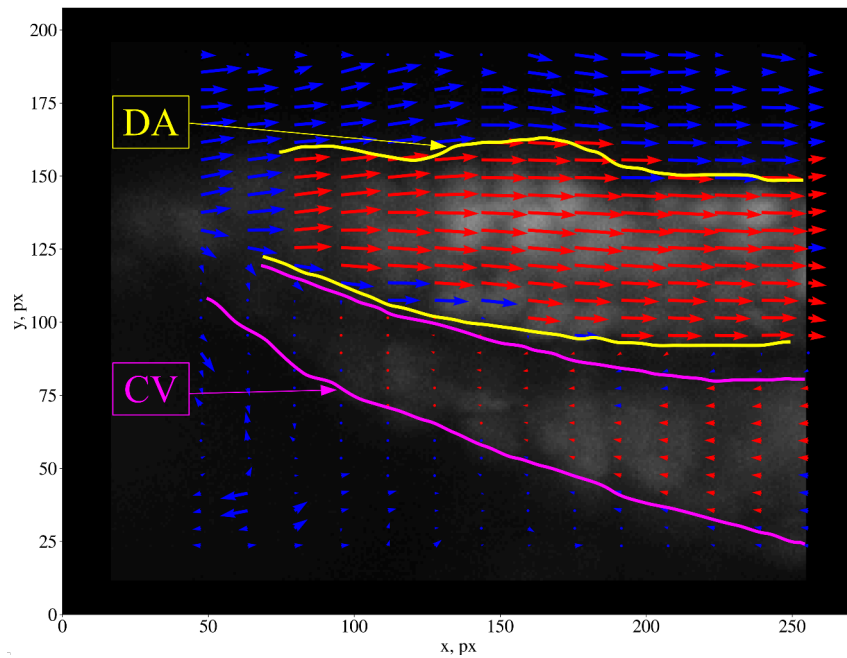
Fig. 4.4 Flow field in the DA and CV in the zebrafish from µPIV analysis using fRBCs as flow tracers. A single plane of velocity vectors overlaid on an MIP of the raw data. The DA is the top vessel, and CV is the bottom one, the tail is on the right of the image. The red vectors indicate measurements which passed the set p2p ratio (see Table 4.1). The blue vectors are previously invalid values, replaced by a weighted average of surrounding vector values (see *replace outliers* function in OpenPIV Python code [1]). A modified OpenPIV version (which allows correlation averaging) was used for all PIV analysis throughout this thesis. Notice that the velocity profile does not drop off to zero at the walls. This is mainly attributed to the fRBC size, and will be further considered in the main text. Note that the yellow and purple lines are a visual guide of approximate vessel wall locations.

69, 90, 146]. In the case of the zebrafish, these tracer cells can be fRBCs, found in the transgenic *Tg(gata1:dsRed)* line. The flow characteristics of these cells are different to those of polystyrene beads and are considered here.

In this experiment, a section of the main blood vessels in a 3 day old zebrafish embryo was imaged using SPIM, to reveal the motion of fRBCs. The sample preparation and mounting (in an Fluorinated Ethylene Propylene (FEP) tube) was carried out as described in the previous section. The parameters used for the μPIV analysis are summarised in Table 4.1. Sum of Absolute Differences (SAD) was used as the algorithm for obtaining Cross-Correlation (CC) matrices, and the reason for this choice will be explained later.

It is known that the blood in the zebrafish embryos operates at a low Reynolds number ($\ll 2000$), which means that the flow is not turbulent, but expected to be laminar. As was explained in chapter 2, for a laminar flow the expected flow profile is a paraboloid. However, due to the large size of fRBCs (details presented later in this section), such profile was not observed, see Figure 4.4. The higher velocities between the two vessels were found to be in the artery and peaked at just over $2\,\mathrm{mm/s}$. Using the heart phase recovery routines described in chapter 2, correlation averaging was performed to improve the reliability of measurements. This also allowed investigating the temporal changes of the flow profile in 3D. The recovered phase information was divided into 32 equal phase bins, which approximately equals $15.6\,\mathrm{ms}$. The *xy* and *yz* flow profiles are shown for 7 out of 32 phase bins in Figure 4.5a and Figure 4.5b. Notice that the flow profiles in *xy*-plane begin almost flat and then become somewhat more parabolic. However, these profiles do not reach zero at the estimated location of the vessel walls (edges of the plots). In contrast, the *yz*-profile exhibits a parabolic shape which drops off more rapidly, but still does not reach zero values at the walls. A possible explanation to this is that during *z*-sectioning the outer planes of the blood vessel imaged, are likely to contain traces of signal from the fRBCs which pass very close to the vessel wall. This means that unlike in the case of *xy*-profile as shown in Figure 4.4, there are essentially no fRBCs flowing at slightly different velocities (shear still negligible) along the height of a single IW. The flow features were further inspected by considering the flow rate through the cross section of the vessels.
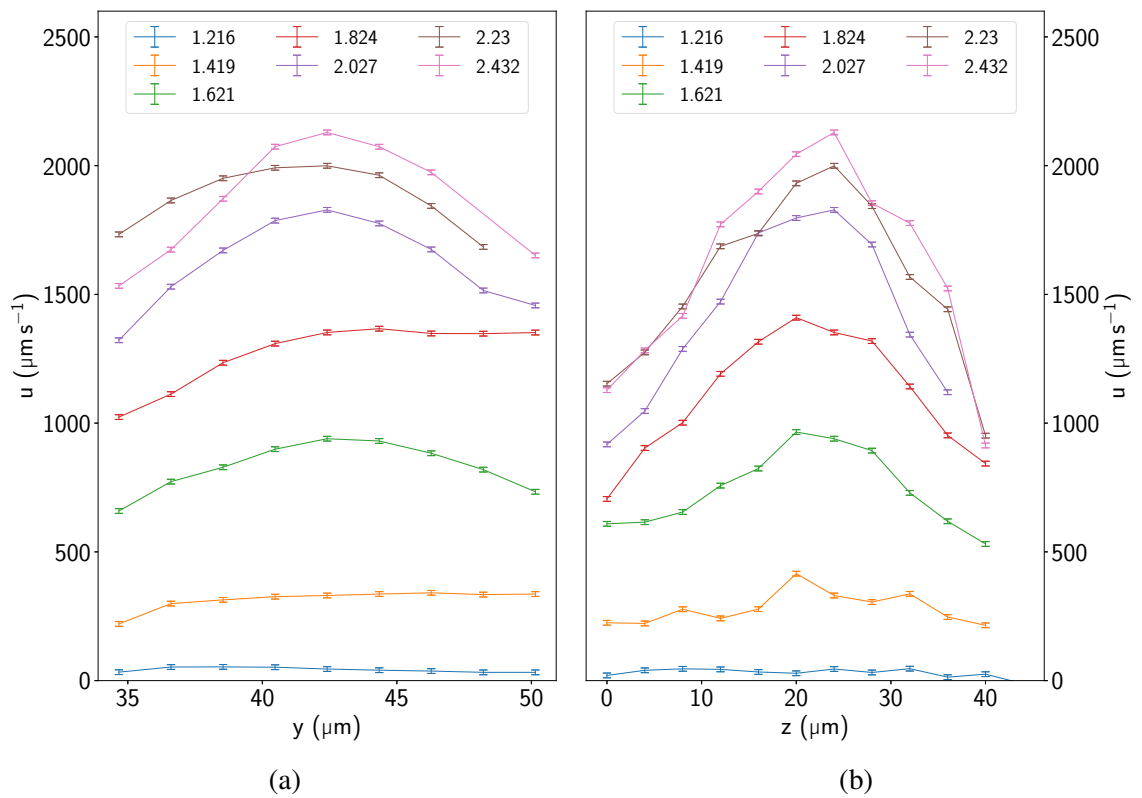
Fig. 4.5 Flow profiles of fRBCs in the DA of a 3 day old zebrafish at 7 different phase bins, see Figure 4.6. a) shows the *u*-component velocity in the *xy*-plane at $z = 24\mu m$ (see heatmaps in Figure 4.6) and a chosen *x* coordinate. b) displays the flow profile of the *u*-component in depth (or *yz*-plane) at the same *x* coordinate as data shown on the left column. The size of the fRBCs limit the available spatial resolution, and an expected flow profile which falls to zero at the vessel walls is not observed.

(a)

(b)

(c)

(d)
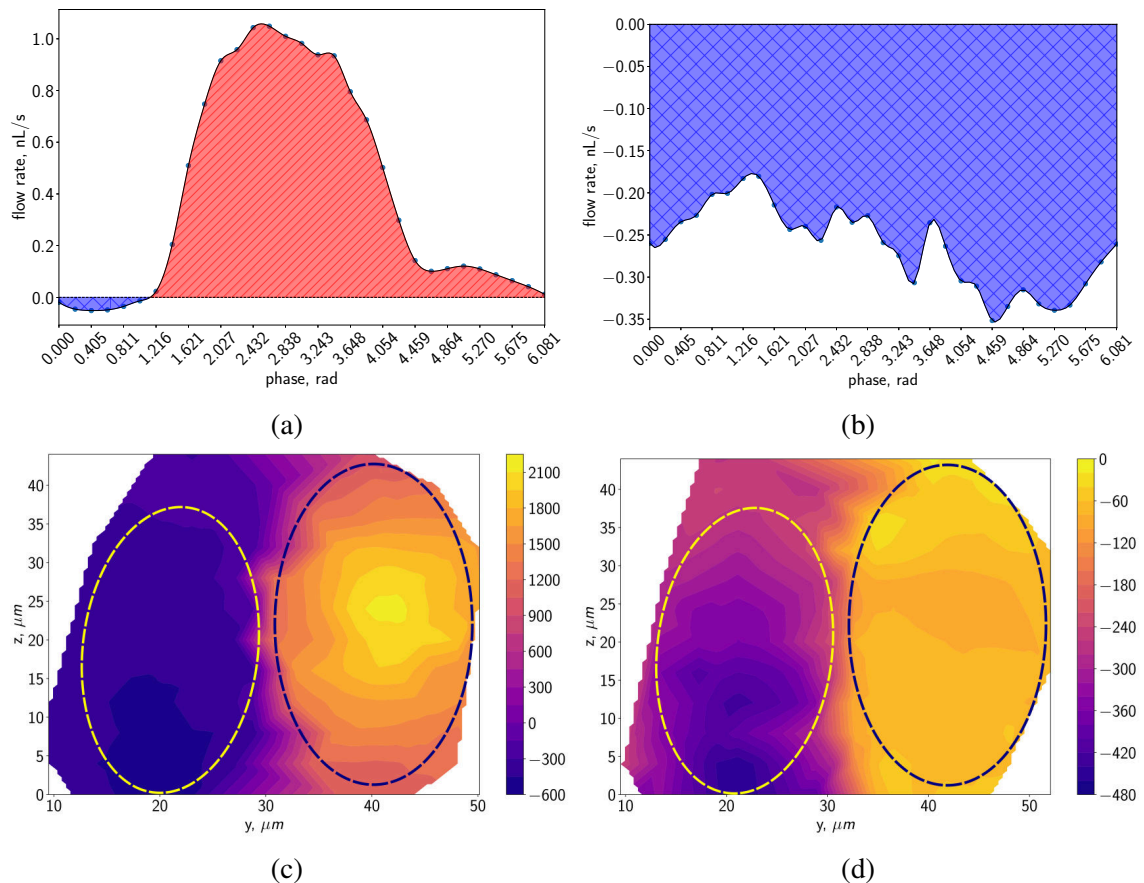
Fig. 4.6 Flow rate and instantaneous velocity of blood in the main vessels using fRBCs as tracers. Measurements of flow rate through a single plane in depth (i.e. plane perpendicular to the direction of the flow) of DA, (a), and CV, (b). These graphs reveal a pulsatile and a semi-constant flow through the respective vessels. The heatmaps (c,d) show the horizontal component of the velocity values when looking into the vessel (i.e. plane perpendicular to the flow) at phases 2.635 and 0.405 respectively. The estimated vessel locations are annotated with dashed lines. The CV is on the left of the heatmaps (always negative values) and the DA is on the right. Heatmaps have units of μm/s. Notice that the cross section of the vessels is not a perfect circle, but is closer to an ellipse. This is further illustrated in a 3D rendering shown in Figure 4.7.

Flow rate through a *yz*-plane, at a particular *x* position was calculated by integrating the *u*-component velocities over the cross-section of the DA and CV. Because the μPIV analysis was performed with 50 % small IW overlap, only non-overlapping area between IWs was used to integrate flow rate. This corresponded to $2 \times 4 \mu$m patch in the sample. It was found that the flow in DA is pulsatile, with a slight regurgitation (or backflow) phase Figure 4.6a. This regurgitation can be explained due to the lack of fully developed valves valves in the heart (discussed further in section 4.3). The largest absolute difference between the minimum and maximum flow rate through a chosen plane was found to be just over 1nL/s for the DA. Contrary to DA, the CV displays a weakly varying flow, with the peak difference of around 0.1 nL/s, see Figure 4.6b. There is no change in direction of the flow in the vein throughout the heartbeat. Heatmaps in Figure 4.6c and Figure 4.6d further
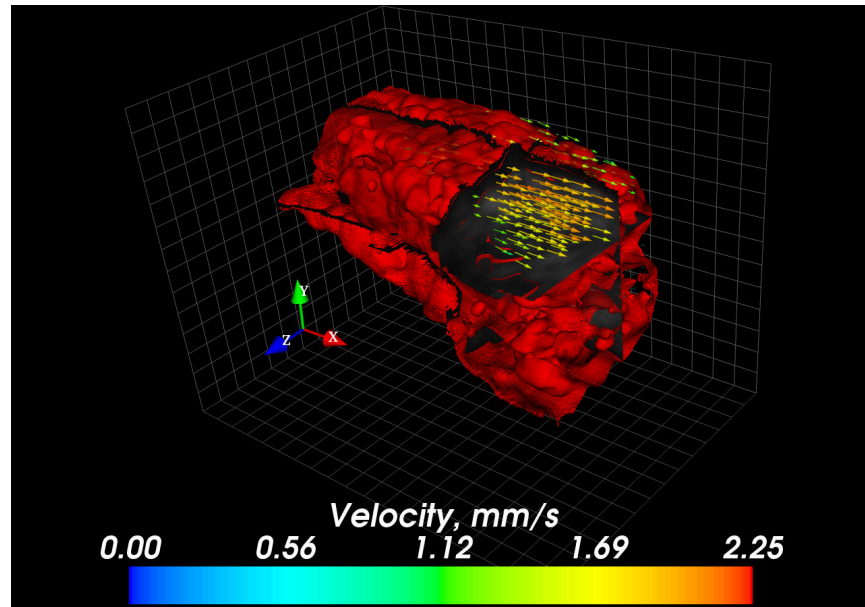
Fig. 4.7 3D cut-plane visualization of flow in the zebrafish blood vessels (same data as presented in 2D in Figure 4.4). Since flow in the blood vessels is not expected to have a significant out-of-plane motion component, the 3D2C μPIV analysis results can be considered as a good representation of the true motion of fRBCs. The DA is the top vessel, and CV is the bottom one, the tail is on the right of the image. Note that the blood vessels are slightly elliptical. Visualization created with Mayavi [4].

illustrate the horizontal velocity components passing through the blood vessels, at phases which correspond to the peak flow and regurgitation times in the DA. Note that there is a clear velocity separation between the two vessels, indicating that SPIM-μPIV analysis successfully resolved the boundary between the two vessels (also visible in Figure 4.4).

In general, using fRBCs as tracers provides a convenient way to image blood flow in the embryonic zebrafish. However, since PIV resolution is ultimately defined by the particle image size [126], if greater resolution is necessary to recover flow features of the plasma (which makes up more than 50 % of the total blood volume), introduction of artificial tracers is necessary, which is discussed in the next section.

4.2.2 Flow of beads in the main vessels

A transgenic line, Tg(flk1:GFP), zebrafish was microinjected with bead and Phosphate-buffered saline (PBS) mixture in the Common Cardinal Vein (CCV), as described at the begin of this chapter. 0.39 μm diameter fluorescent particles were used for injection. This size provided acceptable signal levels, and allowed more imaging time, as smaller beads tend to deposit to the vessel walls at a slower rate, than larger particles (such as 1.04 μm diameter beads tested but not shown here). It is worth noting that imaging time was observed to be closely related to the number of beads injected. Imaging blood with higher particle seeding density allows building up the necessary signal via correlation averaging sooner. On the other hand, there are more beads that deposit in the vessel walls immediately after injection,
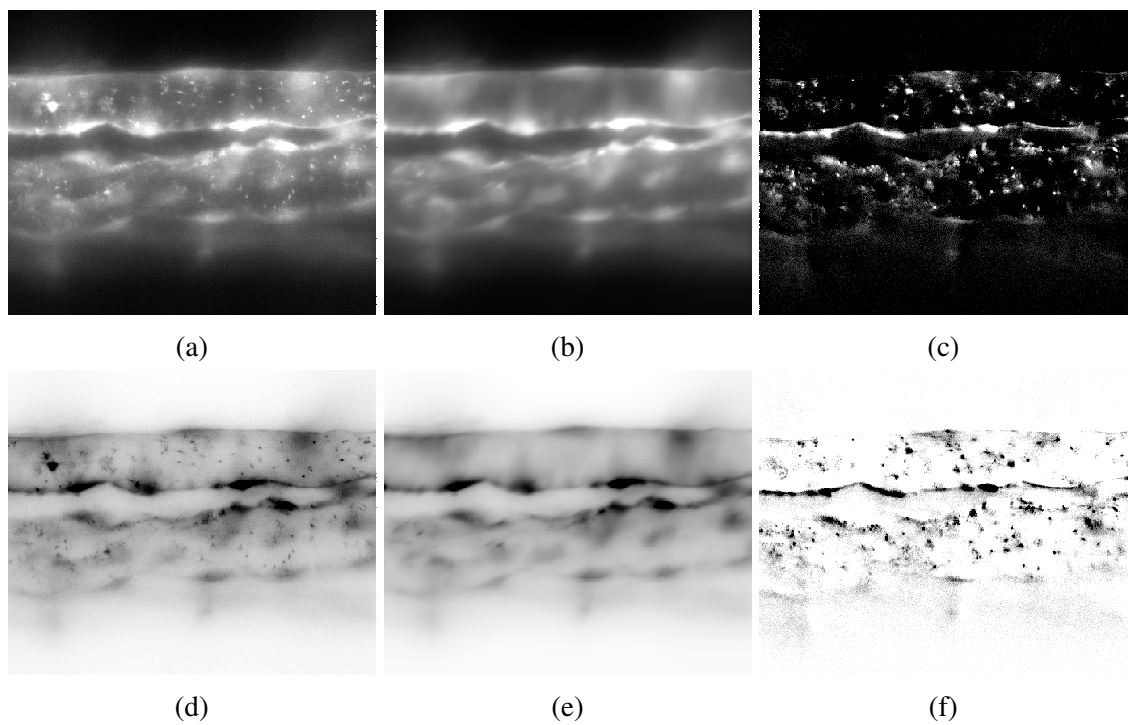
Fig. 4.8 Raw and filtered data of a zebrafish blood vessels with microinjected beads. The beads and the vessel wall are excited by the same wavelength, and their emission spectra is very similar. Therefore, both features are visible in the raw data, like shown in (a). Images averaged over time, shown in (b), are approximated to be static and can be used to remove most of the wall features. (c) The average-subtracted removes a significant amount of vessel fluorescence, and the remaining images with the vessel wall outline visible are sufficient for µPIV analysis. The bottom row shows the black-and-white inverted images of the top row, to aid comprehension of image features. The contrast of all images presented was enhanced.

distorting the illumination and imaging path, and potentially significantly disturbing the true flow pattern. The opposite is true when sparser particle seeding is used. However, correlation averaging needs to be performed for a longer time in order to artificially increase the effective number of beads. Therefore the imaging time and bead concentration balance must be carefully considered for a particular experiment.

The µPIV analysis presented here was carried out on a single plane data of blood vessels in the embryonic zebrafish. Since the sample was not scanned through the light sheet, more time could be spent imaging the single plane, which enabled the use of relatively low bead concentration. Since the injected beads had a similar excitation/emission spectra (*Dragon Green* 480/520nm), both the beads and vessels were visible, see Figure 4.8a. In order to increase the contrast of beads, the contribution of flk1:GFP signal in the inside of the blood vessels was minimised by taking the average image, Figure 4.8b and subtracting it from the raw images. Average image filter was used due to its simplicity. The filtered image, Figure 4.8c, preserved the outline of the vessels which acted as a useful landmark for qualitatively evaluating whether or not the flow dropped off to zero at the wall boundary.

Unlike the µPIV analysis results using fRBCs as flow tracers, the smaller size of the fluorescent beads allowed the use of IWs with smaller height, see Table 4.1. This meant that the flow features throughout the blood vessel, and particularly at the walls, could be resolved better. Indeed it was observed that flow profile of the beads approaches null velocity at the wall boundary, see Figure 4.9a. In general, the velocimetry results were found to be qualitatively successful - for most of the region the flow vectors are contained within the blood vessel boundaries (i.e. they follow the shape of the blood vessels). Furthermore, the recovered flow profile in time, through a line across the DA reveals a much more prominent change in the shape of the flow profile compared to the fRBC data.
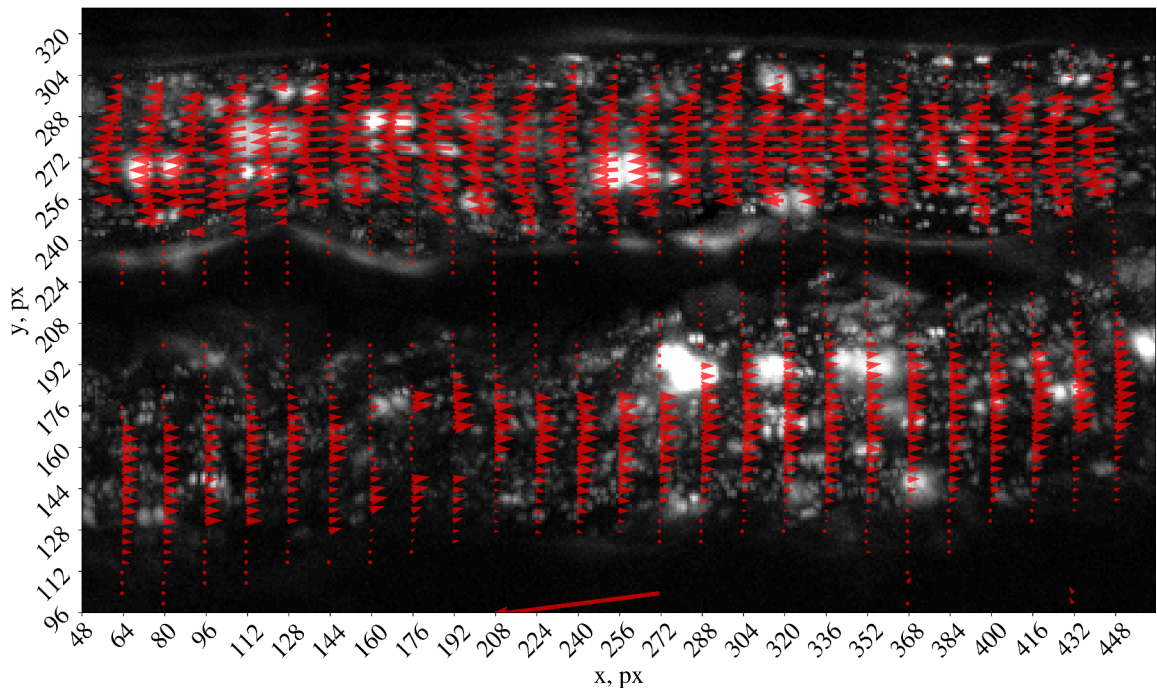
(a)
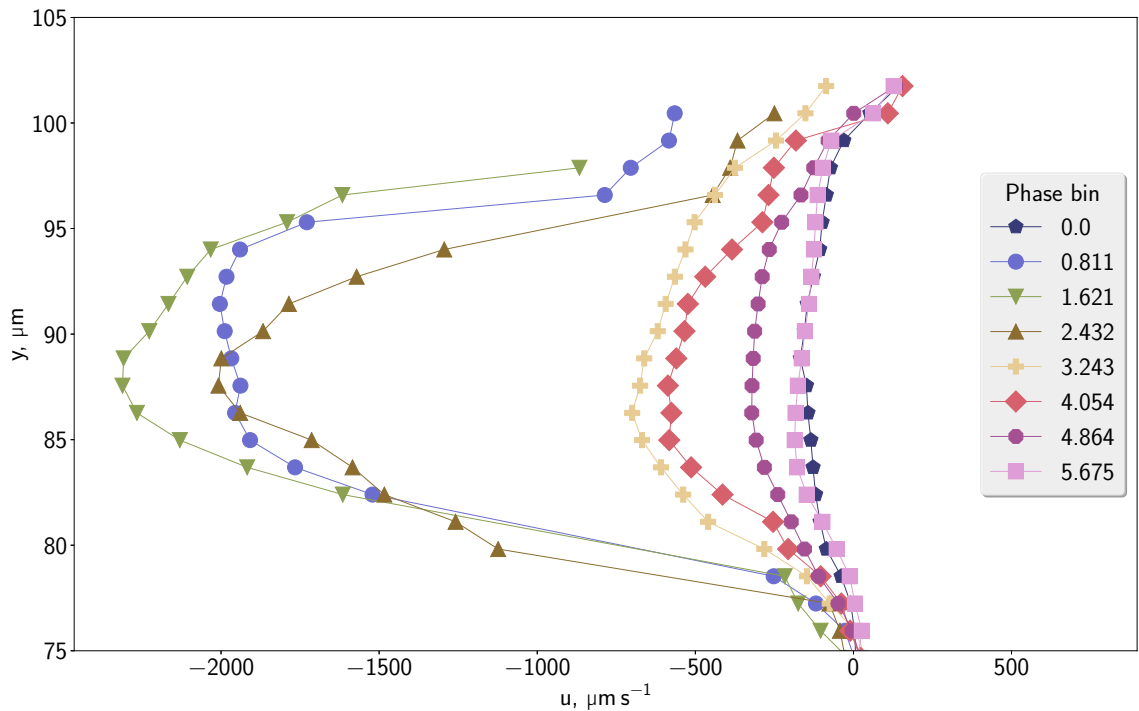
(b)

Fig. 4.9 Flow fields in the DA and CV in the zebrafish from µPIV analysis using fluorescent 0.39µm diameter beads as flow tracers. A single plane of velocity vectors overlaid no an MIP of the raw data at a particular phase, shown in (a). The DA is the top vessel, and CV is the bottom one, the tail is on the left of the image. Note the parabolic flow profiles - in general they approach zero velocities at the visible wall boundaries. The large bright blobs are aggregated beads, which likely formed after injection. (b) shows the time varying profile in the dorsal aorta at $x = 256$ for several phases. The profile has a more significant change of shape in time compared to fRBC results presented in Figure 4.5.

As a verification that the flow measurements are plausible, flow profiles at three adjacent 2D cross-sections (i.e. lines crossing a through 3 x-locations) of DA and CV were plotted for 4 different phase bins, illustrated in Figure 4.10. The purpose of this is to examine if there is a rapid change in flow profile over a small distance, which would not make physical sense in the flow conditions observed in the blood vessels. The horizontal spacing between these cross-sections were 5.16μm, and were centred on $x = 256$px, see Figure 4.9a for reference. Disregarding any small changes in the blood vessel geometry over the 10.32μm, it is expected that the flow profiles will be very similar. Indeed, this is in general the case as can be seen in Figure 4.10. The only exception might be at phase bin 4.054 for the CV, see right column, 2nd row from the bottom in Figure 4.10. This requires more investigation, however, raw data shows that a blob of aggregated beads passes through the region of one of the beads, which might have affected the correlation result significantly.
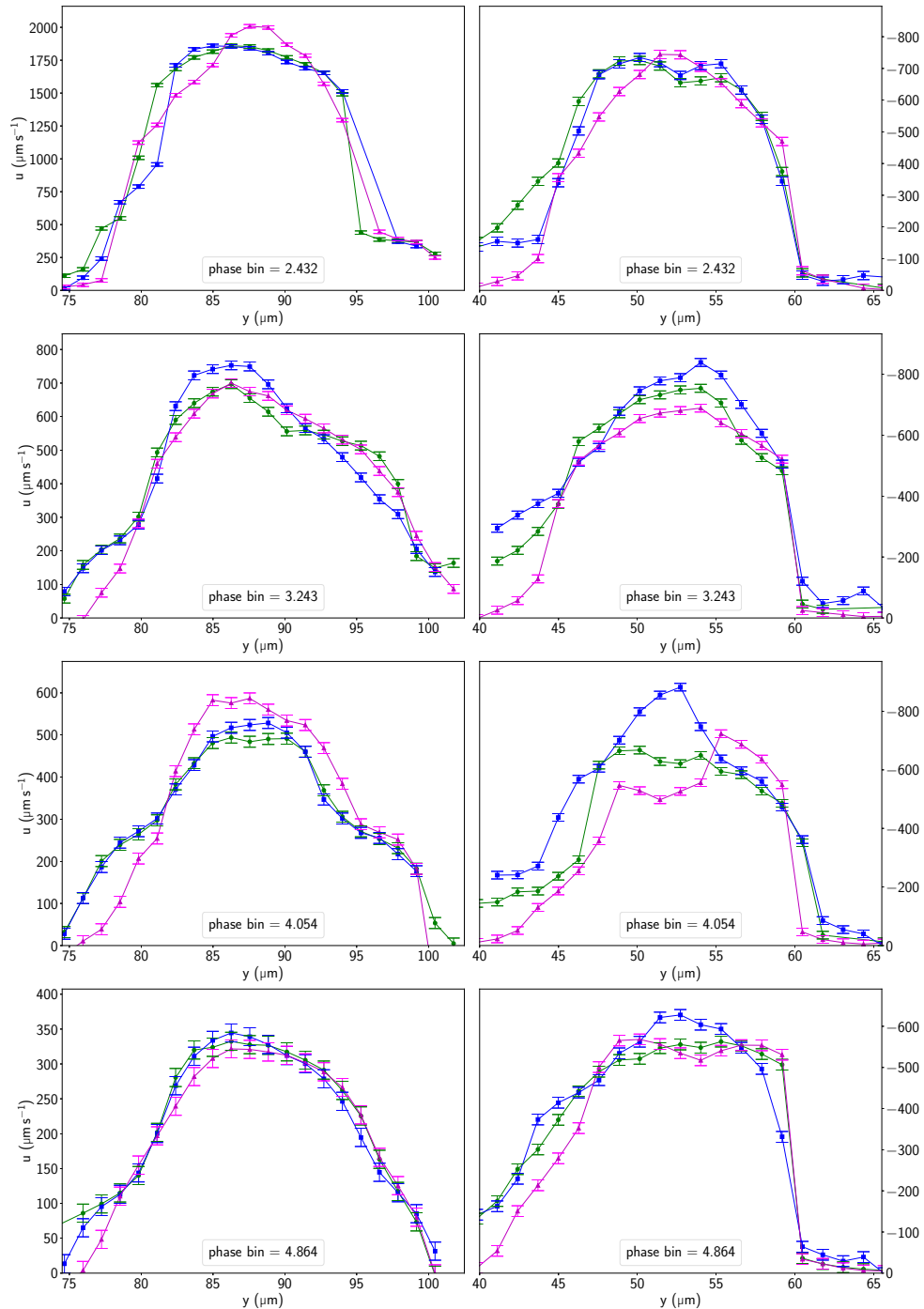
Fig. 4.10 Flow profiles of fluorescent beads in the DA and CV of a 4 day old zebrafish at four different phases. First column shows the *u*-component velocity in the at three nearby *x* coordinates, centred on $x = 256$ pixels at the DA, see Figure 4.9a. Column on the right displays the same, but for the CV. Since the data is from locations spaced closely along the length of the vessels, little variation is expected in the 3 profiles. Note that unlike the flow profiles for fRBC measurements, shown in Figure 4.5, velocity rapidly drops off to zero at the vessel walls. Note, the velocity magnitudes had a $\pm$ sign swap for easier comparison to fRBC flow profiles. The *y*-scale is varying (increasing from top to bottom) in order to show the details of each profile better. Moreover, the *x*-axis does not start at zero on the left column, as these correspond to the location in the full FOV, as shown in Figure 4.9. Error bars correspond to 0.1 pixel which represents the maximum subpixel fitting uncertainty.

The results presented in this section suggest that using injected beads yields better spatial resolution, particularly near the walls. However, this might not necessarily mean that fRBC measurements are inferior. In fact, it can be reasoned that different *flows* are imaged (i.e. flow of fRBCs and flow of plasma mapped by small tracer particles). To gain a better insight in the reasons for these differences, the flow properties of individual tracer particles will be explained in the following sections.

4.2.3   Flow of individual red blood cells

The most obvious difference between microspheres and fRBCs is their shape and size. The fRBC can be approximated as a disk of $\approx 2.5 \times 6.5\,\mu m$. Unlike spherical particles, fRBCs can be seen tumbling as they flow through the vessel, see Figure 4.11 for an example. On the other hand, they also tend towards a preferred orientation where they are aligned length-wise with the direction of the flow [158]. It appears that the fRBCs somewhat stabilize in that orientation (i.e. are less likely to tumble). It is important to consider this tumbling, because if the change in orientation of the fRBCs would be significant between successive frames, this could potentially diminish the correlation peak of the true underlying flow. Recall that the CC peak of the true motion diminishes with increasing shear (see chapter 2). To investigate the fRBC motion in more detail, 3 individual cells were captured in 7 successive frames were annotated as shown in Figure 4.11. The blood cell annotated in solid magenta line undergoes almost a 90 deg rotation between time t_0 and t_3. On the other hand, there appears to be no tumbling between a frame pair, as can be seen in pairs (t_0 to t_3). In fact, in experiments carried out in this work, the degree of tumbling in a single frame pair was not observed to be large enough to have detrimental effects on the CC results.

However, the tumbling can have an effect on the theoretical single-particle resolution. If the fRBCs were always aligned with the flow, the smallest IW height[2] , would be the width of the fRBC. However, if the fRBC is perpendicular to the flow, then the minimum IW size would be the length of the fRBC. However, if there truly is a preferential orientation of the fRBCs, performing correlation averaging for an extended period of time, should allow the use of IW with the height of the same dimension as the fRBC width. In practice this tumbling means that velocity vector for each IW is a spatial average across the height.

Another clear difference between fRBC and beads, is that the amount of fluorescence from fRBCs varies significantly, as can be seen in Figure 4.11. Recall that standard algorithms to calculate CC rely on intensity product, and can be biased towards very bright features, rather than the correct flow pattern, as explained in chapter 2. This brightness variation in the fRBC fluorescence, combined with their large size[3] is the main reason for the use of SAD algorithm for µPIV analysis when erythrocytes are used as tracer particles. Moreover, even though small fluorescent beads were used for injections, the bright regions

---

[2]The IW height here is the size along the diameter of the vessel in the example considered in Figure 4.4.
[3]Recall the error analysis of synthetic images with varying bead diameter in chapter 2.
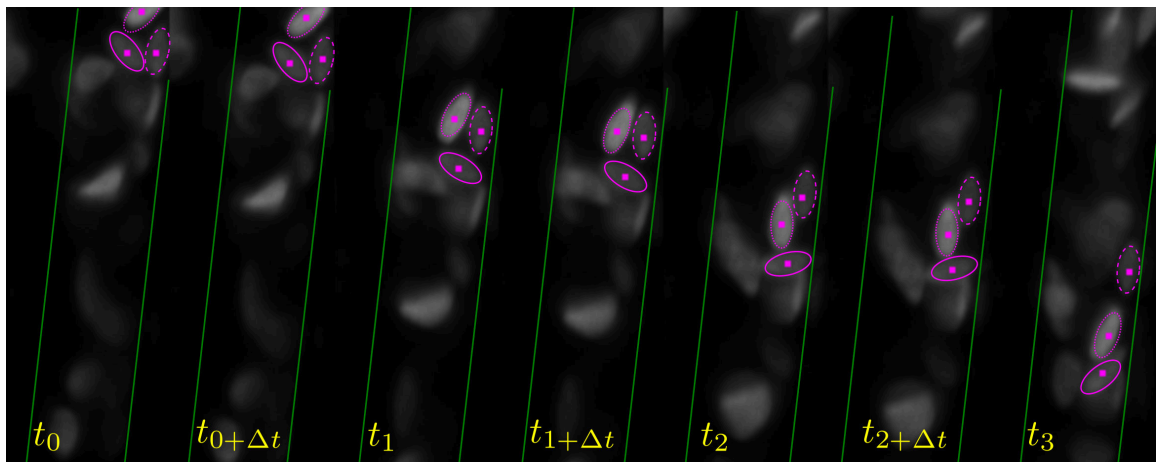
Fig. 4.11 Flow of red blood cells in a zebrafish blood vessel imaged with SPIM. The approximate shape of three different fRBCs are annotated with dashed, solid, and dotted magenta coloured lines. The green lines gives a rough outline of the vessel walls. The images are shown from different times, where Δt indicates the second image in a frame pair taken after a small time increment (recall the "PIV mode" data acquisition explained in chapter 2). The blood cells do not noticeably change their orientation in the frame pair (ant t and $t + \Delta t$ pair). On the other hand, a clear change in orientation can be seen between several separate frame pairs (for example, compare t_0 and t_2 pairs). Also note that the blood cell at the periphery has the lowest velocity, as expected for a flow in a tube approaching the walls (the flow profile will be revisited later in this chapter). The preferential alignment of blood cells with the flow can be seen in t_1 and t_2 image pairs, where 2 out of 3 annotated cells remain oriented in the direction of the flow. Notice that the fRBCs naturally differ in fluorescence intensity and size.

at the walls could again bias the Fast Fourier Transform Cross Correlation (FFTCC) results towards these regions. Therefore, SAD algorithm was used here as well to mitigate this, despite having slightly higher bias and random error for synthetic images with no such features.

4.2.4 Direct comparison between fRBC and bead flow

It was already shown that using fRBCs and fluorescent microspheres as tracer particles yields a different profile shape of the flow in zebrafish blood vessels. The intuitive and straightforward explanation for this would be simply the size difference between cells and beads. However, it is also possible that beads flow differently to cells due to their shape, density, or surface charge. In order to explore the differences in flow between the two tracers, their flow in the blood vessels were imaged simultaneously, using the same camera sensor.

This concurrent imaging was facilitated by the large emission tail of the *Dragon Green* fluorescent dye spectrum of the beads, and the wide dsRed emission spectrum of the fRBCs. The overlap between the two spectra meant that it was possible to excite both fluorophores using 488 nm light, yields sufficient signal for imaging through a 607 nm emission filter. A very small concentration of beads was injected using the aforementioned procedure to minimise any influence on the motion of fRBCs. By taking the sum of all images in time, an estimation of the inner blood vessel region was made. An outline of this region was overlaid on the images of beads and fRBCs, which are shown in intensity inverted form in Figure 4.12. 4 different image pairs were selected with a different combination of bead and cell position across the vessel.

The beads tend to follow the theoretical parabolic profile quite well, as shown in A2 and C2 in Figure 4.12. It can also be seen in B and C pairs, that beads can flow very close to the wall, where the flow is very low. In general, fRBCs were not observed to flow at such low velocities near the wall. This can be understood by considering the cross-section of the fRBC perpendicular to the flow direction, and the rate of change of velocity across the vessel. Because the velocity changes very quickly [4] over a small length segment near the wall (increasing towards the centre), different parts of the fRBC will be affected by different velocities. Because the cross-sectional area of the fRBC is relatively large compared to the vessel diameter (which is around $20 - 40\,\mu m$ in the semi-minor/major axis of an elliptical vessel), it is not possible to resolve the velocity profile variations in the plasma in the same way, that the smaller, $0.4\,\mu m$ diameter beads allow.

Furthermore, consider the case when the fRBC is oriented with its length perpendicular to the direction of the flow, approximately in the centre of the blood vessel, as shown in the bottom of pair C in Figure 4.12. Because the cross-sectional area of the fRBC which is affected by the fluid forces is much larger, the velocity measured would be significantly

---

[4]Recall the definition of Wall Shear Stress (WSS) in chapter 1
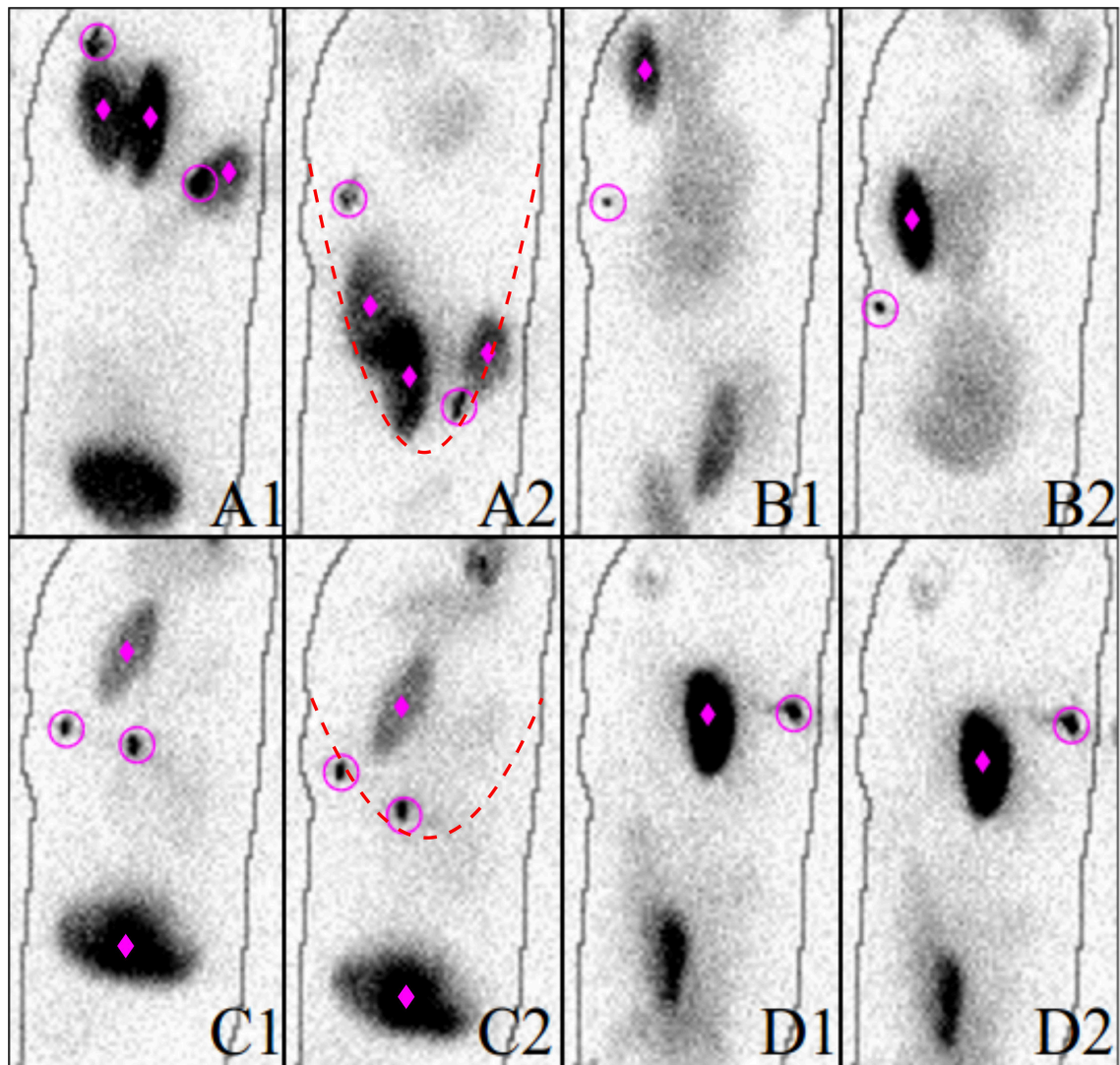
Fig. 4.12 Comparison between simultaneously imaged flow of beads and blood cells. Black and white inversion was used to aid comprehension. The approximate location of vessel wall is indicated by the gray curves. Bead images are annotated with a magenta circle, and the approximate centre of fRBCs are marked with a magenta diamond. Letters indicate a time sequential image pair. Beads can be observed flowing closer to the vessel walls compared to fRBCs, and hence much slower. The reason fRBCs do not flow at such velocities are discussed in the main text. When fRBCs are aligned with the direction of the flow, they predict the parabolic flow profile reasonably well, as can be best seen in A and B image pairs. However, when the fRBCs are facing perpendicular to the flow, their cross-section extends over a much larger fraction of the parabolic flow profile. This means, that the velocity will be averaged along the length of the fRBC. For example, the fRBC at the bottom of C1 measures the velocity to be 17.7% lower than the bead above it.

lower compared to a bead at the same location. In addition to this, recall that the equation for the lag velocity, Equation 2.1, depends on the square of the particle diameter, and the difference of particle and fluid densities. The diameter dependency implies that the drag force is much higher on an fRBC than on a much smaller fluorescent bead. Recall that in chapter 2 the worst-case scenario lag for an fRBC was found to be $\approx 0.264\,\mu m/s$, while it was only $\approx 5 \times 10^{-4}\,\mu m/s$ for the fluorescent bead.

As far as density is concerned, it is unclear what the value is for plasma or red blood cells in the zebrafish, despite the efforts in literature review. However, since the blood cell size, and the blood cell to plasma ratio in the zebrafish is similar to that of human (see [159]), it can be very crudely approximated that the fRBC and plasma densities will be similar. That is assuming that the blood cell density is around $1.1\,g/ml$ [108], and that blood plasma density is close to $1.025\,g/ml$ [160], implies that the density of polystyrene beads ($1.05\,g/ml$) should be better suited than fRBCs for measuring the motion of plasma.

However, it is important to consider the fact that simply because the flow profiles recovered with fRBCs are different, does not invalidate the measurements of *blood cell* flow. In other words, the motion of the fRBC is measured to the accuracy of the SAD and subpixel fitting algorithms The fRBCs are simply expected to flow differently, due to aforementioned reasons. If on the other hand, precise information about the motion of the blood *plasma* is necessary particularly at the vessel walls, smaller tracer particles are necessary. In the ideal case, such particles should be endogenous, such as fluorescent thrombocytes for example. As a final note, if wall information is available, then it is should be possible to interpolate the flow pattern of plasma using fRBC information.

4.2.5 Possible extensions to these experiments

The experiments explained previously are not an exhaustive exploration of the flow features in the blood vessels in the zebrafish embryo, and could be improved and/or extended. Here potential next steps are summarised.

- Since the flow in the main blood vessels was approximated as a simple laminar flow in a tube, a comment was made in Figure 4.7, that due to the expected lack of any significant Out-of-Plane Motion (OOPM), the recovered 3D2C flow profiles should be a good representation of the true 3D flow profile. However, verification of this fact was not done due to lack of time, but a suggested first step would be to acquire a *z*-scan of the blood vessels at two (or more) different orientations, and comparing the measured velocities (or the flow rates through a plane).

- The obvious next step for measurements with fluorescent beads would be to extend them with depth-sectioned data. Due to deposition issues there are several possible solutions. a) Use of relatively sparse *z*-scanning to minimise acquisition time, and the use of interpolation techniques to recover the missing data, b) use of a system capable

of rapidly scanning the light sheet through the sample (such as SCAPE microscopy [161]) or one capable of extending the detection volume through wavefront-coding techniques [162], or c) by investigating the use of much smaller particles, such as quantum dots (recall that Brownian motion effects can be handled with the use of correlation averaging chapter 2).

- The artefacts remaining in the microinjected data after filtering were mostly ignored, as SAD was generally found to be robust against such features. However, improving the post-processing could benefit the analysis by enabling the use of FFTCC, which yielded motion estimation with less random error and bias chapter 2. This becomes particularly if quantum dots are used. One example of an alternative filter would be the use of standard deviation filtering. Using this method, the highest standard deviation in the images would be in locations of the highest change in pixel values (namely, where the beads flow).

- Finally, the analysis with microinjected beads was limited to a 3 day old zebrafish, as it becomes increasingly challenging to perform injections in older fish. If high spatial resolution information on the motion of blood plasma was necessary, transgenic lines expressing fluorescence in smaller cells such as thrombocytes should be sought.

4.2.6   Conclusion

The main goal of this section was a proof-of-concept validation that SPIM-µPIV can be used in an *in vivo* setting. The flow fields recovered using fRBCs, and fluorescent beads were both qualitatively (smooth and continuous) and quantitatively (peak velocity lower than in the heart) sound. This strongly suggests that it is indeed possible to measure flows in a living organism using SPIM-µPIV.

Moreover, the differences between velocity information recovered using the two tracer particle types, was investigated further by considering the motion of *individual* particles. It was concluded that there is no fundamental flaw in either of the measurements, but the differences arise simply due to genuine difference in the way these particles flow in the blood vessels. This also suggested the tracer choice depends on the question the experimenter is interested.

For example, if high resolution information of the flow of plasma at the walls is required, artificial tracer particles could be used. On the other hand, using endogenous fRBCs provide the advantage of a non-invasive measurement, at the cost of somewhat lower spatial resolution.

This section described the crucial validation experiments, which were necessary in order to confidently carry out the final, and most important experiments of the whole of this thesis described in the next section.

4.3 Blood flow in the zebrafish heart

The previous experiments described were performed in a relatively simple system: the fluid flow pattern is well predicted in tube-like vessels, and even conventional widefield microscopy can provide reasonable flow estimation [146]. That is, by assuming circular symmetry (i.e. approximating the vessel as a tube), the 2D projection of the flow in the centre of a vessel provided by widefield microscopy, is sufficient to extrapolate the volumetric flow profile (of course effects of Depth of Correlation (DOC) have to be taken into account). The heart, on the other hand, has a more much more complex structure and function compared to the blood vessels. And any approximations of the heart structure (i.e. assuming a sphere/ellipsoid) can be expected to have a significant negative impact on the estimation of the volumetric flow features. Recall that at 3 days old, the zebrafish heart already has multiple chambers with developing valves in between, along with complicated inner wall structure Figure 1.1.

However, the most severe layer of complexity is the highly dynamic nature of the heart. The full heartbeat frequency of 2-3 times per seconds, puts a significant demand on temporal resolution necessary to reconstruct motion at peak contraction of the heart. This rapid change in shape of the heart also implies a need for highly accurate phase retrieval in order to facilitate meaningful correlation averaging for blood flow measurements. In this section, by relying on the theory, and experimental validations presented in chapter 2 and chapter 3 as well as in the previous section, the most important novel results of the whole of this thesis - 4D blood flow measurements in the zebrafish heart using light sheet microscopy.

4.3.1 3D2C blood flow measurements

This section will demonstrate *z*-resolved blood flow measurements in the zebrafish heart between days 3 and 5 of its development. This age range is interesting because the heart begins to develop its heart valves at day 3, which fully mature at day 5. By acquiring depth-resolved flow information, it is possible to investigate how the amount of flow pumped in a heartbeat changes, as the valves grow. Moreover, at this age range, the heart "shifts" toward the surface of the torso of the fish, which means that the path that the excitation/emission light has to pass through becomes less, hence the expected light scattering is decreased (recall Figure 1.1, and Figure 4.3), which yields better image quality.

The data acquisition for results obtained here were performed in a similar fashion to the blood vessel imaging experiments, and the considerations for sample handling and imaging were discussed at the beginning of this chapter. The key difference between imaging different ages, was that the Brightfield (BF) data for the 3 days post fertilization (dpf) fish was obtained using a BF which relied on a continuously refocusing lens (configuration A in Figure 2.16), whereas BF information for the 4 and 5 dpf was obtained by imaging through the launch objective (configuration B in Figure 2.16). This was simply done as a refinement

Parameter	3 dpf	4 dpf	5 dpf
Laser pulse length, ms	1	0.5	0.25
Inter-pulse time, ms	1.5	0.5	0.25
z-step, µm	8	4	4
Effective magnification	20×	10×	10×
Camera pixel binning	2×2	1×1	1×1
Frame pairs per z-step	≈ 50	≈ 75	≈ 90
Small IW (LxH), pixel	24×24	16×16	16×16
Big IW (LxH), pixel	72×48	64×64	64×48
Peak-to-peak threshold	1.07	1.05	1.07
Mask around peak	7×7	7×7	7×7

Table 4.2 µPIV analysis parameters used for the recovery of depth and time-resolved blood flow measurements in 3, 4, and 5 dpf zebrafish hearts. Increased number of pairs in 4 and 5 dpf datasets permitted using somewhat smaller IWs.

of the system and either method would work (i.e. we are not suggesting that different BF imaging method should be used for different ages).

Another difference was the Fluorescence (FLR) cameras used: the 3 dpf zebrafish heart was imaged using a *QImaging QiClick* camera, while the 4 and 5 dpf fish were imaged using a high-speed *Andor Zyla* camera. The essential difference here was the higher temporal "sampling" density facilitated by the *Zyla* camera (the advantages of this will become apparent later in the text). The parameters used in the micro Particle Image Velocimetry (µPIV) analysis of the blood flow in the differently aged zebrafish hearts are summarised in Table 4.2.

In the remainder of this section, qualitative overview of µPIV measurements in each fish will be provided, before analysing quantitative features such as flow rate through a cross-section of the heart.

Blood flow in the atrium of a 3 day old zebrafish   The orientation and position of the heart in a 3 day old zebrafish makes the atrium a good target for imaging blood flow. In addition to this, the atrium has a less complex geometry compared the ventricle (no trabeculae, as shown in Figure 1.1). Moreover, the lack of fully formed valves, particularly at the Sinus Venosus (SV) junction, suggests that a less drastic peak blood acceleration is likely to be observed. This is because when the valves are matured and functioning, they isolate different chambers at different phases in the cardiac cycle by rapidly opening and closing. If there is no valve, the flow pressure does not build up as much. Furthermore, at this age the junction between the atrium and SV is rather large. From simple conservation of mass arguments, if the there is no significant cross-sectional area difference between two fluid vessels, there will be little change in the velocities moving from one vessel to another (in this case these vessels are the atrium and SV).
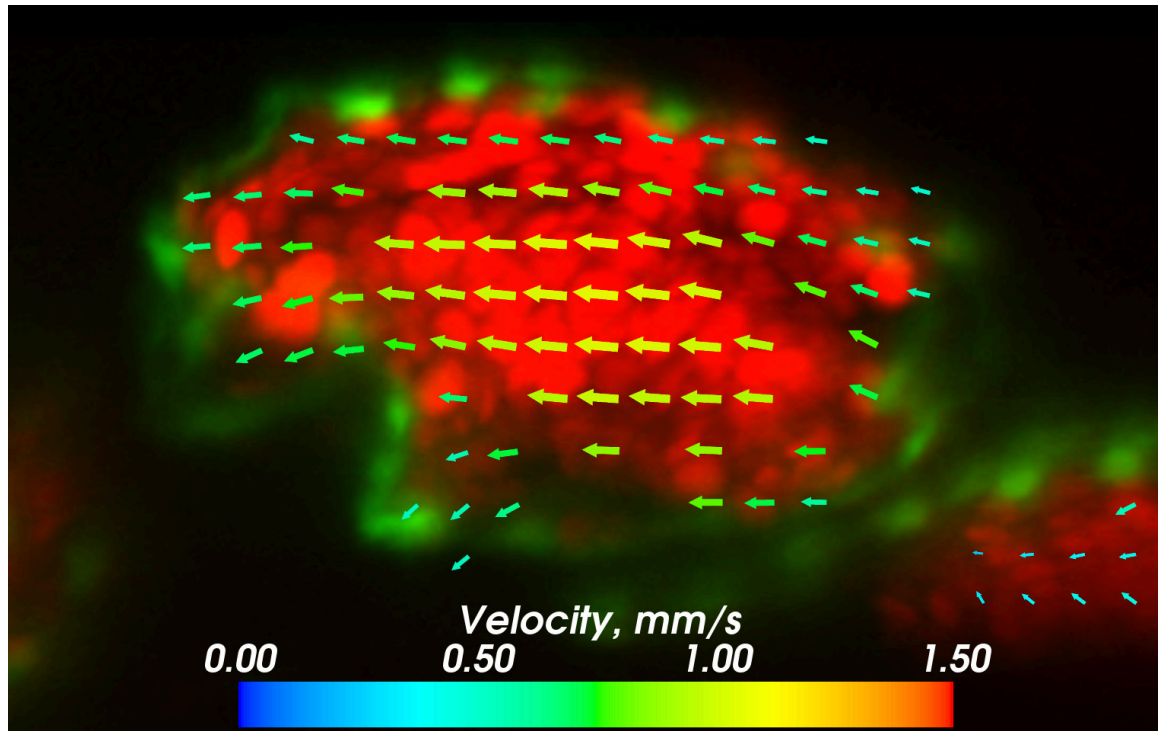
Fig. 4.13 Single plane flow field in the zebrafish atrium recovered with SPIM-µPIV. The velocity vectors are scaled to the square root of their magnitude and overlaid over an MIP of fRBC images (in red) and the inner heart wall (endocardial cells in green). Some vectors rejected due to not passing a strict p2p thresholding, however, could be easily filled in using basic interpolation approaches. Visualization created with Mayavi [4]. Figure as published in [135].

In essence, this means that the dynamic range of the velocities should be lower than in the hearts of older fish. This means that less of a compromise is needed between choosing which velocities are better temporally resolved: recall the discussion on the choice of Inter-Pulse Time (IPT) and Laser Pulse Length (LPL) in chapter 2 (see also Figure 2.17). Smaller IPT can resolve high velocities (e.g. at peak systole of the heart), but cannot resolve relatively slow flow (e.g. mid diastole), and the measurements would indicate no motion at all. Figure 4.13 shows a single plane of SPIM -µPIV measurements of blood flow (fRBCs shown in red) in the atrium, with the image of a heart wall (shown in green) overlaid. The rejected vectors were not replaced, to reveal the number of vectors which did not pass the p2p threshold. Very few such vectors exist, and as can be seen from the smoothness for the vector field, they could be easily interpolated from surrounding IWs. Note that the velocities are highest in the centre of the heart, and reduce towards the wall. This is expected due to no-slip boundary assumption, and hence the results appear qualitatively reasonable. The accompanying Figure 4.14 illustrates the full depth-resolved measurements in a 3D rendering, where the atrium and the ventricle is annotated with A and V respectively. Notice the blood enters the atrium from the SV through a large cross-sectional area, as described previously.
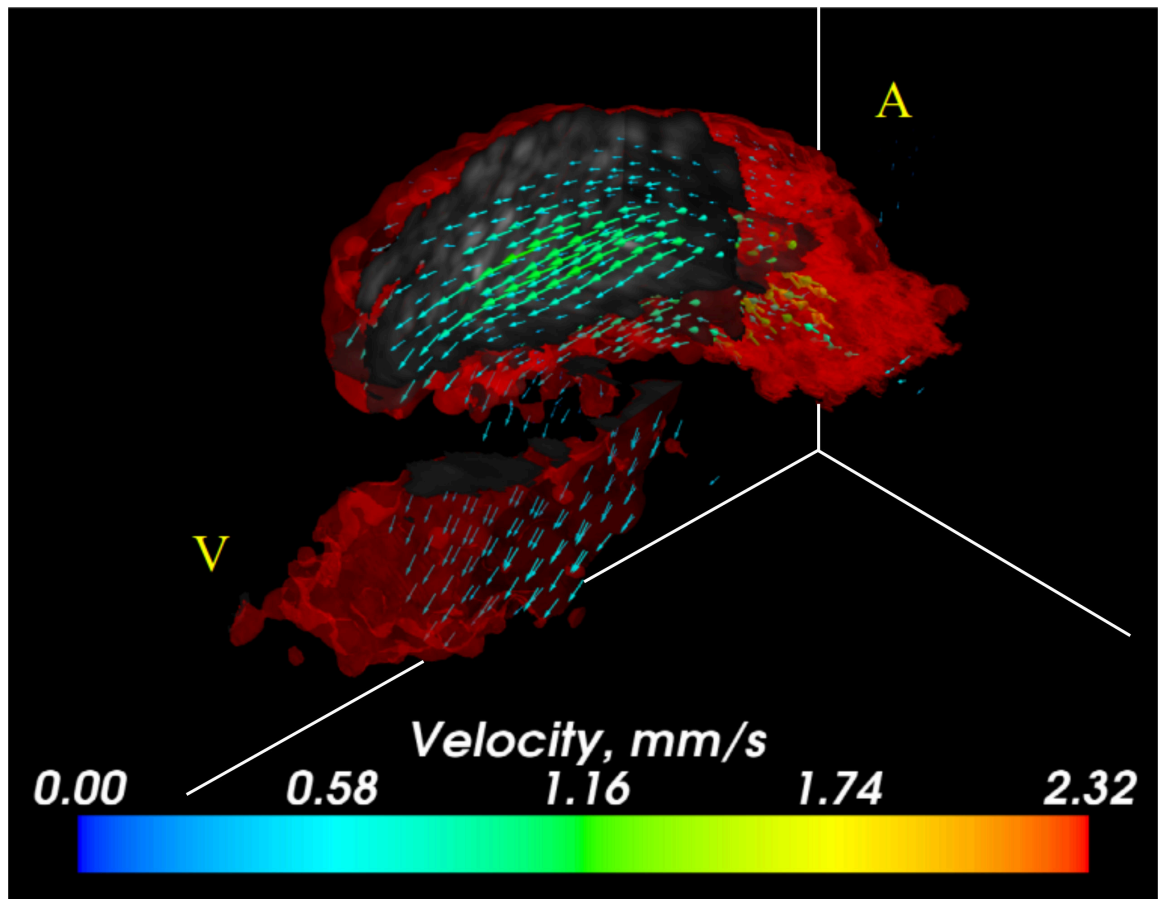
Fig. 4.14 Depth-resolved flow measurements in a 3 day old zebrafish heart. A cut-plane visualization of the same heart at a different phase to that shown in Figure 4.13. The atrium is annotated with A, and the partially captured ventricle with V. The size of Atrium-SV junction is significantly larger than the developing A-V valve in the 3 day old zebrafish and does not yet have a fully functioning closing mechanism. This means that blood regurgitation from the atrium to the SV can be significant at this age. Vectors are scaled to the square root of their magnitude to reveal the large dynamic range of velocity values. Visualization created with Mayavi [4]. Figure as published in [163].
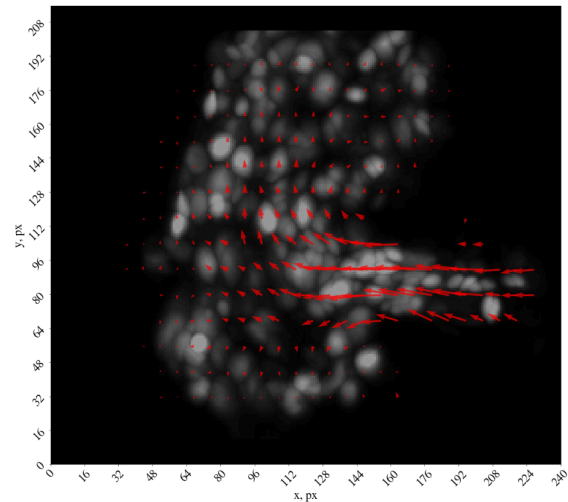
(a)
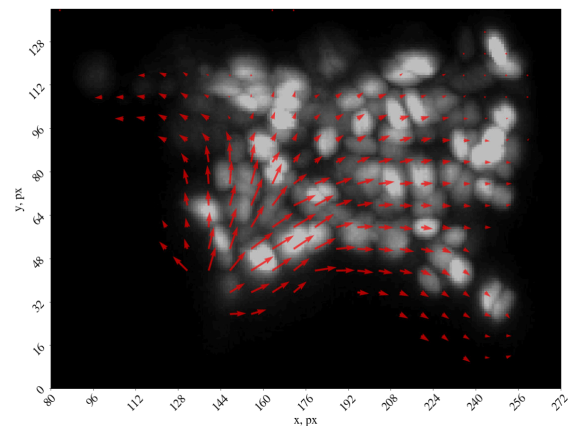
(b)

Fig. 4.15 Blood flow measurement in ad 4 and 5 day old zebrafish hearts. Single plane μPIV measurements overlaid on an MIP of the SPIM images of fRBCs in a single phase bin. The force exerted by the fast moving blood rushing through the AV valve is proposed to play a significant role in the formation of the trabeculae, since trabeculation is expressed most strongly in the ventricle on the wall facing the AV valve [164, 165].

Blood flow in the ventricle of a 4 day old zebrafish   In contrast to the 3 day old fish, from day 4 onwards, the ventricle (a long with the bulbus arteriosus) is generally the preferred target to image due to optical access. At this time, the valves begin to perform significantly better than in the 3 day old fish. However, by this stage the trabeculae have developed significantly, which contribute to a somewhat more complex flow features at the wall. For example, fRBCs can be seen occasionally getting stuck in the trabeculae for several heartbeats. Such cells can affect the flow measurements at the heart wall, if the correlation averaging is not performed sufficiently long, or if the semi-stationary cell is the major feature throughout the imaging time at a particular plane of the heart. Single plane velocity field is illustrated in Figure 4.15a.

Age, dpf	Pumped, nL/s	Regurgitated, nL/s	Net, nL/s
3	0.34	0.101	0.239
4^A	0.74	0.004	0.736
4^B	0.62	0.019	0.601
5^A	0.443	0.005	0.438
5^B	0.361	0.018	0.362

Table 4.3 Flow rate through a plane in a heart chamber of different aged fish. The superscripts *A,B* represent data obtained at different orientation. Before the valve formation there is a significant amount of flow which is regurgitated ($\approx$30%). A different fish was imaged at each age, with different µPIV analysis parameters, therefore the results should not be interpreted as a generalization of flow properties. Moreover, the flow rate analysis in the 3 day old fish was performed in the atrium, as opposed to the ventricle as in the older fish. However, net flow measurement should not be affected by this. The flow rate was estimated by using a simple "area under the curve" calculation using Trapezium rule.

Blood flow in the ventricle of a 5 day old zebrafish   At first glance, the flow features in the 5 day old fish, shown in Figure 4.15b, do not appear to differ from the 4 day old fish. This is not unexpected, as by day 4 the fish has undergone the most significant structural changes. However, we observed that as the fish age, the number of strongly fluorescing cells, as well as general signal level from other cells, increases. Furthermore the yolk sac of the fish is near depletion, which means somewhat less tissue around the heart, and hence the expected light scattering should be less. Single plane velocity field is illustrated in Figure 4.15a.

4.3.2   Pumping performance

Depth-sectioned velocimetry results enable inspection of the heart pumping performance quantitatively by calculating the flow rate through a cross-section in the heart. This is achieved by integrating the flow through each IW through an area perpendicular to the main direction of the flow, in much the same way as described in flow rate measurements in the blood vessels, earlier in this chapter. Note that similarly, the area of overlap between small IWs was excluded, in order to avoid summing the same values multiple times.

3 day old heart   Because of the lack of fully functioning valves, about one third of the blood passing through the 3 dpf atrium, is regurgitated (i.e. pushed back into the SV) Figure 4.16. This is substantially more compared to the results in the ventricles of 4 and 5 dpf, summarised in Table 4.3. The peak flow rate through a cross-section of the atrium is also noticeably lower than in the older fish. This could be attributed to the large atrium-SV junction, discussed in the previous section. The two positive flow rate peaks correspond to the filling of the atrium (blood flowing in from the SV) and ejection of blood from the atrium to the ventricle.
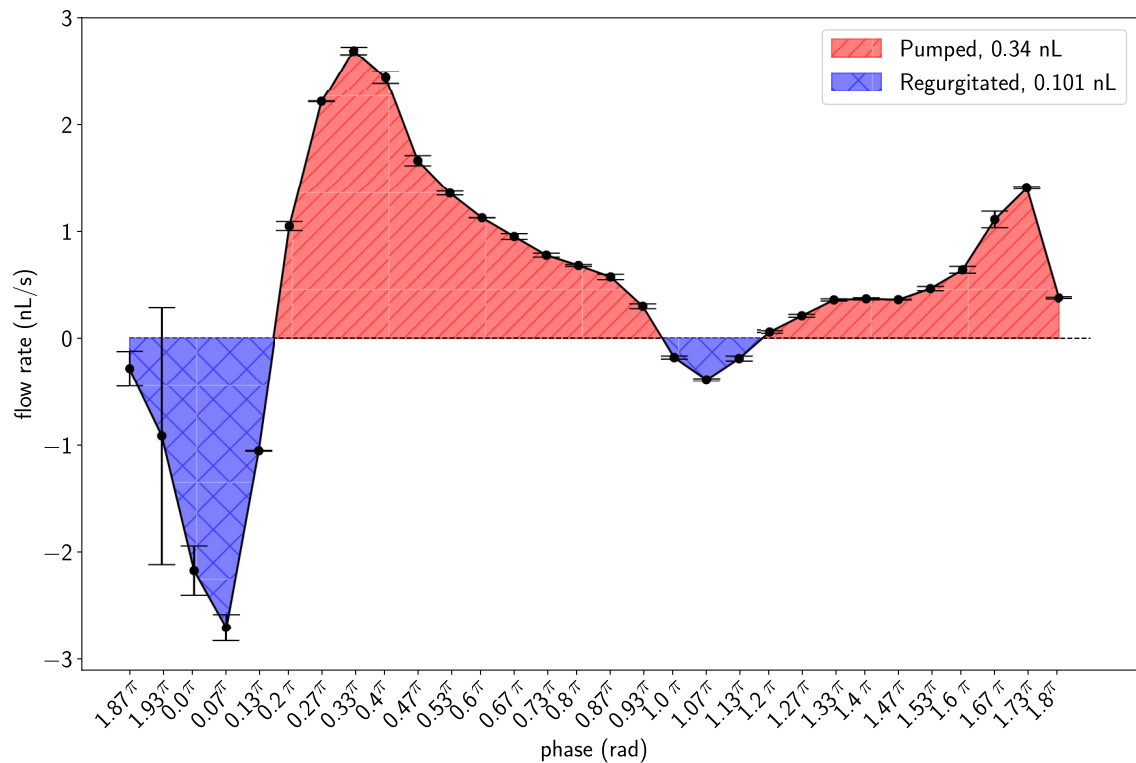
Fig. 4.16 Flow rate through a plane in the atrium of a 3 day old zebrafish heart. Due to the a lack of fully formed and functioning heart valves, a large fraction of blood (phases 1.87π-0.13π), is regurgitated back to the SV from the atrium. Note that the significantly large error at phase 1.93π coincides with the full contraction of the atrium. During this phase, very few, extremely fast fRBCs pass through the atrium. This error could be mitigated by increasing the imaging time or improving the temporal resolution.

4 and 5 day old heart   Compared to a 3 dpf fish, the peak flow rate increases substantially in a 4 dpf zebrafish ventricle, as shown in Figure 4.17. This can be attributed to the maturing cardiac muscle, as well improvement in the valve efficiency. Notice that there exists a small amount of regurgitation - this was found to be constrained in a single chamber, where the blood cells are slightly displaced by the valves closing without mixing with other chambers. That is, at the moment the valve through which the blood was flowing closes, a small pressure difference is created which affects the fRBCs nearby. These fRBCs then appear to move backwards through the cross-section of interest. Again, the key point here is that unlike in the 3 day old fish, the blood does not mix between chambers.
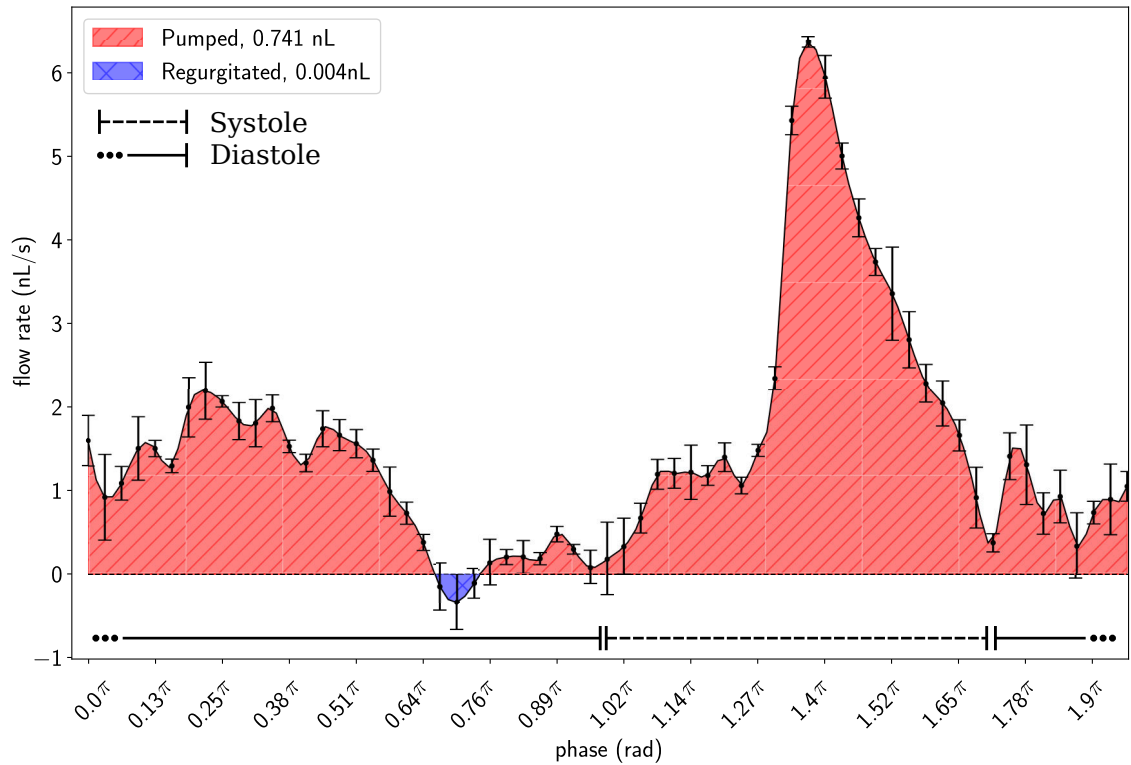
(a)
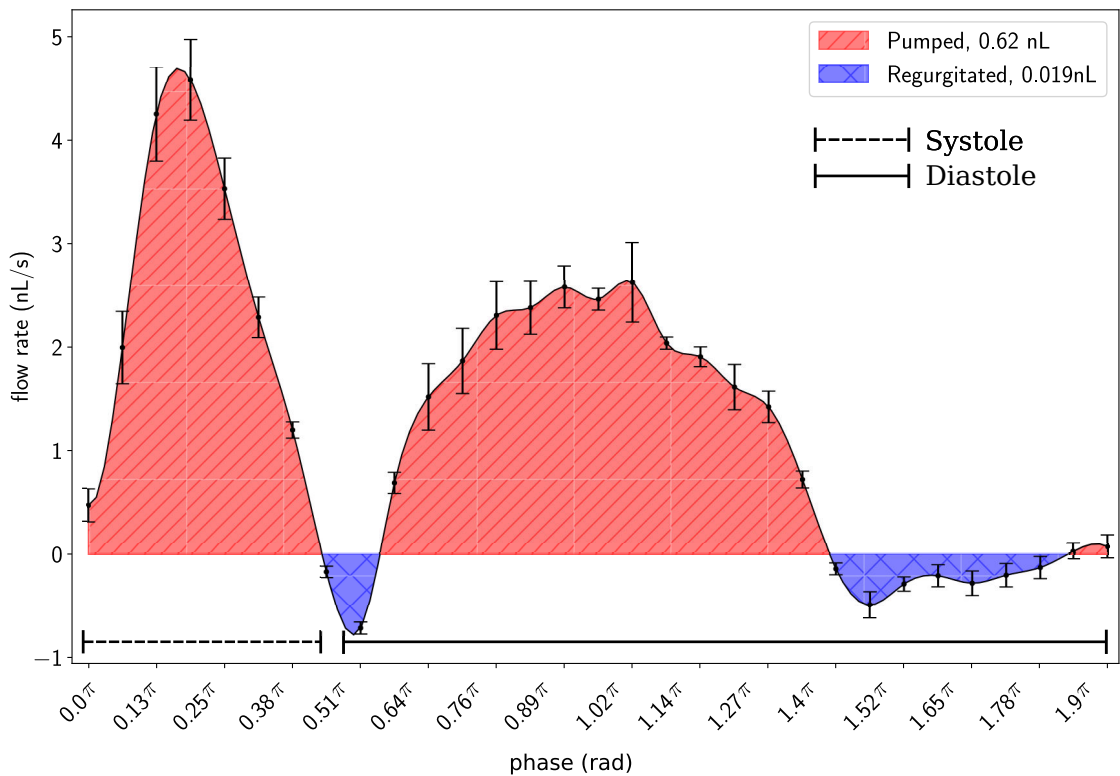
(b)

Fig. 4.17 Flow rate through a plane in the ventricle of a 4 day old zebrafish heart imaged at two different orientations. Phase is not registered between the two sets and is arbitrary. The shape of the flow rate in time is similar between the two orientation, with the main difference being an additional local regurgitation region in (b), between phases 1.4π and 1.78π. This differences comes from the fact that there was a rough estimation of where the regions of interest overlap between the two orientations. Since there are two valves associated with a chamber, their closing can both cause a local regurgitation. Note that (a) dataset was split into twice as many phase bins.
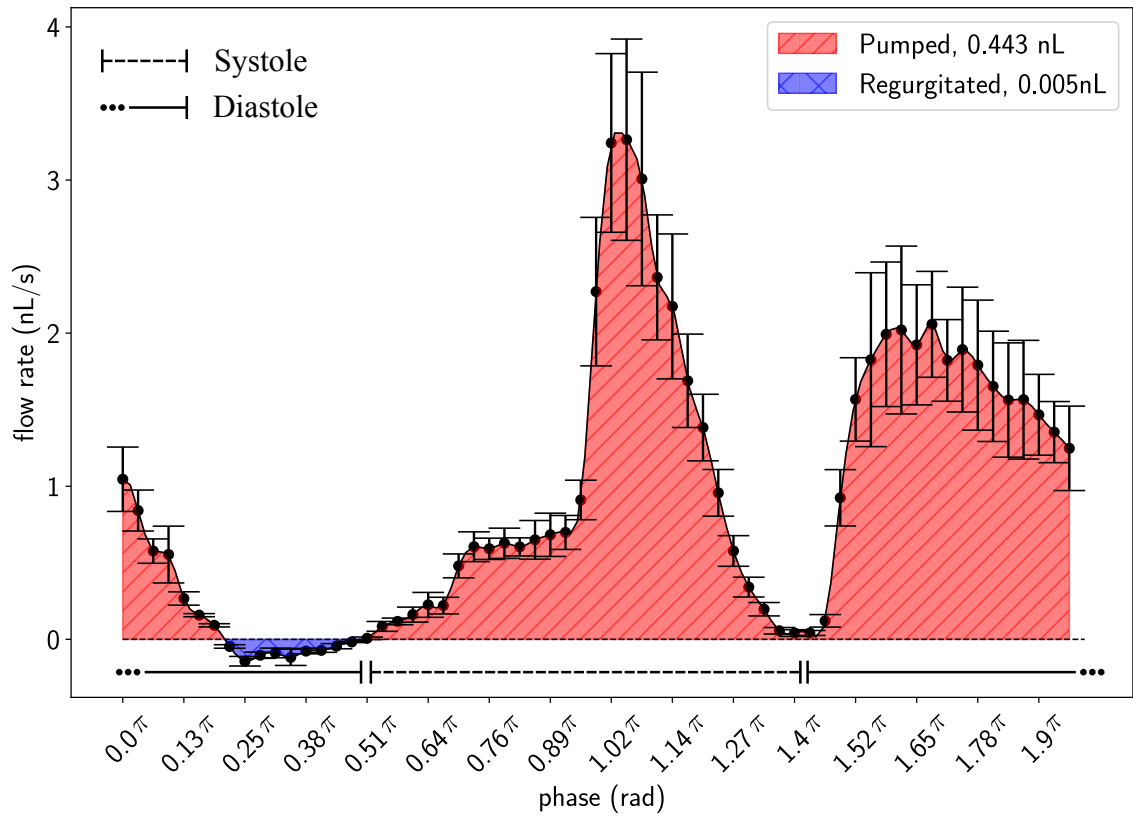
(a)
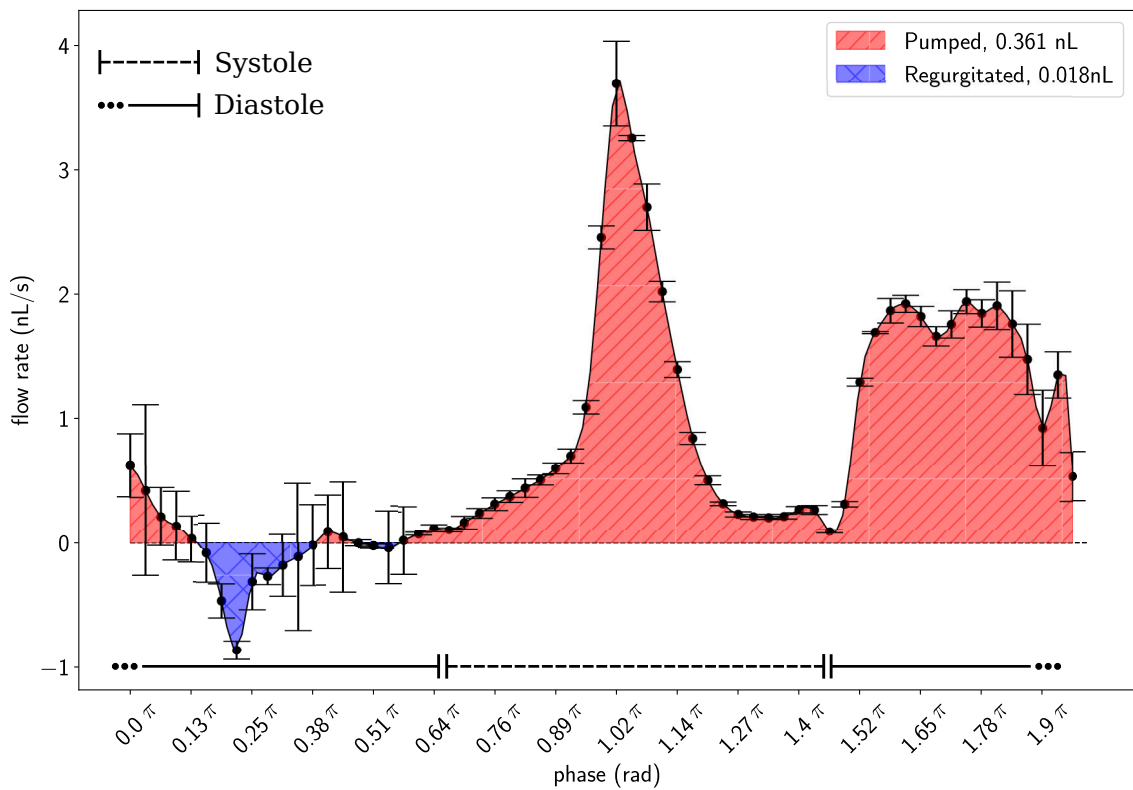
(b)

Fig. 4.18 Flow rate through a plane in the ventricle of a 5 day old zebrafish heart imaged at two different orientations. Similarly to results shown in Figure 4.17, there is a good similarity between the shapes of the flow rate profiles in time between two imaging orientations. Phase is not registered between the two sets and is arbitrary. An overlay of the two plots is shown in Figure 4.19.

The general features of the flow rate in a 5 dpf, Figure 4.17, are very similar to 4 dpf. On the other hand, the peak flow rate has noticeably decreased (see Table 4.3), and the lower positive flow rate "humps" are slightly shorter in time. The biological reasons for this were not investigated, as they are beyond the scope of this thesis. A more important aspect of these measurements is the reproducibility of measurements between different orientations, described in the next paragraph.

4.3.3   Comparison of flow rate from different orientations

The imaging of 4 and 5 dpf fish were performed at two different sample orientations at each age. The fish were rotated about 85 and 65 degrees between complete z-stacks for the 4 and 5 dpf specimen respectively. In principle, flow rate measurements through the same cross-sectional area of the heart, should yield the same flow rate measurement, regardless of imaging orientation (rotation axis is parallel to the main flow direction in the ventricle). Qualitatively, the flow rates from different orientations do look similar, up to a phase shift (see (a),(b) in both Figure 4.17 and Figure 4.18). In fact, by visually aligning the flow profiles from different orientations in phase, a relatively good agreement can be seen in Figure 4.19. The reasons why it is challenging to synchronize between different orientations will be explained later.
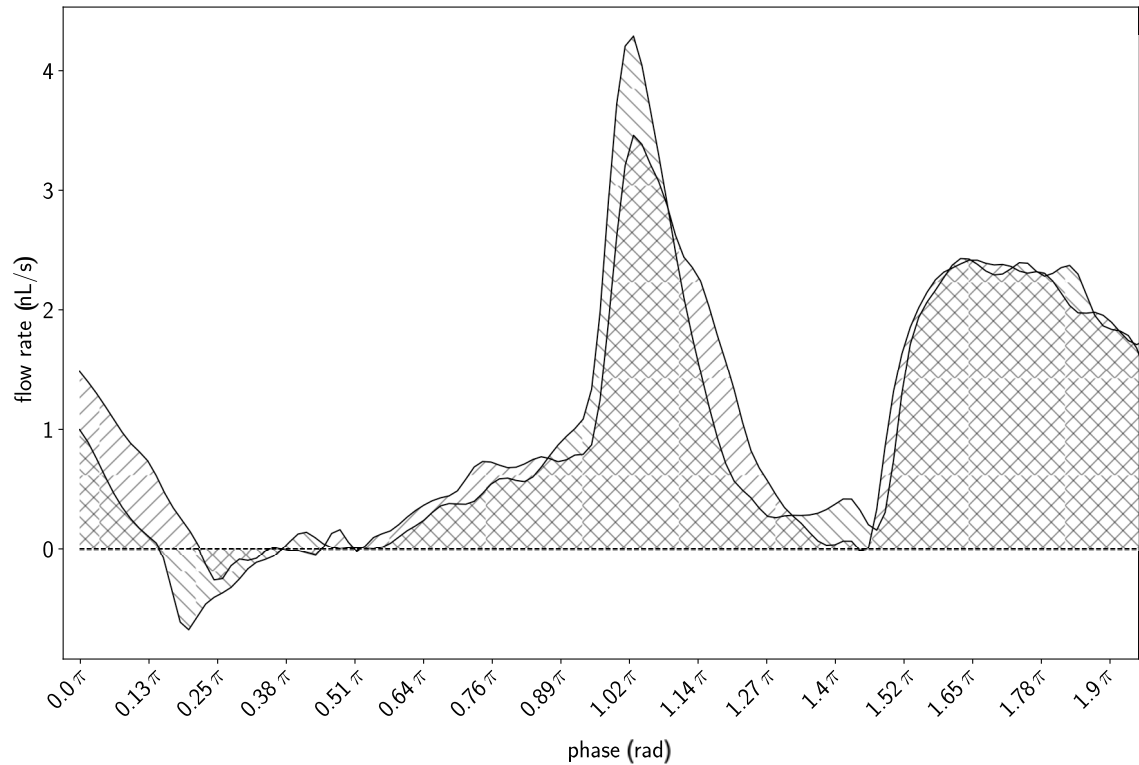
Fig. 4.19 Overlap of flow rate data obtained at different views for a 5 day old zebrafish ventricle, shown in Figure 4.18. The overlapping regions are indicated by a square pattern. While there are some clear differences between the two flow rate measurements, taking the fact that the phases or geometry of the heart was registered, there exists a reasonable match. This suggests that a) OOPM effects were not significant, and b) that it should in principle be possible to perform multi-view data acquisition to reconstruct 3 component velocity vectors.

Error estimation   So far the origin of error bars shown in the flow rate plots were not stated, so as to not present a distraction. The calculation of errors on the flow rate measurements was performed in the following way; Firstly, the full dataset was split into two halves for μPIV analysis. Secondly, the flow rate was calculated using the new velocity measurements for both half-datasets. Then, for each phase bin, the absolute difference between the flow rates of the two sets was calculated. Finally, this was used as the standard deviation of the results. Essentially, this approach removes half the particles which contributed to the correlation averaging. In general main reasons for large errors can be summarised in the following way, which also serves as a reminder of chapter 2:

- Insufficient temporal resolution. This is likely to happen at regions where acceleration of the blood flow is really high (spatially and temporally). The simplest solution is to decrease the IPT, to accommodate the high flow velocities.

- Insufficient particle number. At full contraction of the heart chambers, there is little volume for a large number of fRBCs to pass, which can yield Cross-Correlation (CC) results with potentially poor p2p ratio values. The simplest solution for this, is to perform correlation averaging for longer.

- Significant shear at the chamber junctions. Because of the geometry of the heart, there is potential for very large spatial gradients at the vicinity of heart valves. Solution to this would require advanced Particle Image Velocimetry (PIV) analysis techniques, such as IW deformation which were briefly mentioned in chapter 2.

- Loss of particles due to significant OOPM. The areas that require caution when interpreting Three Dimension-Two Component (3D2C) µPIV results are at the heart walls. While the contraction of the heart is more complicated than a simple perpendicular motion towards the centre of the heart, there could be locally large OOPM components close to the heart wall. The most practical solution to alleviate this, would be to decrease the IPT.

For the flow rate measurements presented here, only the first two bullet points were observed to play a role. In fact, the large error at phase bin beginning at 6.074, is due to combination of both effects. At that time, the atrium is fully contracted, and there are very few, extremely fast blood cells squeezing through the small remaining volume. Large shear considerations were not relevant because the flow rate was measured measured approximately at the centres of the chambers of interest. OOPM, on the other hand, had to be carefully considered. As explained above, there could be significant OOPM at the peak contraction and expansion of the heart wall, if it was approximated as a uniformly contracting sphere. However, since it is known that the contraction of the heart can be better described as a travelling (contraction) wave [166]. In addition to this, the pressure gradient between the chambers of the heart means that there should be significant velocity component along this gradient. This suggests that in-plane motion is expected to be dominant at the heart wall as well. In fact, experimental evidence for lack of significant OOPM in the heart is presented in the next section.

Possible improvements The results presented in this section could be further improved by a) increasing the phase sampling (i.e. smaller phase bins). The flow rate measurement comparison between two orientations would benefit from b) improving the sample rotation apparatus and/or using a robust image registration routine, and c) improving phase registration between two BF channels of the same heart, but at different orientations.

The potential pitfall that limited phase sampling presents is velocity averaging over time. Currently, it is assumed that the velocity does not significantly change over a single phase, and the average *instantaneous* velocity values are measured. The straightforward solution is to simply increase the imaging time and decrease the bin size. However, this also depends on the assumption that phase recovery is robust, and does not drift over time. This will be investigated by considering the individual frame pair velocity measurements later in this chapter.

In order to meaningfully compare flow rate measurements between two orientations, it is essential to measure the same cross-sectional area through the heart. In theory, the

solution would be to align the centre of the cross-section of interest of the heart, with the axis of rotation, and then rotate without introducing any translation or tilt of the sample. However, it does not appear to be feasible in practice at the moment, as there are practical limitations at a larger scale; for instance, the Fluorinated Ethylene Propylene (FEP) tube and the syringe which it is mounted in, are not sufficiently precisely aligned with the axis of the rotation stage. An alternative would be to use computational registration algorithms in post-processing case. This could in principle be achieved by using fluorescent endocardial cells in the *flk1:GFP* transgenic line for example.

Finally, to precisely compare flow rate measurements from multi-view data, registering the phase of heartbeats is also important. Currently, this cannot be implemented using the similarity metric used in prospective optical gating method, simply because the images differ too significantly between different sample orientations. In a specific case when the heart is rotated precisely 90 deg, this problem could in principle be solved by imaging the heart on two BF channels (i.e. combining configurations A and B in Figure 2.16). This would mean that the same view of the heart is imaged, and therefore it should be possible to register the heartbeats in time. However, recall the consideration for "optimum" angles, which are $\pm \approx$ 30-45 deg from some starting point. Alternatively, the approach previously used by Jamison et al. [90], where flow measurements in the BF channel were used for phase retrieval, could be implemented for our work too. Recall that in essence, by matching the velocity profiles in time through a particular IW they were able to assign a phase to the heartbeat (see chapter 1).

4.3.4   Summary of μPIV analysis

The results shown in this section qualitatively confirm the feasibility of the use of SPIM-μPIV as a system for measuring blood flow in the zebrafish heart. It was shown that the recovered velocity fields in the hearts of different ages exhibit expected features, such as higher velocity values in the centre of the heart chamber, and lower velocities at the walls. The qualitative agreements between flow rates through a cross-section in a heart chamber of different orientations suggested that the measurements are reproducible. The error estimation was explained, and issues with the above described analysis were also discussed. During this discussion, further investigation of degree of OOPM, and robustness of phase recovery algorithms was deemed necessary. The next two sections present experimental results addressing this need.

4.3.5   Out-of-plane motion at different inter-pulse times

As discussed previously, OOPM can have a significant effect on the cross-correlation results in PIV analysis. On the other hand, it was also empirically shown that correlation averaging enables recovery of velocity profiles with acceptable uncertainty in flows with up to $\approx$ 4μm

OOPM. However, the true extent of OOPM is not precisely known in the zebrafish heart. In the previous section, we considered a simplified case where the heart wall contracts uniformly towards its geometrical the centre, which could imply a large component of OOPM assuming a cylindrically symmetric heart.

However, since there exists a pressure gradient between the valves in the heart chamber, it was assumed that the velocity components in the direction of the pressure difference should be the dominant feature. If the sample is aligned with the light sheet in a way that the dominant inflow and outflow is parallel to the light sheet (in practice this means having the chamber length-wise parallel to the light sheet), the effects of OOPM should be minimal. Despite this assumption, we have investigated the maximum vertical motion (which under the symmetry assumption would be the maximum z-motion for the 3 day old fish [135]). It was found that the maximum y-component, throughout the whole heartbeat, did not exceed $4\,\mu m$ at the main part of the atrium. This value was only exceeded at the SV junction, but since it was at $\approx 45\,deg$, this did not invalidate the analysis. In order to further investigate whether there is a significant amount of OOPM in the ventricle, time sequential images of the blood cell motion were acquired with high speed *Andor Zyla* camera running at ≈ 400 Frames Per Second (FPS). The high framerate allowed capturing 2 or more frame pairs in the same phase bin (that is a sequence of 4+ frames). This is important because if there was a significant loss/introduction of particles due to the third velocity component, it should be clearly visible in the time sequential images (i.e. cells moving in and out of the light sheet). Furthermore, more subtle effects of OOPM could be investigated by comparing velocity values which were obtained in the same phase bin, but with a slightly different IPT. The rationale here was that if there was a constant OOPM in the flow, the measured velocities would not scale with IPT.

Qualitative assessment of OOPM   To qualitatively test the above, blood flow in a single plane of a 4 dpf zebrafish heart was imaged at 0.75, 1.0, and 1.25 ms effective time difference, Δt_{eff}. Effective time difference is the IPT plus the LPL, as the time between the centres of adjacent LPLs was taken as the Δt_{eff} (e.g. for an LPL of 0.25 ms and IPT of 0.5 ms, $\Delta t_{\text{eff}} = 0.75$ ms). A time-colour coded sequence of images, for the three different IPTs are shown in Figure 4.20. The flow is compared at a similar phase in the cardiac cycle between the different IPTs, and shows the general trend that the fRBCs remain visible throughout the chamber. The exception to this is the junction between the bulbus arteriosus (BA) and the ventricle, where due to the sudden narrowing of the cross-sectional area and extremely high speeds, the blood cells appear to disappear at that region. While the μPIV resolution is severely limited at the regions of these drastic peak velocities, the middle of the atrium does not seem to suffer from apparent loss/introduction of particles. Hence, this qualitative analysis suggests that the previous flow rate measurements should not be affected (as a cross-section in the middle of the chamber was examined) and hence valid. To further
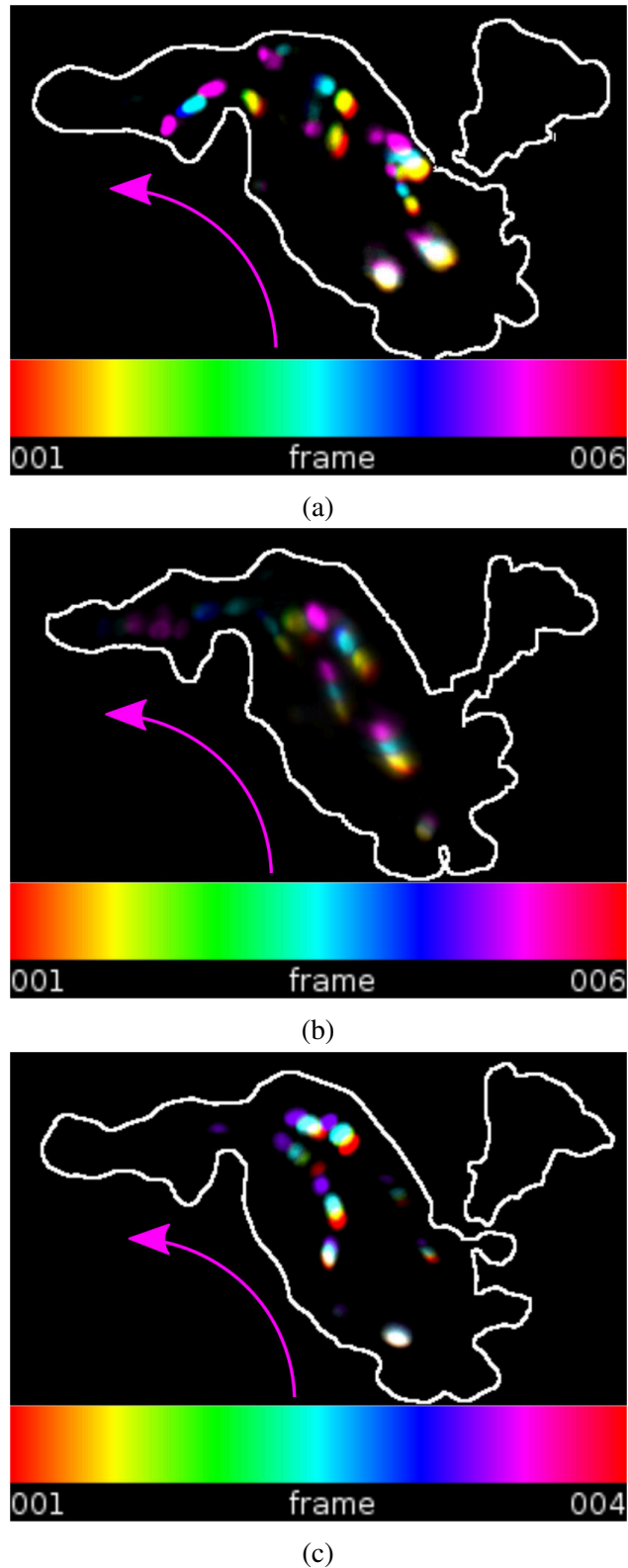
Fig. 4.20 Flow of blood cells at different inter-pulse times. Black and white inverted images of MIPs of several sequential frames in a chosen phase bin are shown for different IPTs. The effective time difference between two image pairs are 0.75 (a), 1.0 (b), and 1.25ms (c). The direction of the flow is indicated by the magenta line. These images suggest that the same blood cells remain visible over the phase bin, which indicates that the OOPM component is not significant. Note that for Δt_{eff} of 0.75 and 1.0 ms, shown in (a) and (b) respectively, 6 sequential frames are captured. The extra two frames give an illusion of more motion in (a) and (b) than in (c). Visualised with *FIJI* [140].

support this claim, a quantitative analysis was performed in the region potentially affected by the OOPM - the bulbus venosus.

Flow measurements with potential OOPM   If a region in the heart with no OOPM is measured with slightly different Δt_{eff}, the measured velocities should only differ by the ratio of different Δt_{eff}. On the other hand, if the OOPM was significant, this Δt_{eff} ratio difference prediction would fail, as correlation of the true flow would be lost due to particles moving in and out of the light sheet. With the IPTs used here, the expected fractional change in measured velocities should be 0.8 between the 0.75 and 1.0 ms Δt_{eff}, and 0.75 between 1.0 and 1.25 ms Δt_{eff}. By comparing0 the u-component velocity measurements at the bulbus venosus using different IPTs, it was found that the average ratios were 0.773 ± 0.152 and 0.796 ± 0.128. The large standard deviation is due to the relatively short correlation averaging and a rather small number of sufficiently bright fRBCs for this sample at the LPL used. Further it is possible that even at these small time differences, there is some change in the flow rate (i.e. it is possible that there is some time averaging of the velocity). Despite the size of the standard deviation, there is an acceptable match between the expected and measured values, therefore any underlying OOPM in the measured region does not seem to have a significant effect.
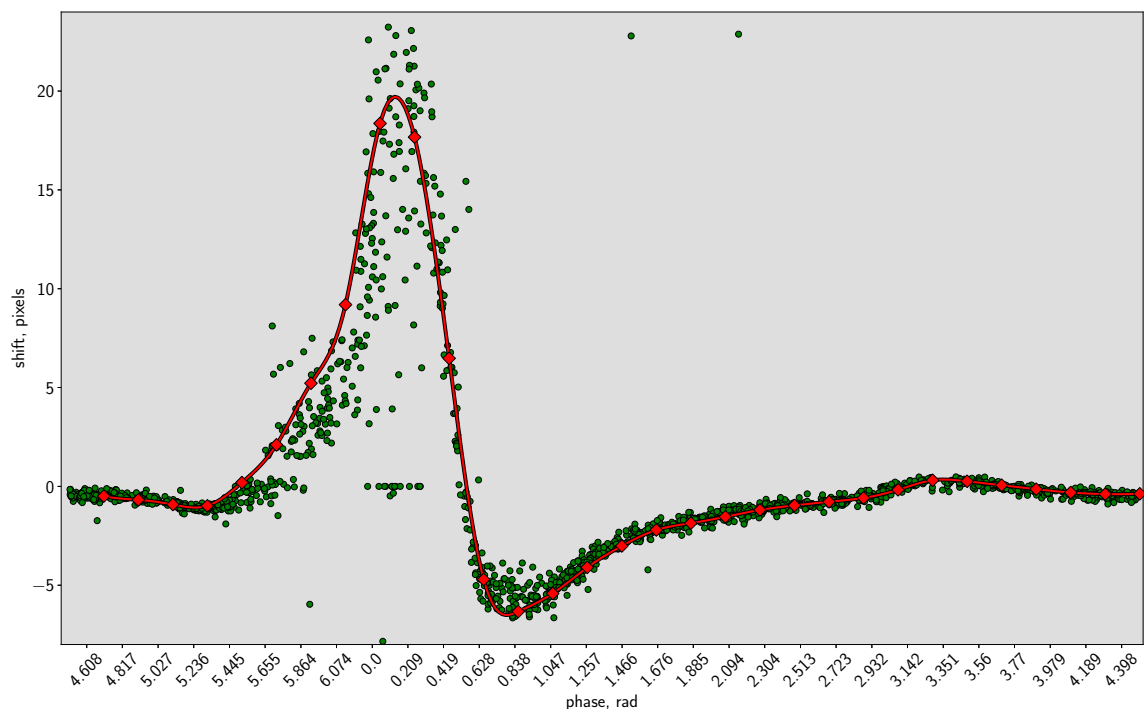
Fig. 4.21 Comparison of correlation averaged (red line with squares) and single-pair (green dots) u-component measurements (raw data) for 31 phases for a chosen interrogation window in the atrium. Phases are the same as shown in Figure 4.16. Failure of phase matching over time would manifest in the spread of velocity values over time. Since the time profile of velocity values does not appear to shift in time, the phase matching can be considered successful. Figure as published in [135].

4.3.6   Reliability of phase matching

In order for the correlation averaged μPIV measurements to have a meaningful representation of the true underlying flow at a particular phase in the heartbeat, it is crucial that phase recovery is robust. In general, past research indicates that the zebrafish heartbeat is highly predictable, despite natural variations [14, 16, 76] and this is the main assumption of optical gating techniques. The occasional mismatch of phase assignment, for example due to some abnormal singe heartbeat length, would not be particularly detrimental to the velocity measurements. This is because vast majority of other flow information would correspond to the correct phase, and correlation averaging should remain unaffected by the inclusion of flow data from a random phase. However, if the phase recovery starts "drifting" over an extended imaging period, this would result in a velocity averaging over different phases in time. If there was a drift in phase recovery, then a significant spread in time in the raw velocity values would be expected over a phase bin. On the other hand, there is a possibility that the *flow* is not as reproducible beat-to-beat as the gross motion of the heart wall is. For instance, one could consider a situation where the flow is perturbed by a slight variation of the heart valve closure. Therefore, even if the heart wall motion is periodic and the phase recovery is faithful, there is a possibility that the velocity fields at the same phase bins differ significantly (beat-to-beat) and hence invalidate the correlation averaging approach used here. To investigate this, the raw and correlation averaged pixel shift values were examined at a particular IW in the hearts of the different aged fish (see Figure 4.21 ,Figure 4.22, Figure 4.23).
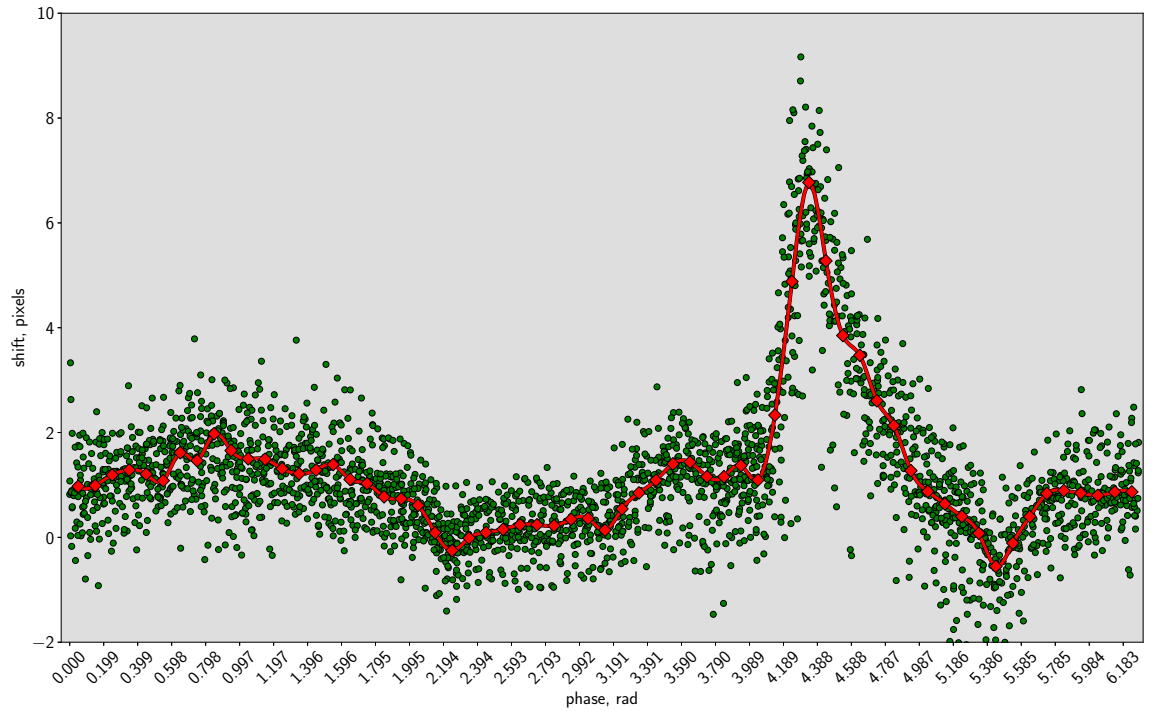
(a)
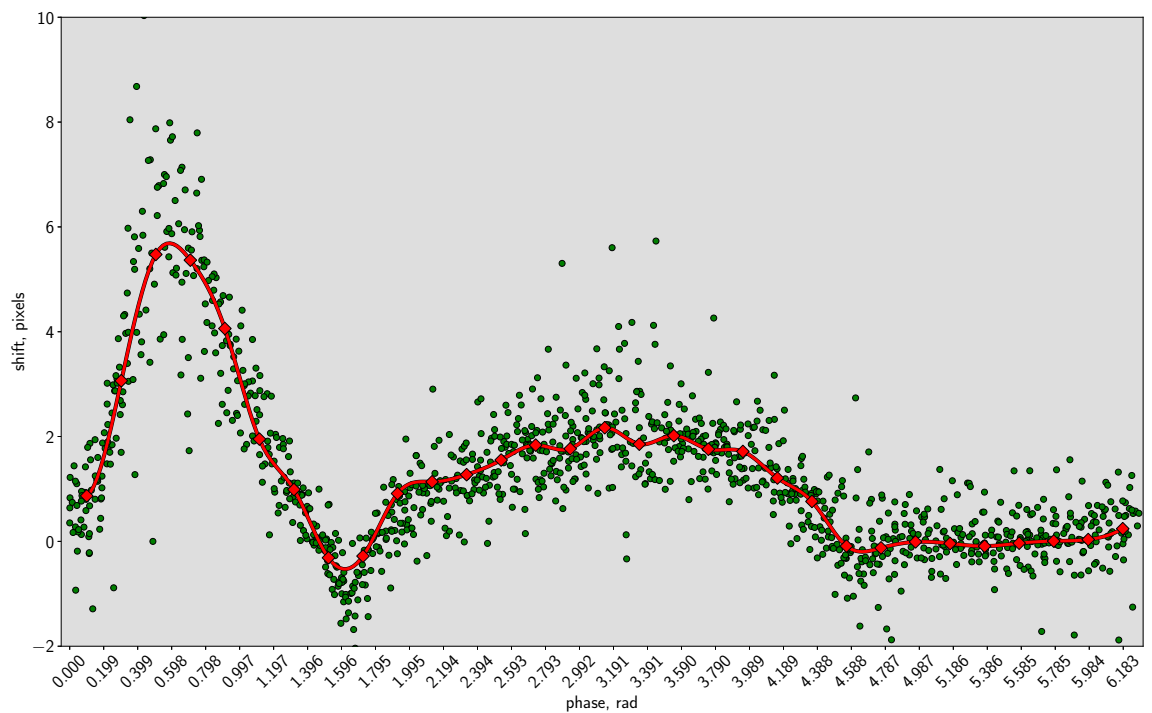
(b)

Fig. 4.22 Comparison of correlation averaged (red line with squares) and single-pair (green dots) *u*-component measurements (raw data) for (a) 64 and (b) 32 phase bins for interrogation window at similar locations (roughly estimated based on flow features). The phases are not registered and are arbitrary. Note that the peak can be clearly seen, and the lack of significant spread in time suggests that phase matching performed reasonably well.

There does not appear to be any significant spread in velocity values in phase in the measurements of a 3 dpf zebrafish atrium. However, the results from 4 dpf and more so in 5 dpf zebrafish ventricle, are more noisy (in particular the velocity magnitude variation is greater compared to the 3dpf results) and require a closer inspection. In both of these results, the highest peak seems to drop off less sharply than in the 3 dpf zebrafish. Of course, this could be simply due to a different temporal flow profile in the ventricle (compared to flow in the atrium of a 3 dpf fish). However, there appears to be a second peak visible in Figure 4.23b at around phase 3.590, might suggest an issue with the phase recovery or flow reproducibility.

If phase recovery was the cause of the second peak, this could be due to the differences in the way the BF channel data was acquired. Namely the 4 and 5 dpf datasets were obtained using configuration B, whereas the 3 dpf obtained using configuration A (recall Figure 2.16). In principle, this BF data acquisition should not affect the reliability of phase recovery, but further investigation would be necessary to validate this assumption. Moreover, all of the phase values should shift, but since there is a clear location of the peak flow, it is unlikely that the cause for this second peak is due to failure of phase-stamping.

The other potential cause for the more noisy results when imaging the 4 and 5 dpf fish, could be the use of a much faster camera. It was briefly mentioned in the previous section, that this much higher acquisition rate can yield 2 or more frame pairs in one phase bin, and this was shown in Figure 4.20. It is possible that the velocity changes significantly between sequential frame pairs, which leads to the velocity broadening (in magnitude) seen in Figure 4.22 and Figure 4.23. This could be investigated by splitting the phase bins in half and observing if the broadening reduces, but was not done here due to limited time. This would also imply that a clear change within a phase bin should be visible.
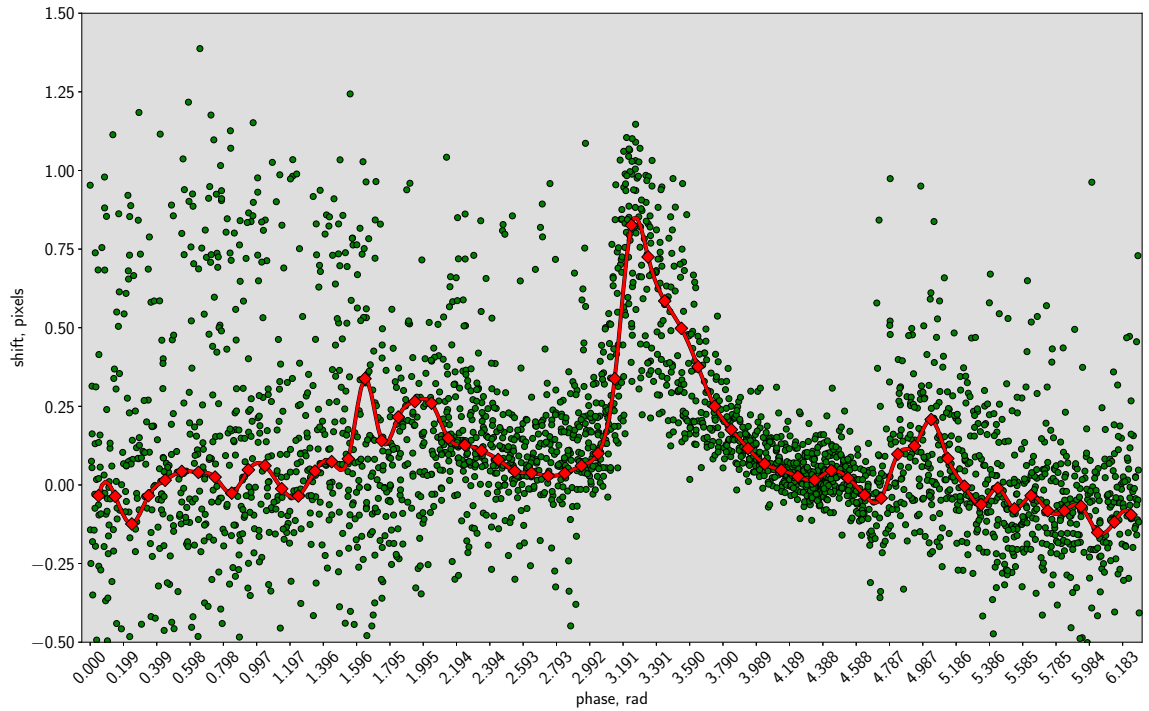
(a)
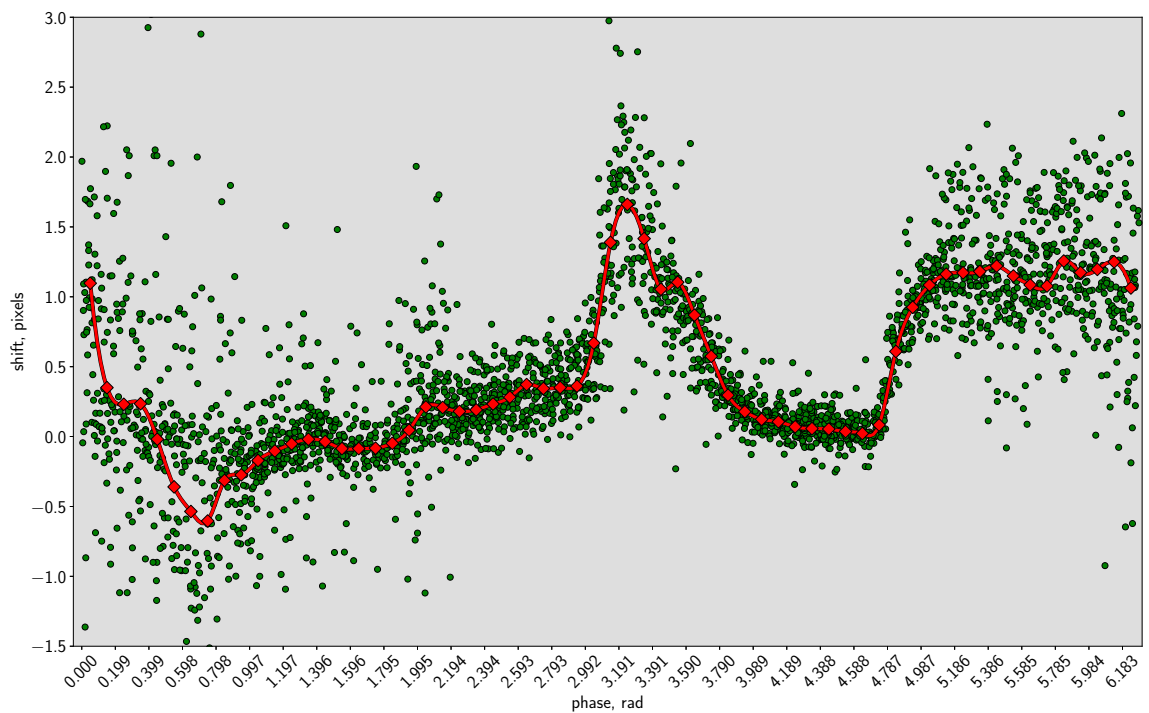
(b)

Fig. 4.23 Comparison of correlation averaged (red line with squares) and single-pair (green dots) u-component measurements (raw data) for 64 phases at a single IW in the ventricle. Figure (a) has a significant amount of spread in the pixel shift compared to (b). This requires further analysis to inspect if the spread is a genuine feature of the flow or if the phase matching is failing. However, the fact that the region from phase 2.194 to 4.588 is reasonably well contained suggests that there should not be any critical failures in phase assignment. The results shown here and also in Figure 4.22 have a larger spread on the velocity measurements than the results shown in Figure 4.21. Therefore it is not surprising that the 4 and 5 dpf plots look more disordered than the 3 dpf, even assuming perfect phase-stamping.

4.3.7 Future improvements

The preliminary results of this study appear promising, considering the relatively simple μPIV analysis algorithms used. Here, the experimental and analysis aspects not explicitly stated elsewhere in this thesis, will be reviewed. Potential routes to approach these issues are also briefly suggested.

- The ≈ 2.5 μm Full Width at Half Maximum (FWHM) thickness of the light sheet used here, meant that the Rayleigh length does not cover the full length of a single chamber. This means that the velocity at the edges of the heart chamber will be slightly more averaged in depth (i.e. larger DOC). This could be alleviated by using a thicker light-sheet, at the loss of some axial resolution. Increasing the sheet thickness would also be necessary if both chambers of the heart were to be imaged with the same depth sectioning throughout the Field of View (FOV).

- The single-side light-sheet illumination used here meant that the image quality reduced in depth, due to light absorption and scattering. While it was not a significant issue for scanning single chambers, using dual-side light-sheet illumination (using two objectives facing each other) should in principle avoid this problem.

- The measurements here were done on fish from 3 dpf age because younger fish develop their heart very rapidly. Because an extended imaging time is required to build up sufficient data for correlation averaging (around 30 min per z-stack), by the end of the acquisition, the heart would have changed significantly, and the μPIV results would no longer be representative (i.e. the flow would genuinely change over the course of imaging). In principle, this would be alleviated with Light Sheet Fluorescence Microscopy (LSFM) systems capable of rapidly acquiring volumetric data (such as *SCAPE* light-sheet system for example).

- Unlike for flow measurements in the blood vessels, the use of microinjected beads for imaging flow in the heart is significantly more challenging. The main issue is bead deposition in the heart walls, particularly the trabeculae. It is unclear whether smaller particles, such as quantum dots would aggregate more or less in the heart walls, however, it is worth investigating at least in the atrium, where there is no trabeculation.

The issues summarised here, and elsewhere in the text were presented with suggested solutions, which should be practically achievable and would present useful extensions to this work. Perhaps the three most challenging additions to this work would be a) the implementation of advanced PIV algorithms (such as IW deformation technique), b) multi-view 3D volume registration (which would allow calculating the third velocity component), and c) extending the SPIM system for dual-side illumination (to improve the imaging depth with good image quality).

4.4 Conclusion

This chapter presented 3D + time blood flow measurements in the zebrafish heart, which were the chief results of this thesis. The practical aspects of *in vivo* imaging using Selective Plane Illumination Microscopy (SPIM) for micro Particle Image Velocimetry (µPIV) analysis were considered, and subtle yet important experimental steps were explained. The less challenging measurements in the main blood vessels of the fish were presented. The µPIV results obtained there were considered by investigation the motion of individual tracer particles. It was found that using artificial tracers can yield higher spatial resolution, nevertheless, the advantages of using endogenous fluorescent Red Blood Cell (fRBC)s were clearly stated.

Finally, the depth resolved measurements in the hearts of zebrafish of 3, 4, and 5 days old were performed using blood cells as flow tracers. The recovered velocity fields showed qualitatively expected features in the chamber of the heart. These measurements allowed quantifying the blood flow through a cross-section of the heart. This showed that SPIM-µPIV can be useful for quantifying the efficiency of the heart valves as the heart develops. Furthermore, these flow rate measurements also helped illustrating the reasonable match between flow measurements acquired with *z*-stacks of the heart at different orientations. Next, a detailed examination of the possible sources of errors due to Out-of-Plane Motion (OOPM), and the quality of phase recovery, was presented with additional experimental measurements, and focused analysis of velocity measurements. The findings suggested that in the cross-sections considered, the OOPM should not have any significant effect. On the other hand, the analysis of phase-dependent velocity measurements was not conclusive and further work to investigate this more thoroughly was suggested.

All in all, given the challenging nature of imaging thick biological samples, combined with the extra layer of *in vivo* experiments, it seems that SPIM-µPIV is capable of quantifying blood flow in the beating zebrafish heart well. Further, considering that the results presented in this chapter were not pre-processed (in terms of use of any "noise reducing" filters), and used simple (yet robust) µPIV analysis algorithms, these results could in principle be greatly improved.

As a final note, it is worth revisiting one of the applications of flow quantifiaction - the measurements of Wall Shear Stress (WSS) introduced in Chapter 1. While the finite time of this project prevented direct quantification of WSS, the measurement accuracy shown provides a great improvement over conventional volume illumination flow measurement techniques. In particular, it was shown in Chapter 3 that a SPIM-µPIV system can accurately recover flow at the walls in 3D. Furthermore, using artificial flow tracers (fluorescent beads), potential for 1 micron spatial resolution Particle Image Velocimetry (PIV) measurements at the vessel walls exists. However, it is at the moment unclear if such resolution is required, as it could be argued that imaging at the blood cell resolution should suffice. On the other hand, it was shown that there are slight differences in the flow of blood cells and fluorescent

beads. This suggests that blood plasma might flow differently to blood cells, and hence can have implications on the accuracy of WSS measurements. However, the key improvement of this work is extension of flow measurements to higher dimension (Three Dimension-Two Component (3D2C)). Since blood vessels, and especially the heart, are not ideal geometrical shapes, approximating them as tubes or spheres and using single-projection flow measurements (Two Dimension-Two Component (2D2C)) cannot provide adequate information on fluid-structure interaction. Therefore there is a need for full 3D+time information, which SPIM-µPIV can achieve.

Chapter 5

Conclusion and future work

In conclusion, SPIM-µPIV technique is proposed as novel approach for flow measurements in 3D at the microscopic scales. This was firstly motivated by the limitations in conventional µPIV systems which typically do not have optical sectioning ability, and in particular, suffer from erroneous velocity estimation due to Depth-of-Correlation. Secondly, while Light Sheet Fluorescence Microscopy (LSFM) has been utilised to investigate the morphology of the heart wall in the past, quantitative blood flow measurements in 3D+time have not been previously reported. This can be attributed to the highly dynamic nature of the blood flow, presenting a significant challenge for both microscopy and computational analysis. By making use of optical gating techniques to recover heart phase, we showed the potential of SPIM-µPIV system for depth and time-resolved *in vivo* blood flow measurements in the developing zebrafish heart.

The recurring theme in this thesis was rigorous investigation of velocity measurement validity and accuracy. The key aspects investigated in this thesis can be summarised as:

- Comparison of the conventional cross-correlation algorithm, Fast Fourier Transform Cross Correlation (FFTCC), against the Sum of Absolute Differences (SAD). Analysis of synthetic data strongly suggested that SAD exhibits a predictable behaviour in terms of the bias and random error of velocity measurements. On the contrary, FFTCC showed inferior accuracy and precision when particle image diameters used in the analysis reached the sizes of a typical fRBC of a zebrafish.

- Experimental investigation of Depth of Correlation (DOC) in a SPIM-µPIV system. By contrasting velocimetry results of Brightfield (BF) and SPIM for a flow of beads in a 50 µm diameter tube, it was clearly shown that SPIM does not suffer from velocity averaging due to a large DOC like conventional µPIV systems do. It was proposed and experimentally proven that DOC for a SPIM system is confined by the thickness of the light-sheet used, thereby presenting a clear advantage over conventional µPIV systems.

- Empirical measurements of maximum tolerable OOPM. Through the use of real experimental data, it was shown that reliable 2D2C velocity measurements can be recovered even when the OOPM velocity component exceeds 4 µm, as long as correlation averaging is used. This was a crucial validation step for blood flow measurements in the zebrafish cardiovascular system.

These investigations formed the "foundation of validity" for applying SPIM-µPIV for *in vivo* blood flow measurements in the zebrafish, which were the main "proof-of-concepts" results in this thesis, and are reviewed here:

- 3D2C blood flow velocity recovery in the main vessels of the zebrafish embryo. By using endogenous fluorescent blood cells as flow tracers, depth-resolved flow measurements in the Dorsal Aorta and the Cardinal Vein of the zebrafish were presented in section 4.2. The flow rate through these vessels, as well as the flow profiles in time were shown to illustrate the potential analysis that can be carried out with the data recovered with SPIM-µPIV system.

- Comparison of fRBC and fluorescent bead flow. Single plane velocimetry data using microinjected beads revealed an apparently higher spatial resolution than the fRBCs. This prompted an investigation of the flow properties at the single particle level. It was concluded, that flow measurements with either type of tracer is valid, albeit mapping different components of the fluid.

- 3D2C blood flow measurements in the zebrafish heart. The most important and challenging results of this thesis, the depth-resolved measurements of blood flow throughout the full heartbeat of 3, 4 and 5 days post fertilization (dpf) fish were presented in section 4.3. This was achieved by combining the optical sectioning ability of SPIM, optical gating techniques, and correlation averaging. The results allowed, for the first time, to directly measure depth-resolved blood flow in the zebrafish heart.

- Flow rate measurements throughout the cardiac cycle in the heart chambers. The pumping performance of the developing zebrafish heart was evaluated by considering the flow rate through a cross-section in the heart chamber. These measurements should provide a more accurate estimate compared to measurements relying on single 2D projection measurements obtained with conventional microscopy. Furthermore, by considering the flow rate data obtained by imaging the hearts from different orientations, qualitative evidence for measurement reproducibility was shown.

- Validity and reliability of µPIV analysis in the zebrafish heart. The main theme of investigating the validity of results was revisited once again by considering two aspects which can decrease measurement accuracy. Firstly, occurrence of unacceptable

OOPM was investigated both qualitatively and numerically and was found not to be of concern for this study. Secondly, reliability of phase matching necessary for meaningful correlation averaging of SPIM-μPIV data was examined. While the more noisy data from the measurements of the 4 and 5 dpf zebrafish requires further investigation, the general trend of correlation-averaged data suggests that the phase-stamping is working well and the μPIV analysis is valid.

5.1   Future work

Despite the encouraging preliminary results achieved with our Selective Plane Illumination Microscopy (SPIM)-micro Particle Image Velocimetry (μPIV) system, the results should be further improved by addressing some experimental and computational analysis aspects of the technique, these could be summarised as follows:

- Refined sample mount with a motorised rotation stage. In order to simplify 3D volume registration (from samples which were imaged at different orientations), the sample rotation should be precisely known. The current set-up used a manual *Thorlabs CRM1* rotation mount, which was installed on a custom built 3D printed mount. However, manual handling was not ideal, as the sample could be disturbed as soon as the rotation stage was touched by hand. Replacing the manual rotation stage with a motorised one, even controlled with an inexpensive stepper motor, should improve the data acquisition step for multi-view 3D registration.

- Recovery of Three Dimension-Three Component (3D3C) velocity flow field: phase-matching. The above bullet point is necessary for the next logical step of this work - estimation of the third velocity component in the flow of the zebrafish heart. As briefly discussed in chapter 4, this requires robust 3D registration, and the ability to recover phase of the same heart but imaged from different orientation in Brightfield (BF). While the current phase recovery algorithms cannot yet register between two different views. However, there is no fundamental limitation to extracting this information, as clearly if the same heartbeat is imaged from different orientations, and hence the same underlying period information should be preserved. An alternative venue to explore would be investigating if BF images from multiple orientations can be reliably analysed using μPIV analysis to estimate the period (as performed by Jamison et al. [90].

- Recovery of 3D3C velocity flow field: multi-view velocity reconstruction. Provided heartbeat period information is extracted from multi-view BF data, the next step would be to fuse the velocity information recovered with SPIM-μPIV of the heart at different orientations. To this end, the mathematical framework described by Chan and Liebling [94], could be a potentially powerful tool for this problem.

- Beat-to-beat flow reproducibility. The analysis of the flow measurements in the 4 and 5 day zebrafish hearts require a further investigation. The data could potentially be revisited and re-analysed using an array of different µPIV parameters and perhaps even incorporating some image processing routines (i.e. to improve image quality). However, a more informative study could be to analyse a larger number of zebrafish samples, and acquire a long time sequence of single depth-plane flow data from µPIV analysis to investigate whether or not the flow is as periodic as the motion of the heart.

The proposed improvements of the set up and acquisition were suggested for the current system used. However, alternative Light Sheet Fluorescence Microscopy (LSFM) systems could be explored, such as the previously mentioned SCAPE microscopy [161], which should in principle be able to recover the full volume of the zebrafish heart nearly instantaneously. This means that multi-view configuration might not be necessary (and hence only one BF channel would be needed). Regardless of the actual LSFM system used, the depth-resolved *in vivo* µPIV measurements in the zebrafish could be utilised in the following ways:

- Refinement of Wall Shear Stress (WSS) measurements. At the beginning of this thesis, WSS was presented as a parameter of interest in cardiovascular research. SPIM-µPIV can in principle allow full 3D WSS estimation in the hearts and vessels of living, transparent embryos. 3D WSS information could be useful for refining and validating Computational Fluid Dynamics (CFD) simulations, discussed next.

- A very recent work by Vedula et al. [77] used 4D information of the zebrafish heart wall (obtained with SPIM) to quantify mechanical forces acting on the heart, such as the WSS and Oscillatory Shear Index (OSI). While this work is a significant advancement in the understanding of the zebrafish heart function, these measurement have not been validated using blood flow information. However, while our proposed SPIM-µPIV is capable of such measurement, it is likely that tracers other than fluorescent Red Blood Cell (fRBC)s would be required to achieve very high spatial resolution at the heart wall. Such particles could for instance be fluorescent thrombocytes, however, to our knowledge such a zebrafish strain is not yet available.

References

[1] Z. J. Taylor, R. Gurka, G. A. Kopp, and A. Liberzon, "Long-duration time-resolved piv to study unsteady aerodynamics," *IEEE Transactions on Instrumentation and Measurement*, vol. 59, no. 12, pp. 3262–3269, 2010.

[2] W. Thielicke and E. J. Stamhuis, "PIVlab – Towards User-friendly, Affordable and Accurate Digital Particle Image Velocimetry in MATLAB," *Journal of Open Research Software*, vol. 2, oct 2014.

[3] M. Hein, B. Wieneke, and R. Seemann, "Calculation of the weighting function and determination of the depth of correlation in micro-PIV from experimental particle images," *Measurement Science and Technology*, vol. 25, p. 084008, aug 2014.

[4] P. Ramachandran and G. Varoquaux, "Mayavi: 3D Visualization of Scientific Data," *Computing in Science & Engineering*, vol. 13, no. 2, pp. 40–51, 2011.

[5] Inkscape-Project, "Inkscape: Open Source Scalable Vector Graphics Editor, version 0.91." https://inkscape.org, 2015.

[6] J. D. Hunter, "Matplotlib: A 2D Graphics Environment," *Computing in Science & Engineering*, vol. 9, no. 3, pp. 90–95, 2007.

[7] T. E. Oliphant, *Guide to NumPy*. 2006.

[8] E. Jones, T. Oliphant, P. Peterson, *et al.*, "SciPy: Open source scientific tools for Python," 2001–. [Online; accessed <today>].

[9] F. Boselli and J. Vermot, "Live imaging and modeling for shear stress quantification in the embryonic zebrafish heart," *Methods*, vol. 94, pp. 129–134, feb 2016.

[10] P. F. Davies, J. A. Spaan, and R. Krams, "Shear stress biology of the endothelium," *Annals of Biomedical Engineering*, vol. 33, pp. 1714–1718, dec 2005.

[11] C. P. Heisenberg and Y. Bellaïche, "Forces in tissue morphogenesis and patterning," *Cell*, vol. 153, pp. 948–962, may 2013.

[12] K. Greger, J. Swoger, and E. H. K. Stelzer, "Basic building units and properties of a fluorescence single plane illumination microscope," *Review of Scientific Instruments*, vol. 78, no. 2, pp. 1–7, 2007.

[13] R. J. Adrian, "Particle-Imaging Techniques for Experimental Fluid Mechanics," *Annual Review of Fluid Mechanics*, vol. 23, no. 1, pp. 261–304, 1991.

[14] M. Liebling, A. S. Forouhar, M. Gharib, S. E. Fraser, and M. E. Dickinson, "Four-dimensional cardiac imaging in living embryos via postacquisition synchronization of nongated slice sequences," *Journal of Biomedical Optics*, vol. 10, no. 5, p. 054001, 2005.

[15] J. M. Taylor, C. D. Saunter, G. D. Love, J. M. Girkin, D. J. Henderson, and B. Chaudhry, "Real-time optical gating for three-dimensional beating heart imaging.," 2011.

[16] J. M. Taylor, J. M. Girkin, and G. D. Love, "High-resolution 3D optical microscopy inside the beating zebrafish heart using prospective optical gating," *Biomedical Optics Express*, vol. 3, p. 3043, dec 2012.

[17] P. Camacho, H. Fan, Z. Liu, and J.-Q. He, "Small mammalian animal models of heart disease," *American Journal of Cardiovascular Disease*, vol. 6, no. 3, pp. 70–80, 2016.

[18] J. Wittig and A. Münsterberg, "The Early Stages of Heart Development: Insights from Chicken Embryos," *Journal of Cardiovascular Development and Disease*, vol. 3, p. 12, apr 2016.

[19] J. Bakkers, "Zebrafish as a model to study cardiac development and human cardiac disease," *Cardiovascular Research*, vol. 91, pp. 279–288, jul 2011.

[20] N. Milani-Nejad and P. M. L. Janssen, "Small and large animal models in cardiac contraction research: Advantages and disadvantages," *Pharmacology and Therapeutics*, vol. 141, pp. 235–249, mar 2014.

[21] D. Brown, L. Samsa, L. Qian, and J. Liu, "Advances in the Study of Heart Development and Disease Using Zebrafish," *Journal of Cardiovascular Development and Disease*, vol. 3, p. 13, jun 2016.

[22] M. Westerfield, *The Zebrafish Book. A Guide for the Laboratory Use of Zebrafish (Danio rerio)*. University of Oregon Press, Eugene., 4 ed., 2000.

[23] G. J. Lieschke and P. D. Currie, "Animal models of human disease: Zebrafish swim into view," *Nature Reviews Genetics*, vol. 8, pp. 353–367, may 2007.

[24] T. J. A. Chico, P. W. Ingham, and D. C. Crossman, "Modeling cardiovascular disease in the zebrafish.," *Trends in cardiovascular medicine*, vol. 18, pp. 150–5, may 2008.

[25] C. Santoriello and L. I. Zon, "Hooked! modeling human disease in zebrafish," *Journal of Clinical Investigation*, vol. 122, pp. 2337–2343, jul 2012.

[26] S. Tavakoli, H. Rothschild, and L. I. Zon, "Zebrafish as a Model for Human Diseases," in *eLS*, pp. 1–8, Chichester, UK: John Wiley & Sons, Ltd, 2017.

[27] J. Karlsson, J. von Hofsten, and P.-E. Olsson, "Generating Transparent Zebrafish: A Refined Method to Improve Detection of Gene Expression During Embryonic Development," *Marine Biotechnology*, vol. 3, pp. 0522–0527, nov 2001.

[28] Z. R. Tsetskhladze, V. A. Canfield, K. C. Ang, S. M. Wentzel, K. P. Reid, A. S. Berg, S. L. Johnson, K. Kawakami, and K. C. Cheng, "Functional Assessment of Human Coding Mutations Affecting Skin Pigmentation Using Zebrafish," *PLoS ONE*, vol. 7, p. e47398, oct 2012.

[29] Z.-R. Huo, L. Marshall, W. Zhou, Z.-S. Ruan, B. Xu, B. He, and X.-L. Xu, "Zebrafish models of heart development and cardiovascular diseases," *Journal of Perioperative Science Huo et al. J Perioperative Science*, vol. 2, 2015.

[30] M. Xin, E. N. Olson, and R. Bassel-Duby, "Mending broken hearts: Cardiac development as a basis for adult heart regeneration and repair," aug 2013.

[31] J. M. González-Rosa, C. E. Burns, and C. G. Burns, "Zebrafish heart regeneration: 15 years of discoveries," *Regeneration*, vol. 4, pp. 105–123, jun 2017.

[32] K. D. Poss, L. G. Wilson, and M. T. Keating, "Heart regeneration in zebrafish," *Science*, vol. 298, pp. 2188–2190, dec 2002.

[33] F. Chablais, J. Veit, G. Rainer, and A. Jawiska, "The zebrafish heart regenerates after cryoinjury-induced myocardial infarction," *BMC Developmental Biology*, vol. 11, p. 21, apr 2011.

[34] C. A. MacRae and R. T. Peterson, "Zebrafish as tools for drug discovery," *Nature Reviews Drug Discovery*, vol. 14, pp. 721–731, oct 2015.

[35] D. J. Milan, T. A. Peterson, J. N. Ruskin, R. T. Peterson, and C. A. MacRae, "Drugs that induce repolarization abnormalities cause bradycardia in zebrafish," *Circulation*, vol. 107, pp. 1355–1358, mar 2003.

[36] S. Srinivasan, H. S. Baldwin, O. Aristizabal, L. Kwee, M. Labow, M. Artman, and D. H. Turnbull, "Noninvasive, in utero imaging of mouse embryonic heart development with 40-MHz echocardiography.," *Circulation*, vol. 98, pp. 912–8, sep 1998.

[37] B. M. Tsui and D. L. Kraitchman, "Recent advances in small-animal cardiovascular imaging," *J Nucl Med*, vol. 50, pp. 667–670, may 2009.

[38] J. Laufer, F. Norris, J. Cleary, E. Zhang, B. Treeby, B. Cox, P. Johnson, P. Scambler, M. Lythgoe, and P. Beard, "In vivo photoacoustic imaging of mouse embryos," *Journal of Biomedical Optics*, vol. 17, no. 6, p. 061220, 2012.

[39] Y. Wang and G. Yao, "Optical tractography of the mouse heart using polarization-sensitive optical coherence tomography," *Biomedical Optics Express*, vol. 4, p. 2540, nov 2013.

[40] X. Qin, S. Wang, M. Shen, X. Zhang, S. Lerakis, M. B. Wagner, and B. Fei, "3Din vivoimaging of rat hearts by high frequency ultrasound and its application in myofiber orientation wrapping.," *Proceedings of SPIE–the International Society for Optical Engineering*, vol. 9419, 2015.

[41] S. A. Boppart, G. J. Tearney, B. E. Bouma, J. F. Southern, M. E. Brezinski, and J. G. Fujimoto, "Noninvasive assessment of the developing Xenopus cardiovascular system using optical coherence tomography," *Proc. Natl .Acad. Sci. USA*, vol. 94, pp. 4256–4261, apr 1997.

[42] B. Hogers, L. van der Weerd, H. Olofsen, L. van der Graaf, M. C. DeRuiter, A. C. Gittenberger-de Groot, and R. E. Poelmann, "Non-invasive tracking of avian development in vivo by MRI," *NMR in Biomedicine*, vol. 22, no. 4, pp. 365–373, 2009.

[43] F. Kober, T. Troalen, and M. Bernard, "Recent Developments in Small Animal Cardiovascular MRI," feb 2014.

[44] L. Sun, C. L. Lien, X. Xu, and K. K. Shung, "In Vivo Cardiac Imaging of Adult Zebrafish Using High Frequency Ultrasound (45-75 MHz)," *Ultrasound in Medicine and Biology*, vol. 34, pp. 31–39, jan 2008.

[45] P. Beard, "Biomedical photoacoustic imaging," *Interface Focus*, vol. 1, pp. 602–631, aug 2011.

[46] Q. Chen, T. Jin, W. Qi, X. Mo, and L. Xi, "Label-free photoacoustic imaging of the cardio-cerebrovascular development in the embryonic zebrafish," *Biomedical Optics Express*, vol. 8, p. 2359, apr 2017.

[47] R. Raghunathan, M. Singh, M. E. Dickinson, and K. V. Larin, "Optical coherence tomography for embryonic imaging: a review," *Journal of Biomedical Optics*, vol. 21, p. 050902, may 2016.

[48] A. L. Lopez, S. Wang, K. V. Larin, P. A. Overbeek, and I. V. Larina, "Live four-dimensional optical coherence tomography reveals embryonic cardiac phenotype in mouse mutant," *Journal of Biomedical Optics*, vol. 20, p. 090501, sep 2015.

[49] L. Kagemann, H. Ishikawa, J. Zou, P. Charukamnoetkanok, G. Wollstein, K. A. Townsend, M. L. Gabriele, N. Bahary, X. Wei, J. G. Fujimoto, and J. S. Schuman, "Repeated, noninvasive, high resolution spectral domain optical coherence tomography imaging of zebrafish embryos.," *Molecular vision*, vol. 14, no. November, pp. 2157–70, 2008.

[50] J. Jonkman and C. M. Brown, "Any way you slice it—A comparison of confocal microscopy techniques," *Journal of Biomolecular Techniques*, vol. 26, pp. 54–65, jul 2015.

[51] M. Minsky, "Memoir on inventing the confocal scanning microscope," *Scanning*, vol. 10, no. 4, pp. 128–138, 1988.

[52] S. Waldchen, J. Lehmann, T. Klein, S. Van De Linde, and M. Sauer, "Light-induced cell damage in live-cell super-resolution microscopy," *Scientific Reports*, vol. 5, p. 15348, oct 2015.

[53] M. Weber and J. Huisken, "In vivo imaging of cardiac development and function in zebrafish using light sheet microscopy," *Swiss Medical Weekly*, vol. 145, dec 2015.

[54] P. J. Keller, A. D. Schmidt, J. Wittbrodt, and E. H. Stelzer, "Reconstruction of zebrafish early embryonic development by scanned light sheet microscopy," *Science*, vol. 322, no. 5904, pp. 1065–1069, 2008.

[55] E. G. Reynaud, J. Peychl, J. Huisken, and P. Tomancak, "Guide to light-sheet microscopy for adventurous biologists," *Nature Methods*, vol. 12, pp. 30–34, jan 2014.

[56] Z. R. Siedentopf H., "Über Sichtbarmachung und Groessenbestimmung ultra-mikroskopischer Teilchen, mit besonderer Anwendung auf Goldrubinglaesern.," *Annalen der Physik*, vol. 10, pp. 1–39, 1903.

[57] J. Huisken and D. Y. R. Stainier, "Selective plane illumination microscopy techniques in developmental biology," *Development*, vol. 136, pp. 1963–1975, jun 2009.

[58] A. H. Voie, D. H. Burns, and F. A. Spelman, "Orthogonal-plane fluorescence optical sectioning: Three-dimensional imaging of macroscopic biological specimens," *Journal of Microscopy*, vol. 170, pp. 229–236, jun 1993.

[59] P. J. Keller and H. U. Dodt, "Light sheet microscopy of living or cleared specimens," feb 2012.

[60] J. Huisken, J. Swoger, F. Del Bene, J. Wittbrodt, and E. H. Stelzer, "Optical sectioning deep inside live embryos by selective plane illumination microscopy," *Science*, vol. 305, pp. 1007–1009, aug 2004.

[61] P. G. Pitrone, J. Schindelin, L. Stuyvenberg, S. Preibisch, M. Weber, K. W. Eliceiri, J. Huisken, and P. Tomancak, "OpenSPIM: An open-access light-sheet microscopy platform," jul 2013.

[62] P. A. Santi, "Light sheet fluorescence microscopy: A review," feb 2011.

[63] R. M. Power and J. Huisken, "A guide to light-sheet fluorescence microscopy for multiscale imaging," *Nature Methods*, vol. 14, pp. 360–373, apr 2017.

[64] O. E. Olarte, J. Andilla, E. J. Gualda, and P. Loza-Alvarez, "Light-sheet microscopy: a tutorial," *Advances in Optics and Photonics*, vol. 10, p. 111, mar 2018.

[65] A. J. Sehnert, A. Huq, B. M. Weinstein, C. Walker, M. Fishman, and D. Y. R. Stainier, "Cardiac troponin T is essential in sarcomere assembly and cardiac contractility," *Nature Genetics*, vol. 31, pp. 106–110, may 2002.

[66] S. S. Chopra, D. M. Stroud, H. Watanabe, J. S. Bennett, C. G. Burns, K. S. Wells, T. Yang, T. P. Zhong, and D. M. Roden, "Voltage-gated sodium channels are required for heart development in zebrafish," *Circulation Research*, vol. 106, pp. 1342–1350, apr 2010.

[67] D. Panáková, A. A. Werdich, and C. A. MacRae, "Wnt11 patterns a myocardial electrical gradient through regulation of the L-type Ca2+channel," *Nature*, vol. 466, pp. 874–878, aug 2010.

[68] D. W. Staudt, J. Liu, K. S. Thorn, N. Stuurman, M. Liebling, and D. Y. R. Stainier, "High-resolution imaging of cardiomyocyte behavior reveals two distinct steps in ventricular trabeculation," *Development*, vol. 141, pp. 585–593, feb 2014.

[69] J. R. Hove, R. W. Köster, A. S. Forouhar, G. Acevedo-Bolton, S. E. Fraser, and M. Gharib, "Intracardiac fluid forces are an essential epigenetic factor for embryonic cardiogenesis," *Nature*, vol. 421, pp. 172–177, jan 2003.

[70] H. J. Auman, H. Coleman, H. E. Riley, F. Olale, H. J. Tsai, and D. Yelon, "Functional modulation of cardiac form through regionally confined cell shape changes," *PLoS Biology*, vol. 5, pp. 0604–0615, feb 2007.

[71] M. Liebling, J. Vermot, A. S. Forouhar, M. Gharib, M. E. Dickinson, and S. E. Fraser, "Nonuniform temporal alignment of slice sequences for four-dimensional imaging of cyclically deforming embryonic structures," in *3rd IEEE International Symposium on Biomedical Imaging: Nano to Macro, 2006.*, pp. 1156–1159, April 2006.

[72] M. Liebling, A. S. Forouhar, R. Wolleschensky, B. Zimmermann, R. Ankerhold, S. E. Fraser, M. Gharib, and M. E. Dickinson, "Rapid three-dimensional imaging and analysis of the beating embryonic heart reveals functional changes during development," *Developmental Dynamics*, vol. 235, pp. 2940–2948, nov 2006.

[73] P. P. Laissue, R. A. Alghamdi, P. Tomancak, E. G. Reynaud, and H. Shroff, "Assessing phototoxicity in live fluorescence imaging," *Nature Methods*, vol. 14, pp. 657–661, jun 2017.

[74] B. Desjardins and E. A. Kazerooni, "ECG-Gated Cardiac CT," *American Journal of Roentgenology*, vol. 182, pp. 993–1010, apr 2004.

[75] S. S. Dhillon, É. Dóró, I. Magyary, S. Egginton, A. Sík, and F. Müller, "Optimisation of Embryonic and Larval ECG Measurement in Zebrafish for Quantifying the Effect of QT Prolonging Drugs," *PLoS ONE*, vol. 8, p. e60552, apr 2013.

[76] J. M. Taylor, "Optically gated beating-heart imaging," *Frontiers in Physiology*, vol. 5, p. 481, 2014.

[77] V. Vedula, J. Lee, H. Xu, C. C. Kuo, T. K. Hsiai, and A. L. Marsden, "A method to quantify mechanobiologic forces during zebrafish cardiac development using 4-D light sheet imaging and computational modeling," *PLoS Computational Biology*, vol. 13, p. e1005828, oct 2017.

[78] R. J. Adrian and J. Westerweel, *Particle Image Velocimetry*. Cambridge University Press, 2011.

[79] J. Westerweel, G. E. Elsinga, and R. J. Adrian, "Particle Image Velocimetry for Complex and Turbulent Flows," *Annual Review of Fluid Mechanics*, vol. 45, pp. 409–436, jan 2013.

[80] R. Lindken, M. Rossi, S. Große, and J. Westerweel, "Micro-Particle Image Velocimetry (μPIV): Recent developments, applications, and guidelines," *Lab on a Chip*, vol. 9, p. 2551, sep 2009.

[81] S. T. Wereley and C. D. Meinhart, "Recent Advances in Micro-Particle Image Velocimetry," *Annual Review of Fluid Mechanics*, vol. 42, no. 1, pp. 557–576, 2010.

[82] M. Raffel, C. E. Willert, S. T. Wereley, and J. Kompenhans, *Particle Image Velocimetry: A Practical Guide*. Springer, Berlin, Heidelberg, 2007.

[83] D. Fortun, P. Bouthemy, C. Kervrann, D. Fortun, P. Bouthemy, and C. Kervrann, "Optical flow modeling and computation : a survey To cite this version : Optical flow modeling and computation : a survey," *Computer Vision and Image Understanding*, vol. 134, pp. 1–21, 2015.

[84] T. Liu and L. Shen, "Fluid flow and optical flow," *Journal of Fluid Mechanics*, vol. 614, pp. 253–291, nov 2008.

[85] D. Heitz, E. Mémin, and C. Schnörr, "Variational fluid flow measurements from image sequences: Synopsis and perspectives," *Experiments in Fluids*, vol. 48, pp. 369–393, mar 2010.

[86] A. Doshi and A. G. Bors, "Robust processing of optical flow of fluids," *IEEE Transactions on Image Processing*, vol. 19, pp. 2332–2344, sep 2010.

[87] P. Vennemann, R. Lindken, and J. Westerweel, "In vivo whole-field blood velocity measurement techniques," *Experiments in Fluids*, vol. 42, pp. 495–511, mar 2007.

[88] M. G. Olsen and R. J. Adrian, "Out-of-focus effects on particle image visibility and correlation in microscopic particle image velocimetry," in *Experiments in Fluids*, vol. 29, pp. S166–S174, Springer-Verlag, dec 2000.

[89] A. S. Forouhar, M. Liebling, A. Hickerson, A. Nasiraei-Moghaddam, H. J. Tsai, J. R. Hove, S. E. Fraser, M. E. Dickinson, and M. Gharib, "The embryonic vertebrate heart tube is a dynamic suction pump," *Science*, vol. 312, pp. 751–753, may 2006.

[90] R. A. Jamison, A. Fouras, and R. J. Bryson-Richardson, "Cardiac-phase filtering in intracardiac particle image velocimetry," *Journal of Biomedical Optics*, vol. 17, no. 3, p. 036007, 2012.

[91] R. A. Jamison, C. R. Samarage, R. J. Bryson-Richardson, and A. Fouras, "In Vivo Wall Shear Measurements within the Developing Zebrafish Heart," *PLoS ONE*, vol. 8, p. e75722, oct 2013.

[92] B. Mustin and B. Stoeber, "Effect of linear image processing on the depth of correlation in micro PIV," *Experiments in Fluids*, vol. 55, p. 1817, sep 2014.

[93] J. Lu, F. Pereira, S. E. Fraser, and M. Gharib, "Three-dimensional real-time imaging of cardiac cell motions in living embryos," *Journal of Biomedical Optics*, vol. 13, no. 1, p. 014006, 2008.

[94] K. G. Chan and M. Liebling, "Estimation of divergence-free 3D cardiac blood flow in a zebrafish larva using multi-view microscopy," in *Proceedings - International Symposium on Biomedical Imaging*, vol. 2015-July, pp. 385–388, IEEE, apr 2015.

[95] F. Pereira and M. Gharib, "Defocusing digital particle image velocimetry and the three-dimensional characterization of two-phase flows," *Measurement Science and Technology*, vol. 13, pp. 683–694, may 2002.

[96] L. Fieramonti, E. A. Foglia, S. Malavasi, C. D'Andrea, G. Valentini, F. Cotelli, and A. Bassi, "Quantitative measurement of blood velocity in zebrafish with optical vector field tomography," *Journal of Biophotonics*, vol. 8, pp. 52–59, dec 2015.

[97] P. F. Davies, A. Remuzzi, E. J. Gordon, C. F. Dewey, and M. A. Gimbrone, "Turbulent fluid shear stress induces vascular endothelial cell turnover in vitro.," *Proceedings of the National Academy of Sciences of the United States of America*, vol. 83, pp. 2114–7, apr 1986.

[98] R. E. Poelmann, A. C. Gittenberger-de Groot, and B. P. Hierck, "The development of the heart and microcirculation: Role of shear stress," *Medical and Biological Engineering and Computing*, vol. 46, pp. 479–484, may 2008.

[99] L. D. Casa, D. H. Deaton, and D. N. Ku, "Role of high shear rate in thrombosis," apr 2015.

[100] M. M. Samyn and J. F. LaDisa, "Novel Applications of Cardiovascular Magnetic Resonance Imaging-Based Computational Fluid Dynamics Modeling in Pediatric Cardiovascular and Congenital Heart Disease," in *Assessment of Cellular and Organ Function and Dysfunction using Direct and Derived MRI Methodologies*, InTech, oct 2016.

[101] D. Katritsis, L. Kaiktsis, A. Chaniotis, J. Pantos, E. P. Efstathopoulos, and V. Marmarelis, "Wall Shear Stress: Theoretical Considerations and Methods of Measurement," *Progress in Cardiovascular Diseases*, vol. 49, pp. 307–329, mar 2007.

[102] E. Lauga, M. P. Brenner, and H. A. Stone, "Microfluidics: The no-slip boundary condition," in *Springer Handbook of Experimental Fluid Mechanics*, pp. 1219–1240, Berlin, Heidelberg: Springer Berlin Heidelberg, 2005.

[103] A. Sinha, G. C. Shit, and P. K. Kundu, "Slip Effects on Pulsatile Flow of Blood through a Stenosed Arterial Segment under Periodic Body Acceleration," *ISRN Biomedical Engineering, Hindawi Publishing Corporation*, vol. 2013, p. 10 pages, aug 2013.

[104] V. Mihalef, R. I. Ionasec, P. Sharma, B. Georgescu, I. Voigt, M. Suehling, and D. Comaniciu, "Patient-specific modelling of whole heart anatomy, dynamics and haemodynamics from four-dimensional cardiac CT images," *Interface Focus*, vol. 1, pp. 286–296, jun 2011.

[105] S. N. Doost, D. Ghista, B. Su, L. Zhong, and Y. S. Morsi, "Heart blood flow simulation: A perspective review," *BioMedical Engineering Online*, vol. 15, p. 101, aug 2016.

[106] E. Rozbicki, M. Chuai, A. I. Karjalainen, F. Song, H. M. Sang, R. Martin, H. J. Knölker, M. P. Macdonald, and C. J. Weijer, "Myosin-II-mediated cell shape changes and cell intercalation contribute to primitive streak formation," *Nature Cell Biology*, vol. 17, pp. 397–408, apr 2015.

[107] A. Melling, "Tracer particles and seeding for particle image velocimetry," *Measurement Science and Technology*, vol. 8, no. 12, pp. 1406–1416, 1997.

[108] O. Linderkamp, E. Friederichs, T. Boehler, and A. Ludwig, "Age dependency of red blood cell deformability and density: studies in transient erythroblastopenia of childhood," *British Journal of Haematology*, vol. 83, pp. 125–129, jan 1993.

[109] F. Pedocchi, J. E. Martin, and M. H. García, "Inexpensive fluorescent particles for large-scale experiments using particle image velocimetry," *Experiments in Fluids*, vol. 45, no. 1, p. 183, 2008.

[110] R. D. Keane and R. J. Adrian, "Theory of cross-correlation analysis of PIV images," *Applied Scientific Research*, vol. 49, no. 3, pp. 191–215, 1992.

[111] J. Westerweel, "Fundamentals of digital particle image velocimetry," *Measurement Science and Technology*, vol. 8, no. 12, pp. 1379–1392, 1997.

[112] C. E. Willert and M. Gharib, "Digital particle image velocimetry," *Experiments in Fluids*, vol. 10, pp. 181–193, jan 1991.

[113] J. Westerweel, *Digital particle image velocimetry: Theory and application.* PhD thesis, 1993.

[114] S. E. Bulau, "Simulations Of Various Centroiding Algorithms," vol. 0627, p. 680, International Society for Optics and Photonics, oct 1986.

[115] N. Bobroff, "Position measurement with a resolution and noise-limited instrument," *Review of Scientific Instruments*, vol. 57, pp. 1152–1157, jun 1986.

[116] A. Patwardhan, "Subpixel position measurement using 1D, 2D and 3D centroid algorithms with emphasis on applications in confocal microscopy," *Journal of Microscopy*, vol. 186, pp. 246–257, jun 1997.

[117] H. Nobach and M. Honkanen, "Two-dimensional Gaussian regression for sub-pixel displacement estimation in particle image velocimetry or particle position estimation in particle tracking velocimetry," *Experiments in Fluids*, vol. 38, pp. 511–515, apr 2005.

[118] O. Ronneberger, M. Raffel, and J. Kompenhans, "Advanced evaluation algorithms for standard and dual plane particle image velocimetry.," in *9th international symposium on applications of laser techniques*, 1998.

[119] J. Westerweel, D. Dabiri, and M. Gharib, "The effect of a discrete window offset on the accuracy of cross-correlation analysis of digital PIV recordings," *Experiments in Fluids*, vol. 23, pp. 20–28, may 1997.

[120] J. Westerweel, "On velocity gradients in PIV interrogation," *Experiments in Fluids*, vol. 44, pp. 831–842, may 2008.

[121] D. Di Florio, F. Di Felice, and G. P. Romano, "Windowing, re-shaping and re-orientation interrogation windows in particle image velocimetry for the investigation of shear flows," *Measurement Science and Technology*, vol. 13, pp. 953–962, jul 2002.

[122] A. K. Prasad, R. J. Adrian, C. C. Landreth, and P. W. Offutt, "Effect of resolution on the speed and accuracy of particle image velocimetry interrogation," *Experiments in Fluids*, vol. 13, pp. 105–116, jun 1992.

[123] A. Sciacchitano and B. Wieneke, "PIV uncertainty propagation," *Measurement Science and Technology*, vol. 27, p. 084006, aug 2016.

[124] I. Azijli, A. Sciacchitano, D. Ragni, A. Palha, and R. P. Dwight, "A posteriori uncertainty quantification of PIV-based pressure data," *Experiments in Fluids*, vol. 57, p. 72, may 2016.

[125] J. Chen and J. Katz, "Elimination of peak-locking error in PIV analysis using the correlation mapping method," *Measurement Science and Technology*, vol. 16, pp. 1605–1618, aug 2005.

[126] E. Overmars, N. Warncke, C. Poelma, and J. Westerweel, "Bias errors in PIV: the pixel locking effect revisited," *International Symposium on Applications of Laser Techniques to Fluid Mechanics*, pp. 5–8, 2010.

[127] P. E. Freudenthal, M. Pommer, C. D. Meinhart, and B. D. Piorek, "Quantum nanospheres for sub-micron particle image velocimetry," *Experiments in Fluids*, vol. 43, no. 4, pp. 525–533, 2007.

[128] J. Santiago, S. Wereley, and C. Meinhart, "A particle image velocimetry system for microfluidics," *Experiments in Fluids*, vol. 25, pp. 316–319, 1998.

[129] C. D. Meinhart, S. T. Wereley, and J. G. Santiago, "A PIV algorithm for estimating time-averaged velocity fields," *Journal of Fluids Engineering*, vol. 122, no. June 2000, pp. 285–289, 2000.

[130] C. J. Bourdon, M. G. Olsen, and A. D. Gorby, "The depth of correlation in micro-PIV for high numerical aperture and immersion objectives," *Journal of Fluids Engineering-Transactions of the Asme*, vol. 128, no. 4, pp. 883–886, 2006.

[131] M. G. Olsen, "Directional dependence of depth of correlation due to in-plane fluid shear in microscopic particle image velocimetry," *Measurement Science and Technology*, vol. 20, no. 1, pp. 15402–9, 2009.

[132] M. G. Olsen, "Depth of correlation reduction due to out-of-plane shear in microscopic particle image velocimetry," *Measurement Science and Technology*, vol. 21, p. 105406, oct 2010.

[133] B. Mustin and B. Stoeber, "On the effect of velocity gradients on the depth of correlation in μPIV," *Measurement Science and Technology*, vol. 27, p. 035302, mar 2016.

[134] J. Huisken and D. Y. R. Stainier, "Even fluorescence excitation by multidirectional selective plane illumination microscopy (mSPIM)," *Optics Letters*, vol. 32, p. 2608, sep 2007.

[135] V. Zickus and J. M. Taylor, "3D + time blood flow mapping using SPIM-microPIV in the developing zebrafish heart," *Biomedical Optics Express*, vol. 9, pp. 2418–2435, may 2018.

[136] F. O. Fahrbach, V. Gurchenkov, K. Alessandri, P. Nassoy, and A. Rohrbach, "Light-sheet microscopy in thick media using scanned Bessel beams and two-photon fluorescence excitation," *Optics Express*, vol. 21, p. 13824, jun 2013.

[137] T. Vettenburg, H. I. C. Dalgarno, J. Nylk, C. Coll-Lladó, D. E. K. Ferrier, T. Čižmár, F. J. Gunn-Moore, and K. Dholakia, "Light-sheet microscopy using an Airy beam," *Nature Methods*, vol. 11, pp. 541–544, may 2014.

[138] E. Hecht, *Optics*. Addison-Wesley, 4th ed., 2002.

[139] D. Hill, "How to Convert FWHM Measurements to 1/e-Squared Halfwidths." http://customers.zemax.com/os/resources/learn/knowledgebase/how-to-convert-fwhm-measurements-to-1-e-squared-ha, 2007. [Online; accessed 8-April-2018].

[140] J. Schindelin, I. Arganda-Carreras, E. Frise, V. Kaynig, M. Longair, T. Pietzsch, S. Preibisch, C. Rueden, S. Saalfeld, B. Schmid, J.-Y. Tinevez, D. J. White, V. Hartenstein, K. Eliceiri, P. Tomancak, and A. Cardona, "Fiji: an open-source platform for biological-image analysis," *Nature Methods*, vol. 9, pp. 676–682, jul 2012.

[141] G. van Rossum, "Python tutorial," 1995.

[142] I. H. . S. LLC, "Fittings Primer." https://www.idex-hs.com/education-and-tools/educational-materials/fittings-primer, 2016. [Online; accessed 6-February-2018].

[143] B. Wieneke, "PIV uncertainty quantification from correlation statistics," *Measurement Science and Technology*, vol. 26, p. 074002, jul 2015.

[144] S. P. Sutera and R. Skalak, "The History of Poiseuille's Law," *Annual Review of Fluid Mechanics*, vol. 25, pp. 1–20, jan 1993.

[145] E. K. Fishman, D. R. Ney, D. G. Heath, F. M. Corl, K. M. Horton, and P. T. Johnson, "Volume Rendering versus Maximum Intensity Projection in CT Angiography: What Works Best, When, and Why," *RadioGraphics*, vol. 26, no. 3, pp. 905–922, 2006.

[146] C. Poelma, A. Kloosterman, B. P. Hierck, and J. Westerweel, "Accurate Blood Flow Measurements: Are Artificial Tracers Necessary?," *PLoS ONE*, vol. 7, p. e45247, sep 2012.

[147] S. J. Williams, C. Park, and S. T. Wereley, "Advances and applications on microfluidic velocimetry techniques," jun 2010.

[148] C. Cierpka and C. J. Kähler, "Particle imaging techniques for volumetric three-component (3D3C) velocity measurements in microfluidics," feb 2012.

[149] F. Strobl, S. Klees, and E. H. K. Stelzer, "Light Sheet-based Fluorescence Microscopy of Living or Fixed and Stained Tribolium castaneum Embryos," *Journal of Visualized Experiments*, apr 2017.

[150] C. B. Kimmel, W. W. Ballard, S. R. Kimmel, B. Ullmann, and T. F. Schilling, "Stages of embryonic development of the zebrafish," *Developmental Dynamics*, vol. 203, pp. 253–310, jul 1995.

[151] M. Weber, M. Mickoleit, and J. Huisken, "Multilayer Mounting for Long-term Light Sheet Microscopy of Zebrafish," *Journal of Visualized Experiments*, p. e51119, feb 2014.

[152] M. A. Denvir, C. S. Tucker, and J. J. Mullins, "Systolic and diastolic ventricular function in zebrafish embryos: Influence of norepenephrine, MS-222 and temperature," *BMC Biotechnology*, vol. 8, p. 21, feb 2008.

[153] R. Kopp, B. Pelster, and T. Schwerte, "How does blood cell concentration modulate cardiovascular parameters in developing zebrafish (Danio rerio)?," *Comparative Biochemistry and Physiology - A Molecular and Integrative Physiology*, vol. 146, pp. 400–407, mar 2007.

[154] M. P. Craig, S. D. Gilday, D. Dabiri, and J. R. Hove, "An Optimized Method for Delivering Flow Tracer Particles to Intravital Fluid Environments in the Developing Zebrafish," *Zebrafish*, vol. 9, no. 3, pp. 108–119, 2012.

[155] H. Anton, S. Harlepp, C. Ramspacher, D. Wu, F. Monduc, S. Bhat, M. Liebling, C. Paoletti, G. Charvin, J. B. Freund, and J. Vermot, "Pulse propagation by a capacitive mechanism drives embryonic blood flow," *Development*, vol. 140, pp. 4426–4434, nov 2013.

[156] M. Mickoleit, B. Schmid, M. Weber, F. O. Fahrbach, S. Hombach, S. Reischauer, and J. Huisken, "High-resolution reconstruction of the beating zebrafish heart," *Nature Methods*, vol. 11, pp. 919–922, sep 2014.

[157] Y. Sugii, S. Nishio, and K. Okamoto, "In vivo PIV measurement of red blood cell velocity field in microvessels considering mesentery motion.," *Physiological measurement*, vol. 23, pp. 403–16, may 2002.

[158] H. J. Klose, E. Volger, H. Brechtelsbauer, L. Heinich, and H. Schmid-Schönbein, "Microrheology and light transmission of blood - I. The photometric effects of red cell aggregation and red cell orientation," *Pflügers Archiv European Journal of Physiology*, vol. 333, no. 2, pp. 126–139, 1972.

[159] J. Lee, T. C. Chou, D. Kang, H. Kang, J. Chen, K. I. Baek, W. Wang, Y. DIng, D. D. Carlo, Y. C. Tai, and T. K. Hsiai, "A Rapid Capillary-Pressure Driven Micro-Channel to Demonstrate Newtonian Fluid Behavior of Zebrafish Blood at High Shear Rates," *Scientific Reports*, vol. 7, p. 1980, may 2017.

[160] R. J. Trudnowski and R. C. Rico, "Specific gravity of blood and plasma at 4 and 37 °c," *Clinical Chemistry*, vol. 20, no. 5, pp. 615–616, 1974.

[161] M. B. Bouchard, V. Voleti, C. S. Mendes, C. Lacefield, W. B. Grueber, R. S. Mann, R. M. Bruno, and E. M. C. Hillman, "Swept confocally-aligned planar excitation (SCAPE) microscopy for high-speed volumetric imaging of behaving organisms," *Nature Photonics*, vol. 9, pp. 113–119, feb 2015.

[162] O. E. Olarte, J. Andilla, D. Artigas, and P. Loza-Alvarez, "Decoupled illumination detection in light sheet microscopy for fast volumetric imaging," *Optica*, vol. 2, p. 702, aug 2015.

[163] V. Zickus and J. Taylor, "4D blood flow mapping using SPIM-microPIV in the developing zebrafish heart," in *Progress in Biomedical Optics and Imaging - Proceedings of SPIE* (T. G. Brown, C. J. Cogswell, and T. Wilson, eds.), vol. 10499, p. 40, SPIE, feb 2018.

[164] L. A. Samsa, B. Yang, and J. Liu, "Embryonic cardiac chamber maturation: Trabeculation, conduction, and cardiomyocyte proliferation," *American Journal of Medical Genetics, Part C: Seminars in Medical Genetics*, vol. 163, pp. 157–168, aug 2013.

[165] S. J. Rasouli and D. Y. Stainier, "Regulation of cardiomyocyte behavior in zebrafish trabeculation by Neuregulin 2a signaling," *Nature Communications*, vol. 8, p. 15281, may 2017.

[166] F. Boselli, J. B. Freund, and J. Vermot, "Blood flow mechanics in cardiovascular development," jul 2015.